



**HAL**  
open science

# Data-driven discovery approach to tackle turbulence in fusion plasmas

Luigui Salazar

► **To cite this version:**

Luigui Salazar. Data-driven discovery approach to tackle turbulence in fusion plasmas. Physics [physics]. Université de Lorraine, 2023. English. NNT : 2023LORR0327 . tel-04584452

**HAL Id: tel-04584452**

**<https://hal.univ-lorraine.fr/tel-04584452>**

Submitted on 23 May 2024

**HAL** is a multi-disciplinary open access archive for the deposit and dissemination of scientific research documents, whether they are published or not. The documents may come from teaching and research institutions in France or abroad, or from public or private research centers.

L'archive ouverte pluridisciplinaire **HAL**, est destinée au dépôt et à la diffusion de documents scientifiques de niveau recherche, publiés ou non, émanant des établissements d'enseignement et de recherche français ou étrangers, des laboratoires publics ou privés.



**UNIVERSITÉ  
DE LORRAINE**

**BIBLIOTHÈQUES  
UNIVERSITAIRES**

## AVERTISSEMENT

Ce document est le fruit d'un long travail approuvé par le jury de soutenance et mis à disposition de l'ensemble de la communauté universitaire élargie.

Il est soumis à la propriété intellectuelle de l'auteur. Ceci implique une obligation de citation et de référencement lors de l'utilisation de ce document.

D'autre part, toute contrefaçon, plagiat, reproduction illicite encourt une poursuite pénale.

Contact bibliothèque : [ddoc-theses-contact@univ-lorraine.fr](mailto:ddoc-theses-contact@univ-lorraine.fr)  
*(Cette adresse ne permet pas de contacter les auteurs)*

## LIENS

Code de la Propriété Intellectuelle. articles L 122. 4

Code de la Propriété Intellectuelle. articles L 335.2- L 335.10

[http://www.cfcopies.com/V2/leg/leg\\_droi.php](http://www.cfcopies.com/V2/leg/leg_droi.php)

<http://www.culture.gouv.fr/culture/infos-pratiques/droits/protection.htm>

# Data-driven discovery approach to tackle turbulence in fusion plasmas

## THÈSE

présentée et soutenue publiquement le 14 décembre 2023

pour l'obtention du

**Doctorat de l'Université de Lorraine**

**Spécialité: Physique des plasmas**

par

Luigui Salazar

### Composition du jury

<i>Président :</i>	M. Etienne Gravier	Professeur des Universités, IJL, Université de Lorraine
<i>Rapporteurs :</i>	M. Zwinglio de Oliveira	Professeur des Universités, FAP, Universidade de São Paulo
	Mme. Laure Vermare	Chargée de recherche, LPP, École polytechnique
<i>Examineur :</i>	M. Jorge Morales	Chercheur, IRFM, CEA-Cadarache
<i>Invités :</i>	M. John Edward Rice	Professeur des Universités, PSFC, Massachusetts Institute of Technology
	M. Andreas Krämer-Flecken	Chercheur, IEK-4, Forschungszentrum-Jülich
<i>Directeur :</i>	M. Stéphane Heuraux	Professeur des Universités, IJL, Université de Lorraine
	M. Roland Sabot	Directeur de recherche, IRFM, CEA-Cadarache

## Abstract

One way to achieve fusion on Earth is through toroidal magnetic confinement, in which the main devices are tokamaks and stellarators.

One of the main limiting phenomena is turbulence. This is the result of a mixture of instabilities on different temporal and spatial scales interacting with the plasma properties to produce what is known as turbulent transport.

This thesis aims to contribute to the understanding of turbulent transport using a data-driven approach. Data-driven approaches, such as machine learning and data analysis, offer the opportunity to take advantage of the vast amounts of data generated by various diagnostic tools. The data-driven approach can help to integrate and extract valuable information from these different data sources. Data-driven approaches can also enable the transfer of knowledge and models between different fusion devices, accelerating progress and benefiting the wider fusion research community.

Among the spectrum of instabilities inducing this phenomenon, only the core of these toroidally magnetised plasmas is considered, as is the focus of this work, where electrostatic turbulence ( $\tilde{\phi}$ ) is considered over magnetic turbulence ( $\tilde{B}$ ).

The main instabilities in this context are the Ion Temperature Gradient (ITG) modes, the Trapped Electron Modes (TEM) and the Electron Temperature Gradient (ETG) modes. At low wave numbers  $k_{\perp}$  normalised to the Larmor radius  $\rho_i$  ( $0.1 < k_{\perp}\rho_i < 1$ ) the dominant micro-instabilities are the ITG and the TEM. An important property of these electrostatic modes is that they both have a threshold above which they are unstable. Since the ITG and TEM are driven by different gradients, they can either both be stable, or both coexist, or give way to a single dominant mode (ITG or TEM).

It has been found that these different instabilities produce different turbulent transport behaviours, so it becomes imperative to be able to distinguish them in order to improve the understanding of turbulent transport.

The aim is then to distinguish between these different instabilities coexisting on the same scales. During the ohmic regime of these toroidally magnetised plasmas, observations have been made showing 2 sub-regimes, the Linear Ohmic Confinement (LOC) and the Saturated Ohmic Confinement (SOC), on which some investigations have been carried out showing the potential discrimination of TEM and ITG, in fact the fluctuation spectrum in these 2 sub-regimes are different, narrow-band signature in LOC and broadband signature in SOC, the first signature would be made by TEM and the second one by ITG.

To investigate this phenomenon further, reflectometry was used as a diagnostic tool to probe the plasma and relate the signal produced to these signatures in the fluctuation spectrum.

---

The reflectometry signal spectrum has several spectral components: The Low Frequency (LF) component, the Broadband (BB) component, the noise and also a narrow band mode referred to as Quasi-Coherent (QC) modes in the LOC sub-regime, then these QC modes would be directly related to the TEM.

Gyrokinetic analysis and identification by observation were used to investigate this relationship, which was then validated in some fusion devices, but limited to a certain number of discharges. This highlights the need for a refined methodology not only to identify these QC modes but also to extract them, to access their properties and to try to validate this relationship between QC modes and TEM through a comprehensive statistical study. On the other hand, it is also necessary to go into their QC dynamics to have a deeper understanding of the QC modes, because it is believed that analysing the energy exchange with other modes in the QC dynamics could reveal a signature of the mechanism behind it, so if all QC modes are related to TEM, they should have the same dynamic signature.

This thesis focuses on the analysis of these reflectometry signals, which exhibit non-stationarity, non-ergodicity and non-determinism, in order to perform a discrimination of the spectral components.

This work is considered exploratory because there were no methods to access the properties and dynamics of the spectral components, so this analysis aims to integrate signal processing methods with machine learning techniques, a field that is developing in plasma fusion.

An algorithm then extracts each of these spectral components. The algorithm part for the QC modes mainly follows a roadmap such as data cleaning, data transformation and feature extraction, the first step is to discriminate only signals in the framework of fixed frequency reflectometry, the second step is to transform the signal with continuous wavelet transform to obtain a representation in time scale or frequency scale, the third step is to extract the QC modes from there.

The low frequency component and the broadband component are mainly extracted using the Asymmetric Generalised Gaussian (AGG) and signal reconstruction, where the sum of each spectral component must be equal to the original signal.

The noise is extracted following a pink noise behaviour.

The properties of the QC modes are then analysed not only in different fusion devices (tokamaks and stellarators), but more generally in different magnetic configurations: Tore-Supra (limiter), WEST (divertor) and W7X (island divertor).

The analysis started with the ToreSupra(TS) database. The results of this statistical study show a clear decrease in the ratio of the energy content in the QC modes to the energy content

in the broadband component, from the LOC to the SOC sub-regimes, however some sets of QC modes still appear in and after this transition.

From this, a probability of occurrence map of QC modes was constructed, showing a clear high probability of occurrence associated with the LOC sub-regime, more accentuated in the LFS, but also represented at a lower level in the HFS. This strengthens the relationship between QC modes and TEM. Furthermore, other QC modes were found outside the LOC sub-regime, 2 additional 'classes', one at low current and another at high current.

Spectral descriptors and the multifractal spectrum were used to characterise the QC modes properties. No distinction could be made because many QC modes properties among these three clusters were similar.

To confirm this behaviour, the analysis was extended to the WEST database. The algorithm was then generalised for the context of multi-magnetic configurations.

Clusters were also found in the probability of occurrence map that were similar to the clusters found in ToreSupra, but with lower probability values.

For a more refined analysis using both databases, the position of the  $q=1$  surface was taken as a reference, as it is thought to act as a barrier transport. A high energy content in the LF component was widely found, raising the question of whether the LF component could interact with the QC modes; this high energy behaviour was found in both the LOC and SOC regimes and was located within the  $q = 1$  surface.

Other global properties were also analysed, such as the evolution of the probability of occurrence of the QC modes over  $n_e$ , to show the predominance of the QC modes in these ohmic sub-regimes.

The broadband component was also analysed, as it is believed to be related to the microturbulence. The spectral amplitude of the broadband (BB) component, as determined by the AGG, is mainly characterised by the parameters  $\mu$  and  $\beta$ . These parameters, representing spectral asymmetry and shape respectively, show variations during the transition.

On the other hand, the analysis of the dynamics of the QC modes by means of an algorithm developed in this thesis showed a recurrent interaction between the QC modes and the modes in the LF component.

Thanks to this algorithm, the energy evolution is obtained, visually showing "the energy transfer" from the LF component to the QC modes. For a deeper analysis, the central frequency of these modes in interaction and their frequency bandwidth are also calculated to study their dynamics.

Finally, in order to better discriminate the QC modes, the concept of transfer entropy is used to analyse the causality in this interaction. In most cases where the energy content in the LF is high, it is the latter that causes the QC modes. Taking first the ToreSupra database,

some cases belonging to this phenomenon are those in which it seems that the mode in the LF component corresponds to the sawtooth instability, its different phases are observed and correlated with the energy evolution using the developed algorithm.

All this analysis of dynamics and also causality is then applied to Tore Supra, WEST and W7X, where there is a similar dynamic for signals with bi-directional causality, i.e. not only from the LF component to the QC modes, but also from the QC modes to the BB component.

In addition, electron cyclotron resonance heating (ECRH) is studied for the TS database, which shows a decrease in the probability of QC modes as the ECRH power increases.

Since these QC modes occur in different magnetic configurations, the ultimate goal is to discover whether all these QC modes are produced by the same mechanism, since it is believed that there must be a universal mechanism underlying the physics in fusion plasmas.

## Résumé étendu

Afin de réaliser la fusion sur Terre, l'un des moyens pour y parvenir est le confinement magnétique toroïdal dont les principales configurations sont les tokamaks et les stellarators.

L'un des paramètres principaux limitant la fusion sur Terre est la turbulence, qui résulte d'un mélange d'instabilités à différentes échelles temporelles et spatiales, qui interagissent avec les propriétés du plasma pour produire ce que l'on appelle le transport turbulent.

Parmi le spectre de ces instabilités, seules celles qui interagissent dans le cœur du plasma sont prises en considération dans cette thèse. Au cœur du plasma, la turbulence électrostatique domine sur la turbulence magnétique.

Les principales instabilités dans ce contexte sont les Ion Température Gradient (ITG), les Trapped Electron Mode (TEM) et Electron Température Gradient (ETG). A faible nombre d'onde  $k_{\perp}$  normalisé au rayon de Larmor  $\rho_i$  ( $0.1 < k_{\perp}\rho_i < 1$ ) les micro-instabilités dominantes sont les ITG et les TEM. Une propriété importante de ces modes électrostatiques est qu'ils ont tous deux un seuil au-dessus duquel ils sont instables. Comme les ITG et les TEM sont excités par des gradients différents, ils peuvent soit être stables tous les deux, soit coexister, soit céder la place à un seul mode dominant (ITG ou TEM).

Il a été constaté que ces différentes instabilités produisent des comportements de transport turbulent différents, il devient donc impératif de pouvoir les distinguer afin d'améliorer la compréhension du transport turbulent.

Il est donc important de discriminer ces différentes instabilités coexistant aux mêmes échelles. Dans un plasma de tokamak en régime ohmique, i.e. chauffé uniquement pas le courant circulant dans le plasma, les observations montrent qu'il existe deux sous-régimes, le Linear Ohmic Confinement (LOC) et le Saturated Ohmic Confinement (SOC). Des investigations ont été menées montrant la discrimination potentielle entre les TEM et les ITG à partir du spectre de fluctuation de densité dans ces 2 sous-régimes sont différents, une signature à bande étroite dans le sous-régime LOC et une signature à bande large dans le sous-régime SOC, la première signature serait faite par les TEM et la seconde par les ITG.

Afin d'étudier ce phénomène, la réflectométrie à fréquence fixe a été utilisée comme outil de diagnostic pour sonder le plasma et relier ce signal de réflectométrie produit aux signatures dans le spectre de fluctuation. Le spectre du signal de réflectométrie comporte plusieurs composantes spectrales : La composante Low Frequency (LF), la composante Broad Band (BB), le bruit et également un mode à bande étroite appelé modes Quasi-Cohérents (QC).

Un lien entre les modes QC et les TEM a été identifié dans le régime LOC par des analyses expérimentales dans plusieurs tokamaks et confirmé par quelques simulations gyrocinétique. Les analyses expérimentales étaient limitées à un nombre de décharges.

---

Cela souligne la nécessité d'une méthodologie pour une étude statistique complète non seulement pour identifier ces modes QC, mais aussi pour les extraire, accéder à leurs propriétés et tenter de valider cette relation entre les modes QC et le TEM. D'autre part, il est également nécessaire d'étudier leur dynamique afin de mieux comprendre les modes QC, car une analyse d'échange d'énergie avec d'autres modes pourrait révéler une signature du mécanisme sous-jacent, de sorte que si tous les modes QC sont liés aux TEM, ils devraient avoir la même signature dynamique.

Cette thèse se concentre sur l'analyse de ces signaux de réflectométrie qui sont non-stationnaires, non ergodiques et non-déterministes, afin d'effectuer une discrimination des différentes composantes spectrales. Cette thèse est qualifiée d'exploratoire car il n'existait pas de méthodes pour accéder aux propriétés et à la dynamique de ces modes QC. Cette analyse vise donc à intégrer des méthodes de traitement du signal avec des techniques de Machine Learning, un domaine qui se développe dans le domaine des plasmas de fusion.

Dans la thèse, un algorithme a été développé afin d'extraire donc chacun de ces composants spectraux. Cet algorithme suit principalement trois étapes: data cleaning, data transformation et feature extraction.

La première étape consiste à éliminer les mesures aberrantes (bruit trop fort, signal réfléchi trop faible, etc.). Une méthode du semi-supervised learning (branche du machine learning) appelée label propagation a été utilisée, à partir d'un groupe des données bien identifiées cette méthode arrive à les propager à l'aide du kernel k-nearest neighbors (KNN). Finalement les bons signaux sont identifiés et sélectionnés.

La deuxième étape consiste à transformer le signal avec la transformée en ondelettes continue (CWT) pour obtenir une représentation en temps-échelle ou à temps-fréquence. Nous avons choisi d'utiliser l'ondelette de Morlet complexe pour ses propriétés d'analyse des signaux fluctuants complexes.

La troisième étape est la méthode d'extraction dans la CWT, les échelles les plus prédominantes sont choisies à partir de la courbe de densité d'énergie en fonctions des échelles, dans cette bande d'échelles une méthode de unsupervised learning est appliquée (Minibatch K-means) afin d'extraire seulement les coefficients qui correspondent aux modes QC.

La composante spectrale LF et la composante spectrale BB sont principalement extraites à l'aide de la gaussienne généralisée asymétrique (AGG) et de la reconstruction du signal, où la somme de chaque composante spectrale doit être égale au signal d'origine.

Le bruit est extrait au début de l'algorithme, sa densité spectrale de puissance suit un comportement de bruit rose.

Les propriétés des modes QC sont ensuite analysées non seulement dans différents dispositifs de confinement magnétique (tokamaks et stellarators), mais plus généralement

dans différentes configurations magnétiques : Tore Supra (limiteur), WEST (divertor) et W7X (Island divertor).

L'analyse a commencé par la base de données Tore Supra. Les résultats de cette étude statistique montrent une nette diminution du rapport entre le contenu énergétique des modes QC et le contenu énergétique de la composante BB, dans la transition du régime LOC au régime SOC, bien que certains ensembles de modes QC apparaissent encore pendant et après cette transition.

À partir de là, une carte de probabilité d'occurrence des modes QC a été construite, montrant clairement une forte probabilité d'occurrence en régime LOC, plus accentuée dans le coté externe (Low Field Side), mais également représentée à un niveau plus faible dans le coté interne (High Field Side). Ces observations confortent le lien entre les modes QC et les instabilités TEM. Néanmoins, en régime LOC, des modes QC peuvent être observés et 2 classes, l'une à faible courant et l'autre à fort courant ont été identifiées.

Les descripteurs spectraux et le spectre multifractale ont été utilisés pour caractériser les propriétés des modes QC. Certaines de ces propriétés des modes QC se sont avérées similaires entre ces trois classes. Des analyses complémentaires étaient donc nécessaires pour différencier ces trois classes.

Pour confirmer ce lien entre les modes QC et les TEM, l'analyse a été étendue à la base de données WEST, l'algorithme a ensuite été généralisé afin de s'appliquer à différentes configurations magnétiques. Pour séparer les régimes LOC et SOC une échelle empirique appelée échelle de Rice est utilisée. Des classes de modes QC ont également été trouvées dans la carte des probabilités d'occurrence, qui sont similaires aux classes trouvées dans Tore Supra, mais à un faible niveau de probabilité. En fait, les statistiques de WEST sont inférieures à celles de Tore Supra.

Pour une analyse approfondie, prenant en compte les deux bases de données, la surface  $q=1$  a été prise comme référence, car en régime ohmique, elle peut être vue comme une barrière de transport, séparant ainsi différents comportements de transport turbulent. Un contenu énergétique élevé dans la composante LF a été largement constaté à l'intérieur de la surface  $q=1$ , ce qui a soulevé la question de savoir si la composante LF pouvait interagir avec les modes QC, ce comportement énergétique élevé ayant été constaté à la fois dans les régimes LOC et SOC.

D'autres propriétés globales ont également été analysées, telles que l'évolution de la probabilité d'occurrence des modes QC en fonction de la densité électronique, pour montrer la prédominance des modes QC dans ces sous-régimes ohmiques.

---

La composante BB qui est liée à la microturbulence a aussi été étudiée. L'asymétrie ( $\mu$ ) et la forme spectrale ( $\beta$ ) de cette composante, approximée par une fonction gaussienne assymétrique généralisée, varient pendant la transition.

D'autre part, l'analyse de la dynamique des modes QC à l'aide d'un algorithme développé dans cette thèse a montré une interaction récurrente entre les modes QC et les modes de la composante LF.

Grâce à cet algorithme, l'évolution de l'énergie est obtenue, montrant visuellement le transfert d'énergie de la composante LF vers les modes QC. Pour une analyse plus approfondie, la fréquence centrale de ces modes en interaction et leur largeur de bande sont également calculées pour étudier leur dynamique.

Enfin, pour mieux distinguer les modes QC, le concept de Transfer d'entropie (TE) est utilisé pour analyser la causalité dans cette interaction. Le TE quantifie le degré d'incertitude réduit dans la prévision des valeurs futures d'un signal en fonction de la connaissance d'un autre signal. En termes plus simples, dans le cas de deux signaux,  $A_t$  et  $B_t$ , si la connaissance du passé de  $A_t$  aide à prédire l'avenir de  $B_t$  mieux que la simple connaissance du passé de  $B_t$  lui-même, cela suggère une influence causale directionnelle de  $A_t$  vers  $B_t$ .

Dans la plupart des cas où le contenu énergétique du LF est élevé, c'est ce dernier qui provoque les modes QC. En prenant d'abord la base de données Tore Supra, certains cas appartenant à ce phénomène sont ceux dans lesquels il semble que le mode dans la composante LF corresponde à l'instabilité sawtooth, ses différentes phases sont observées et corrélées avec l'évolution de l'énergie à l'aide de l'algorithme développé. Par contre il est encore difficile de savoir s'il y a une relation directe entre cette instabilité et les modes QC, il se peut que ce soit les sawtooths qui provoquent un changement de gradient et que celui-ci guide les modes QC, ce qui est sûr est qu'il y a un interplay entre les 2. Toute cette analyse de la dynamique et de la causalité est ensuite appliquée à ToreSupra, WEST et W7X, où l'on observe une dynamique similaire pour les signaux montrant une cascade de causalité, c'est-à-dire non seulement de la composante LF vers les modes QC, mais aussi des modes QC vers la composante BB.

L'effet du chauffage cyclotron électronique (ECRH) est également examiné pour la base de données TS. On observe une diminution de la probabilité des modes QC à mesure que la puissance ECRH augmente ainsi qu'une interaction entre les QC modes et la LF lors du passage du chauffage ECRH au chauffage ohmique.

Des investigations sont menées pour voir si le taux de particules piégées est en lien avec la génération des QC. En outre cette recherche montre bien la nécessité de choisir les bons signaux en fonction de leur dynamique afin de rentrer dans un contexte où potentiellement il y aurait un seul mécanisme sous-jacent.

Comme ces modes QC apparaissent dans différentes configurations magnétiques, l'objectif ultime est de découvrir si tous ces modes QC sont produits par le même mécanisme, car on pense qu'il doit y avoir un mécanisme universel qui sous-tend la physique dans les plasmas de fusion.

## Acknowledgements

The work presented in this manuscript is the result of my doctoral research. It has been an incredible journey and I am grateful for the support and guidance I have received along the way.

First and foremost, I would like to thank my supervisors, Stéphane Heuraux of the Institut Jean Lamour (IJL) and Roland Sabot of the IRFM CEA Cadarache, for their mentorship and expertise throughout my research. Their support, feedback and commitment to the advancement of plasma physics have been instrumental in shaping this thesis.

I would also like to thank my research colleagues at IJL and IRFM CEA Cadarache. The collaborative and intellectually stimulating environment has fostered my growth as a scientist.

I would like to acknowledge the financial support provided by the Region Lorraine and the IRFM CEA-Cadarache, which made this research possible. Their commitment to the advancement of scientific knowledge is commendable.

I would like to thank all my family and my friends, and during the writing of this manuscript, my girlfriend, for their encouragement and understanding during this challenging journey.

**I dedicate this thesis to my parents, Carlos Salazar and Doris Cabrera, and my brother, Mateo Salazar. Their support, motivation and unwavering love have been the foundation of my life's achievements. A special dedication goes to my mother, Doris Cabrera, who not only encouraged my academic pursuits, but also always raised me to be an excellent person in every aspect of life. Mamá, this achievement is as much yours as it is mine.**

Thank you all for being part of this chapter of my academic and professional life.



# Table of contents

<b>1</b>	<b>Introduction</b>	<b>1</b>
1.1	Energy issues in the society . . . . .	1
1.2	Nuclear fusion . . . . .	2
1.2.1	Nuclear fusion in the Sun . . . . .	3
1.2.2	Nuclear fusion on Earth, a challenge . . . . .	4
1.3	Fusion with Magnetic Confinement . . . . .	8
1.3.1	General motion of charged particles . . . . .	8
1.3.2	Magnetic configuration : Tokamak and Stellarator . . . . .	10
1.3.3	Trapped and passing particles . . . . .	13
1.3.4	Heating systems . . . . .	17
1.3.5	Confinement regimes . . . . .	19
<b>2</b>	<b>Turbulence and transport</b>	<b>23</b>
2.1	Transport in Tokamaks and Stellarators . . . . .	24
2.1.1	Classical and Neoclassical transport . . . . .	24
2.1.2	Turbulent transport . . . . .	26
2.2	Electrostatic turbulence . . . . .	26
2.2.1	Drift-wave turbulence . . . . .	27
2.2.2	Interchange modes . . . . .	28
2.2.3	Zonal flows and Geodesic acoustic modes . . . . .	29
2.2.4	Micro-instabilities . . . . .	29
2.3	MHD activities . . . . .	32
2.4	Quasi-coherent (QC) modes . . . . .	35
2.5	Looking for universality . . . . .	35
2.5.1	Turbulence dynamics characterised by energy exchange . . . . .	35
2.5.2	Focus of PhD Research . . . . .	37

<b>3</b>	<b>Diagnostics: Reflectometry</b>	<b>39</b>
3.1	Propagation of electromagnetic waves in the plasma . . . . .	40
3.1.1	Plasma assumptions . . . . .	40
3.1.2	Propagation equations . . . . .	41
3.1.3	Polarisation modes . . . . .	42
3.1.4	Different regions of wave propagation . . . . .	43
3.2	Fixed-frequency conventional reflectometry . . . . .	45
3.3	Physical phenomena associated with density fluctuations . . . . .	47
3.4	Poloidal correlation reflectometry (PCR) . . . . .	48
3.5	Experimental setup . . . . .	51
3.5.1	Tore Supra-WEST Tokamaks . . . . .	52
3.5.2	TEXTOR Tokamak . . . . .	53
3.5.3	W7X Stellarator . . . . .	53
3.6	Reflectometry signal spectrum . . . . .	55
3.7	Previous study . . . . .	60
<b>4</b>	<b>Intelligent signal processing approach</b>	<b>65</b>
4.1	Generalities on Machine learning (ML) . . . . .	66
4.1.1	Potentialities of AI/ML . . . . .	67
4.1.2	Application to plasma science . . . . .	68
4.2	Integrating ML and signal processing . . . . .	70
4.2.1	Data cleaning . . . . .	71
4.2.2	Data transformation . . . . .	71
4.2.3	Data dimensionality reduction . . . . .	75
4.2.4	Feature extraction . . . . .	76
4.2.5	Analysis and classification . . . . .	80
4.3	How to have access to QC modes properties and dynamics . . . . .	82
<b>5</b>	<b>Application for distinguishing spectral components</b>	<b>85</b>
5.1	Extraction of each spectral component . . . . .	86
5.1.1	Selection of signals according to CFR . . . . .	86
5.1.2	Noise estimation . . . . .	88
5.1.3	Extraction of the QC modes and extension to any narrow-band spectral mode . . . . .	90
5.1.4	Extraction of the LF component and BB component . . . . .	94
5.2	Preserving physical and statistical properties . . . . .	96
5.2.1	LOC-SOC transition . . . . .	96

5.2.2	Short Range Poloidal Correlation (SRPC) . . . . .	99
5.3	Towards multi-magnetic configuration study . . . . .	102
<b>6</b>	<b>Dynamics &amp; Properties of Quasi-Coherent Modes in different magnetic configurations</b>	<b>103</b>
6.1	Systematic analysis of QC modes in ohmic plasmas . . . . .	104
6.1.1	QC modes likelihood of occurrence . . . . .	104
6.1.2	Predominance of the QC modes in and outside $q = 1$ . . . . .	108
6.1.3	Energy content of QC modes on LFS and HFS . . . . .	110
6.2	QC mode classes in connection with LF and BB components . . . . .	112
6.2.1	Distinction between QC mode classes . . . . .	112
6.2.2	QC mode relationships with microturbulence at different $\rho$ and $q$ . . . . .	119
6.2.3	Energy content in the LF component at different $\rho$ and $q$ . . . . .	124
6.3	Dynamics of QC modes and energy exchange with other components . . . . .	126
6.3.1	Algorithm for the study of energy exchange . . . . .	126
6.3.2	Tracking of QC modes' intrinsic spectral bandwidth over time . . . . .	129
6.3.3	Evidence of energy exchange between components using causality . . . . .	130
6.3.4	QC modes in interaction with sawtooth . . . . .	130
6.3.5	Dynamics across different magnetic configurations . . . . .	131
6.4	QC modes characteristics in ECRH plasmas . . . . .	135
6.5	Are QC modes properties and dynamics driven by universal mechanism? . . . . .	135
<b>7</b>	<b>Conclusion &amp; Perspectives</b>	<b>139</b>
7.1	Conclusion . . . . .	139
7.2	Perspectives . . . . .	141
7.2.1	QC mode excitation and stabilisation . . . . .	141
7.2.2	Classes of QC Modes and extension to MHD modes . . . . .	142
7.2.3	Further developments to improve the energy exchange studies . . . . .	143
7.2.4	Other applications of our algorithms . . . . .	144
	<b>References</b>	<b>145</b>
	<b>Appendix A Exploratory phase for spectral components discrimination</b>	<b>159</b>
A.1	First attempt: direct classification . . . . .	159
A.2	Second attempt: data cleaning . . . . .	160
A.3	Third attempt: data transformation . . . . .	161

<b>Appendix B</b>	<b>Extraction of the QC modes: Initial algorithm</b>	<b>165</b>
B.1	Screening technique . . . . .	166
B.2	Clustering technique . . . . .	169
<b>Appendix C</b>	<b>Spectral decomposition of the LF component</b>	<b>173</b>

# Chapter 1

## Introduction

### Contents

---

<b>1.1</b>	<b>Energy issues in the society</b>	<b>1</b>
<b>1.2</b>	<b>Nuclear fusion</b>	<b>2</b>
1.2.1	Nuclear fusion in the Sun	3
1.2.2	Nuclear fusion on Earth, a challenge	4
<b>1.3</b>	<b>Fusion with Magnetic Confinement</b>	<b>8</b>
1.3.1	General motion of charged particles	8
1.3.2	Magnetic configuration : Tokamak and Stellarator	10
1.3.3	Trapped and passing particles	13
1.3.4	Heating systems	17
1.3.5	Confinement regimes	19

---

### 1.1 Energy issues in the society

Throughout human history, the search for new sources of energy has been a paramount challenge. While we have been able to tap into certain energy sources for a time, we have also faced energy crises that have driven us to search for alternatives. In 2008, oil prices reach their highest level 147 dollars/bbl [1]. Since a few years ago energy markets began to tighten because of a variety of factor including the extraordinarily rapid economic rebound following the pandemic. But the situation got worse into a full-blown global energy crisis following Russia's invasion of Ukraine in February 2022. The price of natural gas reached

record highs, and as a result so did electricity in some markets. Oil prices hit their highest level since 2008.

Today's energy crisis compared to the 1970's is quite different because it involves all fossil fuels, also the entire world economy is much more interlinked than it was 50 years ago, we can refer to this as the first truly global energy crisis.

As society's energy demands continue to grow, it has become increasingly clear that we must seek out sustainable solutions to meet them. In fact, experts estimate that humans demand for primary energy will have grown 25% by 2040, and will be close to doubling by the end of the century. These predicted scenarios will required an investment of more than 2 trillion dollars per year in new energy sources according to the World Energy Outlook 2018, published by the International Energy Agency (IEA) [2]. If this amount is not reached and a viable solution is not found it could lead to a large-scale energy crisis.

Through the process of searching for new energy sources, we got ourselves drawing inspiration from the nature. Indeed, throughout human history nature provides us with a vast array of efficient and optimized systems, processes, and designs that have evolved over billions of years.

Different energy sources have been explored then. Among all of these, the fusion power stands out as the principal one: safe, clean and "limitless".

## 1.2 Nuclear fusion

Nuclear fusion is the process by which two light atomic nuclei combine to form a single heavier one, releasing massive amounts of energy in the process.

Similar to nuclear fission, which has been used to generate electricity for many years, nuclear fusion releases energy by converting mass into energy, following Einstein's famous equation:

$$\Delta E = \Delta m \cdot c^2 \tag{1.1}$$

Significantly, neither fusion nor fission emits carbon dioxide or other greenhouse gases, making it an environmentally friendly energy solution. Fusion and fission involve changes in the atomic nucleus. In fission, energy is produced by splitting heavy nuclei, such as uranium, into lighter elements. Unlike fission, fusion reactions are not chain reactions, so there is no risk of divergence. Both fission and fusion involve changes in nuclear binding energy [see figure 1.1]. In fission, energy is released when the binding energy of the resulting fragments is greater than that of the original nucleus. In fusion, energy is released when the binding

energy of the resulting nucleus is greater than the combined binding energy of the original nuclei.

In general, nuclear reactions yield substantial amounts of energy. This is because the binding energy between protons and neutrons, governed by the strong force interaction, is immense, orders of magnitude greater than the chemical bond energies involved in combustion processes.

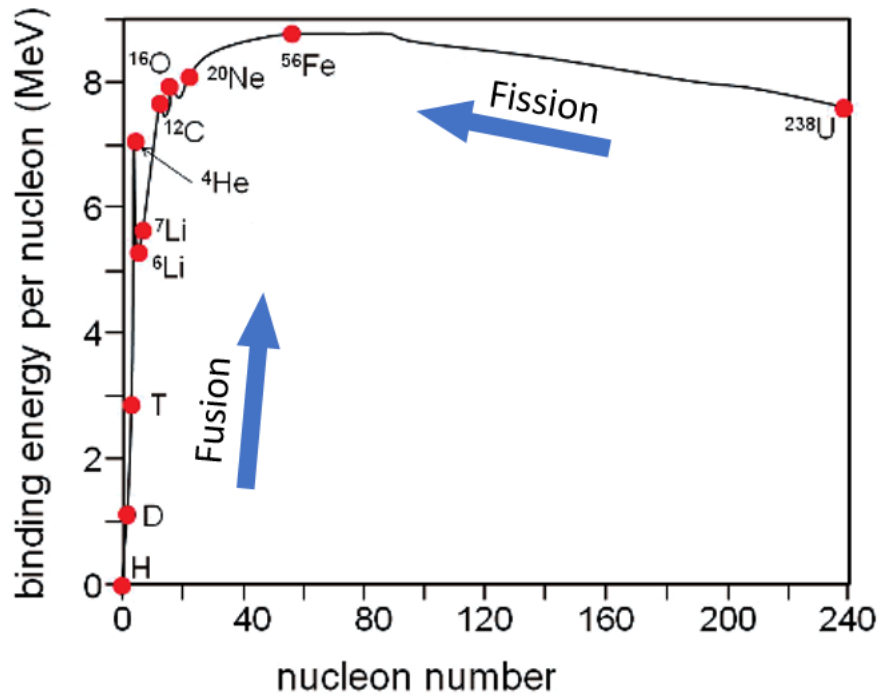


Fig. 1.1 Binding energy per nucleon as a function of the nucleon number

### 1.2.1 Nuclear fusion in the Sun

The sun, along with all other stars, is powered by nuclear fusion. For fusion to happen in our sun, nuclei need to collide with each other at extremely high temperatures, around ten million degrees Celsius. The high temperature provides them with enough energy to overcome their mutual electrical repulsion. Once the nuclei come within a very close range of each other, the attractive nuclear force between them will outweigh the electrical repulsion and allow them to fuse. For this to happen, the nuclei must be confined within a small space to increase the chances of collision. In the sun, the extreme pressure produced by its immense gravity creates the conditions for fusion. This fusion process goes through several stages for the main fusion reaction, as shown in the figure 1.2:

Two protons unite to form deuterium also called heavy hydrogen (D or  $2\text{H}$ , a hydrogen atom whose nucleus has a proton, but also a neutron), while emitting a positron ( $e^+$ ) and a neutrino ( $\nu$ ). Deuterium captures a proton for form helium 3 ( ${}^3\text{He}$ ) by issuing a gamma ray ( $\gamma$ ). Finally, the reaction of two helium 3 produces helium 4 ( ${}^4\text{He}$ ) and two protons. Each of these reactions converts mass to kinetic energy according to the Einstein formula [equation 1.1]. Finally, the transformation of hydrogen into helium is done.

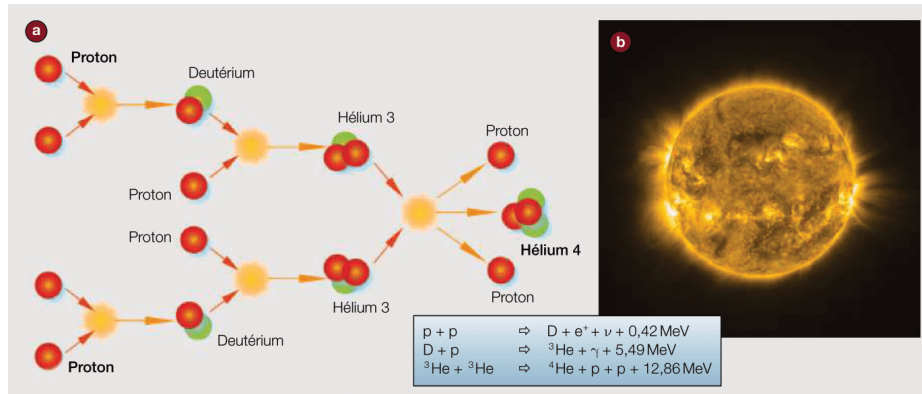


Fig. 1.2 (a) Stages of the main fusion reaction (proton-proton chain) that takes place on (b) the Sun.

## 1.2.2 Nuclear fusion on Earth, a challenge

Indeed, recreating the conditions for fusion on Earth is highly challenging compared to the natural processes occurring in the Sun. The confinement needed on Earth has to occur in a significantly reduced space and over a much shorter duration than it does in the Sun. Employing fusion reactions to build a system that yields energy requires the execution of a huge number of such reactions every second. This involves keeping the nuclei in close confinement and preventing the plasma, a state of matter that makes up more than 99% of the known matter in the universe, from flying apart by confining it for a period long enough to allow a significant number of fusion reactions to take place.

While the Sun's massive gravitational force naturally induces fusion as described previously, achieving such a reaction on Earth requires even higher temperatures due to the absence of comparable gravitational forces. On Earth, we need temperatures of over 100 million degrees Celsius to make deuterium and tritium fuse [see figure 1.3], while sustaining the fusion reaction long enough to produce more energy than was needed to start the reaction.

### The nuclear process

Nuclear fusion could generate four times more energy per kilogram of fuel than fission and nearly four million times more energy than burning oil or coal. Most of the fusion reactor concepts under development will use a mixture of deuterium and tritium, hydrogen atoms that contain extra neutrons. In theory, with just a few grams of these reactants, it is possible to produce a terajoule of energy, which is approximately the energy one person in a developed country needs over sixty years.

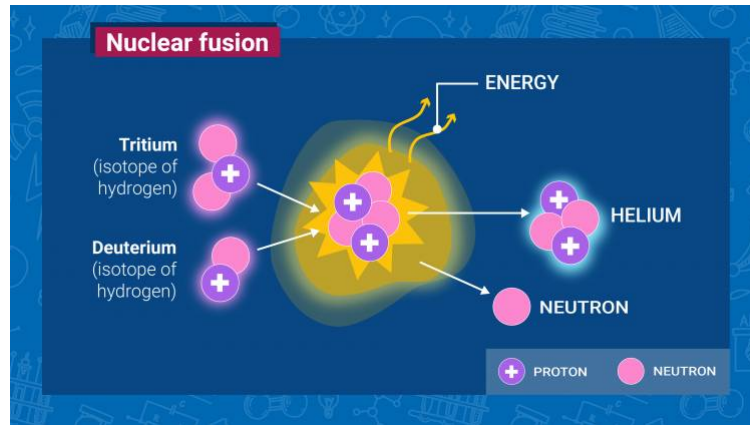


Fig. 1.3 Nuclear fusion reaction on Earth. Adapted from IAEA Nuclear fusion.

Deuterium can be obtained cheaply from seawater, while tritium is currently produced as a by-product of the Canadian pressurised heavy water reactor. In a fusion reactor, tritium is produced in situ from the reaction between the neutron from the D-T reaction and lithium (Li).

This Deuterium-Tritium reaction can be described as follows:



The energy is liberated in form of kinetic energy of the neutron and the Helium, where the neutron carries 80% of the energy due to momentum conservation.

Therefore the energy obtained from the fusion processes has to be greater than the energy to heat the plasma to such high temperatures. Hence it is required a minimum density  $n$  together with a sufficient energy confinement time  $\tau_E$ , this latter can be considered basically as a thermal relaxation time [3] and has extensively been studied. The product of the two quantities with the temperature  $T$  is required to overcome a certain threshold given by the Lawson criterion :

$$nT\tau_e > 3 \times 10^{21} \text{ m}^{-3} \text{ keVs}^{-1} \quad (1.3)$$

This condition ensures that the rate of energy production through fusion reactions is greater than the rate at which energy is lost from the plasma.

### **Two main types of confinement methods**

With the aim of developing a viable fusion reactor, two essential methods have been pursued. Each of these striving to meet the Lawson criterion via distinct approaches.

- **Inertial confinement (ICF):** The confinement times are extremely short, but particle densities are remarkably high. A minimal amount of fusible material is compressed to extremely high densities and temperatures by the application of powerful laser beams. This is done using a capsule consisting of a spherical shell filled with deuterium-tritium gas [4]. The two most important examples of inertial confinement are the National Ignition Facility [5] and the Laser Mega Joule [6].
- **Magnetic confinement (MCF):** It seeks to confine plasma at relatively low densities for extended periods of time, with a focus on maintaining stability and confinement over time. The underlying principle of this confinement method is the application of an appropriate magnetic field, which is possible due to the charged state of the particles within the high-temperature plasma [7].

While MCF is generally more mature and has achieved significant plasma temperatures and confinement times, ICF has the potential for high energy densities, but it suffers of poor efficiency to generate powerful compressor beams and a too low repetition rate to reach the requirements for a fusion power plant.

### **A potential plan**

The main example of the attempt to achieve fusion on Earth is the ITER project (International Thermonuclear Experimental Reactor), the world's largest project based on the tokamak concept: it's a partnership between the European Union, China, Japan, Russia, India, South Korea and the United States.

As the head of the Experimental Physics Department of the National Fusion Laboratory at CIEMAT explains, this development will take place in three phases:

- **Short term:** Construction of ITER, research and development program in support of ITER, deuterium-tritium operation in the JET tokamak in the self-heating regime; design of DEMO (a demonstration nuclear fusion reactor); construction of a device for the validation of fusion materials (IFMIF-DONES) and development of the stellarator line.

- Medium term: First scientific/technological exploitation of ITER. First scientific/technological use of IFMIF-DONES; engineering design of DEMO; development of the stellarator concept and development of reactor technology and materials.
- Long term: Optimisation and integration of ITER physics and technology; completion of DEMO design and construction; demonstration of electrical production and commercialisation of fusion technology and the industrial phase of fusion.

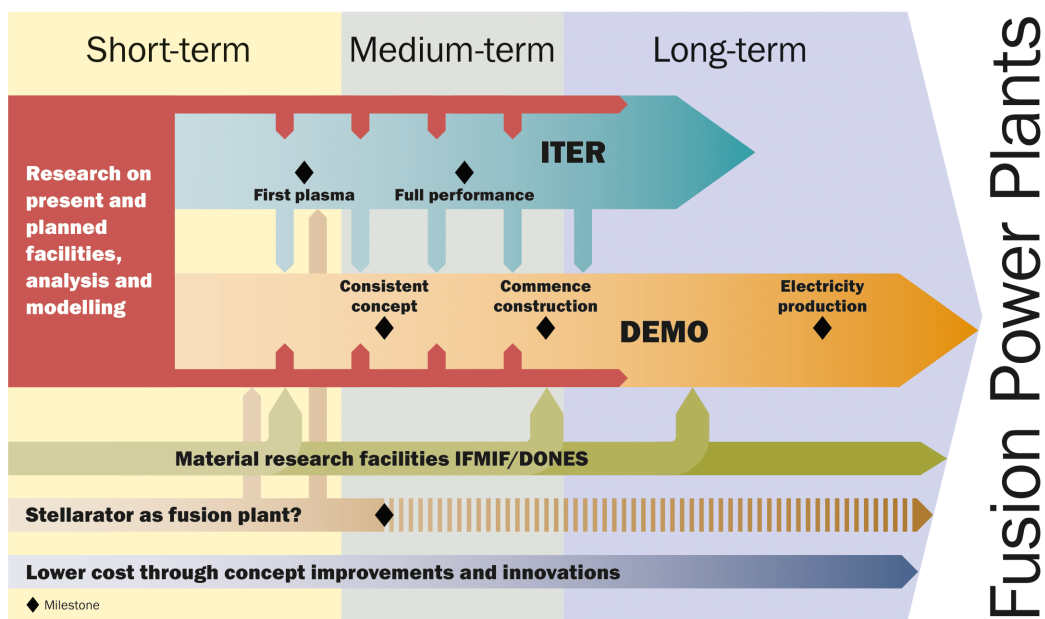


Fig. 1.4 European Roadmap of nuclear fusion on Earth

While ITER is a major international research project, it is not the only one. Other notable projects include laser-induced fusion research at the Lawrence Livermore National Laboratory in the USA, the Experimental Advanced Superconducting Tokamak (EAST) on Science Island in the Chinese province of Anhui, and the Wendelstein 7-X Stellarator (W7X) in Germany. The Massachusetts Institute of Technology (MIT) has committed itself to the SPARC project, a high magnetic field tokamak based on high-temperature superconductors, the aim of which is to create, within about 15 years, a power station capable of producing enough heat to continuously generate 200MW, enough energy to supply a city of about 200,000 people, without producing  $CO_2$  in the process of generating the energy [8].

Research is also being carried out into other cross sectional magnetic configurations, such as negative triangularity, which appear to hold great promise as a candidate reactor configuration due to their improved confinement [9].

However, all current projects have long timelines and, according to Johannes Schwemmer, Director of Fusion for Energy (the European agency managing the ITER project), fusion power will not be industrialised and commercialised until at least 2060 [8].

Ultimate success also depends on a steady flow of investment. The ITER project alone is estimated to cost €22 billion. However, over 80% of this investment is in components that the partner countries will build within their own industries. The European Union is funding 45.6% of the project, with the remainder divided equally between the other 6 partners. The United Kingdom has been excluded from the ITER project because it refused to remain part of the Euratom agreement after Brexit.

The ultimate goal of international research is to develop fusion power plants that are safe, reliable, sustainable, environmentally responsible and economically viable.

Overall, fusion can only take place under strict operating conditions, and if these conditions are not met, for example in the event of an accident or system failure, the plasma would naturally cease to exist. It would quickly lose its energy and extinguish, preventing any permanent damage to the reactor. Creating these conditions for fusion on Earth requires the development of inherently safe fusion devices that are not expected to produce high activity or long-lived nuclear waste. This thesis focuses on magnetic confinement, specifically tokamaks and stellarators.

## 1.3 Fusion with Magnetic Confinement

As mentioned previously, magnetic confinement is based on the application of an appropriate magnetic field for a prolonged period of time. When a magnetic field is applied, the charged particles of the plasma are forced into helical trajectories along the field lines, allowing limited lateral and unrestricted longitudinal motion to avoid wall contact.

### 1.3.1 General motion of charged particles

This state of matter, previously referred to as "plasma", is a hot, charged gas of positive ions and free-moving electrons with unique properties that distinguish it from solids, liquids or gases. The plasma state is a unique phase of matter in which long-range electromagnetic interactions between particles dominate over short-range interatomic or intermolecular forces.

Plasma physics includes statistical physics, relativity, atomic physics, molecular physics, nuclear physics, etc.

In a defined magnetic confinement configuration, a fundamental plasma parameter is the plasma frequency or electron plasma frequency, which represents the collective behaviour of the electrons, depends on the electron density ( $n_e$ ) and is independent of the magnetic field strength ( $B$ ).

$$\omega_{pe} = \sqrt{\frac{n_e q_e^2}{m_e \epsilon_0}} \quad (1.4)$$

where  $n_e$ ,  $q_e$ ,  $m_e$  are the electron density, electron charge and electron mass respectively,  $\epsilon_0$  is the vacuum permittivity.

The charged particles undergo the so-called gyro-motion in which they follow the magnetic field lines as showed in the figure 1.5, and can drift if a force exists.

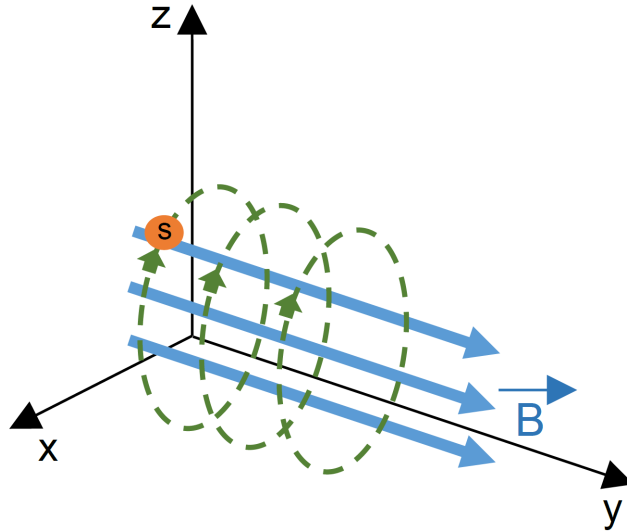


Fig. 1.5 Gyro-motion of a charged particle "s" in a uniform magnetic field  $B$

In the direction parallel to  $B$ , the parallel velocity ( $v_{\parallel}$ ) of the particle is constant. In the direction perpendicular to  $B$ , the particle undergoes a gyro motion with velocity  $v_{\perp}$ , and in relation to this, the cyclotron frequency  $\omega_{cs}$  can be defined as:

$$\omega_{cs} = \frac{q_s B}{m_s} \quad (1.5)$$

where  $q_s$  and  $m_s$  corresponds to the particle charge and the particle mass respectively,  $B$  is the magnitude of the magnetic field. The characteristic radius i.e. the gyro-radius is described by:

$$\rho_s = \frac{m_s v_{\perp}}{q_s B} \quad (1.6)$$

The properties of the motion of these particles are of great importance for understanding the phenomena in our study.

Overall, the aim is to create a suitable magnetic configuration, preferably with a toroidal shape, to keep the particles in a closed orbit. However, the decreasing field strength with radius causes the particles to drift outwards. It is therefore necessary to twist the field lines to compensate for the radial field component. Several concepts for toroidal confinement are being pursued, of which this thesis focuses on the tokamak and the stellarator.

### 1.3.2 Magnetic configuration : Tokamak and Stellarator

The objective is to have an equilibrium between the plasma pressure and the magnetic forces, so it is relevant to find an adequate way to twist the magnetic field, in other words it is necessary to have a rotational transform ( $\iota$ ) of the toroidal magnetic field.

Spitzer[10] and Mercier[11] proposed three methods for this twisting of the toroidal magnetic field: creating a poloidal field with a toroidal current, changing the poloidal cross section around the torus, and making the magnetic axis non-planar. Tokamaks achieve this twist with a toroidal plasma current  $I_p$ , while stellarators typically use the last two methods with external non-axisymmetric coils.

In tokamaks, the primary magnetic field is the toroidal field  $B_{\phi}$ ; a poloidal magnetic field  $B_{\theta}$  is also required as a vertical magnetic field to ensure the stability of the tokamak plasma. The combination of these magnetic fields produces magnetic field lines that follow a helical trajectory around the torus, as shown in the figure 1.6. These field lines are wound on torii, called magnetic surfaces, which are nested around a magnetic axis. The toroidal magnetic field is generated by toroidal coils while the generation of the poloidal magnetic field is induced by the  $I_p$  current circulating within the plasma. This  $I_p$  current is induced by a central solenoid, analogous to a transformer [figure 1.6], and the other poloidal coils are used to control the position and shape of the plasma.

Stellarators, on the other hand, are inherently current-less and therefore able to maintain the plasma in a steady state.

The geometric parameters also differ between tokamaks and stellarators. Tokamaks typically have an aspect ratio  $\frac{R_0}{a}$  (where  $R_0$  and  $a$  represent the major and minor radii, respectively) in the range of 2.5 to 6; this value is even smaller for spherical tokamaks. Conversely, stellarators are designed to have small rotational transforms per period to avoid

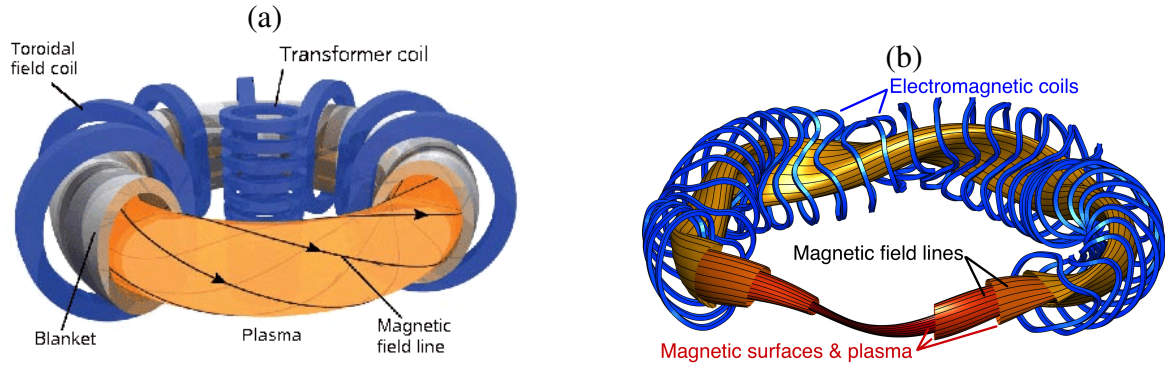


Fig. 1.6 Schematics of magnetically confined plasmas in (a) tokamaks; (b) stellarator configurations. In the tokamak, the rotational transform of a helical magnetic field is formed by a toroidal field produced by external coils together with a poloidal field produced by the plasma current. In the stellarator, the twist field is generated entirely by external non-axisymmetric coils.

resonances between the field lines and harmonics of the configuration symmetry, leading to much larger aspect ratios (in the range of 5 to 12) in contemporary stellarators.

In tokamaks, the rotational transformation is often replaced by its inverse, the safety factor  $q = 2\pi/\iota$ . If  $q$  is a rational number, the field line will return to its starting point after a finite number of toroidal rotations. The safety factor is a measure of the helicity of the magnetic field and can be defined in a circular plasma as follows:

$$q = \frac{rB_\phi}{R_0B_\theta} \quad (1.7)$$

A further difference lies in the shape of the plasma cross-section. In tokamaks, the plasma cross-section is toroidally symmetric, while in a three-dimensional stellarator the shape varies as a function of the toroidal angle [see figure 1.6].

A more detailed schematic representation of tokamaks is given in figure 1.7. The magnitude of  $B_\phi$  decreases with increasing major radius ( $B_\phi \propto 1/R_0$ ). Consequently, the magnetic field has an inherent gradient  $\nabla B$ , which is always directed towards the axis of rotation [see figure 1.11]. This characteristic gives rise to the nomenclature where the outer region of the torus is referred to as the Low Field Side (LFS), while the inner region is referred to as the High Field Side (HFS).

In these different magnetic configurations, the plasma is thus confined within closed magnetic flux surfaces, and as the closed magnetic fields open there is a boundary called the separatrix, this second region between the plasma and the machine wall components is commonly referred to as the scrape-off layer (SOL), which is defined by a solid surface (limiter) or topologically by magnetic field perturbations (divertor) [see figure 1.8].

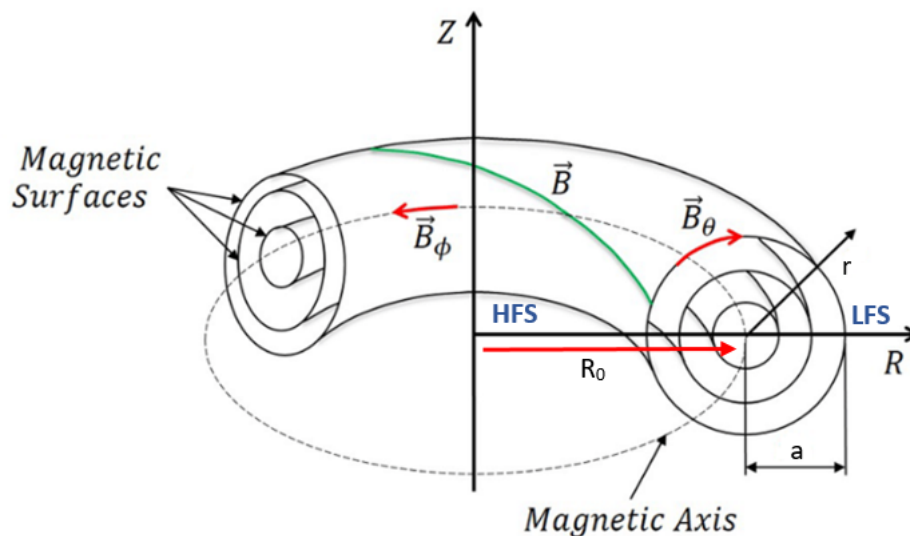


Fig. 1.7 Illustration of a simple circular tokamak cross section to define the basic parameters of the tokamak configuration.

In the divertor configuration, plasma particles and energy leaving the confinement region are directed to the divertor target plate by open field lines. For the poloidal divertor in tokamaks, the separatrix of the SOL is formed by additional poloidal magnetic field coils, which break up the nested flux surfaces into a single or double null divertor configuration.

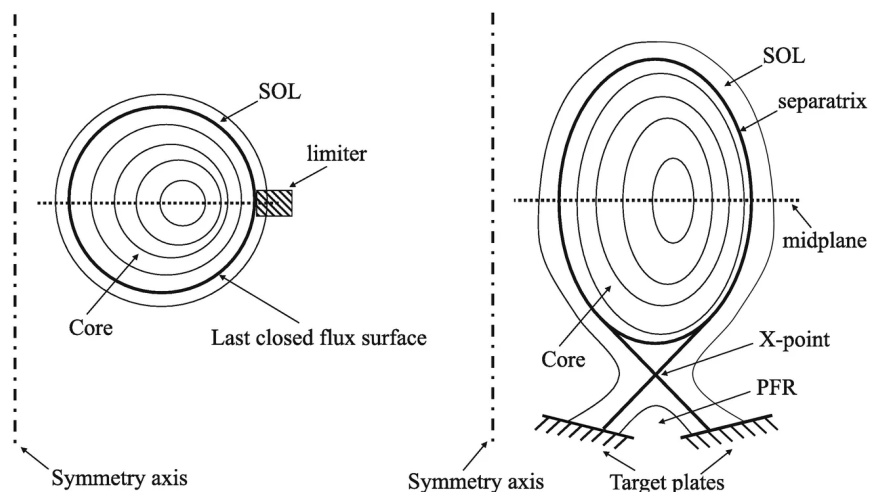


Fig. 1.8 Cross-section of Limiter and Divertor magnetic configurations.

In the case of stellarators, another design is proposed, the Island divertor. The divertor configuration is intrinsically developed on the basis of special edge magnetic structures

arising from the small radial field resonant with the rational surface [12]. However, stellarator divertor geometries may differ depending on the global magnetic shear.

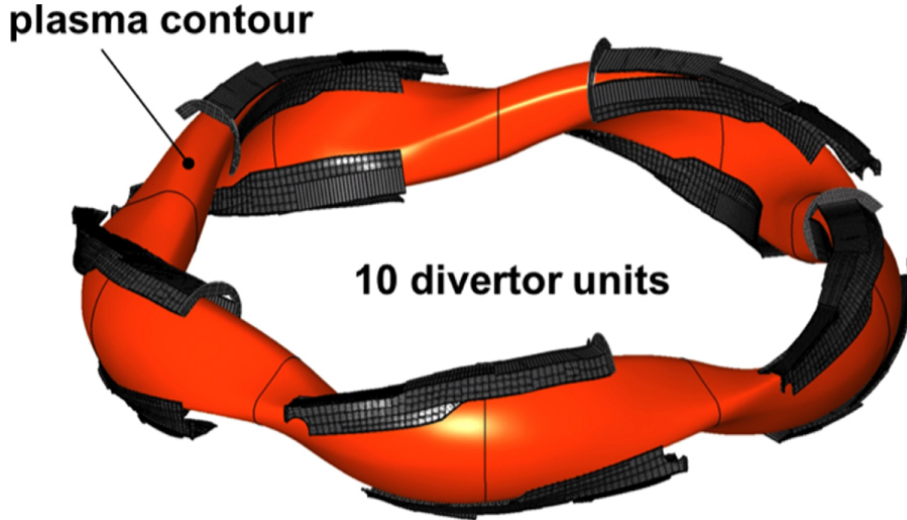


Fig. 1.9 The geometry of the Island divertor and the plasma shape in W7X.

Ten Test Divertor Units (TDUs) are distributed according to the five-fold symmetry of the W7-X unit, with each of the five modules containing an upper and a lower TDU [see figure 1.9]. Each TDU consists of a horizontal ( $\sim 1.86m^2$ ) and a vertical ( $\sim 0.55m^2$ ) divertor plate separated by the pumping gap [13]. The installation of this island divertor in W7X allowed significant improvements in fusion performance, as the triple product (Lawson criterion) increased by a factor of 8.

Regarding the divertor transport, a significant difference in the control of this for tokamaks and stellarators is the field line pitch, which is typically 0.1 for tokamaks and 0.001 for stellarators [12]. Because of the relatively large pitch angle, in tokamaks most of the heat flux across the SOL is carried by parallel heat conduction, especially for the electrons. In stellarators, the small pitch angle makes the parallel and perpendicular transport much more comparable, even for electrons [14].

### 1.3.3 Trapped and passing particles

In addition to the gyro-motion described previously, the particles can be trapped due to  $\nabla B$ , so two types of trajectories can be followed: the trapped particles and the passing particles trajectories.

The condition for the particles to be trapped depends on the ratio between their the parallel velocity ( $v_{\parallel}$ ) and their perpendicular velocity ( $v_{\perp}$ ),  $\frac{v_{\parallel}}{v_{\perp}} < \sqrt{\frac{2r}{R_0-r}}$ . This can be illustrated in the figure 1.10.

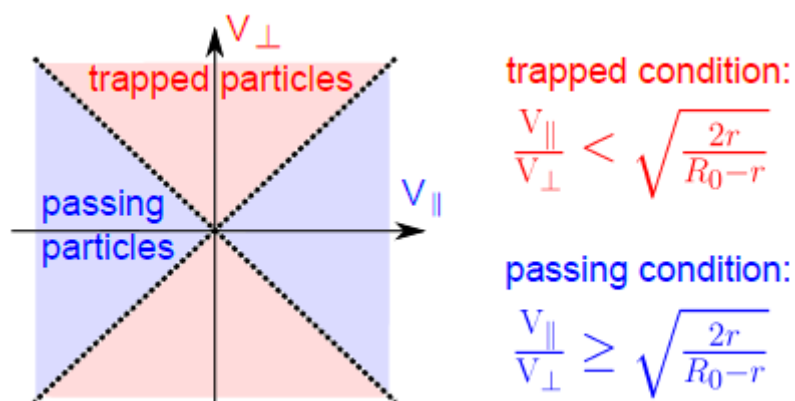


Fig. 1.10 Schematic representation of the passing and trapping conditions for  $\theta = 0$  as a function of the perpendicular and parallel velocities.

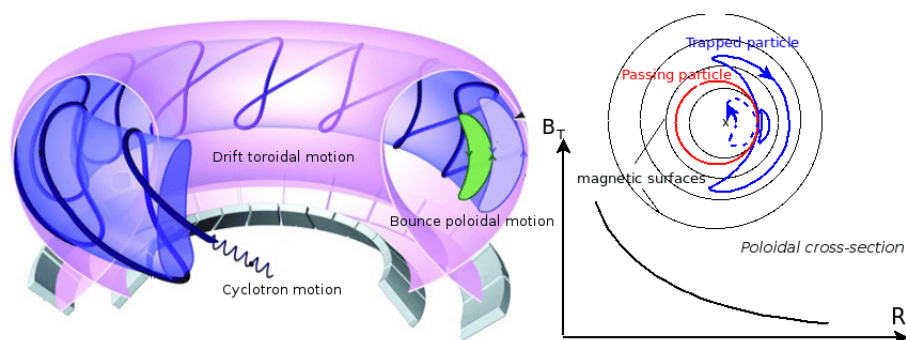


Fig. 1.11 (a) Trapped particle trajectory and (b) poloidal projection of a trapped and passing particle. Adapted from Nguyen 2009 [15].

Their occurrence can be explained by the conservation of the magnetic moment. When a particle on the low field side (LFS) moves towards the high field side (HFS), the magnetic field,  $B$ , experiences an increase, which requires a simultaneous increase in the perpendicular velocity,  $v_{\perp}$ , to keep the magnetic moment,  $\mu$ , constant. Due to the conservation of energy, the parallel velocity,  $v_{\parallel}$ , then decreases, eventually reaching zero at some point, causing the particle to reverse direction. As a result, the particle is trapped at the LFS, where  $v_{\parallel} < v_{\perp}$ .

The particles that satisfy the trapping condition, can be detrapped by collisions and enter the "passing region" (blue region in Figure 1.10).

Consequently, in the poloidal cross-section of the tokamak, some particles follow a trajectory that oscillates back and forth due to multiple reflections, resulting in a banana-shaped path when projected onto the cross-section. This banana orbit is formed by the particles undergoing reflection and confinement within specific regions of the tokamak's magnetic field [see figure 1.11].

The banana width characterizing these orbits can be expressed as:

$$\delta_b = \frac{2q_s \rho_s}{\sqrt{r/R_0}} \quad (1.8)$$

These trapped particles oscillate at a characteristic frequency  $\omega_b$  as they bounce between the high and low magnetic field regions.

$$\omega_b = \frac{v_\perp}{qR_0} \left( \frac{r}{2R_0} \right)^{1/2} \quad (1.9)$$

In a tokamak, the degree of trapping depends on factors like the magnetic field strength, the energy of the particles, and the pitch angle (the angle between the particle's velocity vector and the magnetic field lines). The fraction of trapped particles is a measure of particles within the plasma that are trapped within the magnetic field lines as they spiral around the torus :

$$f_t = \sqrt{\frac{2r}{R_0 + r}} \quad (1.10)$$

Depending on the inverse aspect ratio  $r/R_0$ , the fraction of trapped particles may follow the next curve [figure 1.12]:

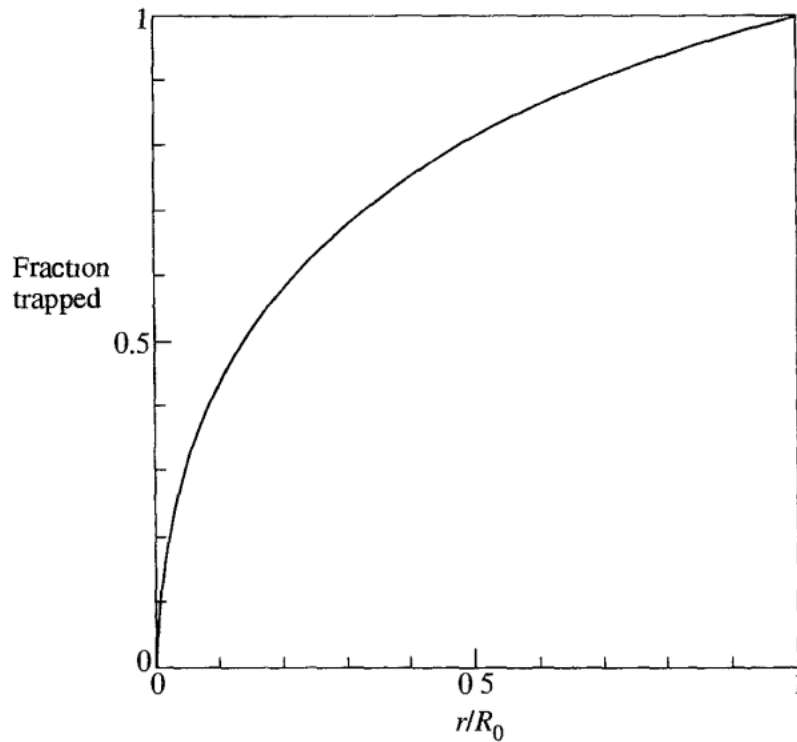


Fig. 1.12 Graph of the fraction of trapped particles as a function of the inverse aspect ratio of the magnetic surface  $r/R_0$ . Adapted from Wesson 2011 [16].

In this trapping mechanism, collisions exist and set some conditions as well which allow particle trapping. Collisions cause these particles to diffuse away. The condition for collisions to prevent trapping is that the detrapping time must be less than the bounce time:

$$\begin{aligned} \tau_{detrapp} &\simeq \frac{2r}{R_0} \tau_{coll} \\ \tau_{detrapp} &< \omega_b^{-1} \end{aligned} \tag{1.11}$$

Thus, the fraction of trapped particles in tokamaks is proportional to the square-root of the inverse aspect ratio, so that in a typical tokamak a fraction of about 50% is found. While in stellarators as Wendelstein 7-X has a much higher aspect ratio of around 10, so that a lower fraction of trapped particles could be expected, there are still several tens of percent of trapped particles found near the core due to the additional trapping in the toroidal direction [see figure 1.13].

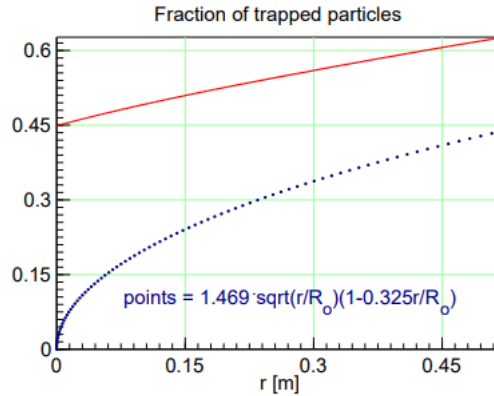


Fig. 1.13 The fraction of trapped particles in W7-X as a function of radius (red curve) and the fraction of trapped particles for a tokamak with a comparable aspect ratio. Adapted from Proll 2014 [17]

In the three-dimensional magnetic field configurations of stellarators, there are not only the toroidally generated trapped particles that dominate in tokamaks, but also a third class of particles that are locally trapped in the helical waves.

Furthermore, as the plasma is heated to fusion conditions, the fraction of trapped particles will increase because this heating changes the parallel and perpendicular velocity distributions.

### 1.3.4 Heating systems

Once a plasma is magnetically confined, heating systems are needed to achieve the high temperatures required for fusion reactions. The first heating system used was ohmic heating based on the Joule effect, which is possible in tokamaks but not in stellarators.

#### Ohmic Heating

This is a method of heating the plasma by passing an electric current through it. It relies on the fundamental principle that when a current ( $I_p$ ) flows through a conducting medium like a plasma, it encounters resistance, which leads to the generation of heat [18].

The power generated by ohmic heating in a plasma is proportional to the square of the plasma current  $I_p$ :

$$P_{\text{Ohmic}} = \frac{I_p^2}{\sigma} \quad (1.12)$$

where  $\sigma$  is the electrical conductivity of the plasma. As the temperature is increased, the conductivity also increases and then  $P_{\text{Ohmic}}$  saturates. The majority of the cases studied in this PhD research are centred around this form of heating.

### **Neutral beam injection (NBI)**

This heating system is installed on the majority of the world's nuclear fusion experiments as the most powerful among the heating systems. Its principle is the injection of fast hydrogen with a power of several megawatts into the fusion plasma. In collisions with the ions and electrons in the plasma, the fast neutral hydrogen isotopes ( $^1\text{H}$ ,  $D$  and  $T$ ) become ionized and subsequently confined in the magnetic field. They transfer their energy to the electrons and ions in the plasma and thereby heat the plasma. Furthermore, the injected beam can drive a current in the plasma that can partially substitute for the inductively driven current [19].

### **Ion cyclotron resonance heating (ICRH)**

Electromagnetic waves in the frequency range of ion cyclotron motion, typically tens of megahertz, can be absorbed by plasma. When absorbed, this wave energy is converted into kinetic energy for the resonant ions, increasing their energy levels. This increased kinetic energy is transferred to other plasma particles via collisions, ultimately leading to heating of the plasma.

### **Electron cyclotron resonance heating (ECRH)**

The electrons are heated by microwaves in the frequency range of hundreds of GHz. Electron cyclotron wave injection has been shown to be an efficient way of inducing current and heating in tokamaks and in stellarators for plasma generation and heating. Compared with the ICRH system, the ECRH has the advantage that the beam can be transmitted through a vacuum, which simplifies the design and allows the antenna to be located far from the plasma, making maintenance easier. ECRH is well suited for the control and/or suppression of MHD instabilities such as sawtooth crashes and neoclassical tearing modes (NTM).

### **Lower-hybrid (LH)**

This heating uses electromagnetic waves in the frequency range 1-8 GHz, which is between the ion and electron cyclotron frequency. Lower hybrid waves are also used for current drive (LHCD), this is used to modify the current profile with the aim of obtaining advanced tokamak performance in plasmas with parameters similar to those that would be required

for ITER [20]. In tokamaks, LH is used to produce very long discharges by generating the plasma current.

### 1.3.5 Confinement regimes

The confinement time ( $\tau_e$ ), introduced in the Lawson criterion equation 1.3, can be defined as the ratio of the stored plasma energy  $W$  to the absorbed heating power  $P$ , subtracted for the variation of the plasma energy:  $\tau_e = \frac{W}{P - \frac{dW}{dt}}$ .

As the heating power increases, the energy confinement time  $\tau_e$  tends to degrade.

#### Ohmic confinement regime

It occurs when no additional heating is applied to the plasma in tokamaks other than the ohmic heating. More precisely, 2 adjacent (in density) sub-regimes have been found:

- The linear Ohmic confinement (LOC) : During the 1970s, extensive research on energy confinement in purely Ohmically heated plasmas took place [21]. By varying electron density through gas puffing, a significant finding emerged: the confinement time increases linearly with the electron density, also called Alcator scaling. Then, from series of individual Alcator C-Mod discharges a neo-Alcator scaling was deduced :  $\tau_{nA}(ms) = 70n_e q_{(a)} \sqrt{\kappa} a R^2$ .
- The Saturated Ohmic confinement(SOC) : This confinement regime is reached when the energy confinement time in the LOC regime saturates above a critical density  $n_{crit}$ .

Both sub-regimes were found ubiquitously in every tokamak in the world.

#### From Linear Ohmic Confinement (LOC) to Saturated Ohmic Confinement (SOC)

Despite the estimation of the neo-Alcator scaling, discrepancies with experimental data remain, as highlighted in [22], and the critical density could not be estimated. An approximation to the critical density was found by Shimomura in 1985 [23], when an empirical scaling of the energy confinement time was attempted.

$$n_{crit} \approx 5I_p \cdot \mu_0 \cdot \pi^{-1} \cdot a^{-2} \cdot A_i^{0.5} \cdot \kappa^{0.5} \cdot 2^{-0.5} \quad (1.13)$$

where  $A_i$  is the atomic number and  $\kappa$  is the elongation.

Discrepancies with experimental data were still found, so some measurements were made in various fusion devices to estimate this critical density more accurately. Observed features include:

- The flip of the turbulent phase velocity [24, 25]
- Plasma toroidal velocity changes at a critical density and is independent of causal relationships [26].
- A change in the electron fluctuation frequency spectra [27].
- As the trapped electron fraction decreases with increasing collisionality,  $v_i$  or ion temperature gradient (ITG) modes eventually dominate, leading to saturation of the confinement (the SOC regime) [28].
- Gyrokinetics simulations explored the transition dynamics, showing that TEMs dominate in LOC while ITG modes dominate in SOC [29].
- An increase in collisionality had effects beyond reducing the trapped electron fraction, including enhanced electron-ion coupling and decreased impurity content ( $Z_{eff}$ ), which influenced mode stability and thermal conductivity, impacting confinement [30].
- The density profile's peaking was studied, revealing a maximum near the LOC/SOC transition [31].
- Rotation reversals in the LOC-SOC transition [32].

The neo-Alcator, as previously described, shows discrepancies with observations in numerous fusion devices, indicating the need to include more plasma parameters such as  $Z_{eff}$ , impurity content and aspect ratio in regression analyses, as these could potentially influence the scaling. The observations suggest that classical SOC cases show a steady confinement slope, while specific cases show different trends beyond the critical LOC/SOC density, due to potential impurity effects and different density profiles.

Comparison with gyro-kinetic simulations suggests that the effects of sub-dominant TEMs are important in the LOC sub-regime while ITG dominates in the SOC sub-regime. [22].

Rice in [22], with results from nearly 20 devices, found an empirical scaling for estimating the LOC/SOC transition, it occurs at a critical value of the product of the critical density, edge safety factor and device major radius. In addition, this product increases with the toroidal magnetic field [see figure 1.14].

$$\frac{B_0}{n_e^{crit} qR} \approx constant \quad (1.14)$$

It supports the notion of critical collisionality [32] since the ratio of the collision frequency to the bounce frequency is equivalent to  $\nu^* \approx 0.011 8n_e qR Z_{eff} / (T_e)^2 \epsilon^{1.5}$ .

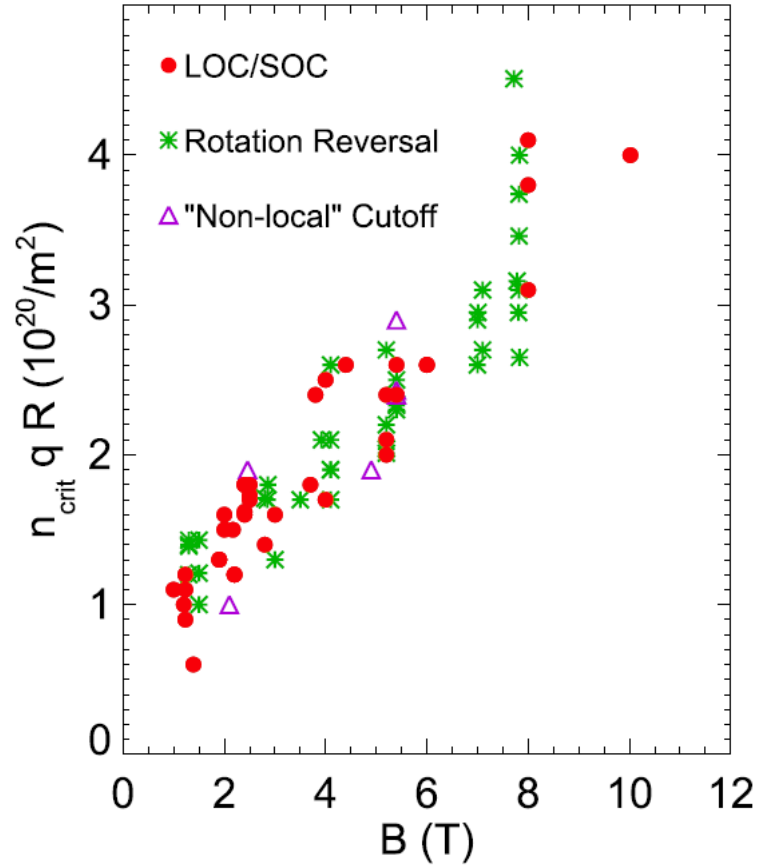


Fig. 1.14 The product of  $n_e^{crit}$ , the edge  $q$  value and  $R$  as a function of toroidal magnetic field from 18 individual tokamaks. Red dots are from the LOC/SOC transition, green asterisks are from rotation reversals and purple triangles are from the ‘non-local’ cut-off. Adapted from Rice 2020 [22].

Regarding the critical density for the particular case of Tore Supra, Sun decided to look for an empirical law, since Shimomura’s equation overestimated the critical density in a number of dedicated discharges in Tore Supra [33]. Using the entire Tore Supra database, he took for each  $I_p = cte$  and calculated the median of the  $\tau_e$  vs  $n_e$  curve, then looked for its knee point where the trend changed. Having found the knee point for each curve, he derived the following empirical equation:

$$n_{crit} = 2.6 \times I_p \quad (1.15)$$

For WEST, the empirical scaling is estimated by taking the equation 1.16 and applying the relationship corresponding to the equation 1.14.

$$n_{crit} = 5.3 \times I_p \quad (1.16)$$

**Low mode confinement regime (L-mode)**

With additional heating, the plasma goes beyond the ohmic confinement and reaches the so-called low mode confinement (L-mode). Increasing the heating power leads to confinement degradation, allowing energy to escape from the confined plasma and thus reducing the confinement. On the other hand, as was found at ASDEX in 1982, if the applied heating power is increased beyond a critical value, the plasma undergoes a transition to high confinement (H-mode).

**High mode confinement regime (H-mode) and Improved confinement regimes**

In the H-mode the confinement improves abruptly when sufficient power is applied. It was found that tokamak operation makes an abrupt transition from the low confinement mode (L-mode) to the high confinement mode (H-mode) when the auxiliary heating power reaches a critical value. The underlying physical mechanisms of the L-H transition are still unclear, but it is known to be related to the suppression of turbulent transport [34].

In addition to the H-mode, many other types of improved confinement regimes have been achieved by local turbulence suppression, such as Improved Ohmic Confinement (IOC), the V-H mode, etc. In addition, internal transport barriers (ITBs), i.e. regions where turbulence is reduced or quenched, are now routinely created and maintained in tokamaks. Flow shear and/or magnetic shear play a central role in the formation and maintenance of these transport barriers [35]. ITBs have been observed in tokamaks, with devices such as JET and ASDEX Upgrade demonstrating their potential for enhanced plasma performance. These regimes are usually reached above a critical level of heating power which should be minimised.

Each confinement regime is characterised by a turbulent transport behaviour that leads to a degradation of the confinement. This turbulent transport results from the interplay of fluctuations, instabilities, plasma properties and so-called turbulence. These different concepts will be discussed in the next chapter.

# Chapter 2

## Turbulence and transport

### Contents

---

<b>2.1</b>	<b>Transport in Tokamaks and Stellarators . . . . .</b>	<b>24</b>
2.1.1	Classical and Neoclassical transport . . . . .	24
2.1.2	Turbulent transport . . . . .	26
<b>2.2</b>	<b>Electrostatic turbulence . . . . .</b>	<b>26</b>
2.2.1	Drift-wave turbulence . . . . .	27
2.2.2	Interchange modes . . . . .	28
2.2.3	Zonal flows and Geodesic acoustic modes . . . . .	29
2.2.4	Micro-instabilities . . . . .	29
<b>2.3</b>	<b>MHD activities . . . . .</b>	<b>32</b>
<b>2.4</b>	<b>Quasi-coherent (QC) modes . . . . .</b>	<b>35</b>
<b>2.5</b>	<b>Looking for universality . . . . .</b>	<b>35</b>
2.5.1	Turbulence dynamics characterised by energy exchange . . . . .	35
2.5.2	Focus of PhD Research . . . . .	37

---

The concept of turbulence can be traced back to Landau's theory in fluids outlined in [36]. According to his theory, turbulence arises as a result of a series of instabilities. Each instability introduces a new degree of freedom characterised by an indeterminate phase, resulting in time-periodic behaviour with progressively increasing and non-commensurate frequencies (not harmonics). The resulting motion is a superposition of these modes, leading to a quasi-periodic state.

In fusion plasmas, turbulence can be defined as a consequence of complex dynamics arising from a variety of factors, including collisions, fluctuations, perturbations, intermittency

and more [37], which can collectively contribute to the modification of temperature ( $T$ ), plasma density ( $n$ ) and magnetic field ( $B_0$ ) gradients. These dynamical processes manifest themselves at different scales and are driven by non-linear interactions. Fusion plasmas then have to deal with a high degree of non-linearity in their dynamics, with a different type of turbulence compared to fluids, microturbulence, which has many different sources.

In fact, there is a complex interplay between turbulence, plasma properties and inherent instabilities, resulting in what is commonly referred to as turbulent transport. This phenomenon can manifest itself as the chaotic movement of particles, heat and momentum across magnetic field lines and has a significant impact on the efficiency and stability of nuclear fusion reactions [38].

The approach used to study these complex dynamics is based on the assumption of a clear distinction in space and time scales between the equilibrium state and the fluctuations. This assumption is the basis for the formulation of a mean-field transport theory. The typical approach to constructing most transport models is to combine a quasi-linear theory with a rule based on mixing length principles.

The descriptions in this chapter are brief and focused on what is relevant to this thesis. More detailed explanations of the different transport mechanisms can be found in [39]. The link between turbulence and transport is detailed in [40]. The gyrokinetic framework and simulations for the computation of turbulent transport in fusion plasmas can be found in [41].

## 2.1 Transport in Tokamaks and Stellarators

Understanding transport is crucial to achieve and maintain the conditions necessary for sustained and efficient nuclear fusion reactions. Transport involves the study of how particles and energy diffuse across magnetic field lines and how their behaviour affects plasma confinement. The ultimate goal is to optimise plasma confinement and minimise losses to achieve a self-sustaining fusion reaction.

Depending on the components of the transport, it can be classified first as classical (Coulomb interaction effects), then as neoclassical (trapped particle effects) and finally as turbulent transport, which reduces the confinement time.

### 2.1.1 Classical and Neoclassical transport

Classical transport takes into account Coulomb interactions and is based on a simple cylindrical geometry. It assumes a steady state plasma and therefore does not consider transport due to fluctuations. Classical transport usually dominates along the field lines, but is therefore

not suitable for describing the perpendicular transport of interest, which is related to the confinement losses in the perpendicular direction.

In toroidal devices, the magnetic field is inhomogeneous. It's stronger on the inside of the torus than on the outside. This variation in magnetic field strength, combined with its curvature, gives rise to additional forces and drifts. The resulting collisional transport resulting from this inhomogeneous curved field is called neoclassical transport.

For tokamaks, the step size of the neoclassical random walk is usually limited by the banana width (the radial width of the guiding centre orbit of a trapped particle on the outside of the torus), and hence the transport is always local if the width is smaller than the scale length of the local gradient. However, for stellarators with low collisionality, the step size can be very large due to the influence of the helical magnetic ripple. This can break the localisation of the transport, i.e. energy and particles can be transported over larger distances [42].

In tokamaks, the variation of neoclassical transport coefficients ( $D$ ) with collision frequency ( $\nu$ ) is normally divided into three regimes: the banana regime with low  $\nu$ , the Pfirsche-Schluter regime with high  $\nu$  and a plateau in between [see figure 2.1].

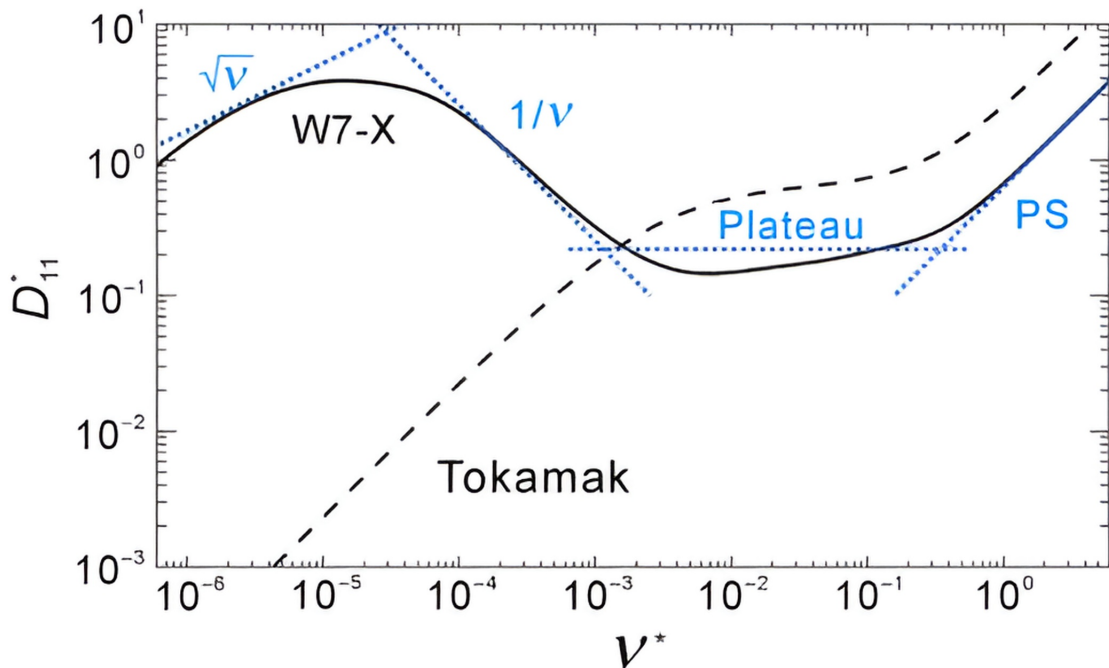


Fig. 2.1 Comparison of neoclassical transport coefficients versus collisionality between tokamaks (dotted curve) and the W7-X stellarator (solid curve) in different regimes. Adapted from Xu 2016 [14].

In stellarators, there exist more regimes in low collisionality cases, which are scaled as  $\nu^{0.5}$  and  $\nu^{-1}$ . Moreover, the electrons and ions are often in different regimes, and there is a larger diffusivity of ions than electrons.

At low collisionality, the diffusion coefficient in stellarators is much larger than in tokamaks [see figure 2.1]. Therefore, in stellarators, neoclassical transport losses are expected to dominate at high electron temperature, which seems to be a disadvantage to be overcome for stellarators.

### 2.1.2 Turbulent transport

The measured transport coefficients are significantly higher than those predicted by classical and neoclassical theories, hence the confinement time is much worse than neoclassical predictions. Fluctuations give rise to what's known as anomalous or turbulent transport; these fluctuations can be classified into two types: electrostatic turbulence ( $\tilde{\phi}$ ), in which the confining magnetic field is unchanged and transport is due to fluctuating electric fields, and magnetic turbulence ( $\tilde{B}$ ), in which the confining magnetic field is significantly perturbed by fluctuating current flows in the plasma. These fluctuations are thought to appear as the non-linear saturated state of micro-instabilities [16].

As mentioned previously, turbulent transport can manifest itself as a chaotic movement of heat, particle and momentum.

Heat transport in fusion devices refers to the flow of thermal energy within the plasma. Turbulent fluctuations, driven by instabilities, can cause heat to diffuse radially across magnetic field surfaces. Inadequate heat transport can lead to cooling of the plasma and disruption of fusion processes [43]. Particle transport involves the movement of ions and electrons within the plasma. Momentum transport refers to the transfer of angular momentum within the plasma. Uncontrolled momentum transport can lead to undesirable effects such as plasma instabilities and disruptions [44].

The theoretical picture of turbulent transport is that the free energy, such as temperature or density gradient, drives a very broad spectrum of micro/macro-scale drift-type instabilities, which at the same time release energy to drive a steady level of fluctuations in the associated perturbed quantities. Thus a radial transport of particles and energy is generated.

## 2.2 Electrostatic turbulence

Electrostatic here means that perturbations of the magnetic field are ignored, so that only the perturbed electric field matters. This assumption is appropriate if the plasma beta  $\beta$  is below

the instability threshold for electromagnetic interchange modes [45]. This simplification is actually questionable at the edge of tokamaks, where electromagnetic effects are known to be important. Also, the electron temperature profile is supposed to be stable with respect to small scale electron temperature gradient driven modes [46].

### 2.2.1 Drift-wave turbulence

In addition to the motion described for particles in the 1.3 section, they can also undergo drifts due to interaction with electric and magnetic fields. The total velocity can be expressed as :  $\mathbf{v}_{tot} = \mathbf{v}_{gyro} + \mathbf{v}_{\parallel} + \mathbf{v}_g$ , where  $\mathbf{v}_{gyro}$  is the gyro-motion [see section 1.3.1] and  $\mathbf{v}_g$  is the drift velocity and is the responsible of the perpendicular transport which lead to a loss of the confinement. It contains mainly three physical components, the  $\mathbf{E} \times \mathbf{B}$  drift, the grad-B drift and the curvature drift.

$$\mathbf{v}_g = \mathbf{v}_{E \times B} + \mathbf{v}_{\nabla B} + \mathbf{v}_c, \quad \text{the drift velocity} \quad (2.1)$$

$$\mathbf{v}_{E \times B} = \frac{\mathbf{E} \times \mathbf{B}}{B^2}, \quad \text{the } E \times B \text{ drift} \quad (2.2)$$

$$\mathbf{v}_{\nabla B} = \frac{\mu_s \mathbf{B} \times \nabla B}{q_s B^2}, \quad \text{the grad-B drift} \quad (2.3)$$

$$\mathbf{v}_c = \frac{\mathbf{B}}{q_s B^2} \times \left( m_s v_{\parallel}^2 \frac{\mathbf{N}}{R} \right), \quad \text{the curvature drift} \quad (2.4)$$

with  $\mathbf{N}$  the unit vector normal to the magnetic field lines.

The fluctuations generated by drift wave interactions contribute to turbulence in the plasma. In electrostatic turbulence, the transport is set by the fluctuations in  $E \times B$  drift because  $v_{\nabla B}$  and  $v_c$  do not depend on the electric field.

$$\tilde{\mathbf{v}}_{E \times B} = \frac{\mathbf{B} \times \nabla \tilde{\phi}}{B^2} \quad (2.5)$$

The drift waves arise from the interaction between the plasma density ( $n$ ) and the magnetic field ( $B$ ). They are generally stable waves, i.e. the potential ( $\phi$ ) and the electron density ( $n$ ) are in phase [see figure 2.2] and the electron response to a  $\delta\phi$  can then be considered instantaneous, i.e. adiabatic.

$$\frac{\delta n_e}{n_e} = \frac{e \delta \phi}{T} \quad (2.6)$$

Drift waves can interact non-linearly with each other and with other plasma modes. The non-linear interactions lead to the transfer of energy between different scales of motion,

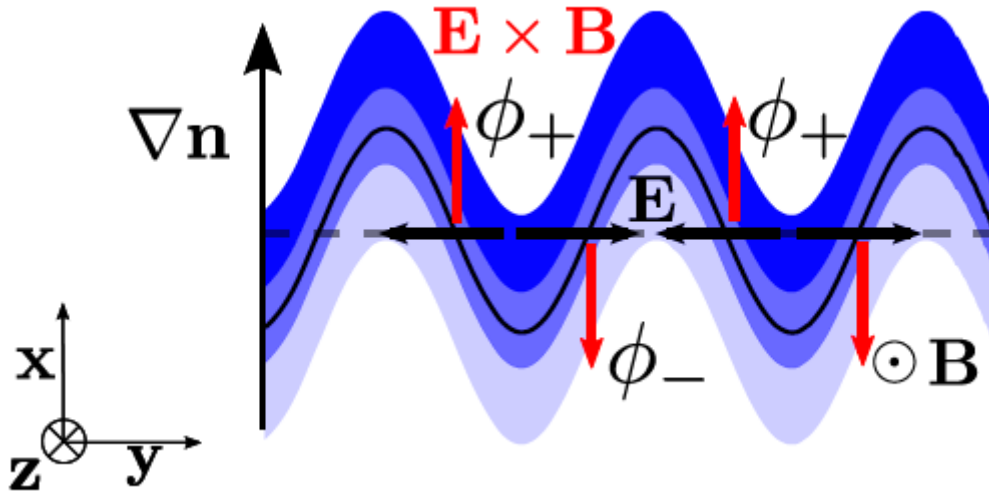


Fig. 2.2 Drift wave mechanism. The electrostatic potential ( $\phi$ ) leads to an electric field (black arrows), so that the maximum of the resulting  $E \times B$  drift (red arrows) is shifted by  $\pi/2$  from the maximum of the density perturbation. The perturbation thus propagates in the  $y$ -direction, which would correspond to a poloidal propagation direction in a torus. Adapted from Proll 2014 [17].

resulting in the development of fluctuations in plasma properties. Furthermore, the curvature of the magnetic field lines leads to differential particle drifts, which can drive the growth of drift waves [47].

### 2.2.2 Interchange modes

The interchange modes are the result of the combination of  $v_{\nabla B}$ ,  $v_c$  and the density or pressure gradient. They involve the interchange of plasma along magnetic surfaces, causing regions of higher pressure to move towards regions of lower pressure. They become unstable when the magnetic field gradient  $\nabla B$  aligns with the equilibrium pressure gradient, allowing the exchange of flux tubes along a field line to release free energy.

In tokamaks, this instability manifests itself mainly on the low-field side (LFS), which is characterised by the accumulation of trapped particles. Conversely, the plasma on the high field side (HFS) remains stable in terms of exchange modes. Consequently, trapped particles are expected to play an important role in the exchange process. In addition, field lines connect locally stable and unstable regions, adding to the complexity of the phenomenon.[3]

### 2.2.3 Zonal flows and Geodesic acoustic modes

Zonal flows are azimuthally symmetric sheared flows spontaneously excited by small scale fluctuations [48]. They are a critical agent of self-regulation for drift wave instabilities and turbulence. The zonal flow originates from nonlinear interactions within the fluctuation spectrum or collection of wave-packets spanning the drift wave frequency range. The mechanism involves both the parametric instability of individual drift waves and the modulational instability of a range of drift wave frequencies [49]. Zonal flows refers generally to the zero-frequency flows.

It is now widely accepted that zonal flow-induced energy transfer from unstable to stable modes is the primary saturation mechanism for ITG turbulence [50, 51]. In addition, the importance of zonal flows in TEM turbulence was found to depend on  $\nabla T_e$  and  $\frac{T_e}{T_i}$  [52].

In stellarators the zonal-flows suffer stronger damping than tokamaks through electron collisions due to non-ambipolar neoclassical transport [14].

Geodesic acoustic modes (GAM) are ubiquitous oscillatory flow phenomena observed in tokamaks and stellarators. They have long been recognised as a non-stationary branch of turbulence-driven zonal flows, and are consequently understood to play a critical regulatory role in cross-field edge turbulent transport, via enhanced velocity shear of turbulent eddies, or by providing an additional sink for turbulence energy dissipation through damping. Their role in moderating turbulence is therefore important for understanding the general behaviour of turbulent transport.

### 2.2.4 Micro-instabilities

Plasma instabilities are localised deviations from the plasma equilibrium that can drive the plasma away from its desired state. While large scale instabilities should not be a major problem in optimised stellarators, it is the small scale instabilities that threaten successful fusion experiments [17]. These so-called micro-instabilities are on the order of the Larmor radius and draw energy from density and temperature gradients.

Micro-instabilities are the signature of an energy transfer from the free energy of the plasma to several plasma modes, which mix together to generate plasma micro-turbulence, characterised by small-scale fluctuations and instabilities.

Microturbulence can occur on quite short time scales, with coherence times of a few  $\mu s$ . These fast fluctuations contribute to the diffusion and radial transport of heat and particles in the plasma, inducing a degradation of the confinement.

The interaction between instabilities and turbulence can be bidirectional. Turbulence can influence the development of instabilities by affecting the gradients in the plasma that

drive these instabilities. Instabilities can drive the turbulence that enhances transport. The interplay between turbulence and instabilities presents a challenge in understanding how they influence each other and contribute to plasma transport and confinement. Although the main instabilities that exist in the plasma have been identified, the resulting turbulent transport remains difficult to understand. For example, the growth of an instability can lead to the formation of turbulent eddies and fluctuations, which in turn enhance the transport of plasma properties.

The Ion Temperature Gradient (ITG), the Trapped Electron mode TEM and the Electron Temperature Gradient which are the main micro-instabilities responsible for anomalous transport of energy and particles in the plasma core.[see figure 2.3]

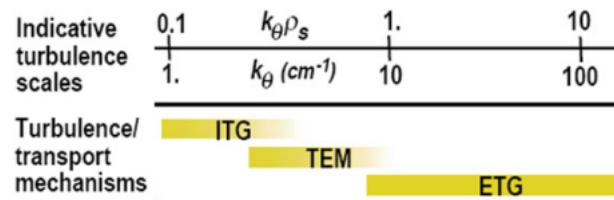


Fig. 2.3 Spatial scales of ITG, TEM and ETG micro-instabilities. Adapted from Doyle 2007 [53].

- Ion temperature gradient (ITG): ITG is driven by the gradient in the ion temperature within the plasma. ITG can arise from the inherent  $v_{\nabla B}$  phenomenon. These drift waves experienced by particles as a result of variations in magnetic field strength are directly proportional to the kinetic energy of the particles. As a result, particles with higher temperatures exhibit more extensive drift than their colder counterparts [54].

ITG can arise from interchange-like instabilities due to the curvature or from drift-wave instabilities in a slab geometry. ITG can also be stabilised by dilution at high  $Z_{eff}$  values when there are fewer major ions in the plasma.

For the collisionless instabilities with electrostatic approximation, the dispersion relation of the curvature-driven ion temperature-gradient (ITG) mode appears to be the same to both tokamaks and stellarators [55].

- Trapped electron mode (TEM): TEM induces electron heat and long-wavelength particle transport in magnetised fusion plasmas. They are named after the trapped electrons [see section 1.3.3] that play a central role in their dynamics. These electrons are confined by the magnetic field in such a way that their motion is predominantly along the field lines, preventing them from escaping easily over the magnetic surfaces.

TEMs are created by a resonance between these trapped electrons and the electromagnetic waves present in the plasma. When the conditions are right, the energy from the trapped electrons can be transferred to these waves, leading to the growth of TEMs [56].

Due to their localisation on the bad curvature of the tokamaks, trapped electrons are favourable to interchange mode driven instabilities operating in this region. An important property of TEM is that they are usually damped by collisionality [57]. Apart from collisionality, magnetic shear can have a stabilising effect on TEM, at high values [58], but also at low or negative values.

- Electron temperature gradient (ETG): ETG is driven by the gradient in the electron temperature within the plasma. ETG arises when the gradient in electron temperature becomes steep enough. The mechanism behind the instability involves the interactions between different modes of oscillations and waves in the plasma.

ETGs are large wavenumber instabilities. Despite their significant linear growth rate, ETGs generally have a weak contribution to transport due to their small scale. However, they can have an important effect on electron transport in the case of electron heating [59] or within internal transport barriers [60]. ETGs have not been studied in the present work because the experimental tool used (conventional reflectometers) is not sensitive to their large wavenumbers.

Ion temperature gradient (ITG) and trapped electron mode (TEM) instabilities are two types of drift-wave microturbulence that are prevalent in Tokamak plasmas, leading to anomalous transport. When the inverse ion temperature gradient scale length exceeds a critical threshold with the inverse electron temperature gradient scale length fixed, ITG microturbulence is dominant, while TEM microturbulence tends to dominate otherwise. The dominant fluctuation wavelengths in ITG and TEM microturbulence can be almost the same or differ significantly. Fluctuation intensities of ITG and TEM microturbulence depend on parameters such as temperature gradient, density gradient, magnetic shear, ratio of electron temperature to ion temperature, collisions, and zonal flows. Zonal flows, which are excited by ITG and TEM microturbulence, can interact with microturbulence and reduce their intensity. Collisions can also affect microturbulence directly or indirectly through reducing the zonal flows.

ITG and TEM modes are unstable in the limit of large wavelengths such that  $k_{\perp} \rho_i < 1$ . In the nonlinear regime they give rise to particle, momentum, electron and ion heat transport. An important property of these modes is the existence of an instability threshold [see figure 2.4]. For a given safety factor profile, the threshold of a pure ion mode (i.e. when the electron

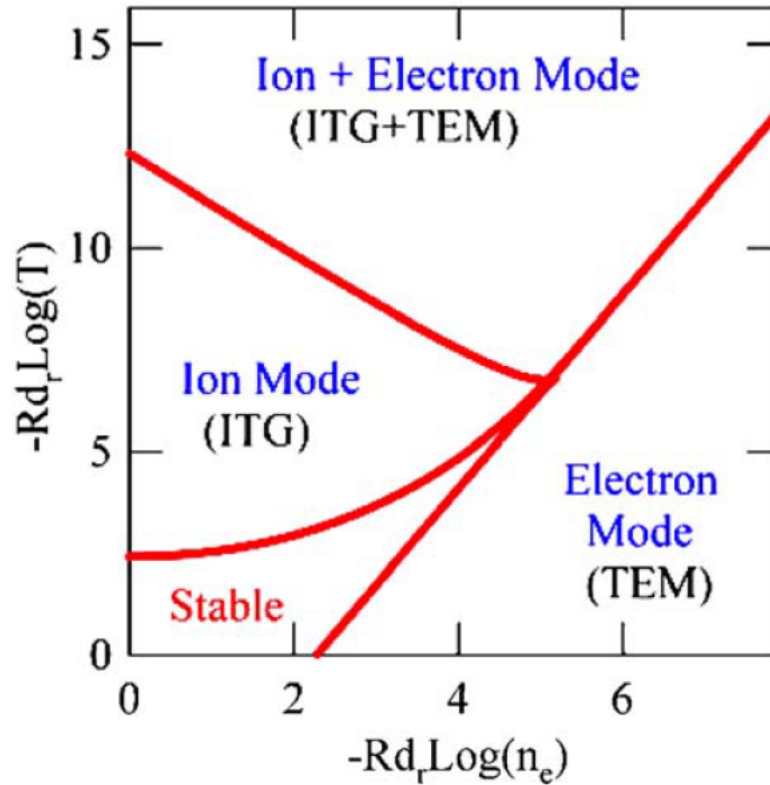


Fig. 2.4 Stability diagram of ITG/TEM modes. Electron and ion temperatures are equal. Adapted from Garbet 2006 [3].

response follows a Boltzmann law) appears as a critical ion temperature logarithmic gradient  $-R\nabla \ln T_i/T_i$ , which depends on the logarithmic density gradient  $-R\nabla \ln n_i/n_i$  and on the ratio of electron to ion temperature  $T_e/T_i$  [3].

While an ion mode usually rotates in the ion diamagnetic direction, trapped electron modes usually rotate in the electron diamagnetic direction and are mainly driven by resonant interaction of the modes with trapped electrons. The threshold is a critical value of  $-R\nabla T_e/T_e$  which depends on  $-R\nabla n_e/n_e$  and the fraction of trapped electrons  $f_t$ .

Whereas in tokamaks the trapped electron mode (TEM), driven by the density gradient, routinely leads to an outward transport flux, in stellarators the TEM is stabilised [61].

## 2.3 MHD activities

Magnetic fluctuations can induce instabilities that can modify the transport and the magnetic equilibrium as well as the neoclassical tearing that disturbs the magnetic structure.

In fusion plasmas, magnetohydrodynamic (MHD) instabilities play a critical role in determining achievable plasma parameters, advanced scenarios and operational limits. The primary destabilising forces for various MHD phenomena, such as sawtooth oscillations, kink instabilities, and both resistive and neoclassical tearing modes, are due to current and pressure gradients, often exacerbated by unfavourable magnetic field curvatures [16]. Ultimately, MHD instabilities can lead to plasma disruption, which in turn affects the lifetime of machine components, especially those involved in handling plasma particles and energy exhaust.

### **Neo-classical Tearing Modes (NTM)**

NTMs are related to the dynamics of magnetic field lines in the plasma and their interaction with the flow and pressure of the plasma, making them a part of the broader category of MHD instabilities. These instabilities, including NTMs, can have significant impacts on the performance and stability of magnetically confined plasmas in devices like tokamaks, which are critical in the pursuit of controlled nuclear fusion.

### **Sawtooth instability**

Tokamak plasmas exhibit susceptibility to diverse large-scale instabilities, potentially degrading plasma confinement. The stability boundaries of these instabilities delineate the tokamak's safe operating regime, with sawtooth instabilities being a primary macroscopic example, impacting significant plasma volume, though rarely leading to discharge termination [62].

The sawtooth instability gets its name from the characteristic shape of the plasma density or temperature profile as it evolves over time during the instability. Imagine the profile resembling the teeth of a saw: the density or temperature rises gradually and then rapidly drops suddenly, creating a distinctive pattern on a graph.

Sawtooth oscillations manifest as periodic core plasma density and temperature relaxations [63]. First identified in 1974 [64], these oscillations have been subsequently observed across all tokamaks and undergo three phases: i) a ramp phase with linear increases in plasma density and temperature over time, ii) a precursor phase marked by growing helical magnetic perturbations, and iii) a fast collapse phase where density and temperature swiftly decline, characterized by magnetic fluctuations (post-cursors) [65] or during the ramp phase [66] [see figure 2.5].

This process results in the rapid transport of hot electrons across flux surfaces to cooler plasma regions, flattening the temperature profile. Simultaneous drops in core temperature are concomitant with edge plasma heating. Recent two-dimensional measurements have

captured the collective behavior of the crash, illustrating the expulsion of the hot plasma core through a poloidally localized point during magnetic reconnection [67].

Understanding the trigger of instability growth is crucial for controlling Sawteeth. The onset of instability aligns with linear stability thresholds, hence, theoretical considerations of such stability are crucial [62]. The precursor oscillation aligns with the topology of the  $n = m = 1$  internal kink mode, a fundamental magnetohydrodynamic (MHD) oscillation [16]. Ideal internal kink displacement appears as a tilt and shift of the core plasma.

Advanced experimental sawtooth control techniques aim either to stabilise by eliminating or delaying the sawtooth crash, or to destabilise to reduce the sawtooth period and hence the likelihood of triggering magnetohydrodynamic (MHD) instabilities. These techniques include manipulating the distribution of energetic ions, altering the radial profiles of plasma current density and pressure, and using electron cyclotron resonance heating (ECRH) to heat electrons within the  $q = 1$  surface [68].

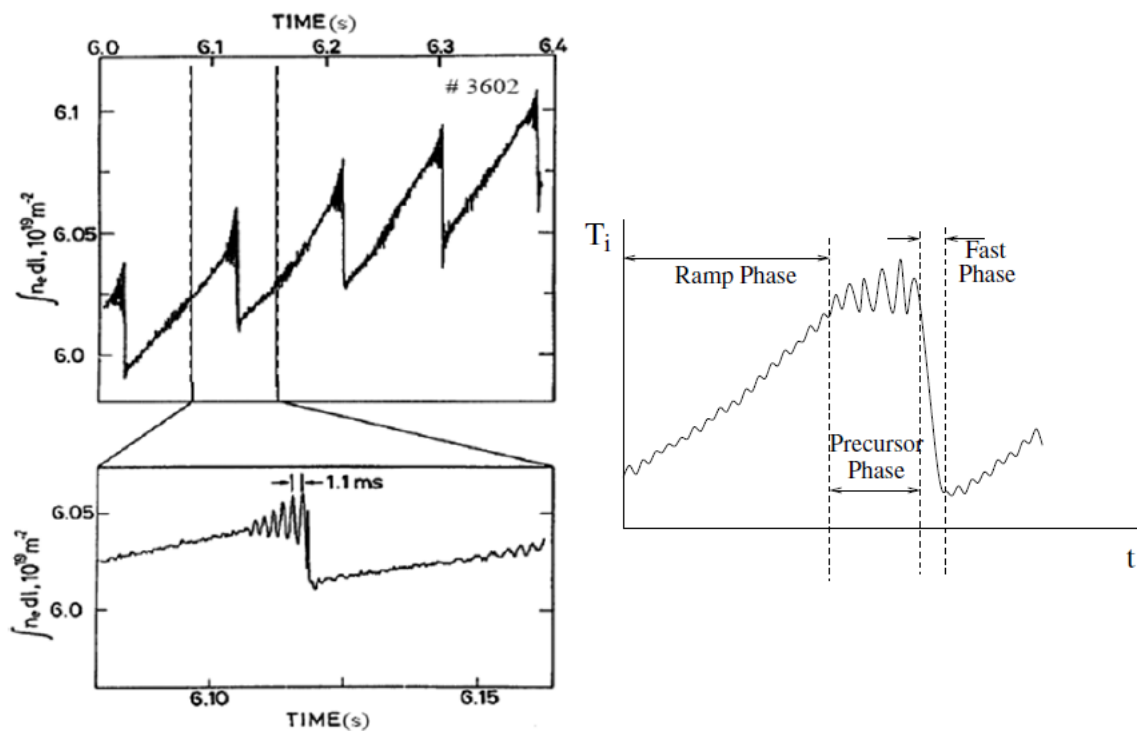


Fig. 2.5 The line-integrated electron density of an early JET sawtooth plasma. The sawtooth oscillation typically consists of a ramp phase, then a precursor oscillation followed by the fast collapse phase. Adapted from Chapman 2010 [68].

## 2.4 Quasi-coherent (QC) modes

The QC modes show a synthesis of properties inherent in both coherent and broadband fluctuations. They resonate around a specific frequency, similar to coherent modes, but their spread over a relatively wide frequency range (around tens of kHz) suggests a potential interrelationship with the underlying turbulence [33].

Comparing frequency spectra derived from nonlinear simulations, reflectometry measurements (discussed in the next chapter) and a synthetic diagnostic, it is suggested that TEM instability can manifest a QC signature in fluctuation spectra. This is attributed to the TEM instabilities converging to a few wave-numbers, inducing a narrow frequency spectrum consistent with the QC modes observed in TEM-dominated regimes [69].

All relevant features and simulation results support the categorisation of QC modes under TEM turbulence, which is known to induce anomalous electron thermal energy and particle transport in tokamak plasmas [70, 71].

The predominantly electrostatic nature of the Quasi Coherent Modes (QCMs) has been demonstrated, being predominantly observed in fluctuations of the electron density or electric potential [72]. In addition, the phase velocities of QC modes are found to be in the electron diamagnetic direction in the plasma frame [73].

QC modes have been observed in various fusion devices such as : KSTAR, J-TEXT, HL-2A, T-10, TEXTOR, Tore Supra, W7X, etc.

## 2.5 Looking for universality

Significant progress has been made in understanding the mechanisms behind turbulent transport in an attempt to achieve fusion on Earth using tokamaks and stellarators. However, the situation is complex because instabilities at different time and space scales can coexist within the same plasma conditions, complicating the causal relationships between these instabilities and turbulent transport associated with energy exchange.

### 2.5.1 Turbulence dynamics characterised by energy exchange

By studying the common sources and their underlying physics in different devices, the aim is to uncover key principles that can lead to a deeper understanding and improved management of fusion. Such insights would improve our understanding of turbulence and potentially optimise confinement.

As seen earlier in this chapter, turbulence has its origins in the study of fluid dynamics, an introduction to which was given by Landau in 1941. In this framework of fluid dynamics, energy transfer plays a crucial role. As we seek to discover the underlying mechanisms that are the sources of turbulent transport, it becomes imperative to understand this transfer mechanism. Energy interactions, both macroscopic and microscopic, are like signposts that lead us closer to the origins of turbulent behaviour. Recognising how energy moves, disperses and reorganises within a system not only reveals the intricacies of turbulence, but also shapes our strategies for managing and harnessing its effects.

Recently, it has also been shown in the context of turbulent plasmas that energy transfer, coherent structures and intermittency can be correlated. It has been shown that the presence of localised coherent structures enhances dissipation processes and improves the kinetic properties of the plasma. A formal approach to quantifying the relationship between scale-to-scale energy transfer and the presence of spatial structures is proposed by analysing data from a high-resolution two-dimensional Hall magnetohydrodynamic simulation. Coherent structures could have a significant influence of spatial structures on the turbulence cascade [74].

Intermittency has been observed in complex systems where nonlinear dynamics play a significant role. As shown and defined in [75], Hirsch defined intermittency as the aperiodic or chaotic behaviour for one-dimensional maps just before a tangent bifurcation occurs. As also described in the theory of dynamical systems, in every dynamical system there exists a certain physical parameter integral to the map (function of the system evolution). For hydrodynamic systems this could be represented by the Reynolds number. In the context of phase transitions, it might correspond to the ratio between the near and next-near coupling constants. In quantum mechanics, it's the ratio of the hopping matrix element to the incommensurate potential. As these parameters evolve, the iterative sequences derived from the map can transform, moving from a regular periodic pattern to unpredictable, aperiodic or even chaotic behaviour once a critical parameter value is reached. Moreover, the principles of scaling and universality, pillars of phase transition theory, have become indispensable [75].

In reversed field pinch plasmas, it has been shown that the probability distribution functions of magnetic field differences are not scale invariant, i.e the wings of these functions are more important at the smallest scales, a classical signature of intermittency. It has been shown that scaling laws also appear in a region very close to the external wall of the confinement device, and there is evidence that the observed intermittency increases moving towards the wall [76].

The concept of energy exchange deals with the transfer of energy between scales to determine whether two different scales are communicating by transferring energy to each

other. This transfer may occur simultaneously, at different times within an interval, or intermittently, correlating with the energy transfer process mentioned above. The key question then arises: can the energy exchange process exhibit intermittency in turbulent transport processes?

### 2.5.2 Focus of PhD Research

The aim of this thesis is to contribute to the understanding of turbulent transport in order to find universal properties of turbulence, based on a data-driven approach. Indeed, data-driven approaches, such as machine learning and signal processing, offer the opportunity to exploit the vast amounts of data generated by different diagnostic tools by integrating and extracting valuable information from these different data sources. Data-driven approaches can also enable the transfer of knowledge and models between different fusion devices, accelerating progress and benefiting the wider fusion research community.

Observations consistently indicate the occurrence of QC modes based on plasma conditions for various fusion devices, as discussed in section 2.4. Among these observations, the occurrence of these plasma condition-dependent QC modes in the LOC sub-regime, but their apparent disappearance in the SOC sub-regime, is the context of this work. Indeed, as mentioned in the chapter 1.3.5, TEM associated with anomalous transport would prevail in the LOC sub-regime and would then have a signature in the fluctuation spectrum corresponding to the QC modes.

Identification of these QC-modes using reflectometry have been performed in various fusion devices. However, these identifications have been limited to specific discharges. This highlights the need for a refined methodology to not only identify but also extract these QC modes. It is essential to reinforce the relationship between QC modes and TEM through a comprehensive statistical study. This will determine the consistency of this relationship and reveal QC modes properties as manifested in different fusion devices.

In addition, given the importance of energy exchange as a means of identifying the mechanisms behind turbulent transport, this concept becomes crucial to confirm the consistency of the relationship of the QC modes with TEM in a deeper way, i.e. if each identified QC mode is related to TEM, they should all have the same energy exchange 'signature'. In order to analyse the energy exchange, it is therefore essential, firstly, to extract the QC modes in such a way as to have access to their temporal evolution and, secondly, to study the interaction that the QC modes could have with the other spectral components (Low Frequency component, Broadband component and noise), in other words, to have access to the dynamics of the QC modes. As will be explained later, a causal analysis is needed to understand these dynamics, to know if these QC modes could have the same cause.

This investigation should not be limited to different fusion devices, but should also be extended to different magnetic configurations.

This research then focuses on characterising the properties and dynamics of QC modes in reflectometry signals, based on a data-driven approach by integrating signal processing methods and machine learning techniques across different magnetic configurations, to end up firstly strengthening the link between QC modes and the LOC sub-regime in different tokamak magnetic configurations through a statistical study, and secondly studying the properties and dynamics of QC modes as a potential universal behaviour, including the W7X stellarator, ultimately looking for a universal mechanism (source of turbulent transport) that is believed to be common to any magnetic configuration.

As the different methods to access the properties and dynamics with reflectometry signals are not yet defined, this work is considered exploratory.

Chapter 3 is dedicated to reflectometry, a diagnostic that allows the study of local density fluctuations in the core region of the plasma. Since turbulence induces fluctuating quantities, their study allows to derive information about the nature of the turbulence.

Chapter 4 introduces the integration of machine learning and signal processing methods to study the reflectometry signals.

Chapter 5 presents the comprehensive algorithms developed for spectral decomposition, highlighting the extraction of the QC modes.

Chapter 6 deals with the properties and dynamics of the QC modes in different magnetic configurations.

In this research, fusion devices such as the Tore Supra tokamak, its upgraded version - the WEST tokamak, the TEXTOR tokamak and the W7X stellarator are being studied.

# Chapter 3

## Diagnostics: Reflectometry

### Contents

---

<b>3.1 Propagation of electromagnetic waves in the plasma</b> . . . . .	<b>40</b>
3.1.1 Plasma assumptions . . . . .	40
3.1.2 Propagation equations . . . . .	41
3.1.3 Polarisation modes . . . . .	42
3.1.4 Different regions of wave propagation . . . . .	43
<b>3.2 Fixed-frequency conventional reflectometry</b> . . . . .	<b>45</b>
<b>3.3 Physical phenomena associated with density fluctuations</b> . . . . .	<b>47</b>
<b>3.4 Poloidal correlation reflectometry (PCR)</b> . . . . .	<b>48</b>
<b>3.5 Experimental setup</b> . . . . .	<b>51</b>
3.5.1 Tore Supra-WEST Tokamaks . . . . .	52
3.5.2 TEXTOR Tokamak . . . . .	53
3.5.3 W7X Stellarator . . . . .	53
<b>3.6 Reflectometry signal spectrum</b> . . . . .	<b>55</b>
<b>3.7 Previous study</b> . . . . .	<b>60</b>

---

Probing the plasma to gain insight into turbulence dynamics requires robust diagnostic techniques. Magnetic diagnostics evaluate the magnetic balance and determine the position and shape of the plasma. Optical techniques such as Thomson scattering provide temperature profiles.

Microwave diagnostics, or more precisely reflectometry, adds another dimension by exploiting the propagation characteristics of electromagnetic waves, making them more suitable and versatile.

Reflectometry, based on the radar principle [77], has been extensively studied by the fusion plasma community to provide valuable insights into the complex dynamics of fusion plasmas. Reflectometry has developed significantly over the years: the first density profile was made by F. Simonet [78], the first ultra-fast heterodyne system for profile reflectometry, which was a major improvement, was made by P. Moreau et al. [79], the use of X-mode polarisation for edge density profile determination [see subsection 3.1.3] on tokamaks by Bottollier-Curtet et al. [80], improvements in density profile reconstruction by F. Clairet et al. [81], reconstruction of hollow regions in density profiles from frequency swept reflectometry by R.B. Morales et al. [82].

Several types of reflectometers are available that allow the measurement of several parameters, mainly under the Wentzel-Kramers-Brillouin (WKB) approximation. These parameters include the radial profile of the electron density, magnetohydrodynamic (MHD) activities [83, 84], detection of Alfvén modes [85], plasma rotation measurements and turbulence characteristics [77].

Reflectometry offers a flexible setup and is able to probe electron density fluctuations accurately. It also provides good temporal resolution (on the order of microseconds) and spatial resolution (with sub-centimeter wavelengths).

## 3.1 Propagation of electromagnetic waves in the plasma

The propagation of electromagnetic (EM) waves is primarily determined by their frequency ( $\omega$ ) and wave vector  $\mathbf{k}$ . However, magnetised plasma is a complex medium that is anisotropic, inhomogeneous, non-linear and highly dispersive due to different gradients in the magnetic configurations and plasma fluctuations. As a result, certain approximations have to be made to develop a model for studying density fluctuations in the plasma. This also applies to the measurement of the density profile.

### 3.1.1 Plasma assumptions

One approximation is to assume that the plasma is not spatially dispersive, meaning that at equilibrium, it consists of a collection of ions and electrons with the same amount of positive and negative charges. This assumption holds when the phase velocity of the wave is much greater than the thermal velocity of the particles. Another assumption is that the external magnetic field,  $B_0$ , is regular and static, and the ions are immobile on the time scale of the probing wave propagation time. This allows us to consider only the influence of electrons on the dielectric tensor.

We also assume that the EM waves are monochromatic and stationary, and can be represented by a plane wave as a natural solution of the wave equation as  $e^{(\mathbf{k}\cdot\mathbf{r}-\omega t)i}$ . Since the amplitude perturbations are significantly lower than the average value, nonlinear terms can be disregarded at first order of approximation. Finally, we assume that there are no external currents or collisions among particles, allowing us to consider the medium as non-dissipative.

In summary, to model the extraction of the density fluctuation properties in magnetized plasma, we make several simplifying assumptions about the nature of the plasma and the properties of the EM waves. These approximations enable us to develop a useful model for studying this complex phenomenon.

### 3.1.2 Propagation equations

The propagation of electromagnetic waves is governed by Maxwell's equations in all physical media from 0 Hz to gamma ray frequencies, these equations are as follows:

$$\begin{aligned}\nabla \times \mathbf{E} &= -\frac{\partial \mathbf{B}}{\partial t} \\ \nabla \times \mathbf{H} &= \mathbf{J} + \frac{\partial \mathbf{D}}{\partial t} \\ \nabla \cdot \mathbf{B} &= 0 \\ \nabla \cdot \mathbf{D} &= \rho\end{aligned}\tag{3.1}$$

where  $\mathbf{E}$  is the electric field and is related to the electric displacement vector  $\mathbf{D}$  as  $\mathbf{D} = \epsilon\mathbf{E}$  ( $\epsilon$  is the dielectric permittivity tensor),  $\mathbf{B}$  is the magnetic induction and is related to the magnetic intensity  $\mathbf{H}$  as  $\mathbf{B} = \mu\mathbf{H}$ , where  $\mu$  is the magnetic permeability of the medium. All these expressions are functions of space and time.

The charge density  $\rho$  and the current density  $\mathbf{J}$  are related through the continuity equation:

$$\begin{aligned}\nabla \cdot \mathbf{J} + \frac{\partial \rho}{\partial t} &= 0 \\ \mathbf{J} &= \sigma \cdot \mathbf{E}\end{aligned}\tag{3.2}$$

The physical properties of the medium are manifested through the quantities  $\epsilon$ ,  $\mu$ , and  $\sigma$ .

For a plasma, the currents are related to the various physical properties of the medium and can be used to define an effective dielectric constant. External currents, however, must be dealt with explicitly, and may not be incorporated into a characterization of the medium through an effective dielectric constant. For a homogeneous plasma, a Fourier transform

in both time and space is made so that the fields vary as  $i\mathbf{k} \cdot \mathbf{r} - i\omega t$ , so that we may define  $\mathbf{D} = \varepsilon\mathbf{E} = \varepsilon_0\mathbf{E} - \frac{\mathbf{J}}{i\omega} = (\varepsilon_0 - \frac{\sigma}{i\omega})\mathbf{E}$

$$\begin{aligned}\varepsilon &= \varepsilon_0 - \frac{\sigma}{i\omega} \\ K &= 1 - \frac{\sigma}{i\omega\varepsilon_0}\end{aligned}\quad (3.3)$$

By integrating the Maxwell equations presented in Eq. 3.1, and considering  $\mathbf{D} = \varepsilon_0 K\mathbf{E}$  along with  $1/c^2 = \mu_0\varepsilon_0$  ( $\mu_0 = 4\pi \cdot 10^{-7} H/m$  and  $\varepsilon_0 = 8.85 \cdot 10^{-12} F/m$ ), we can derive the generalized Helmholtz equation which characterizes a homogeneous and isotropic medium

$$\nabla \times (\nabla \times \mathbf{E}) + \mu_0 \frac{\partial \mathbf{J}}{\partial t} + \frac{K}{c^2} \frac{\partial^2 \mathbf{E}}{\partial t^2} = 0 \quad (3.4)$$

with no external currents, we have the Helmholtz or wave equation:

$$\nabla \times (\nabla \times \mathbf{E}) + \frac{K}{c^2} \frac{\partial^2 \mathbf{E}}{\partial t^2} = 0 \quad (3.5)$$

Introducing the vector refractive index  $\mathbf{N} = \mathbf{k} \frac{c}{\omega}$  then it can be expressed as:

$$\mathbf{N} \times (\mathbf{N} \times \mathbf{E}) - K\mathbf{E} = 0 \quad (3.6)$$

This leads to the propagation relation:  $D = (\mathbf{k}, \omega)$ , which establishes a relationship between the wave frequency and its wave vector. Solving this equation can be used to determine how the wave will propagate.

*Appleton – Hartree* equation allows to find an expression for the refractive index of a wave propagating with an angle  $\theta$  to the medium magnetic field  $B_0$  :

$$N^2 = 1 - \frac{X}{1 - \frac{Y^2 \sin^2 \theta}{2(1-X)} \pm [\frac{Y^4 \sin^4 \theta}{2(1-X)^2} + Y^2 \cos^2 \theta]^{0.5}} \quad (3.7)$$

where  $X = \frac{\omega_{pe}^2}{\omega^2}$  and  $Y = \frac{\omega_{ec}}{\omega}$ ,  $\omega_{pe}$  was defined in the equation 1.4 and  $\omega_{ec}$  was defined in the equation 1.5.

### 3.1.3 Polarisation modes

Electromagnetic waves propagating with a wavenumber perpendicular to the applied magnetic field,  $\mathbf{k} \perp \mathbf{B}_0$  ( $\theta = 0$ ), can have two wave polarisations: the ordinary mode (O-mode), where the wave electric field ( $\mathbf{E}$ ) is parallel to  $\mathbf{B}_0$ , and the extraordinary mode (X-mode), where the

wave electric field ( $\vec{E}$ ) is perpendicular to  $\vec{B}_0$  [see figure 3.1]. This probing wave is launched and propagates until the refractive index is zero, indicating a cut-off layer and providing the cut-off position.

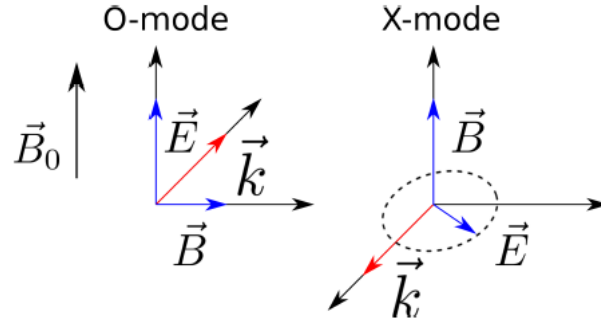


Fig. 3.1 X-mode and O-mode polarization, reproduced from Hornung 2013a [86].

The dispersion relation for each polarization can be deduced for a perpendicular polarization:

$$\begin{aligned} N_O^2 &= 1 - \omega_{pe}^2/\omega^2 \\ N_X^2 &= 1 - \frac{\omega_{pe}^2/\omega^2(1 - \omega_{pe}^2/\omega^2)}{1 - \omega_{pe}^2/\omega^2 - \omega_{ce}^2/\omega^2} \end{aligned} \quad (3.8)$$

for the O-mode  $N_O$  depends only on the electron density, whereas in the X-mode  $N_X$  depends also on the magnetic field  $\vec{B}_0$ .

All along the optic path the wave can behave in different ways depending on the refractive index:

- Propagation ( $N \rightarrow 1$ ): It occurs in vacuum
- Reflection ( $N \rightarrow 0$ ): It occurs when the launched wave reaches the cut-off (measurement area). the equation would give :  $X(1 - X) = 1 - X - 1/2Y^2 \pm 1/2Y^2$
- Resonance ( $N \rightarrow \infty$ ): This behaviour is avoided in reflectometry, but it is used on heating systems as ICRH, ECRH.

### 3.1.4 Different regions of wave propagation

Four different regions of the wave propagation can be distinguished for any density profile [see figure 3.2]:

In the region labelled 1, the vacuum propagation, for the path between the antenna and the plasma edge, the wave propagates at  $c$ .

In the region labelled 2, before reaching the cut-off layer, the refractive index is positive and the Wentzel-Kramers-Brillouin (WKB) approximation can be applied. For the WKB approximation, the length of the density gradient must be much larger than the local wavelength, i.e.  $N$  varies slowly so that the wave equation is locally satisfied.

In the region labelled 3, the refractive index becomes zero as the cut-off layer is approached and the WKB condition is no longer satisfied, so the wave propagation equation must be solved analytically; very close to the cut-off layer, linear behaviour can be considered and then the Airy function can be used to solve.

In 4, the refractive index is imaginary, the wave vanishes and the WKB approximation works again.

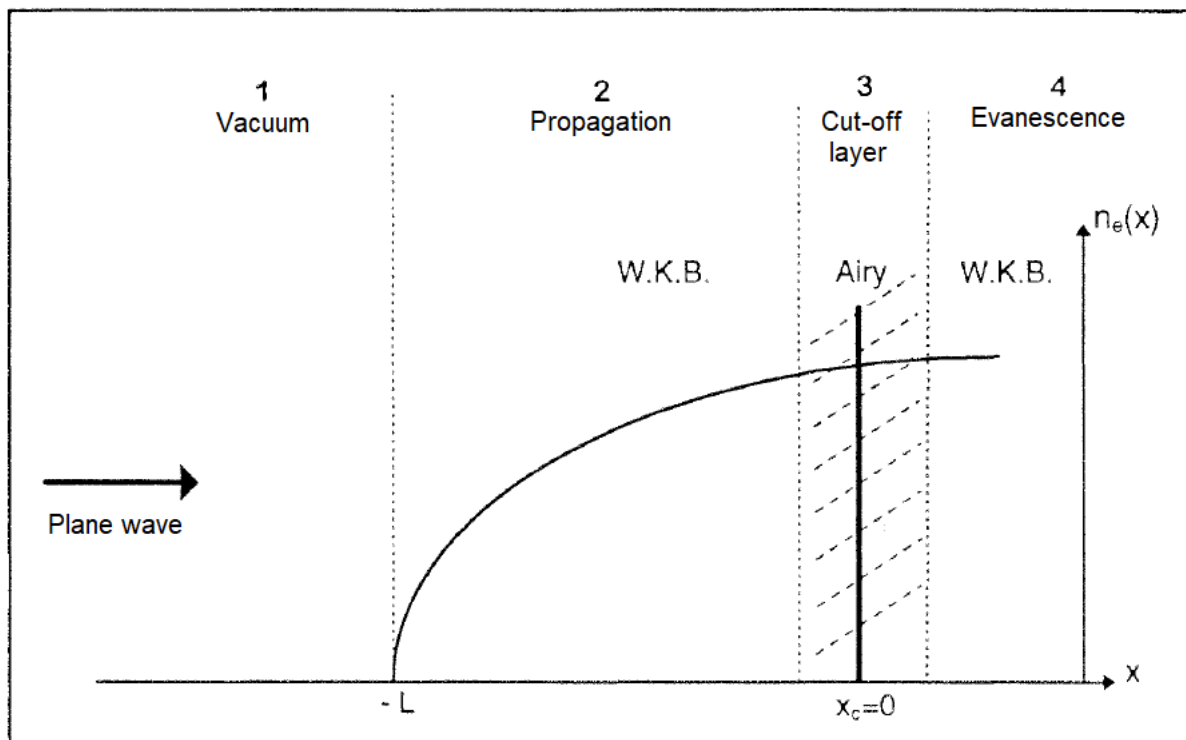


Fig. 3.2 © Different regions for any given density profile. Adapted from Fanack 1997 [87].

As described previously, the aim of the probing wave is to reach the cut-off layer and study their interaction. In relation to this paradigm, two principles can be employed, depending on the angle between the propagation of the wave and the cut-off layer: Fixed-frequency conventional reflectometry, ( $\alpha \approx \pi/2$ ) and Doppler Back Scattering Reflectometry, ( $\alpha < \pi/2$ ) now called Doppler Back Scattering [see figure 3.3]. In addition, Poloidal

Correlation Reflectometry operates on a similar principle to Fixed Frequency Conventional Reflectometry, but is distinguished by the use of multiple receiving antennas, which adds a layer of specificity to its approach.

This thesis focuses primarily on fixed frequency conventional reflectometry (CFR) and poloidal correlation reflectometry (PCR).

## 3.2 Fixed-frequency conventional reflectometry

As discussed previously, the characteristics of the propagation of the electromagnetic waves can be described mainly by their amplitude and phase. These phase and amplitude variations results from the round trip of an electromagnetic wave through a plasma can be monitored by comparing it with a reference signal. The phase is the primary quantity of interest, as it reflects the time delay experienced by the wave, while the amplitude provides information about reflectivity variations due to geometrical effects or interference events. In the framework of the WKB approximation, the dominant part of the phase variation between the antenna located at  $x = 0$  and the reflecting layer at  $x_c$  can be estimated.

The phase can vary due to changes in the probing frequency or the optical path length between the antenna and the cut-off layer along the line of sight. As a result, temporal variations in the phase can be expressed as follows:

$$\phi_p = \frac{4\pi}{c} \cdot f \cdot \int_0^{x_c} N(r, f, t) dr - \pi/2 \quad (3.9)$$

$N$  is the refraction index and the  $-\pi/2$  comes from an evaluation based on the exact solution and its asymptotic development on the propagating side and connecting it to the WKB solution [84]. The result of phase variation can be expressed as follows :

$$\frac{\partial \phi_p}{\partial t} = \frac{4\pi}{c} \cdot \frac{\partial f}{\partial t} \cdot \int_0^{x_c} N(r, f, t) dr + \frac{4\pi}{c} \cdot f \cdot \frac{\partial}{\partial t} \left( \int_0^{x_c} N(r, f, t) dr \right) \quad (3.10)$$

This equation reveals two distinct contributions. The first segment of the equation comes from alterations in the probing wave's frequency, while the second arises due to modifications in the optical path, attributed to the temporal variations in density during the wave's time of flight through the plasma. This phenomenon can be related to a Doppler shift when the time derivative is sufficiently pronounced.

In fixed-frequency conventional reflectometry [see figure 3.3], the second part of the equation 3.10 predominates (at a constant frequency) and it allows for the analysis of density fluctuations at the specified cut-off position.

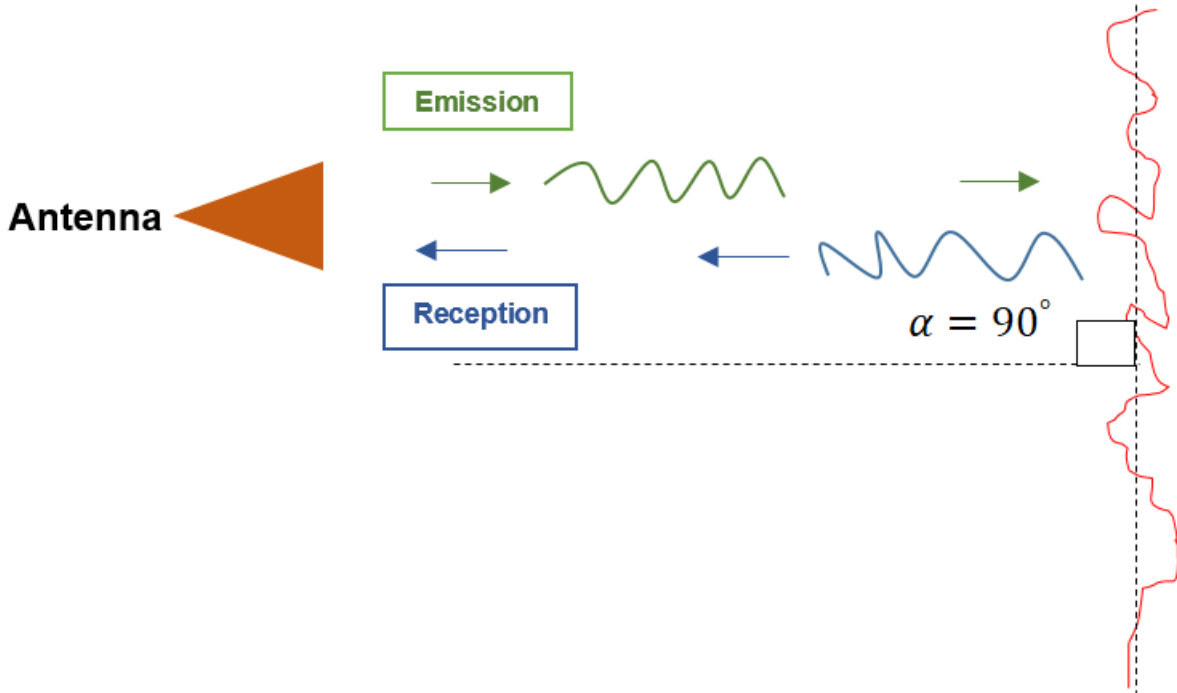


Fig. 3.3 Illustration of fixed-frequency conventional reflectometry.

Conversely, when the first part is significantly dominant, specifically at a rapidly sweeping frequency, the turbulence can be perceived as "frozen" throughout the frequency sweep. This provides the capability to measure electron density profiles and to investigate density fluctuations at each probing frequency in scenarios of ultra-fast-swept frequencies.

In addition, the time delay  $\tau(f)$  is the round trip time to return to the antennae, typically lasting tens of nanoseconds.

$$\tau(f) = \frac{1}{2\pi} \frac{\partial \phi}{\partial t} = f_b \frac{\partial f}{\partial t} \quad (3.11)$$

where the beat frequency is  $f_b = \frac{1}{2\pi} \frac{\partial \phi_p}{\partial t} = f_b \left( \frac{\partial f}{\partial t} \right)$

Note that the measurement process is very fast: the profile measurement time can be as short as  $1\mu s$ . Therefore, the density profile remains essentially constant during the profile measurement, given that the characteristic time of turbulence is a few microseconds. Hence, the turbulence can be seen as frozen during. However, it is important to note that even if  $\phi_p$  remains stable during a single measurement, it will show variations between different measurements.

### 3.3 Physical phenomena associated with density fluctuations

Due to the presence of density fluctuations along the wave propagation path, two major effects are considered: firstly, these fluctuations can scatter the wave. Secondly, they can cause a shift in the cut-off layer by altering the refraction index.

This scattering, corresponding to the first effect, follows the Bragg rule [see figure 3.4], in fact the incident wave  $(\mathbf{k}_i, \omega_i)$  is affected by the fluctuation density  $(\mathbf{k}_f, \omega_f)$ , a part of the energy coming from the incident wave is spread in different directions according to the wave number spectrum. The scattered wave then follows:

$$\begin{aligned} \mathbf{k}_s &= \mathbf{k}_i + \mathbf{k}_f \\ \omega_s &= \omega_i \pm \omega_f \end{aligned} \quad (3.12)$$

The scattering angle is given by  $|k_f| = 2|k_i| \sin(\theta/2)$ , as shown in the following figure 3.4.

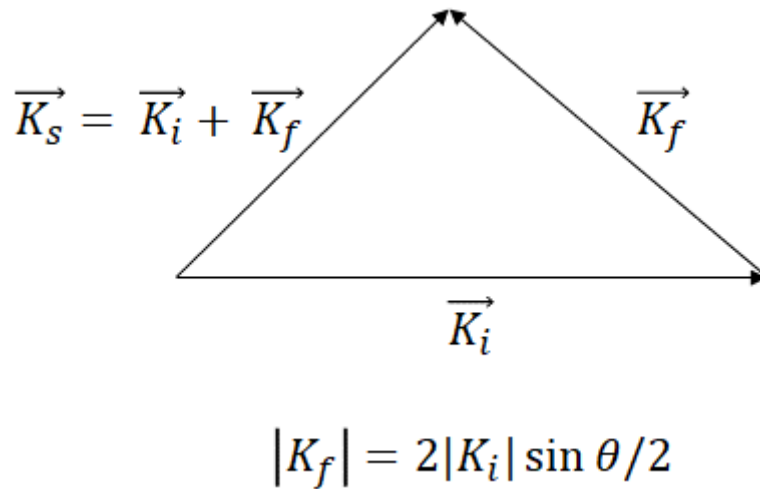


Fig. 3.4 Illustration of the Bragg rule.

When this relationship is satisfied, the  $\mathbf{k}_f$  of fluctuations is resonant and the coupling between  $\mathbf{k}_i$  and  $\mathbf{k}_f$  is maximal.

For  $k_f = -2k_i(x_b)$ ,  $k_i(x_b)$  is the wavenumber of the resonance position of the Bragg back-scattering. This last equation then shows that the Bragg resonance can only occur for density fluctuations whose wavenumber is  $k_f < 2k_0$ , where  $k_0$  is the wavenumber in vacuum.

Even if density fluctuations do not produce a scattering Bragg resonance, they can still induce an oscillation of the cut-off layer and traverse it if  $k_f$  is significantly small. Therefore, the reflection occurs at the initial cut-off position, augmented by a shift.

If  $k_f \ll k_0$  and considering a linear density profile with a large density gradient length  $L$ , the solution becomes  $k_A = 0.63k_0^{2/3}L^{-1/3}$ , denoting the Airy wavenumber, then  $k_f < 2k_A = 0.068k_0$  [88].

In a plasma with density perturbations, denoted as  $\delta n_e$ , the incoming wave may undergo scattering due to these perturbations, which in turn may induce oscillations in the cut-off layer around its equilibrium position. When the amplitude of such density perturbations is considerably small, the Born approximation can be used to linearize the propagation equations, allowing an analytical expression to be obtained. The criterion for considering these density fluctuations to be of small amplitude is:  $\delta n/n \ll (k_0L)^{-2/3}$ .

Considering a normal incidence, the motion of the cut-off is reflected by the phase fluctuations present in the changes of the refractive index. The density fluctuations can then be correlated with the phase fluctuations by the following relationship [77]: (O-mode)

$$\delta n_e/n_e = \left( \frac{c^2 k_{eff}}{4\pi^3 L_\epsilon f^2} \right)^{0.5} \delta \phi \quad (3.13)$$

$L_\epsilon = \left( \frac{\partial \epsilon}{\partial r} \right)^{-1}$  is the scale length of the permittivity  $\epsilon$  at the cutoff position, while  $f$  is the frequency of the probing wave.  $k_{eff}$  is the effective wave number.

In the X-mode, the situation is more complex due to its dependence on the magnetic field.

A phenomenon known as 'phase runaway', present in both O-mode and X-mode, is typically observed in the phase fluctuation signals, making it difficult to extract the phase fluctuation level and establish its relationship to the density fluctuation. In such scenarios, the phase delay increases persistently over time in a way that cannot represent a continuous motion of the cut-off positions relative to the receiver.

### 3.4 Poloidal correlation reflectometry (PCR)

Poloidal Correlation Reflectometry (PCR) follows the same principle as fixed frequency conventional reflectometry, the difference being the use of multiple poloidally spaced receiving antennas [see figure 3.5]. PCR is based on a cross-correlation analysis between  $\delta n_e/n_e$  detected by different antennas.

The strength of Poloidal Correlation Reflectometry (PCR) lies in its inherent ability to exploit a time delay ( $\tau$ ) between two time series or signals [see equation 3.14] due to their poloidal separation. This method enhances recurrent turbulent structures and mitigates

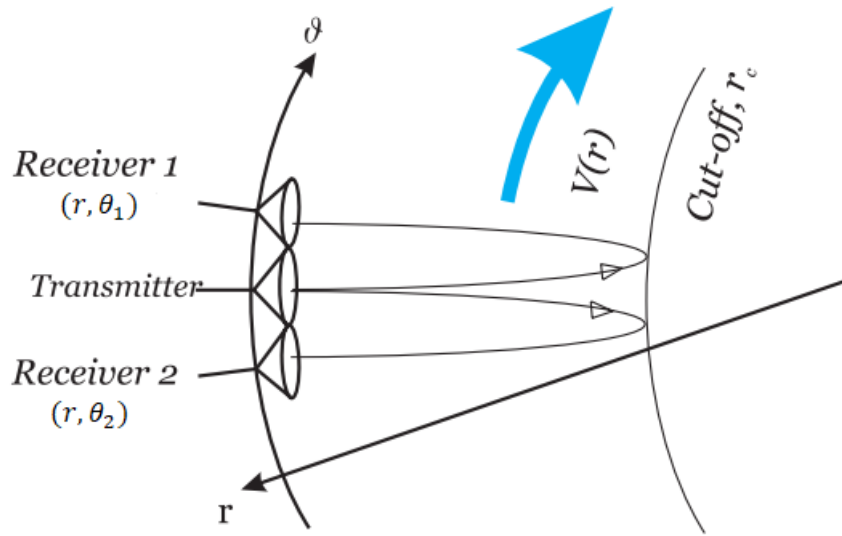


Fig. 3.5 Schematic overview of 2 Poloidal Correlation Reflectometry (PCR) antennas.

the effects of uncorrelated noise. This ability to enhance coherent turbulent structures while attenuating uncorrelated noise is critical to the accurate analysis and understanding of turbulence.

$$(R_1 \star R_2)(\tau) = \int_{-\infty}^{\infty} R_1^*(t) R_2(t + \tau) dt \quad (3.14)$$

$\Gamma_0$ ,  $\Delta t$  and  $\Gamma_{max}$  [see figure 3.6] allow to estimate two important quantities for the analysis of plasma turbulence and transport: the turbulence decorrelation time  $\tau_{dc}$  and the turbulence correlation length ( $\lambda_L$ ).

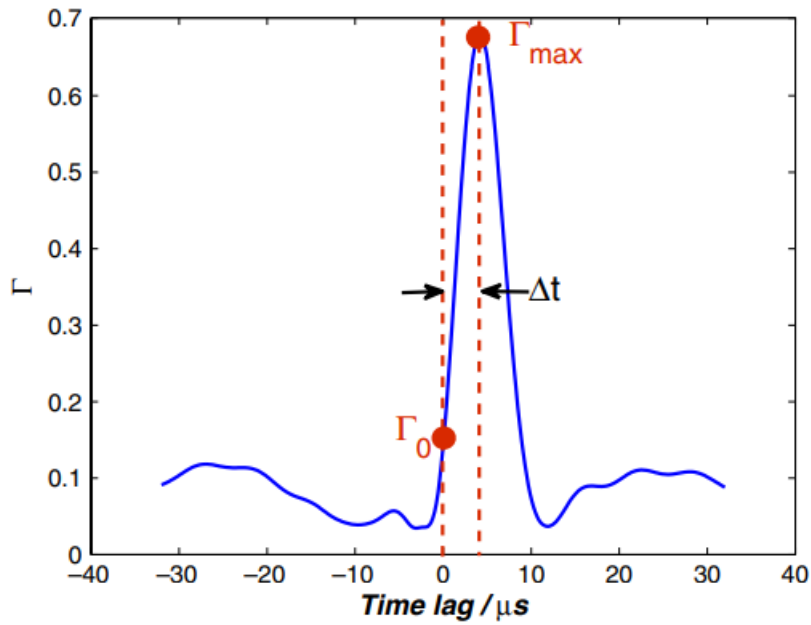


Fig. 3.6 Example of cross-correlation coefficient estimated for a pair of TEXTOR antennas.

In addition, having several antennas aligned in the poloidal direction, the slope of the fitted line for  $(\Delta\theta, \Delta t)$  gives the turbulence rotation  $\Omega_{\perp}$  as illustrated in the figure 3.7.

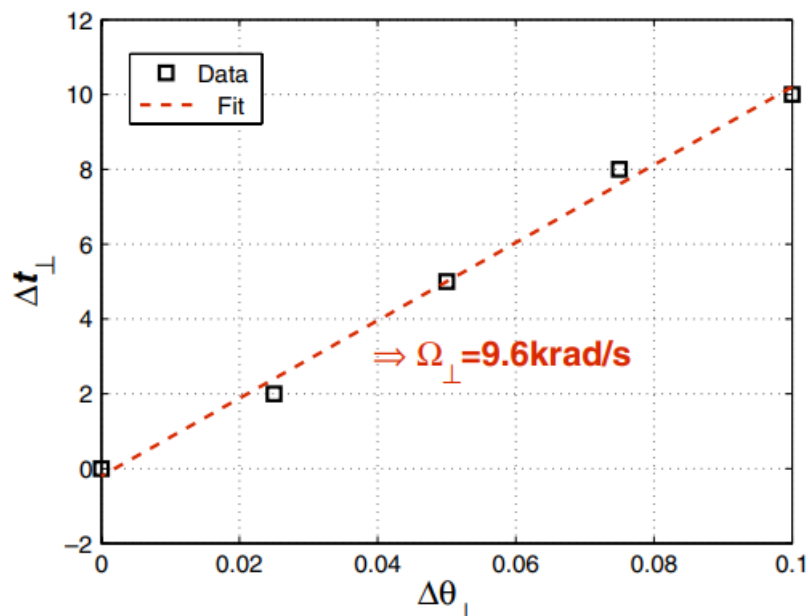


Fig. 3.7 Determination of  $\Omega_{\perp}$  from the slope of five different poloidal angles. Adapted from Krämer-Flecken 2011 [89].

In conclusion, PCR provides some information in turbulent transport. Poloidal structures can be studied, the rotation profile can be monitored, including areas of strong poloidal rotational shear near the barrier region [90]. In addition, as emphasised by Kramer-Flecken in [89] with respect to the TEXTOR tokamak, the possession of multiple antennas aimed at the same flux surface and aligned in the poloidal direction in close proximity allows the acquisition of turbulence decorrelation time ( $\tau_{dc}$ ) and turbulence correlation length ( $\lambda_L$ ) measurements. By having three antennas spaced both toroidally and poloidally, it's possible to measure the tilt angle of the turbulent structures and measure the safety factor [91]. Furthermore, if the antennas are positioned at sufficiently large spatial separations, the study of long-range correlation (LRC) properties can be investigated, facilitating the study of the three-dimensional nature of fluctuations and flows within the plasma.

### 3.5 Experimental setup

Due to their robustness and simplicity in comparison with other diagnostic tools, reflectometers have been installed in fusion devices of various sizes.

As described in the subsection 2.5.2, the fusion devices considered in the present work are the TEXTOR tokamak, the Tore Supra tokamak, the WEST tokamak and the W7-X stellarator. This section examines the experimental configurations of the reflectometers used in these specific fusion devices, providing a comprehensive study of their installation.

Fusion device	Frequency probing	Frequency acquisition	Polarization mode	Operating mode
Tore Supra	105-150GHz	1MHz	X-mode	Fixed-frequency
WEST	105-150GHz	1MHz	X-mode	Fixed-frequency
TEXTOR	24-40GHz	500kHz	O-mode	Fixed-frequency and PCR
W7X	$K_a$ -band: 24-40GHz	5MHz	O-mode	Fixed-frequency and PCR
	$K_U$ -band: 40-60GHz	5MHz	O-mode	Fixed-frequency and PCR

### 3.5.1 Tore Supra-WEST Tokamaks

The Tore Supra, located at the CEA in Cadarache, France, was a tokamak with a circular section limiter. It was designed to explore the intricacies of fusion technology and physics, with a particular focus on long pulse discharge conditions. This fusion device was able to sustain discharges for several minutes thanks to the use of superconducting toroidal field coils. In addition, all components in contact with the plasma were actively cooled to improve operating efficiency.

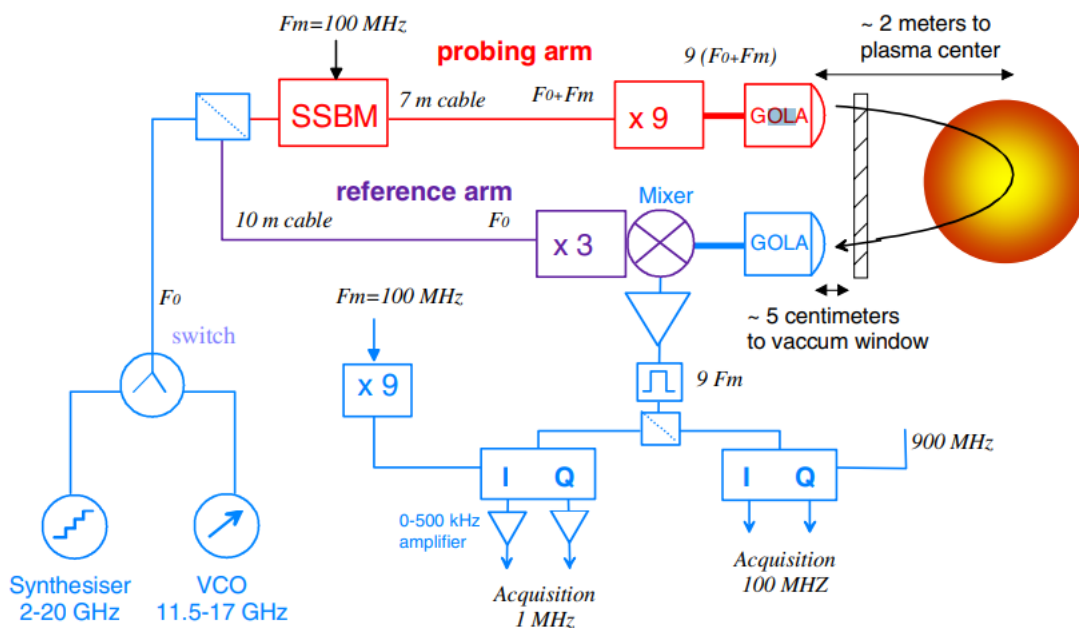


Fig. 3.8 Schema dual reflectometer heterodyne used in Tore Supra and WEST tokamaks.

The reflectometer in Tore Supra probed the core of the plasma in X-mode, from the mid-radius to the inner side. Using the innovative dual-source system introduced by Sabot in 2006, this reflectometer is able to measure density fluctuations at predetermined frequencies and to acquire density profiles in the same plasma pulse. However, this significant capability cannot capture the density profile and fluctuation simultaneously.

This reflectometer contains two independent fluctuation channels, probing multiple fixed frequency steps ranging from 8.192 ms to 50 ms per shot. Fluctuation measurements, typically taken during stable phases of the discharge, were completed in approximately 300 ms. The system also allowed extended acquisitions (up to 500 ms) at, for example, one to four frequency steps to facilitate MHD studies [92].

Subsequently, Tore Supra underwent extensive modifications in 2012 as it evolved into the WEST tokamak. These upgrades included the installation of internal coils and a transition

of the plasma facing components from carbon to tungsten, with the aim of testing ITER divertor monoblocs. The core reflectometer now performs ultra-fast profile measurements and the sampling frequency for fluctuations has been increased to up to 5 MHz.

### 3.5.2 TEXTOR Tokamak

TEXTOR was a circular limiter tokamak with  $R_0 = 1.75m$  and  $a = 0.46m$ . The plasma current and the toroidal magnetic field could be varied over a wide range ( $600kA \leq I_p$ ,  $1.9 \leq B_t \leq 2.7T$ ).

An O-mode heterodyne reflectometry system was installed at TEXTOR to measure the plasma density fluctuation characteristics [see figure 3.9]. It operated in the frequency range  $26GHz$  to  $37GHz$ , corresponding to an electron density range of  $0.8 \times 10^{19}m^{-3} \leq n_e \leq 1.7 \times 10^{19}m^{-3}$ . The reflectometer could be connected to two different antenna arrays via a 3 m  $K_a$  band waveguide. The antenna array consisted of five antennas in the equatorial plane on the low field side and five antennas on the top of the vessel, located on the same poloidal cross section. Five equivalent pyramidal horns, poloidally spaced, formed the equatorial array. The central horn was used as a transmitter and four side horns as receivers. The horns were aligned with the centre of the vacuum vessel. In such an array, the poloidal distance between two reflecting points was proportional to the radius.

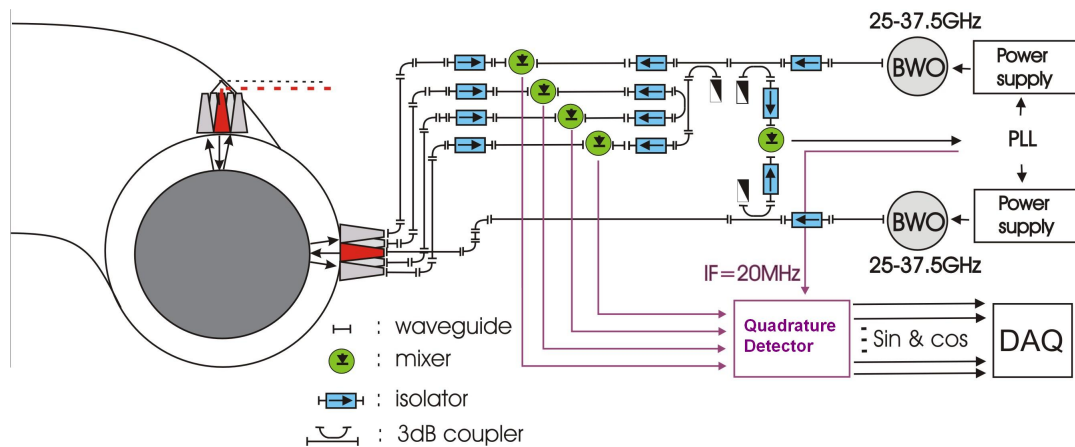


Fig. 3.9 TEXTOR reflectometer setup.

### 3.5.3 W7X Stellarator

Wendelstein 7-X is the world's largest fusion device of the stellarator type. The reflectometer operates in Ka-band and U-band [see figure 3.10] using ordinary wave polarisation (O-mode), giving cut-off densities of  $0.7$  to  $2 \times 10^{19}m^{-3}$ .

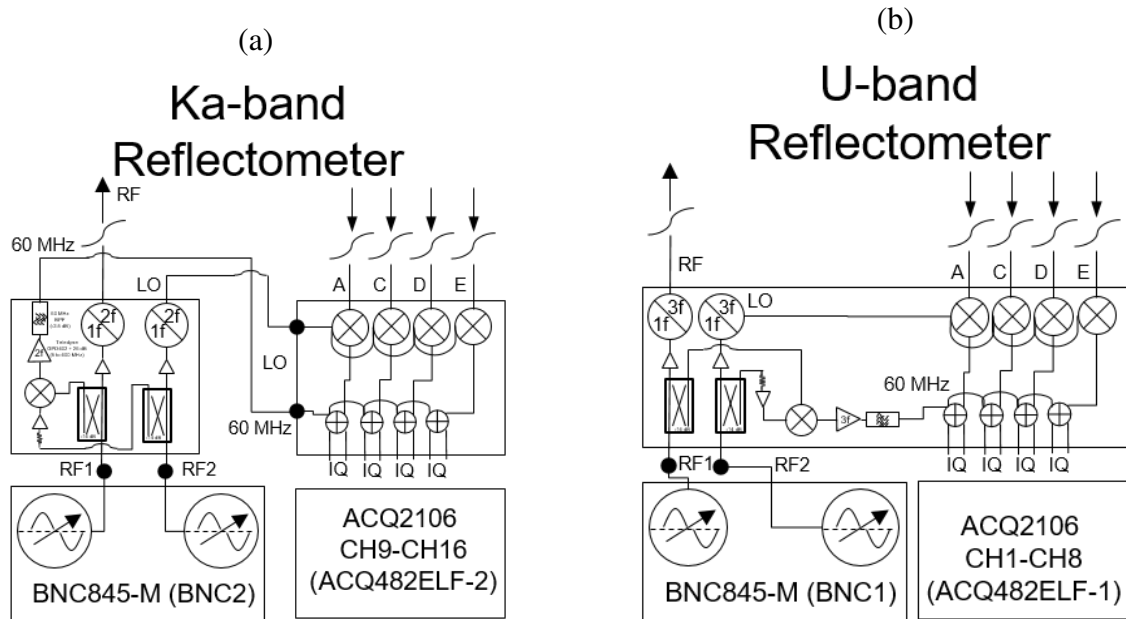


Fig. 3.10 The Ka-band and U-band reflectometers installed at W7X. The U-band is built on the same principle as the TEXTOR reflectometer.

The reflectometer consists of two microwave sources (voltage controlled oscillators, VCO) in the range 10-20 GHz, which are coupled by a phase-locked loop (PLL). After a stage of frequency multiplication, amplification and band-pass filtering, the output power is typically  $P_{\text{out}} \approx 100$  mW. For heterodyne detection, both sources  $f_{1,2}$  are slightly detuned to produce an intermediate beat frequency (IF) of  $f_1 - f_2 = 60$  MHz after frequency multiplication.

PCR can be performed using an antenna array consisting of five pyramidal horn antennas, each with an aperture of  $44.1 \times 34.8$  mm. The conceptual design of the antenna array, together with its supporting structure, is shown in figure 3.11(a). Antenna A is the transmitting antenna and is connected to the signal output of the microwave generator, while antennas B-E are the receiving antennas. They are responsible for measuring the microwave radiation reflected from the cut-off layer.

The antenna array is localized in the elongated beanshaped plane ( $\varphi = 72^\circ$ ), in which the magnetic field approximately scales as  $1/R$  (with  $R$  denoting major radius). The orientation of the antenna line-of-sights is indicated in figure 3.11(b). The line-of-sight of antenna A is designed to be perpendicular to the flux surface of the vacuum magnetic field configuration at the design cut-off layer  $r/a \approx 0.95 - 1$  ( $a = 0.49$  m denotes the minor radius) [93].

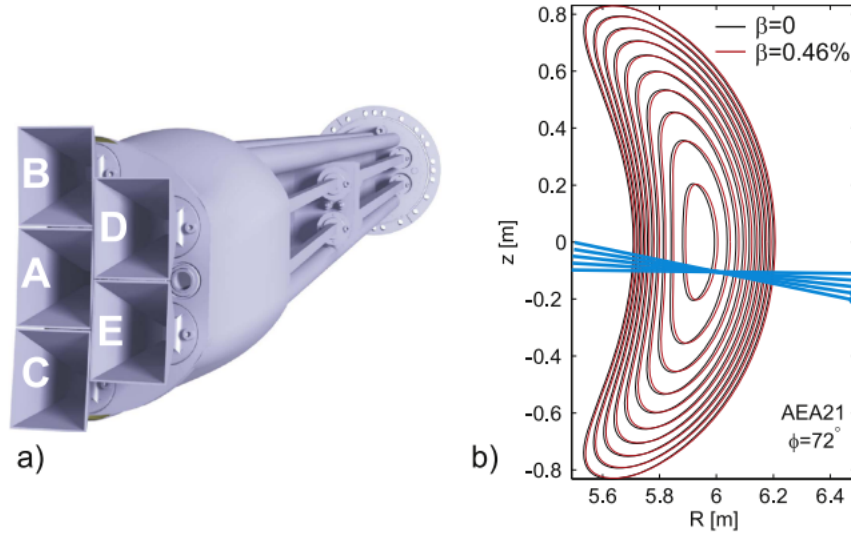


Fig. 3.11 (a) Illustration of the PCR plugin including the antenna nomenclature. (b) Flux-surfaces of the OP1.1 configuration in the beam plane at  $\varphi = 72^\circ$  for two values of the plasma- $\beta$  ( $\langle\beta\rangle = 0$  and  $\langle\beta\rangle = 0.46\%$ ). The antenna array and lines-of-sight are indicated in blue.

### 3.6 Reflectometry signal spectrum

As previously described, phase and amplitude variations result from the round trip of an electromagnetic wave: phase variations are related to the density fluctuations that occur mainly in the vicinity of the cut-off layer, while amplitude variations are the result not only of density fluctuations but also of cut-off layer deformation, interference phenomena, etc.

Each reflectometry signal provides two orthogonal signals,  $A_t \cos(\phi_t)$  and  $A_t \sin(\phi_t)$ , where  $A_t$  and  $\phi_t$  correspond to the amplitude and phase of the fluctuation signals, respectively. Consequently, the complex-valued signal can be expressed as follows:

$$\text{Signal} : R(t) = A_{(t)} \cdot e^{i\phi(t)}, f(t) = A_{(t)} (\cos \phi(t) + i \sin \phi(t)) \quad (3.15)$$

The reflectometry signal has a frequency sampling and a duration imposed by the reflectometer setup [see subsection 3.5]. They can show completely different behaviour over time from one signal to another [see figure 3.12].

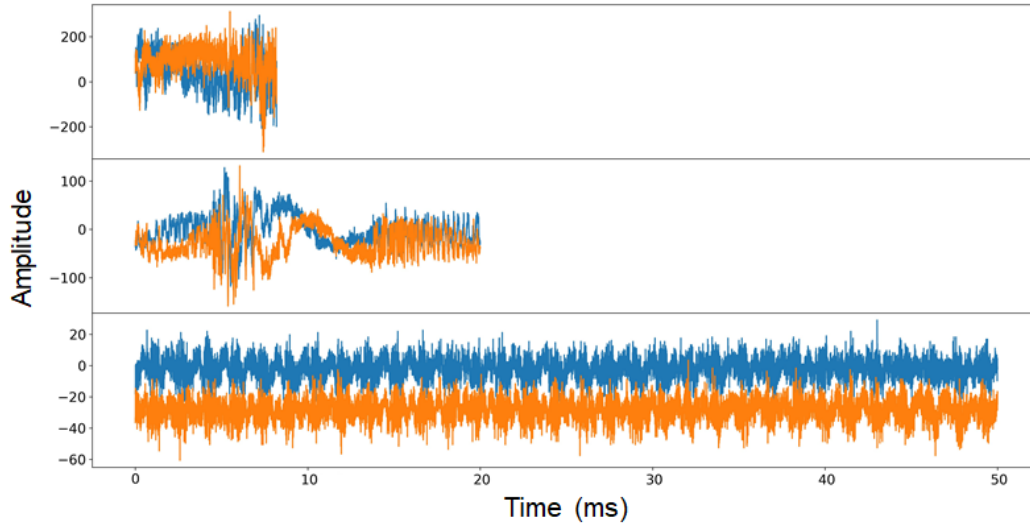


Fig. 3.12 Examples of Reflectometry signals in their real/imaginary parts representation. (a)  $I_p = 1MA$ ,  $n_e = 2.6 \times 10^{19}m^{-3}$  and  $\rho = 0.15$ . (b)  $I_p = 0.5MA$ ,  $n_e = 1.2 \times 10^{19}m^{-3}$  and  $\rho = -0.25$ . (c)  $I_p = 0.6MA$ ,  $n_e = 2 \times 10^{19}m^{-3}$  and  $\rho = 0.37$ .

In previous studies, the use of the Fourier transform has proven to be essential in understanding the distribution of signals in the frequency domain. In particular, the Welch method, when applied after the Fourier transform, has revealed how the energy of the signal is distributed across different frequencies [see figure 3.13]. This method helps to identify dominant frequency components along with their amplitudes, which may be indicative of different physical phenomena, processes or sources contributing to the overall signal.

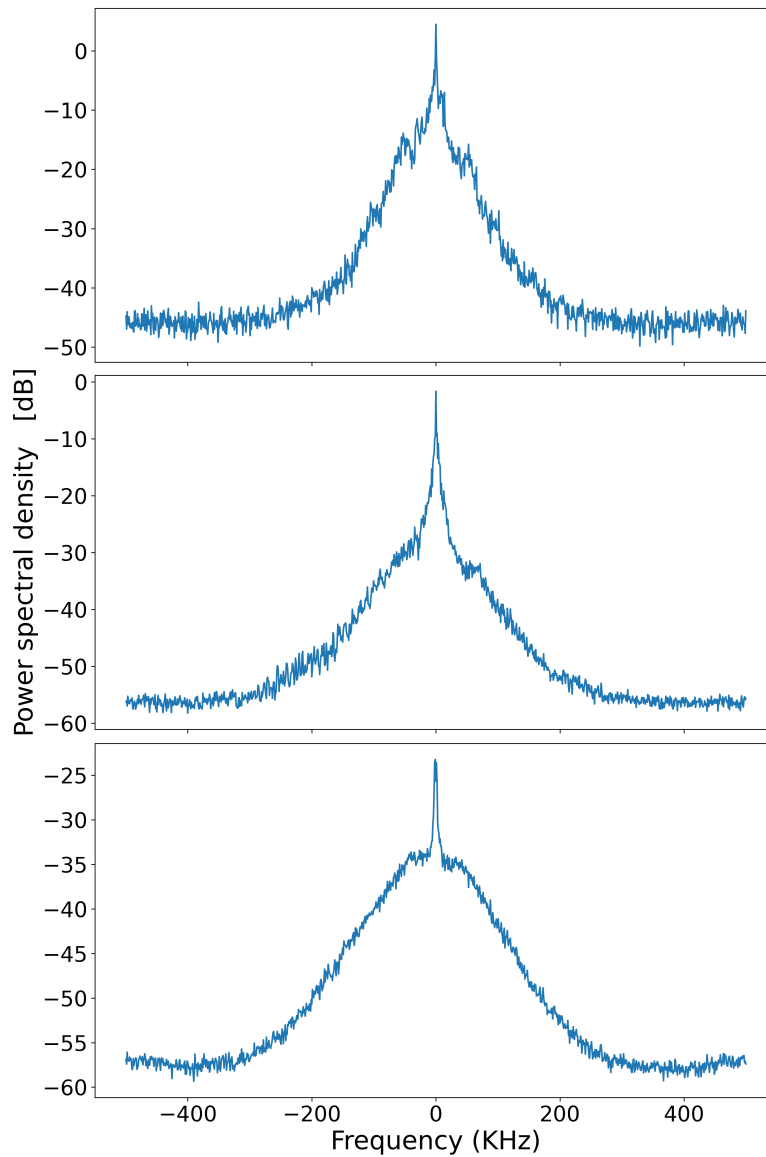


Fig. 3.13 Power spectral density of signals shown in figure 3.12. (a)  $I_p = 1MA, n_e = 2.6 \times 10^{19}m^{-3}$  and  $\rho = 0.15$ . (b)  $I_p = 0.5MA, n_e = 1.2 \times 10^{19}m^{-3}$  and  $\rho = -0.25$ . (c)  $I_p = 0.6MA, n_e = 2 \times 10^{19}m^{-3}$  and  $\rho = 0.37$ .

The frequency is defined as  $f = \frac{1}{2\pi} \frac{\partial \phi}{\partial t}$ . Increments and decrements in the phase then give positive and negative frequencies respectively [see figure 3.14].

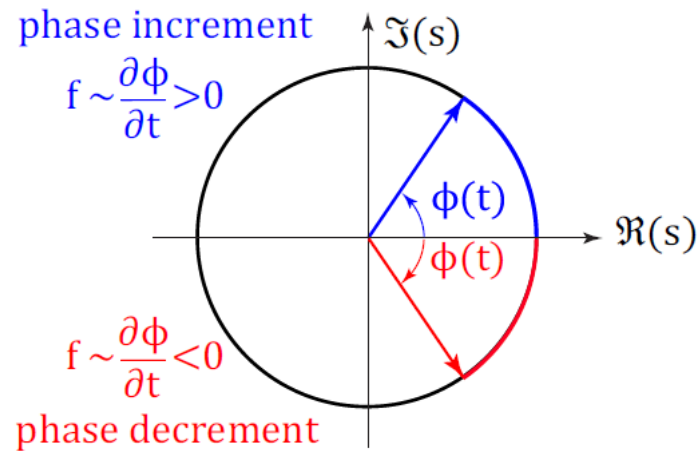


Fig. 3.14 Evolution of the phase of the signal  $R(t)$  in the complex plane with phase increment (blue) and phase decrement (red) corresponding to positive and negative frequencies, respectively, while keeping the amplitude constant. Adapted from Arnichand's thesis.

As a result of all the phase increments and phase decrements, a relevant characteristic of the reflectometry signal spectrum is born: asymmetry. It has been observed that reflectometry spectra are not symmetrical. This has never been clearly and completely explained, but a recent study suggests that a Doppler effect due to the poloidal velocity can cause such asymmetry, which can occur if the reflectometer does not probe the plasma perfectly perpendicular to the cut-off layer (i.e. a misalignment of the reflectometer with respect to the equatorial plane or a vertical displacement of the plasma) [86, 94]. Another possible explanation is the radial asymmetry of the turbulent structures.

In [95], Vershkov undertook an extensive investigation to study the properties of the reflectometry signal. This investigation included both experimental turbulence characterisation and theoretical considerations, including correlation reflectometry. In particular, the reflectometry signal spectrum showed good agreement with theoretical predictions, as validated by extensive 2D full-wave simulations.

Using correlation reflectometry, Vershkov and Krämer-Flecken showed that the reflectometry frequency spectrum is the superposition of several components: Low frequency component, Low and High Frequency Quasi Coherent modes (LFQC & HFQC) and a broadband component, all shown in the amplitude spectrum [see figure 3.15].

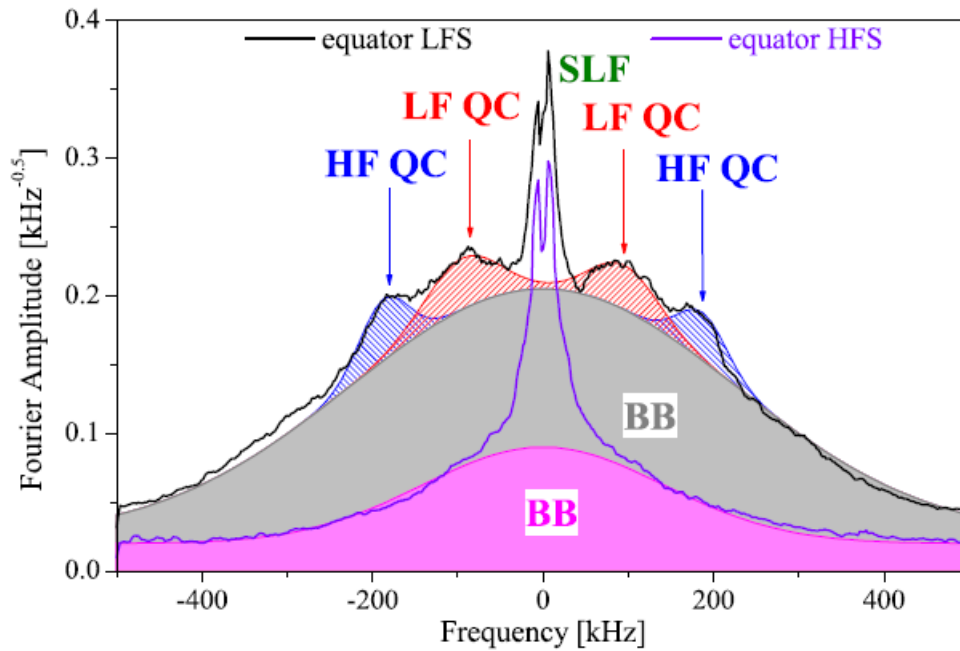


Fig. 3.15 Amplitude of the frequency spectrum of reflectometry signals at LFS (black) and HFS (purple). Adapted from Vershkov 2011 [96].

Several spectral components have been analysed. Some of these components, such as coherent modes like GAMs and MHD, have been linked to their underlying mechanisms.

Previous research performed by Vershkov in 2005 and 2011 [95, 96] indicated that the Broadband component, the LF component and the QC modes exhibit distinct properties, suggesting different underlying mechanisms. For instance, their poloidal ballooning behavior differs, with BB and QC modes ballooning on the Low Field Side (LFS) while LF fluctuations do not [see figure 3.16].

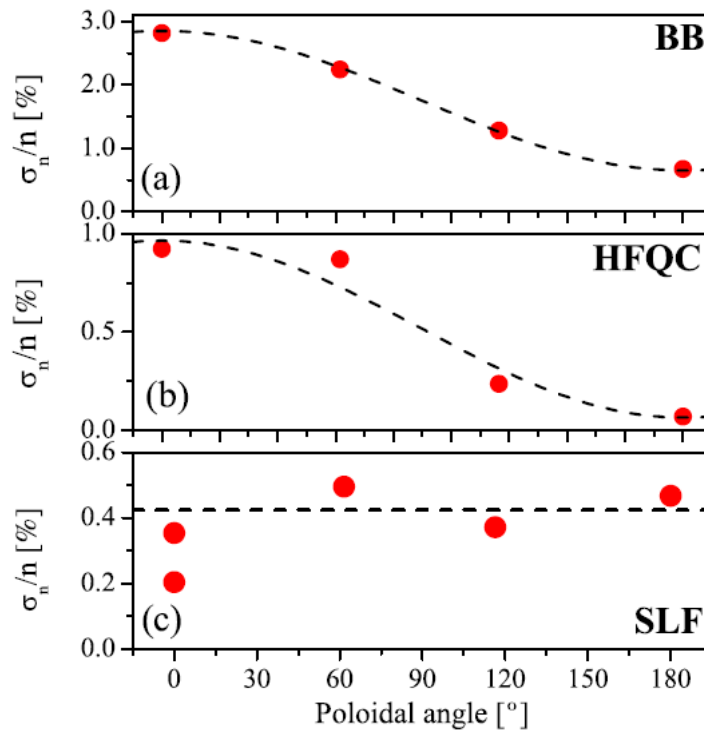


Fig. 3.16 Poloidal dependence of relative level of density perturbation  $\sigma_n/n$  for different fluctuations types. Adapted from Vershkov 2005 [95].

Despite the progress made in understanding the characteristics of the various spectral components, it is important to emphasise that not all the phenomena contributing to these amplitude and phase variations are fully understood. This lack of full understanding is largely due to the influence of turbulence within the plasma. Consequently, the resulting reflectometry signal inherently contains a degree of uncertainty.

### 3.7 Previous study

With the aim of discriminating spectral components in order to characterise their properties, a systematic study was proposed [97] instead of a shot-by-shot analysis (used when interpreting observed data with simulations). This study took into account many years of fixed frequency reflectometry data, 6000 discharges and more than 350 000 signals, from the Tore Supra database.

With reference to the roadmap presented in the next chapter, the approach used in this previous study can be presented as the roadmap shown in the figure 3.17.

The different steps can be described as follows:

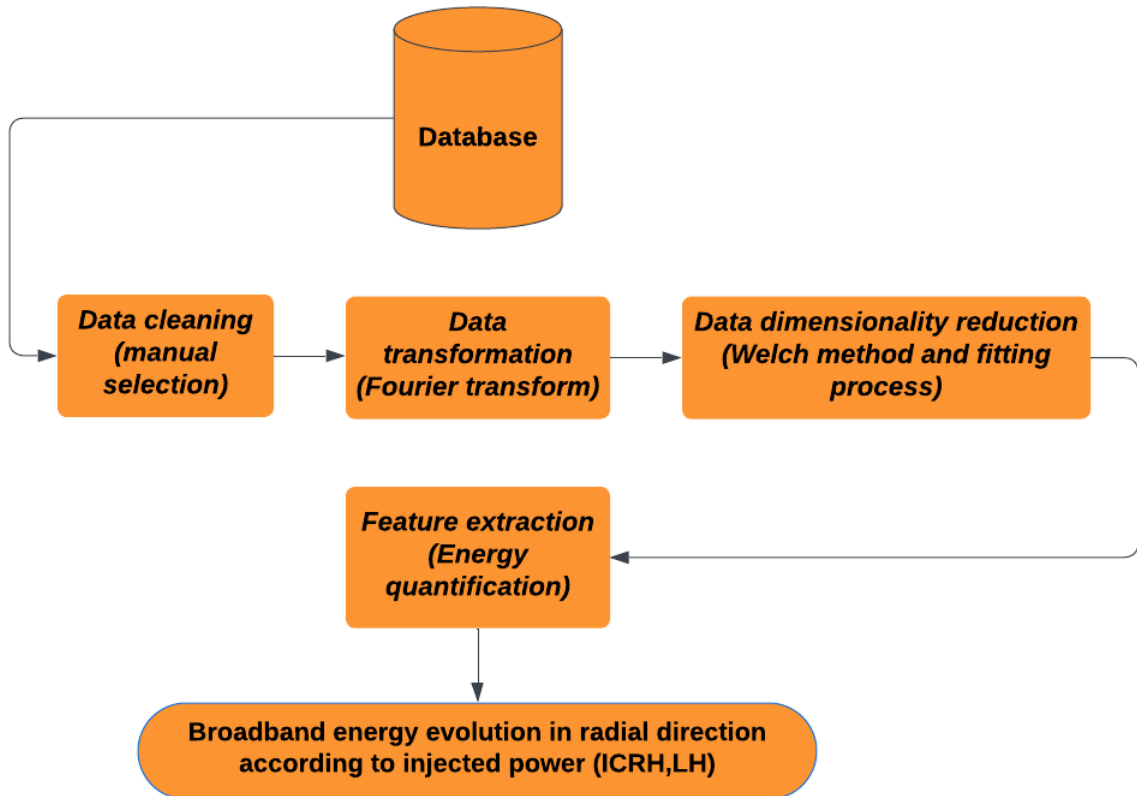


Fig. 3.17 Road-map proposed by Y. Sun

- **Data Cleaning** : Manual data cleaning was performed. The period or discharges when a hardware problem affected the measurement were excluded from the database.
- **Data transformation**: To reduce the complexity of the signals, a transformation from the time domain to the frequency domain is applied.
- **Dimensionality reduction**: After obtaining the frequency representation, two dimensionality reduction techniques were applied. First, the Welch method was used to estimate the power spectral density with specific parameters: a Hamming window, 50% overlap between segments and a resolution of 1025 frequency bins. This resolution was chosen manually to optimise feature extraction. This was followed by a second process which aimed to automatically decompose the power spectral density

(Welch spectrum) into four components: direct current component (central spike), low frequency fluctuations, broadband turbulence and noise level, in order to allow a systematic analysis. To achieve this, various functions such as Generalised Gaussian, Taylor Distribution and Voigt Distribution were used to fit the data [97]. Thus the data dimensionality goes from approximately 10,000 data points (time series) to only 11 parameters (fitting) [see figure 3.18].

- Feature extraction: From the reduced set of 11 parameters, a feature extraction was performed, in which the main feature was the energy content in the Broadband (BB) component ( $E_{BB}$ ).

This study was carried out in some plasma conditions ( $I_p$ ,  $n_e$ , etc.) where prior knowledge of the physics was available, in order to look for some general trends such as the evolution of  $E_{BB}$  in the radial direction [98].

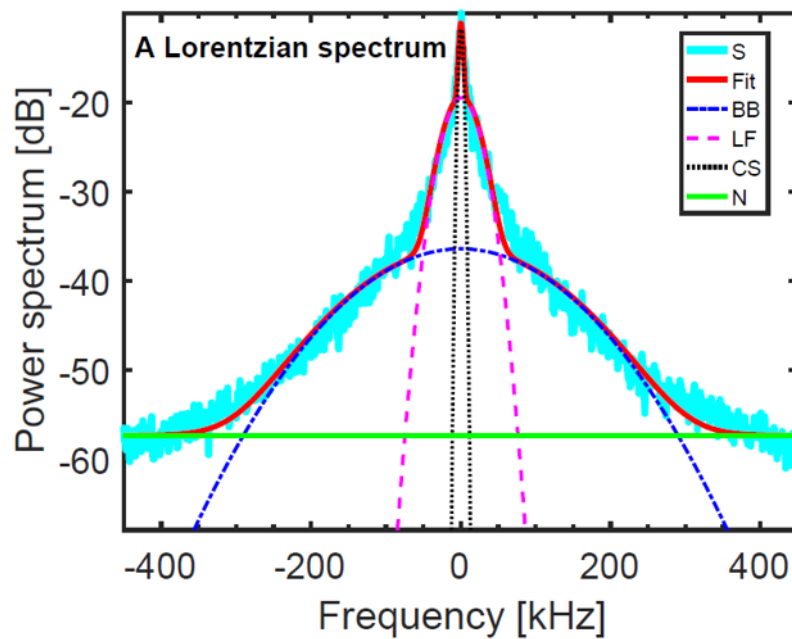


Fig. 3.18 Example of Y. Sun's fitting method: Initial spectrum (magenta curve), BB component (blue curve), LF component (pink curve), central spike (black curve) and noise (green curve).

The critical point in this data processing roadmap is the dimensionality reduction step. Although this analysis is based on a Welch method to estimate the power spectral density, i.e. a window length is considered for an averaging process to consider a steady state of the signal. The choice of this window length remains quite difficult, as it is related to the

coherence time of the spectral components, and these can vary in a very non-linear way along the signal [see figure 3.12]. In fact, the Welch method assumes a stationary turbulence behaviour during the reflectometry sampling time ( $\approx 10ms$ ) for each acquisition.

Another assumption related to the second part of the dimensionality reduction step, the fitting process, is the ad hoc selection of the frequency intervals in which the functions involved in the fitting process were defined [97].

In addition, side-lobe components such as QC modes and high-frequency magnetohydrodynamic modes were integrated into the broadband component and then ignored in the decomposition.

Overall, the Welch method is a robust estimator of power spectral density, providing reliable statistical precision. However, when the goal is to decompose a signal into separate spectral components, such as extracting the QC modes to analyse the dynamics in relation to other spectral elements in highly nonlinear systems, it is crucial to examine the temporal behaviour of these spectral components. As mentioned above, energy exchange can occur at different time and frequency scales, and there's no guarantee that the mechanisms associated with a particular turbulent transport will be uniform across all Welch spectra. It is therefore essential to understand these dynamics as they evolve over time.

Given the complexity of reflectometry raw signals, which exhibit non-stationarity, non-ergodicity and non-determinism, a stationary approach is insufficient for accurate spectral decomposition of these highly non-linear signals. Consequently, a new approach is required to account for these unique characteristics. This revised method aims to abandon the assumptions of the previous technique and eliminate the reliance on ad hoc information.



# Chapter 4

## Intelligent signal processing approach

### Contents

---

<b>4.1</b>	<b>Generalities on Machine learning (ML)</b>	<b>66</b>
4.1.1	Potentialities of AI/ML	67
4.1.2	Application to plasma science	68
<b>4.2</b>	<b>Integrating ML and signal processing</b>	<b>70</b>
4.2.1	Data cleaning	71
4.2.2	Data transformation	71
4.2.3	Data dimensionality reduction	75
4.2.4	Feature extraction	76
4.2.5	Analysis and classification	80
<b>4.3</b>	<b>How to have access to QC modes properties and dynamics</b>	<b>82</b>

---

As the fusion community confronts the complexities of turbulence in distinguishing different instabilities happening at same time and spatial scales, the spirit of this work recognises the need to move towards a physics-informed with data-driven methodology. Within this framework, expert knowledge is seamlessly intertwined with data, providing a robust and promising approach to address the inherent complexities.

The proposed approach seeks to integrate signal processing with machine learning (ML) to improve analysis, reveal hidden patterns and gain insights that may remain elusive when using traditional signal processing or ML techniques alone.

Historically, signal processing was first associated with embedded systems to extract relevant data from large physical systems. The analysed signal embodies the imprint left by a probing wave as it traverses a given physical system. At the same time, ML has matured

rapidly, aided by advances in computational algorithms and hardware. Machine learning embodies the quest to create intelligent machines that can, to some extent, emulate human learning.

This integration of ML with signal processing is increasingly reshaping the modelling, prediction and control of diverse systems, with researchers working in fields as diverse as neuroscience, climatology, robotics and turbulence. This integration in the analysis of reflectometry signals and, more generally, in applications to fusion plasmas is still in its early stages and the best methods have yet to be determined, but it is believed to have the potential to provide a deeper understanding of the dynamics in fusion plasmas.

The proposed approach adopts a new perspective compared to the approach described in the previous chapter [see figure 3.17], which relied on stationary assumptions and ad hoc constraints. The aim is to refine the data cleaning step to ensure that only relevant signals that meet the fixed frequency conventional reflectometry constraints are selected, and to re-evaluate the data transformation step to finally access the properties of the QC modes and capture the dynamics. Once the appropriate signals have been isolated and appropriately transformed, the feature extraction and classification process can be carried out.

Before considering the integration of ML into this strategy, a brief overview of ML characteristics and their applications in fusion plasmas is presented.

## 4.1 Generalities on Machine learning (ML)

Machine learning (ML) is a subset of artificial intelligence (AI). While AI covers a wide range of techniques to emulate human intelligence, ML focuses specifically on enabling machines to learn from data and improve over time by identifying patterns. Both AI and ML rely on optimisation principles to achieve their goals.

Machine learning can be broadly divided into two types: supervised and unsupervised learning. In supervised learning, algorithms are trained on labelled datasets, specific examples of the desired input and output of a model are provided, and regression techniques are used to derive the most appropriate model for the given data through optimisation processes, and then this found model is used to predict or classify unknown data. There are several sub-types of supervised learning:

- Semi-supervised learning: This approach uses partially labelled training data. Some of the expected output for certain inputs is not provided.
- Active learning: In this method, the algorithm is constrained by a limited resources and can only obtain labels for certain instances. It must also be strategic about which

samples to request labels for. In an interactive setting, these samples can be presented to a user for labelling.

- **Reinforcement learning:** Here the model's learning process is guided by rewards or penalties. These feedback mechanisms help shape the regression structure to produce the optimal model.

In contrast, unsupervised learning does not rely on labelled data. These algorithms aim to identify inherent patterns in the data. Their primary goal may be to reveal structures in the data present in low-rank sub-spaces, allowing feature engineering or extraction to construct a fitting model.

### 4.1.1 Potentialities of AI/ML

AI offers several benefits, including the automation of repetitive tasks, increasing efficiency and productivity. It can quickly analyse large amounts of data and extract key insights that humans might miss. With high precision and accuracy, AI reduces errors and improves the quality of results. In addition, it offers continuous 24/7 operation and can scale to handle large volumes of data without significantly increasing resources.

While AI offers a wealth of benefits and opportunities, it also poses certain challenges. For example, the rise of AI could disrupt labour markets, potentially leading to significant displacement in certain sectors. In addition, if not carefully curated, AI algorithms can perpetuate biases present in the training data, leading to discriminatory outcomes. Privacy concerns arise because AI processes large amounts of personal data, and there's an inherent risk of data breaches. Unlike humans, AI lacks nuanced understanding and common sense reasoning, leading to occasional misjudgments. Over-reliance on AI systems could undermine human decision-making skills. In addition, the complexity of AI development not only requires significant resources, but also raises ethical dilemmas around accountability and potential misuse. Deep learning models, in particular, could behave unpredictably, making their results more difficult to decipher. It's also crucial to recognise the evolving nature of jobs: while AI may make certain roles obsolete, it will also require the cultivation of new skills to work effectively with these advanced systems.

It's also important to have the right hardware components to efficiently execute algorithms designed for specific tasks. For example, training neural networks on a large database requires robust hardware to process the data quickly and deliver accurate results. The primary hardware components that perform these operations are central processing units (CPUs) and graphics processing units (GPUs).

CPUs are general purpose processors designed for a wide range of tasks. They have a few powerful cores optimised for sequential processing and are best suited to tasks that require complex decision-making and sequential execution. CPUs have a more complex memory hierarchy than GPUs, with caches optimised for low-latency access to a small amount of data. CPUs are designed for power efficiency and are suitable for tasks that require lower power consumption [99].

GPUs are specialised processors originally designed for graphics rendering, but they excel at parallel processing, being able to perform many simple tasks simultaneously. GPUs excel at parallel processing, making them well suited for machine learning processes that involve performing many similar calculations simultaneously. GPUs are highly efficient at large matrix operations compared to CPUs due to their architectural differences, making them ideal for deep learning frameworks that rely on matrix computations, such as neural network training. GPUs have greater memory bandwidth, which is useful for handling the large datasets commonly used in AI. GPUs consume more power due to their parallel architecture, but offer significant computational power.

In addition, extensive data sets facilitate the creation of surrogate models, which provide alternatives to computationally intensive first-principle simulations. While first-principle calculations remain essential for understanding underlying mechanisms, surrogate models, which require minimal computational time, enable real-time predictions, in line with the goal of reducing the large-scale computational burden in data-driven plasma science.

Challenges remain, in particular the scarcity of experimental data, which varies depending on the application and requires innovative approaches to systematic and rapid data acquisition, such as high-throughput screening. Bayesian inference in experimental design is also widely used to achieve this goal [100].

### **4.1.2 Application to plasma science**

As pointed out, AI/ML is in its early stage regarding plasma science, however some applications in fusion science have already been performed [100], showing relevant improvement compared to classical methods of data processing. AI and machine learning can serve as complementary approaches to efficiently extract the right information.

In diagnostics, analysis timelines range from real-time plasma control to in-depth post-experimental discovery. Traditionally, integrated data analysis using Bayesian methods has been central to progress in magnetic confinement fusion. However, machine learning, in particular neural networks, is now complementing and accelerating this process. A case in point is the W7X stellarator, where the network is used to infer temperature profiles, reducing

analysis time to a few tens of microseconds for a single time point, a dramatic improvement over the approximately 4 hours of Bayesian inference [101].

Recent advances have focused on accelerating plasma mode detection from diagnostic data through supervised learning, benefiting both research and real-time control. Techniques such as reservoir computing have been used to predict Alfvén eigenmodes in the DIII-D tokamak [102]. In addition, convolutional neural networks with dilated convolutions excel at high sampling rate diagnostics, as exemplified by the electron cyclotron emission imaging (ECEI) diagnostics at DIII-D [103].

The power of high performance computing (HPC) is enabling in-depth data analysis to help fusion scientists optimise successive plasma shots [104]. For example, neural networks trained in Bayesian inference can determine the electron temperature from a lithium ion beam emission spectroscopy (Li-BES) diagnostic on the JET tokamak in microseconds - a task that once took tens of minutes per experimental segment [105].

Another example is the simulation-based inference technique of Neural Posterior Estimation (NPE). NPE was used to train a normalising flow model on 10,000 UEDGE simulations, creating a neural network that could then ingest electron/ion density and temperature profiles from diagnostics at the mid-plane and outer divertor, and infer the corresponding anomalous transport coefficients consistent with UEDGE [106].

The construction of surrogate models can be complicated, especially with data from robust physical models that require extensive computational resources. It's therefore crucial to establish efficient computational workflows, implement data validation and selective sampling, and provide output uncertainty quantification for neural networks to ensure reliability.

The global and mission-driven nature of magnetic confinement fusion requires an international collaborative approach. The heterogeneity of multi-decade data requires a unified, federated database and workflow system, merging databases without central duplication. With ITER's continuous data accumulation, estimated in exabytes, data management becomes a challenge [100], but AI/ML techniques hold promise for refining this workflow.

In the field of tokamak control, an exemplary application of AI can be found in [107]. This method offers unprecedented flexibility and generality, significantly reducing the design effort required to introduce new plasma configurations. The researchers successfully demonstrate the generation and control of various plasma configurations, including elongated conventional shapes, negative triangularity and 'snowflake' configurations. Accurate tracking of position, current and shape is also achieved for these configurations. In addition, the approach enables the maintenance of separate plasmas within the tokamak vessel, known as 'droplets'.

Overall, the incorporation of AI/ML techniques is challenging. For the first time, there is a concerted attempt to adequately decompose a reflectometry signal, taking into account its

pronounced non-linearity and the fact that there's no concrete prior knowledge of the signal properties. As mentioned earlier, the idea is to combine this complementary approach offered by AI/ML with signal processing techniques to try to gain access to the spectral components.

## 4.2 Integrating ML and signal processing

The integration of machine learning (ML) with signal processing is a major challenge, as it aims to improve the data cleaning step and to optimise the data transformation process to access the properties and dynamics of the QC modes coming from the raw reflectometry signals. In addition, these signals exhibit non-stationarity, non-ergodicity and non-determinism, as mentioned in the previous chapter. Although there is a wide range of techniques available in AI/ML and signal processing, identifying the most appropriate methods remains an open task.

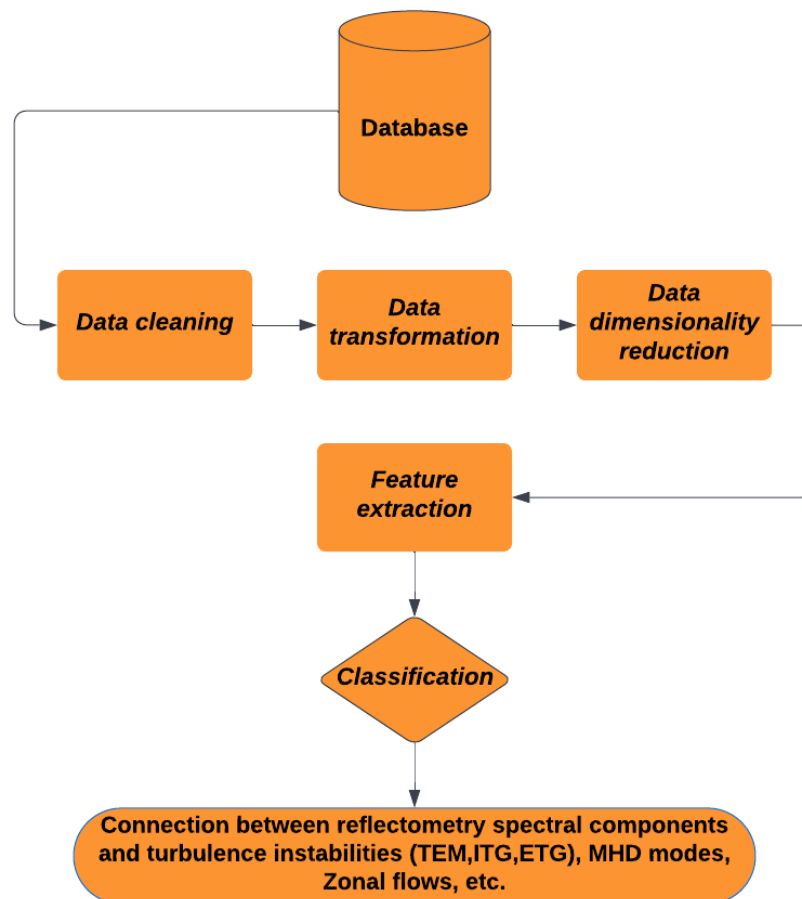


Fig. 4.1 Roadmap of the whole data analysis.

Despite the challenges posed by these complex signals, a global roadmap can be developed, as shown in Figure [4.1], which is oriented towards fixed-frequency reflectometry signals, but can be used to process other signals such as interferometry signals and electroencephalogram (EEG) signals. This roadmap then aims to capture the properties and dynamics of the QC modes in order to classify them and later relate them to turbulence instabilities. This roadmap consists of several steps, the input of which is a univariate signal in its time representation.

### 4.2.1 Data cleaning

This first step removes signals that show inconsistencies based on plasma conditions and fixed frequency reflectometry conditions. In addition, the signal-to-noise ratio can be improved in this first step by adjusting the amplitude or phase of the signal: two common methods are scaling and normalisation, which are used to align the signal within a comparable scale or range. There are also a number of other conventional methods:

- Moving average: its simplest expression is expressed as:

$$MA_{R,k}(t) = \frac{R(t) + R(t+1) + R(t+2) + \dots + R(t+k-1)}{k} \quad (4.1)$$

- Savitsky-Golay filter: This method is based on a polynomial fit over adjacent time intervals using the linear least squares method.
- Locally weighted scatter-plot smoothing (LOESS): it can be seen as a generalization of the Savitsky-Golay filter in which a fitting process is applied to time intervals with a weighted linear least squared regression : weights depends on the proximity on the point being estimated, length time interval and polynomial degree can change over the time.

### 4.2.2 Data transformation

This step looks for a transformation of the signal that highlights the signal properties. To deal with frequency information, the Fourier transform is a widely used technique. In addition, an extension such as the Short-Time Fourier Transform (STFT) or even more so the Wavelet Transform (WT) is often used to incorporate both time and frequency information.

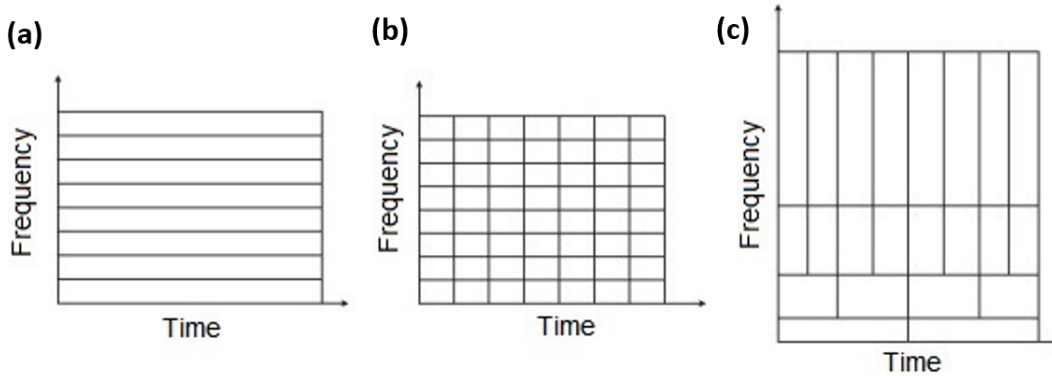


Fig. 4.2 Time-Frequency tiling for (a) FT, (b) STFT and (c) DWT.

### Time-frequency transforms

It transforms the signal to provide both time and frequency information, then a tiling of the time-frequency representation can be derived to visualise how it is divided along time and frequency. Each tile, or more precisely Heisenberg box, then contains the frequency and time information for a portion of the signal called a 'window' [see figure 4.2].

The STFT then provides the time and frequency information by applying the Fourier transform to a window that slices along the signal. A constant Heisenberg box along time and frequency is obtained. It is therefore effective as long as the signal does not contain structures with different time-frequency resolutions, some very localised in time and others very localised in frequency [108].

$$STFTS(u, \varepsilon) = \langle S, g_{u, \varepsilon} \rangle = \int_{-\infty}^{+\infty} R(t)g(t-u)e^{-i\varepsilon t} dt \quad (4.2)$$

$u$  : time step  
 $\varepsilon$  : frequency

The WT is based on a so-called mother wavelet, which can be interpreted as a short oscillation, depending on the characteristics of this latter some transformations can be born. The mother wavelet as its name indicates gives birth to other wavelets which are useful to get the frequency and time information of the signal. All the wavelets obtained form what is called the wavelet dictionary.

Among the various WTs used for signal analysis, certain transforms stand out for their ability to analyse signal properties and dynamics: the Discrete Wavelet Transform (DWT)

[108], the Stationary Wavelet Transform (SWT), the Undecimated Wavelet Transform (UWT) and the Continuous Wavelet Transform (CWT) [109].

The DWT is an orthogonal analysis suitable for determining compact representations of signals. The wavelet dictionary is obtained by shifting the mother wavelet and scaling it by powers of two. where  $j$  is the scale parameter and  $k$  is the shift parameter, both of which are integers. So the number of wavelet used is limited. The SWT and UWT stand out in denoising the signal.

The CWT is based on a non-orthogonal analysis and therefore permits to analyze signals containing a non stationary power at many different frequencies [110]. The wavelets can be chosen to correspond to scales in which there are observed fluctuations, compared to the scales of the DWT in which the number of scales is limited to a discrete set [111]. This transform as described in the next chapter is the main tool used in this thesis, the mother wavelet used by the CWT are : Daubechies wavelet (for denoising purposes), Haar Wavelet, Paul wavelet for phase detection and complex Morlet wavelet (Gaussian envelope of the finite length sinus wave allow a minimization of uncertainty [112]) for detection of fluctuations.

The definition of the CWT includes a time step for time information and a scale, which refers to the associated wavelet, for frequency information. Each scale and the associated frequencies are related to each other based on the wavelet.

$$CWT_{R(t)}(s, u) = \langle S, \psi_{s,u} \rangle = \int_{-\infty}^{+\infty} R(t) \frac{1}{\sqrt{s}} \psi^*\left(\frac{t-u}{s}\right) dt \quad (4.3)$$

$u$  : time step

$s$  : scale

It is important to note that when dealing with complex-valued signals, the frequency information is not symmetrical in Fourier space, and then it is necessary to work with the negative and positive scales or frequencies separately.

### Variational methods

It is a class of techniques that uses optimization principles : Total Variation regularization, L1-norm regularization, gradient descent and augmented Lagrangian methods. Variational methods combines data-driven fidelity terms with regularization terms that capture prior information [113].

The Variational mode decomposition (VMD), a type of variational methods, is based on a variational principle which enables a problem to be solved using calculus of variations

(Euler-Lagrange equation), which concerns finding functions that optimize the values of quantities that depend on those functions.

The classical variational mode decomposition is designed for real-valued signals and follow this equation:

$$\min_{u_k, \omega_k} \left\{ \sum_{k=1}^K \left\| \frac{\partial \left[ (\delta(t) + \frac{j}{\pi t}) * u_k \right] \cdot e^{-i\omega_k t}}{\partial t} \right\|_2^2 \right\}, \sum_{k=1}^K u_k = \text{Signal} \quad (4.4)$$

Some version of the VMD are explored as the Modified Complex VMD ( MCVMD) which aims at analysing complex-valued signals. At first, the complex-valued data is upsampled by adding zeros in the frequency domain. Secondly, the negative frequency components of the up-sampled data are shifted to be positive. Once the data has been upsampled and shifted, analytical signal properties are used to obtain real-valued data. This allows for a standard variational mode decomposition, which can separate the original signal into simpler components. The complex-valued decomposition results are obtained after shifting the frequency components back.

### Empirical Mode Decomposition (EMD)

The Empirical Mode Decomposition (EMD) analyses the signal on the basis of Hilbert analysis, it allows a transformation of the signal into some so-called Intrinsic Mode Functions (IMF)[114].

### Visibility graph network

The Visibility graph converts the signal into a network graph to highlight the fractality and regularity of the signal.

This method is generally applied to the signal amplitude  $A_t$ . The main idea behind this method is the 'visibility' between amplitudes [see figure 4.3]. In fact, two amplitudes/nodes  $A_{t_1}$  and  $A_{t_2}$  are connected if:

$$\forall t \in (t_1, t_2), \frac{A_{t_2} - A_t}{t_2 - t} > \frac{A_{t_2} - A_{t_1}}{t_2 - t_1} \quad (4.5)$$

in which  $t_1$  and  $t_2$  are different time steps in the signal. From this relationship, the visibility graph  $VG$  can be prompted [see figure 4.3]. Complex network theory [115] can then be applied of the extraction of patterns.

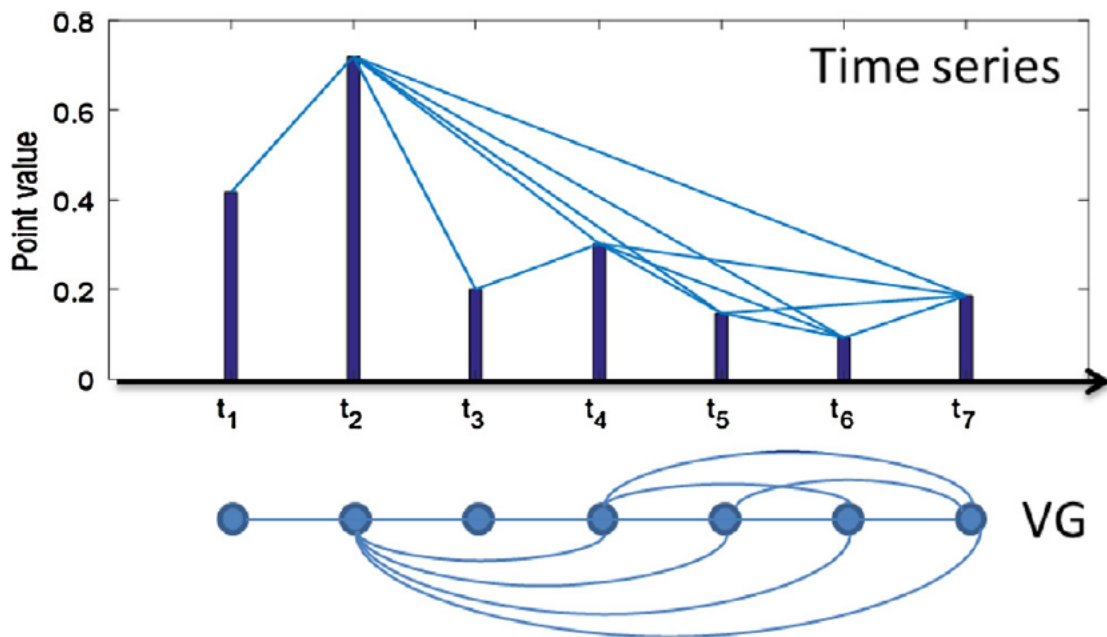


Fig. 4.3 Example of a visibility graph network mapped from a time series showing seven points with different amplitudes.

### 4.2.3 Data dimensionality reduction

Dimensionality reduction techniques primarily aim to reduce the number of dimensions. A common method is the Welch, for the estimation of the power spectral density, which uses the concept of 'interval of stationarity', the frequency resolution and the time windows are key parameters.

#### Kernel Principal Component Analysis (PCA) / Singular Value Decomposition (SVD)

Given the sampling frequency and duration of reflectometry signals, the number of time steps (dimensionality), can approach 50 000.

To overcome this, a matrix can be created. The lag-lag matrix, which segments the entire signal, or the sliding window approach, which shifts a given interval progressively through the time frame of the signal, are some options. Central to these techniques is the notion of 'interval of stationarity' corresponding to the time segment used.

After constructing the matrix as either rectangular or square to encompass all the signal's data, matrix decomposition techniques can be employed. Among these, SVD is recognized for its numerical stability, especially when seeking low-rank matrix approximations. This forms the foundation for algorithms like Principal Component Analysis (PCA) or Kernel

Principal Component Analysis (KPCA), where eigendecomposition of the covariance matrix is executed. Interestingly, SVD can be regarded as a more versatile data-driven technique compared to the Fourier transform, but it requires in general to have a multivariate signal.

### **Isomap algorithm and t-distributed Stochastic Neighbor Embedding (t-SNE)**

Other notable methods include Isomap and t-SNE. Isomap, which requires the construction of a graph, captures global structures, preserving the overall shape of the data manifold, and is a staple of manifold learning. Isomap can be viewed as an extension of the Kernel PCA. Conversely, t-SNE builds a probability distribution that reflects pairwise similarities, ensuring that the local structures and similarities of data points are preserved, which is invaluable for revealing clusters or inherent patterns.

### **Auto-encoder neural network**

In the framework of neural networks, auto-encoders stand out. These networks can recognise meaningful lower dimensional representations through their encoder-decoder structure [see figure 4.4]. Their primary function is to compress data and then reconstruct it to match the original input. Characteristically, auto-encoders use the same data for both input and output. Their improved version, the convolutional autoencoder permits to add convolutional filter for a better extraction of patterns.

## **4.2.4 Feature extraction**

The aim of this step is to obtain the features of interest for signal analysis.

### **Spectral descriptors**

This method is applied to the frequency information of the signal, i.e. the signal must have been transformed in such a way that the frequency information is highlighted in order to apply this method. Spectral descriptors aim to describe this frequency information using the concept of moments.

**Spectral centroid (SC):** This descriptor identifies the centre of mass of the frequency distribution within a signal. It represents the 'average' frequency content and can provide insight into the dominant frequencies present.

**Spectral Bandwidth (SB):** Measures the width of the frequency range that contains a certain percentage of the signal's energy. It quantifies the spread of frequency components around the spectral centroid.

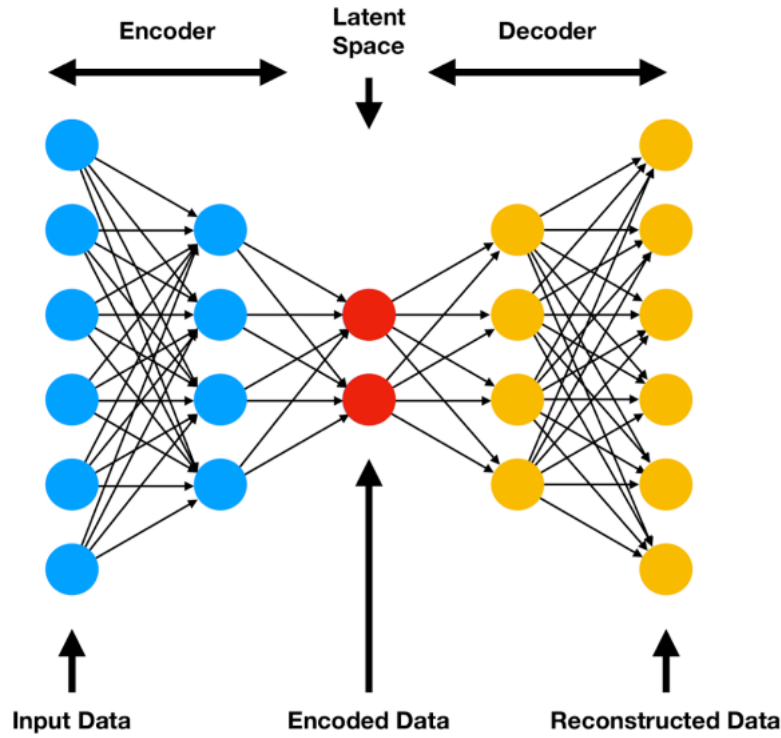


Fig. 4.4 Illustration of an autoencoder neural network, showing its main parameters.

Spectral Skewness (SS) and Kurtosis (SK): Spectral skewness measures the asymmetry of the spectral distribution, indicating whether the distribution is skewed to one side or the other. Spectral kurtosis measures the peakedness or flatness of the distribution.

$$SC = \frac{\sum_i f_i \cdot A_i}{\sum_i A_i} \quad (4.6)$$

$$SB = \sqrt{\frac{\sum_i (f_i - SC)^2 \cdot A_i}{\sum_i A_i}} \quad (4.7)$$

$$SS = \frac{\sum_i (f_i - SC)^3 \cdot A_i}{SB^3 \cdot \sum_i A_i} \quad (4.8)$$

$$SK = \frac{\sum_i (f_i - SC)^4 \cdot A_i}{SB^4 \cdot \sum_i A_i} - 3 \quad (4.9)$$

Where  $A_i$  is the spectral value at bin  $i$ ,  $f_i$  is the frequency corresponding to bin  $i$ . These descriptors can be used for various purposes such as signal classification and pattern recognition.

### Multifractal analysis

Multifractal analysis is based on the Discrete Wavelet Transform (DWT) and aims to identify power-law relationships between scales and then attempt to determine whether there is a law of scale invariance. Specifically, this analysis seeks to identify the presence of a distinctive power-law scaling across different statistical moments and scales. If the scaling behaviour is defined by a single scaling exponent or, equivalently, is linear with respect to the moments, the process is said to be mono-fractal. On the other hand, if the scaling behaviour varies with scale and is a non-linear function of the moments, the process is said to be multifractal.

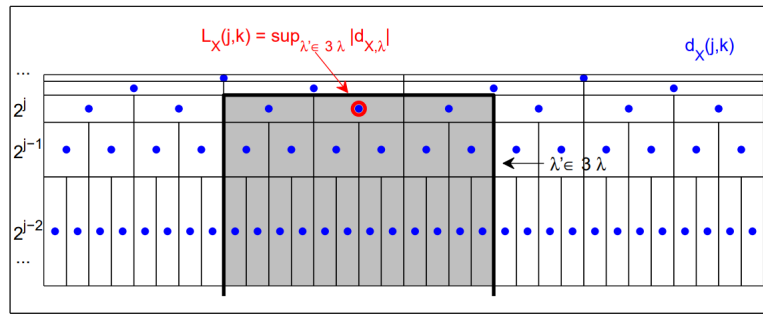


Fig. 4.5 Illustration of the choice of wavelet leaders for multifractal analysis.

Among the different methods to obtain the power scales in the DWT, there is the wavelet leaders method, where a wavelet is considered representative based on its dimensionality and then selected for the power scales study. As shown in the figure 4.5, the wavelet leaders are defined in dyadic interval as:

$$\begin{aligned}\lambda_{j,k} &= [k2^j, (k+1)2^j] \\ 3\lambda_{j,k} &= \lambda_{j,k-1} \cup \lambda_{j,k} \cup \lambda_{j,k+1}\end{aligned}\quad (4.10)$$

From the union of the intervals, the wavelet leader is defined as:

$$L_X(j,k) = \sup_{\lambda' \subset 3\lambda} |d_{X,\lambda'}| \quad (4.11)$$

The Holder exponent  $h(t_0)$  of the wavelet leader is defined  $L_{S_t}(j,k) \approx_{2^j \rightarrow 0} 2^{jh(t_0)}$ . It allows a relationship from the wavelet leaders to the reproduction of the Holder exponent of  $R(t)$  at  $t_0$  by a local power law behaviour in the limit of fine scales ( $2^j \rightarrow 0$ ).

In addition, the structure functions can be defined as well as  $S^L(j,q) = (1/n_j) \sum_{k=1}^{n_j} L_X(j,k)^q$ , in which  $n_j$  denotes the number of wavelet leaders at the scale  $2^j$ . From equations 4.11 :  $S^L(j,q) \simeq F_q 2^{j\zeta^L(q)}$ ,  $2^j \rightarrow 0$ .

Finally, the Multifractal spectrum of  $R(t)$  can be expressed as:

$$\forall h, D(h) = D^L(h) = \min_{q \neq 0} (d + qh - \zeta^L(q)) \quad (4.12)$$

In which the construction is based on the Holder singularities of  $R(t)$ .

The main objective of this feature extraction approach is to study signals whose point-wise Holder regularity may vary greatly from point to point. Therefore, one would like to derive some information about the size of the sets of points where the point-wise regularity exponent takes a certain value  $H$ . This "size" is mathematically formalised as the Hausdorff dimension  $d$ . These dimensions define a function of the exponents  $H$  called the spectrum of singularities of  $f$  and denoted  $df(H)$ .

In anomalous particle transport in tokamaks, different types and scales of turbulence coexist in the plasma, as shown for edge plasma turbulence in [116]. Large intermittent bursts are followed by the formation of coherent structures that are the result of self-organisation. These structures, which can transfer large amounts of energy, have strong correlations and a non-Gaussian probability density function. Multifractality could be related to the generalisation of the classical definition of self-similarity and the underlying cascading process. Multifractal analysis of plasma turbulence was found to provide evidence for the rich scaling property of self-similarity and long-range correlations (i.e. in the range between short times characteristic of local turbulence and very long times characteristic of global behaviour) [117].

### Reallocation analysis

In the case of a time-scale transformation of the signal ( $R(t)$ ), a reallocation of information can be performed so that the time-scale can be converted into a time-frequency representation [118].

It's important to understand that each scale in the CWT is characterised by a specific "weight function" that represents the spectral energy of the corresponding wavelet. Due to the continuous nature of the wavelet transform, the scales partially overlap. The objective is therefore to determine whether a spread of information on the scale axis corresponds to a consistent frequency, and this observation extends over time.

$$CWT_{R(t)}(s, u) = \langle R, \psi_{s,u} \rangle = \int_{-\infty}^{+\infty} R(t) \frac{1}{\sqrt{s}} \psi^*\left(\frac{t-u}{s}\right) dt \quad (4.13)$$

From a wavelet that is concentrated on the positive frequency axis:  $\hat{\psi}(f) = 0$  for  $f < 0$ . By Plancherel's theorem, the equation 4.13 can be rewritten as:

$$\begin{aligned}
CWT_{R(t)}(s, u) &= 1/2\pi \int \widehat{R}(t) s^{0.5} \overline{\widehat{\psi}(sf)} e^{iuf} df \\
CWT_{R(t)}(s, u) &= 1/4\pi \int [\delta(f - \omega) + \delta(f + \omega)] s^{0.5} \overline{\widehat{\psi}(sf)} e^{iuf} df \\
CWT_{R(t)}(s, u) &= (1/4\pi) s^{0.5} \overline{\widehat{\psi}(s\omega)} e^{iu\omega}
\end{aligned} \tag{4.14}$$

### 4.2.5 Analysis and classification

This last step is the one in which, having obtained the right features from the signal, it aims to find common characteristics between the features in order to classify them and also to try to find a possible relationship between them (analysis).

#### Classification

A clear example of classification is the Support Vector Machine (SVM), which has four basic concepts: (i) the separating hyperplane, (ii) the maximum margin hyperplane, (iii) the soft margin, and (iv) the kernel function [119]. SVM is used instead of neural networks when the dimensionality of the features is low.

Extreme Learning Machine (ELM), which belongs to the category of feed-forward neural networks, is specifically designed for fast training and efficient learning, particularly in cases where traditional neural network algorithms may be computationally intensive or require extensive hyperparameter tuning [120].

Dynamic Time Warping (DTW) is a technique for finding an optimal alignment between two given (time-dependent) signals under certain constraints. Intuitively, the sequences are warped in a non-linear way to match each other [121].

Among the various classification methods, clustering can be considered as a type of classification where the classes are not known in advance. There are two basic types of clustering algorithms: partitioning and hierarchical algorithms [122]. The clustering techniques used in this thesis are the partitioning algorithms, which seek to construct a partition of a database  $D$  of objects into a set of  $k$  clusters, where  $k$  is an input parameter for these algorithms, i.e. some domain knowledge is required, which unfortunately is not available for many applications. The partitioning algorithm typically starts with an initial partition of  $D$  and then uses an iterative control strategy to optimise an objective function. Each cluster is represented by the centre of gravity of the cluster (k-means algorithm) or by one of the objects of the cluster located near its median (k-medians algorithm). Consequently, partitioning algorithms use a two-step procedure. First, the  $k$  representatives that minimise

the objective function are determined. Second, each object is assigned to the cluster with the representative that is "closest" to the object in question.

In addition, a third type of clustering algorithm is the density-based clustering, where the Density-Based Spatial Clustering of Applications with Noise (DBSCAN) identifies clusters as dense regions of data points separated by areas of lower point density. By defining a proximity radius ( $\epsilon$ ) and a minimum number of data points required to form a dense region, the algorithm grows clusters by connecting points within the  $\epsilon$ . Data points that aren't part of a cluster due to their sparse environment are treated as noise. DBSCAN is designed to detect clusters of any shape, such as linear, concave, oval, etc.[123]

### **Analysis: Transfer entropy (TE)**

Causality refers to the relationship between cause and effect, where one event (the cause) brings about another event (the effect). In signal processing, establishing causality can be challenging, especially when traditional correlation-based metrics can be misleading.

Compared to traditional metrics that only measure linear relationships, Transfer entropy, which derives from information theory, provides a non-linear, model-free approach. TE quantifies the amount of uncertainty reduced in predicting the future values of one signal given the knowledge of another signal. In simple terms, in the case of 2 signals,  $A_t$  and  $B_t$ , if knowing the past of  $A_t$  helps in predicting the future of  $B_t$  better than just knowing the past of  $B_t$  itself, then it suggests a directional causal influence from  $A_t$  to  $B_t$  [124]. Transfer entropy provides a way to quantify the influence of one process on another, considering their temporal dependencies.

$$\text{Transfer Entropy (TE)} = \sum_{x_t, y_t, y_{t+1}} P(x_t, y_t, y_{t+1}) \log \left( \frac{P(y_{t+1}|y_t)}{P(y_{t+1}|y_t, x_t)} \right) \quad (4.15)$$

The fundamental quantity in this approach is the Shannon entropy, which represents the uncertainty associated with any measurement  $x$  of a random variable  $X$  (logarithms are in base 2, giving units in bits):  $H(X) = -\sum_x p(x) \log(p(x))$ . The conditional entropy of  $X$  given  $Y$  is the average uncertainty that remains about  $x$  when  $y$  is known:  $H(X|Y) = -\sum_{x,y} p(x,y) \log(p(x|y))$ . The mutual information between  $X$  and  $Y$  measures the average reduction in uncertainty about  $x$  that results from learning the value of  $y$ , or vice versa:

$$I(X;Y) = \sum_{x,y} p(x,y) \log \frac{p(x,y)}{p(x)p(y)}, \quad (4.16)$$

$$I(X;Y) = H(X) - H(X|Y) = H(Y) - H(Y|X)$$

The conditional mutual information between X and Y given Z is the mutual information between X and Y when Z is known.

The entropy rate (denoted as  $h_\mu$ ) is the limiting value of the conditional entropy of the next state  $x_{n+1}$  of X given knowledge of the previous  $k-1$  states  $x_n^{(k-1)}$  of X:

$$h_\mu = \lim_{k \rightarrow \infty} H(x_{n+1} | x_n^{(k-1)}) \quad (4.17)$$

More details in Transfer entropy concept or details can be found in [124].

Two applications of TE have attracted interest in the plasma fusion community. The first, causality in the onset of transport barriers, establishes that the combination of free energy injection at the plasma-boundary interface and turbulence propagation provides a robust pathway to a turbulent edge. The final part of the triptych is to demonstrate how turbulent eddies organise to provide access to improved confinement. A fruitful way to approach this problem is to examine the causal chain of events that presides over the onset of edge transport barriers [125].

Radial heat propagation was modified by the shear flows present in the plasma. Analysis of the transfer entropy, applied to numerical results using a resistive MHD model, showed a clear consistency with the evolution of the electron temperature, confirming the relevance of this technique for the analysis of heat transport [126].

The primary objective of the roadmap described is to outline a comprehensive strategy for extracting key signal properties and dynamics, and ultimately relating them to plasma properties and turbulence instabilities. It's important to note that this processing flow is flexible; the sequence and nature of the steps can be adapted or reconfigured based on specific plasma conditions to achieve the desired objectives, e.g. the data dimensionality reduction step can be applied immediately after the data cleaning step, or after the feature extraction step if the number of features is large.

### 4.3 How to have access to QC modes properties and dynamics

Different methods have been highlighted in this general roadmap. For a better data cleaning step it is necessary to develop an ML integrated signal processing algorithm where a manual selection of a set of signals is performed to teach the algorithm the signals that really fulfil the fixed frequency reflectometry characteristics and then this algorithm would be able to learn by itself and perform a classification on the whole database.

Then, in order to extract the characteristics and dynamics of the QC modes, it is essential to distinguish between other spectral components (low frequency (LF) component, broadband (BB) component and noise). As detailed in the next chapter 5, a methodology is proposed to access the temporal representation of each of these spectral components.

As mentioned in chapter 2.5.2, the Tore Supra tokamak, the WEST tokamak, the W7X stellarator and the TEXTOR tokamak are the fusion devices considered in this thesis. However, most of the data used to establish this spectral decomposition have been collected in previous years during different campaigns, mainly on Tore Supra and WEST, and partially on W7X for specific comparisons, but this whole database can be extended as needed.



# Chapter 5

## Application for distinguishing spectral components

### Contents

---

<b>5.1</b>	<b>Extraction of each spectral component . . . . .</b>	<b>86</b>
5.1.1	Selection of signals according to CFR . . . . .	86
5.1.2	Noise estimation . . . . .	88
5.1.3	Extraction of the QC modes and extension to any narrow-band spectral mode . . . . .	90
5.1.4	Extraction of the LF component and BB component . . . . .	94
<b>5.2</b>	<b>Preserving physical and statistical properties . . . . .</b>	<b>96</b>
5.2.1	LOC-SOC transition . . . . .	96
5.2.2	Short Range Poloidal Correlation (SRPC) . . . . .	99
<b>5.3</b>	<b>Towards multi-magnetic configuration study . . . . .</b>	<b>102</b>

---

Prior to the discrimination of each spectral component, an exploratory phase was carried out in order to gain insight into the reflectometry signals by means of the different techniques explained in the previous chapter [see Appendix A]. The main question was the choice of time and frequency analysis to access the characteristics and dynamics of the spectral components.

A first extraction algorithm was developed specifically for the QC modes. However, the main drawback of this initial algorithm was that the extraction conditions [see Appendix B] were not sufficient to uniquely extract the QC modes, other residual spectral components were also extracted.

## 5.1 Extraction of each spectral component

A final algorithm is developed for the extraction not only of the QC modes but also of each spectral component: QC modes, LF component, BB component and noise. The various steps of this algorithm are illustrated in the roadmap 5.1.

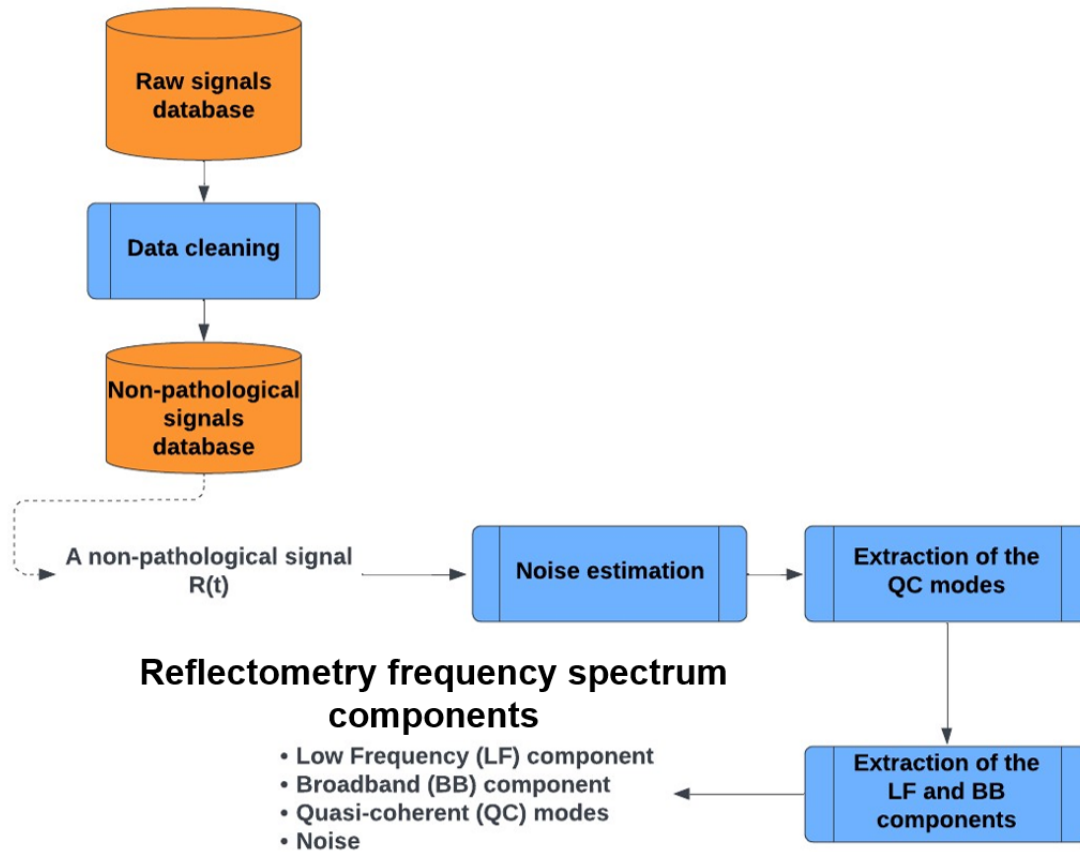


Fig. 5.1 Roadmap for the extraction of reflectometry spectral components.

### 5.1.1 Selection of signals according to CFR

it is important to recall that the focus of this work is in the field of fixed-frequency conventional reflectometry (CFR) and poloidal correlation reflectometry (PCR), which is equivalent to several CFR reflectometers [see section 3.4]. Within this context, a probe wave is perpendicular to the cut-off layer, so that the central peak (direct reflection) must be around 0 kHz. The signals considered are the result of the interaction between electromagnetic waves and the plasma, mainly coming from the vicinity of the cut-off layer.

Consequently, this analysis is restricted to signals that obey this specific physics, which sets two main requirements for the spectral properties of the signal: a low Doppler shift (low asymmetry, see section 3.6), corresponding to a central peak around 0kHz, and a sufficient signal-to-noise ratio (SNR) so that the turbulence measurements stand out from the noise. These two characteristics had been seen by Sun in [97], but the investigation had not been carried out.

Without a selection of signals, extracting modes and their properties would be more challenging due to the potential contamination of reflectometry data with spurious information. Elements such as Doppler shifts and low Signal-to-Noise Ratio (SNR) can blur the derived characteristics if not properly filtered out.

To capture these two parameters, Doppler shift and SNR, a data transformation is performed to obtain the power spectral density (PSD), which shows the power distribution of each signal in the frequency domain. The key parameter at this stage is the frequency resolution, which is the number of frequency bins in the frequency domain and is inherently linked to the coherence times of the spectral components. As indicated in Chapter 2, the coherence times in plasma fusion depend on a set of parameters, extending from several milliseconds to one microsecond for micro-turbulence. Further, precedent systematic studies employing the Welch method for the PSD have illustrated that using a time window of  $1024\mu s$  for a signal spanning  $10ms$  provides a pertinent interval to achieve an adequate level of precision.

After performing the data transformation using the Welch method. The next step is to perform a dimensionality reduction by fitting a parabola to the Welch spectrum on a logarithmic scale:

$$\begin{aligned}
 PSD &: 10\log_{10}(Welch_{R_t}(f)) \\
 parabola &: a(f+h)^2 + k \\
 objective\ function_{a,h,k} &(PSD, a(f+h)^2 + k)
 \end{aligned} \tag{5.1}$$

where  $f$  is the frequency,  $R_t$  is the reflectometry signal and  $a, h$  and  $k$  are the parameters to be found for the fitting process.

Following this procedure, the parabola parameters are projected into a three-dimensional vector space denoted  $(\mathbf{a}, \mathbf{h}, \mathbf{k})$ . The aim is to identify signals with sufficient energy content, a reasonably asymmetric spectrum and a suitable signal-to-noise ratio (SNR).

To do this, a manual selection of spectra is made for each feature in order to discriminate between these three features, and this is fed into a semi-supervised learning method, the label

propagation algorithm [127], which, as described in chapter 4, allows the fusion of labelled and unlabelled data, facilitating then the inclusion of manually selected "good spectra".

The label propagation algorithm uses these three characteristics as the number of clusters to be applied to the vector space  $(\mathbf{a}, \mathbf{h}, \mathbf{k})$ , which then contains both labelled (manual selection) and unlabelled data. A guiding hypothesis here is a similarity principle based on proximity between points. This allows the propagation of labelled data to unlabelled data according to the label propagation algorithm. This algorithm starts with labelled data (manually selected spectra) and propagates in each iteration using the K-Nearest Neighbours (KNN) kernel. As a result, three distinct clusters emerge after propagation. The cluster characterised by sufficiently high  $\mathbf{a}$  (energy content), low  $\mathbf{h}$  (Doppler shift) and adequate  $\mathbf{k}$  (SNR) is selected for the next stage of the algorithm.

Once this specific cluster has been identified, the exploratory phase dedicated to spectral component discrimination can begin. The methods tested and their limitations are briefly described.

Subsequent to this, the spectral decomposition starts with the estimation of noise by means of the Continuous Wavelet Transform (CWT) applied to the signal  $R(t)$ .

### 5.1.2 Noise estimation

The basis of noise estimation is that the signals being analysed,  $R(t)$ , have the property of being highly non-stationary. As explored in [128], pink noise could be associated with a non-stationary process. In fact, this pink noise has an absence of a clear lower cut-off frequency in its power spectral density. As a reminder, the Welch spectrum described is the estimation of the PSD using 1024  $\mu s$  as the time window and 1025 as the frequency resolution.

Before estimating the noise, the frequency interval of the LF component is evaluated using a Savitzky-Golay filter - a second degree polynomial used to smooth the Welch spectrum coupled with a symmetry consideration of the LF extremes with respect to the central peak. In fact, this frequency interval of the LF component is a reference point for noise estimation. Specifically, they represent the minimum frequency used as a reference in the calculation of the CWT of the noise. This is because the noise estimation process deliberately excludes the noise present within the LF interval.

The noise from the LF component is calculated using MCVMD, as explained in the section. This algorithm takes as input 4 for the number of spectral components to be found in the LF component, the first corresponding to the direct reflection of the wave launched by the reflectometer at the cut-off layer, the second and third corresponding to the lateral parts,

a negative part and a positive part. The fourth component with the lowest spectral energy corresponds to the noise in the LF component.

$$Noise_{LF} = \min_{energy}(MCVMD(R(t), 4)) \quad (5.2)$$

Consequently, the noise estimation is started by estimating the Fourier phase and then its amplitude separately.

The first step is to estimate the background noise coming mainly from the very high frequencies using the CWT, a hard thresholding is applied using the 0.2 quantile of the  $|CWT_{R_t}(s, t)|$  distribution as the threshold ( $Threshold_{noise}$ ):

$$T_{noise} = \begin{cases} CWT_{R_t}(s, t), & |CWT_{R_t}(s, t)| \leq Threshold_{noise} \\ 0, & |CWT_{R_t}(s, t)|^2 > Threshold_{noise} \end{cases} \quad (5.3)$$

The CWT coefficients are then reconstructed into a time series representation using the inverse CWT (ICWT), then the Fourier transform is used to find its spectrum and phase.

$$\angle \widehat{noise} \approx \angle \mathcal{F}(CWT^{-1}(T_{noise})) \quad (5.4)$$

For amplitude, the Welch spectrum of  $ICWT(T_{noise})$  is performed and compared with the Welch spectrum of the original signal to find the noise spectrum boundaries with the BB component. Following the pink noise behaviour, the Welch spectrum of the noise is found by extrapolating the  $Welch(ICWT(T_{noise}))$  to the remaining frequencies after  $Welch(noise) \propto \frac{1}{|f|^\beta}$ , where  $\beta < 1$  is low enough to obtain a low 0-frequency power.

Once  $\beta$  is estimated,  $\frac{1}{|f|^\beta}$  can be used to interpolate the frequencies and then move from a 1025 frequency resolution (Welch method) to a frequency resolution,  $newf$ , equal to the time resolution.

$$|\widehat{noise}| \approx \sqrt{\frac{1}{|newf|^\beta}} \quad (5.5)$$

Finally, the inverse Fourier transform can be applied:

$$Noise_{total}(t) = \mathcal{F}^{-1}(|\widehat{noise}| e^{\angle \widehat{noise} i}) + Noise_{LF} \quad (5.6)$$

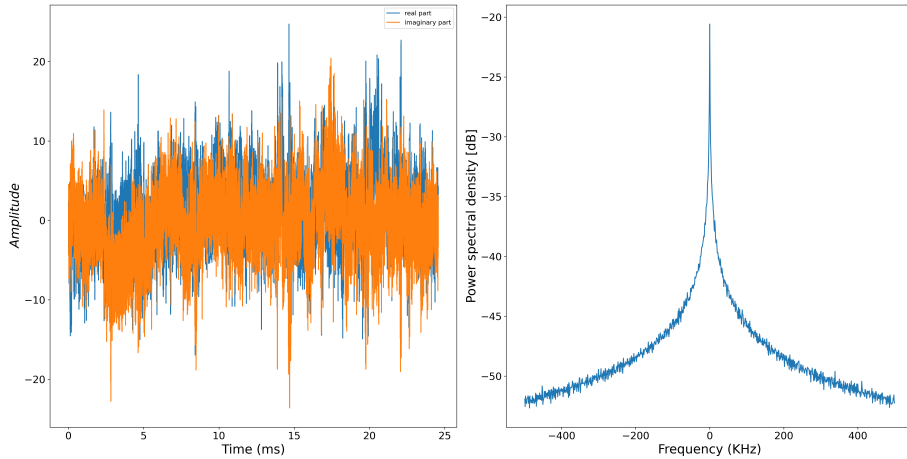


Fig. 5.2 (a) Noise component in the time domain. (b) Welch spectrum of the Noise component.

### 5.1.3 Extraction of the QC modes and extension to any narrow-band spectral mode

Once the noise has been estimated, the next step is to extract the QC modes. For this, the BB interval and the LF frequency interval previously calculated [see figure 5.3] are the limits in the frequency domain, since the QC modes are set to be present at frequencies higher than the LF component and lower than the maximum frequency present in the BB component.

To improve the originally developed QC mode extraction algorithm, an extension is performed to extract any narrow band component. This requires the definition of certain thresholds with respect to the mode to be extracted.

Once these mode thresholds have been set, the algorithm uses a "creaming-off" approach, i.e. it performs the extraction progressively. In each iteration, the algorithm performs two sub-processes: the first identifies potential "modes" based on CWT (Continuous Wavelet Transform) coefficients, and the second is dedicated to extracting the identified "mode". This generalised mode extraction algorithm follows the roadmap of spectral component decomposition, which will be detailed in the subsection 5.1.

#### Mode identification

In the first step, after obtaining the Continuous Wavelet Transform (CWT) of the reflectometry signal ( $R(t)$ ), the Normalised Averaged Energy (NAE) is calculated separately for both negative and positive scales [see equation 5.7], and an identification of the inflection points of the NAE is performed (red points in figure 5.4).

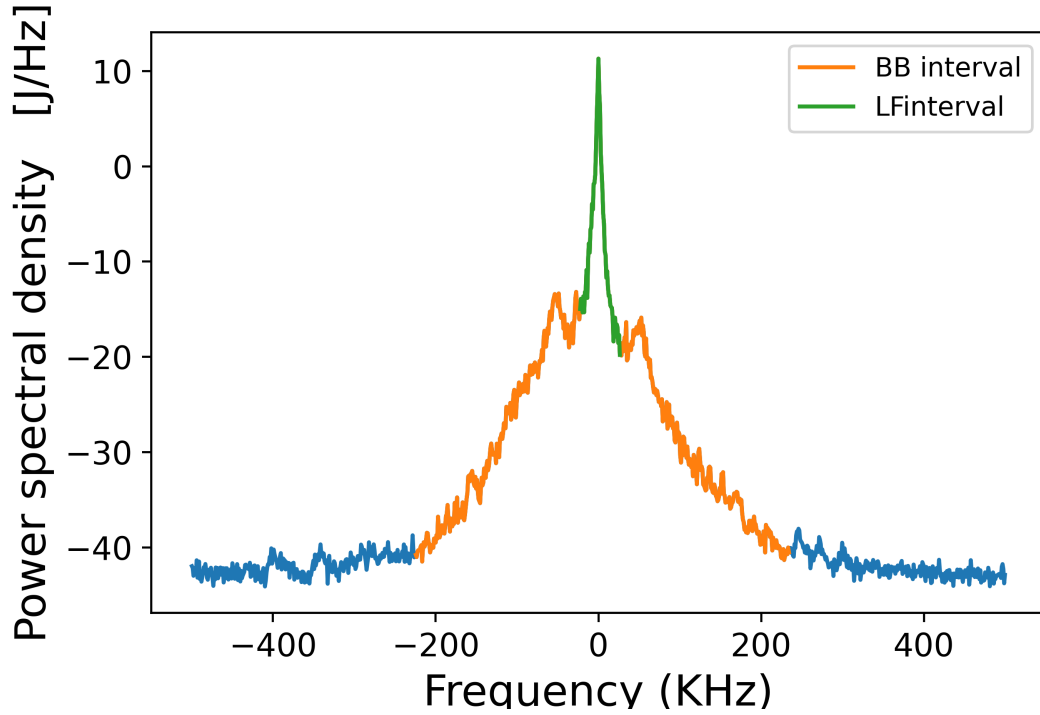


Fig. 5.3 Portions of the PSD associated with the frequency interval of the LF component (green curve) and the frequency interval of the BB component (orange curve).

$$\begin{aligned}
 AE(s) &= \frac{\sum_{t \in T} |CWT_{R_t}(s, t)|^2}{T} \\
 NAE(s) &= \frac{AE(s)}{\max(AE)}
 \end{aligned}
 \tag{5.7}$$

Potential 'modes' are then evaluated by examining the different intervals created by these inflection points: First, intervals are evaluated according to the criteria that the second derivative must be negative, indicating a concave downward shape, and that the Normalised Average Energy (NAE) gradient at the extremes of each interval must exceed a predetermined threshold:

$$\frac{\partial |CWT_{R_t}(s, t)|^2}{\partial s} \geq \text{Threshold}_{NAE}
 \tag{5.8}$$

Secondly as previously mentioned, the CWT representation of a complex-valued signal encompasses both negative and positive scales. Consequently, a level of symmetry is imposed

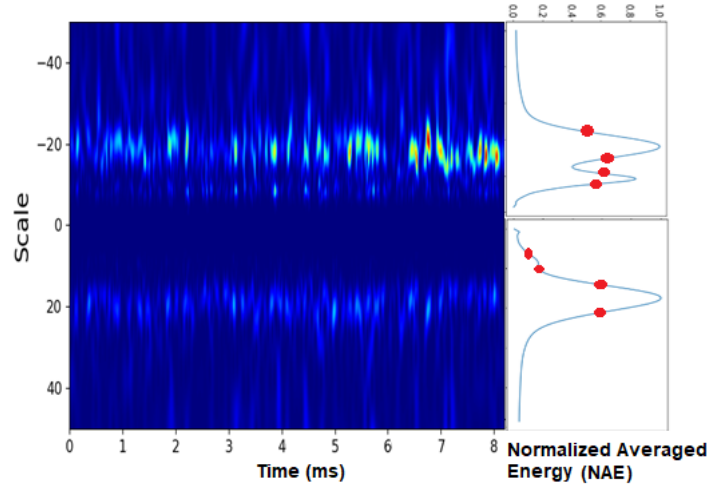


Fig. 5.4 CWT of a signal  $R(t)$  with normalised averaged energy for its negative and positive scales. Red dots indicate inflection points.

between the mode observed in the negative scale and its counterpart in the positive scale, the difference between their NAE centroids must be less than a threshold.

$$NAE_{centroid}^+ - |NAE_{centroid}^-| < \text{Threshold}_{\text{symmetry}} \quad (5.9)$$

### Mode extraction

Once the scale intervals encompassing both negative and positive scales have been identified, each CWT coefficient belonging to the negative and positive interval scales is projected separately into a vector space. Each resulting vector space obeys the properties of a Euclidean space  $\mathbb{R}^2$ . First, the energy of the wavelet coefficients ( $|CWT_{R_t}(s, t)|^2$ ) and the scales ( $s$ ) are normalised as:

$$s_{\text{normalized}} = \frac{s}{s_{\text{max}}} \quad (5.10)$$

$$|CWT_{R_t}(s, t)|_{\text{normalized}}^2 = \frac{|CWT_{R_t}(s, t)|^2}{|CWT_{R_t}(s, t)|_{\text{max}}^2}$$

Then, the vector space is set as following:

$$\mathbf{V} = (s_{\text{normalized}}, |CWT_{R_t}(s, t)|_{\text{normalized}}^2) \quad (5.11)$$

Within this vector space  $\mathbf{V}$ , the mini-batch k-means method is used. This method uses each pair  $(a, b) \in \mathbf{V}$  to form clusters. To speed up the calculation, the algorithm intelligently chooses the number of clusters. Initially, 2 clusters are determined. Clustering is then performed, assigning each pair  $(a, b)$  to a particular cluster and calculating their centroids. The algorithm then calculates a ratio derived from the total normalised energy  $B$  of the cluster containing the maximum  $B$  divided by the sum of the total normalised energy  $B$  of both clusters. This ratio must be less than 0.5 [see figure 5.12]; if it exceeds this threshold, the algorithm adjusts the number of clusters to 3.

$$\frac{B_{\text{cluster1}}}{B_{\text{cluster2}}} < 0.5 \quad (5.12)$$

where  $B_{\text{cluster1}} = \sum_{b \in \text{cluster1}} b$  and  $B_{\text{cluster2}} = \sum_{b \in \text{cluster2}} b$ .

This adjustment of the number of clusters from 2 to 3 aims to achieve a more balanced and more accurate clustering of the data points in the vector space.

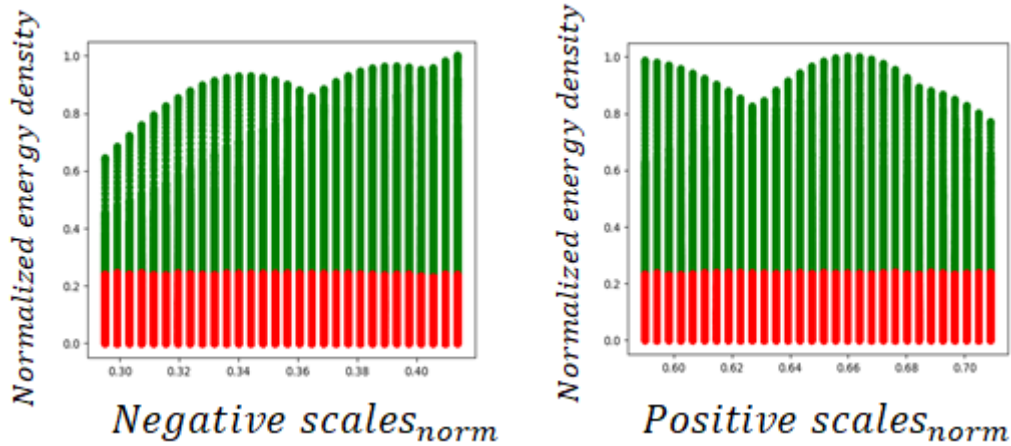


Fig. 5.5 Clustering in the vector space  $\mathbf{V}$ , green clusters correspond to the QC modes while red clusters correspond to the BB component.

This operation, as described, is carried out at each iteration. The algorithm remains in operation as long as certain conditions are met: in addition to the preset parameters (energy threshold 5.8 and a symmetry parameter 5.9), a spreading scale parameter must also be met:

$$(NAE_{\text{centroid}}^{+,-} \text{ at iteration } m+1) - (NAE_{\text{centroid}}^{+,-} \text{ at iteration } m) < \text{Threshold}_{\text{spreading}} \quad (5.13)$$

For regularisation, the power spectral density (PSD) of the residual signal  $(R(t) - \text{mode}(t))$  is evaluated at each iteration using the Welch method (time window of 1024

$\mu s$ ). Thus, at the last iteration, the resulting spectrum should match the Welch spectrum of the broadband (BB) component, taking into account the noise introduced by the method itself.

Regarding the QC modes, the thresholds for this extraction algorithm have been tuned from a set of approximately 10 different signals including low and high QC modes amplitude.

Following the extraction of the QC modes, the spectral complexity is diminished, facilitating the identification and extraction of the remaining spectral components: BB and LF components.

In cases where there are other narrow-band spectral components, such as the low-frequency and high-frequency quasi-coherent modes (LFQC and HFQC), these are also extracted in this step.

#### 5.1.4 Extraction of the LF component and BB component

The next step is the estimation of  $|\widehat{BB}|$  using the Asymmetric Generalised Gaussian (AGG): it allows a wide frequency coverage related to the microturbulence information, since it is assumed that the BB component contains all the information related to the microturbulence near the cut-off layer, and because of the asymmetry characteristics discussed in section 3.6.

In fact, the Asymmetric Generalised Gaussian (AGG) provides us with an approximation to a wide range of spectral shapes such as impulse, Laplacian, Gaussian and uniform distributions.

For the estimation of  $|\widehat{BB}|$ , the Welch spectrum of the initial signal is computed, but only the Welch coefficient,  $Welch_{BB}$ , which are not in the noise frequency interval, LF interval and QC modes frequency interval are used for the fitting process.

The AGG is defined as follows:

$$AGG(f) = \begin{cases} \frac{\beta}{(\alpha_1 + \alpha_2)\Gamma(1/\beta)} e^{-[\frac{-f+\mu}{\alpha_1}]^\beta} & , iff < \mu \\ \frac{\beta}{(\alpha_1 + \alpha_2)\Gamma(1/\beta)} e^{-[\frac{f-\mu}{\alpha_2}]^\beta} & , iff \geq \mu \end{cases} \quad (5.14)$$

in which  $\mu, \alpha_1, \alpha_2$  and  $\beta$  corresponds to the mean, left scale parameter, right scale parameter and shape parameter respectively.  $\Gamma$  is the gamma function and is defined by  $\Gamma(z) = \int_0^\infty e^{-t} t^{z-1} dt$ .

$$\text{objective function}_{\mu, \alpha_1, \alpha_2, \beta}(Welch_{BB}(R(t), AGG)) \quad (5.15)$$

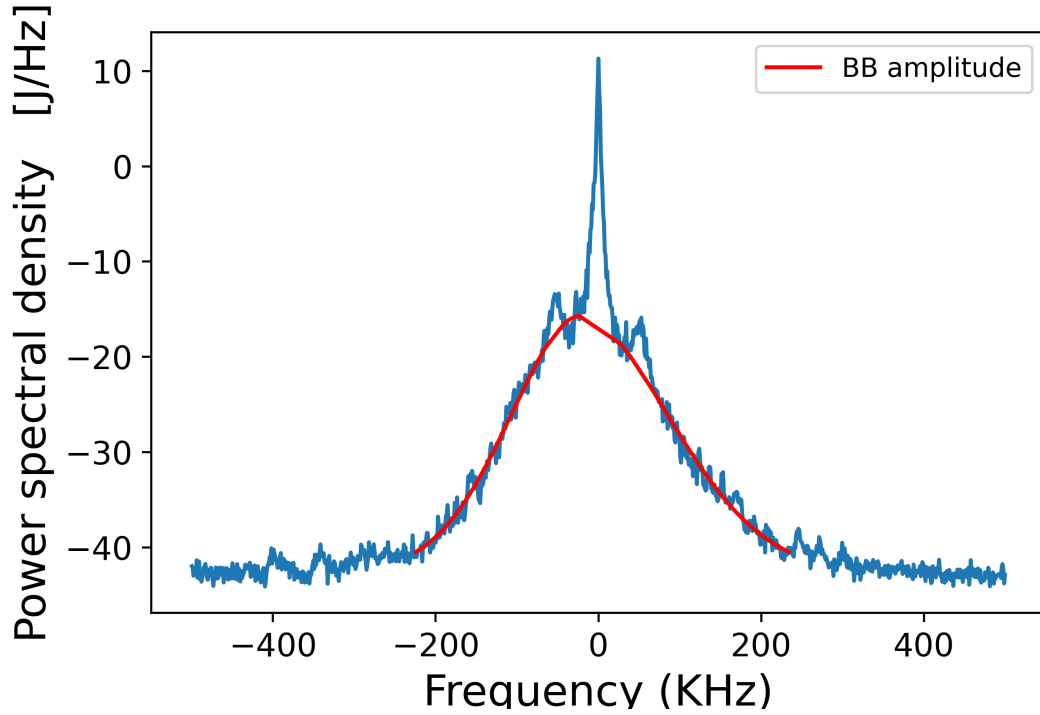


Fig. 5.6 Spectrum of the initial signal ( $R(t)$ ) and amplitude of the BB component ( $|\widehat{BB}|$ ).

As for the noise estimation, an interpolation is performed using the AGG from the 1025 frequency resolution (Welch method) to a frequency resolution,  $newf$ , equal to the time resolution. Finally, the  $|\widehat{BB}|$  can be estimated as:

$$|\widehat{BB}| \approx \sqrt{AGG_{BB}(newf)} \quad (5.16)$$

The spectrum of the initial signal is the sum of the spectral components.

$$\widehat{R}(f) = |\widehat{Noise}|e^{\angle \widehat{Noise}i} + |\widehat{QC}|e^{\angle \widehat{QC}i} + |\widehat{LF}|e^{\angle \widehat{LF}i} + \widehat{BB}e^{\angle \widehat{BB}i} \quad (5.17)$$

In the boundaries of the BB with the LF component and the QC modes, the maximum entropy is applied in order to estimate the phase of each of them [see equations 5.19 and 5.21]. The initial phase distribution of the BB component in the maximum entropy method is the phase distribution of the initial signal ( $\angle \widehat{R}$ ). In the LF component interval:

$$\widehat{R} - \widehat{Noise} = |\widehat{LF}|e^{\angle \widehat{LF}i} + \widehat{BB}e^{\angle \widehat{BB}i} \quad (5.18)$$

$$Maximumentropy(\angle \widehat{BB}(f), \angle \widehat{LF}(f)), \frac{\pi}{2} \leq \angle \widehat{BB}(f) - \angle \widehat{LF}(f) \leq \pi \quad (5.19)$$

$\frac{\pi}{2} \leq \angle \widehat{BB}(f) - \angle \widehat{LF}(f) \leq \pi$  indicates the anti-correlation/orthogonality property imposed between the BB component with the LF component.

In the QC modes frequency interval:

$$\widehat{R} - \widehat{Noise} = \widehat{QC} + |\widehat{BB}| e^{\angle \widehat{BB}} \quad (5.20)$$

$$\text{Maximumentropy}(\angle \widehat{BB}(f), \angle \widehat{QC}(f)), \frac{\pi}{2} \leq \angle \widehat{BB}(f) - \angle \widehat{QC}(f) \leq \pi \quad (5.21)$$

$\frac{\pi}{2} \leq \angle \widehat{BB}(f) - \angle \widehat{QC}(f) \leq \pi$  indicates the anti-correlation/orthogonality property imposed between the BB component with the LF and QC modes.

When  $f$  is outside the LF or QC intervals the expression is reduced to:

$$\widehat{R}(f) - |\widehat{Noise}| e^{\angle \widehat{Noise}} = \widehat{BB} e^{\angle \widehat{BB}i} \quad (5.22)$$

Once the phases and amplitudes are estimated for the whole frequency band, the whole decomposition can be illustrated [see figure 5.7]. The reconstruction signal is the sum of the different spectrum components.

In summary, the initial signal is decomposed into each of its spectral components, while preserving their statistical properties and physical content. This preservation allows these sub-signals to be used to perform studies that may reveal the underlying physics depending on the plasma conditions.

In addition, it has been shown that this spectral decomposition can be applied to time series from other sources, such as EEG signals resulting from brain activity.

## 5.2 Preserving physical and statistical properties

The occurrence of the QC modes in the LOC-SOC transition is used as a reference to validate the preservation of the physical properties, and the correlation properties of the QC modes are used as a reference to validate the preservation of their statistical properties.

### 5.2.1 LOC-SOC transition

The algorithm is applied to the same seven acquisitions shown in Figure 1(c) of [33] to quantify, for the first time, the QC mode energy contribution to the frequency spectrum. Figure 5.8 shows the extracted QC modes (orange curve), in general most of the QC mode contribution is extracted, however the method could not be successfully applied to the last spectrum ( $n_e = 4.6 \times 10^{19} m^{-3}$ ) of Figure 1(c) of [33] because the spectrum is affected by

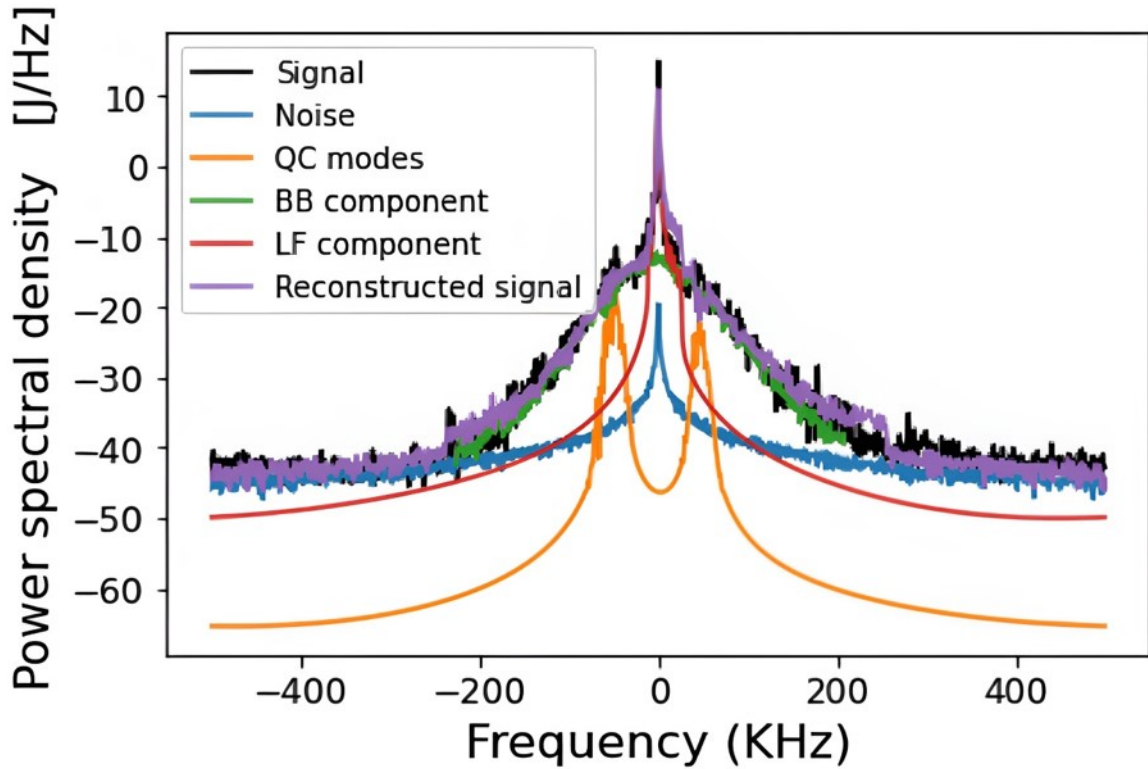


Fig. 5.7 Spectrum of the initial signal and its spectral components. The purple curve is for the reconstructed signal.

Doppler effects. The latter can occur, for example, if the reflectometer does not scan the plasma perfectly perpendicular to the cut-off layer (i.e. a misalignment of the reflectometer with respect to the equatorial plane or a vertical displacement of the plasma). As a result, the method detects a QC mode with the wrong amplitude (also in figures 5.8(d) and (f)). There may also be a harmonic of the QC modes or a high frequency quasi-coherent (HFQC) mode (Figures 5.8(a) and (b)) which interferes with the extraction.

In the LOC regime [see figures 5.8(a-c)], QC modes can be distinguished from the BB component, and the ratio of the QC peak to the BB amplitude is meaningful (blue curve). As mentioned previously, experimental and gyrokinetic codes support this peak. However, it has been observed experimentally that the QC modes disappear in the SOC regime where [see figures 5.8(d-f)] there is a very low ratio between the QC peak and the BB amplitude (blue curve).

Finally, to obtain an estimate of the LOC-SOC transition [see figure 5.9], a density step scan is preferable to analysing a current ramp-up [22]. The same shot range as in [33] (#41003 – #41013) at the same cut-off layer position ( $r/a = 0.3 \pm 0.025$ ) is taken over an extended set of reflectometry measurements. In addition, the extraction of the QC modes is

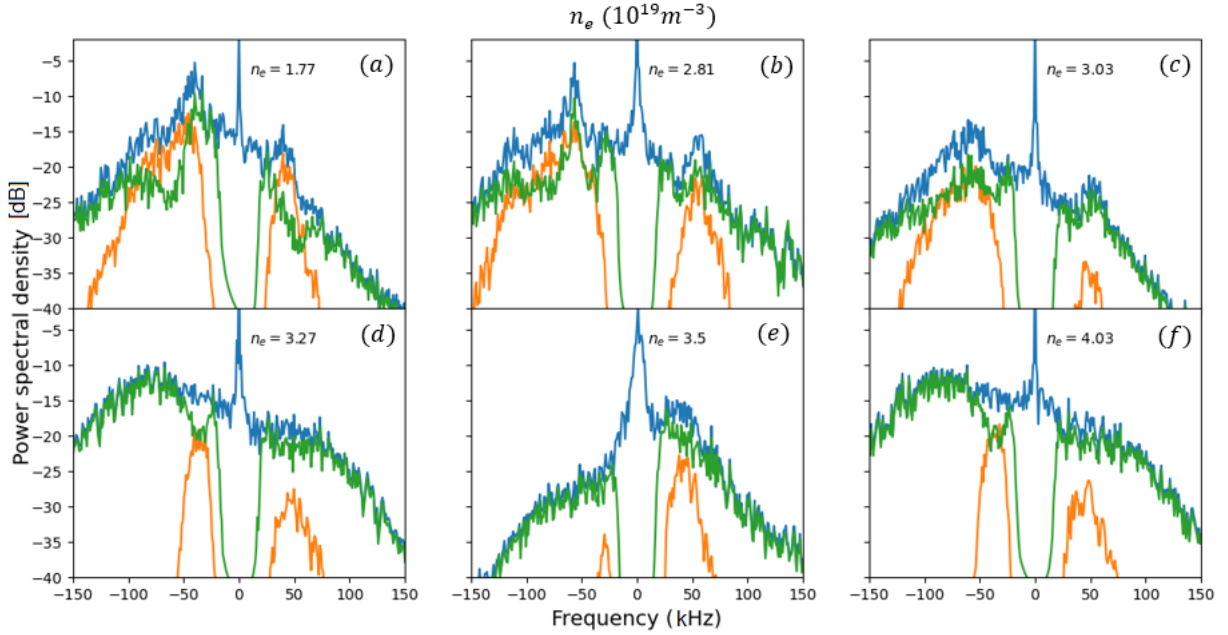


Fig. 5.8 Tore Supra reflectometry spectra during LOC–SOC transition at  $I_p = 1.2MA$  for  $r/a = 0.3 \pm 0.025$  and  $B = 3.8T$  from the shot range of #41003 – #41013.

quite fast (15s for 10 000 time steps). After excluding low SNR acquisitions and those with a Doppler shift associated with the disappearance of the centre frequency, 20 signals with densities ranging from  $1.8 \times 10^{19}$  to  $4.6 \times 10^{19}$  are taken for analysis.

The QC mode energy normalised to the broadband energy shows a clear decrease in the QC mode contribution with increasing density [see figure 5.9(b)]. The transition is around the average line density  $\langle n_l \rangle = 3 \times 10^{19} m^{-3}$ , this threshold being similar to the density threshold for the confinement time observed in figure 5.9(a). Extraction of the QC modes in the LOC-SOC transition highlights four points around  $n_l = 3 \times 10^{19} m^{-3}$ . These points show large fluctuations of this normalised energy with respect to the electron density, which could be related to the plasma parameters governing the LOC-SOC phenomenology. This would depend not only on the parameters mentioned in the subsection 1.3.5, such as the plasma current, the device main radius and the edge safety factor, but also on some other parameters such as  $Z_{eff}$  and background ion species.

To verify that the signal properties are conserved after applying our method, the coherence conservation between two antennas was analysed using Poloidal Correlation Reflectometry (PCR) developed at TEXTOR [129].

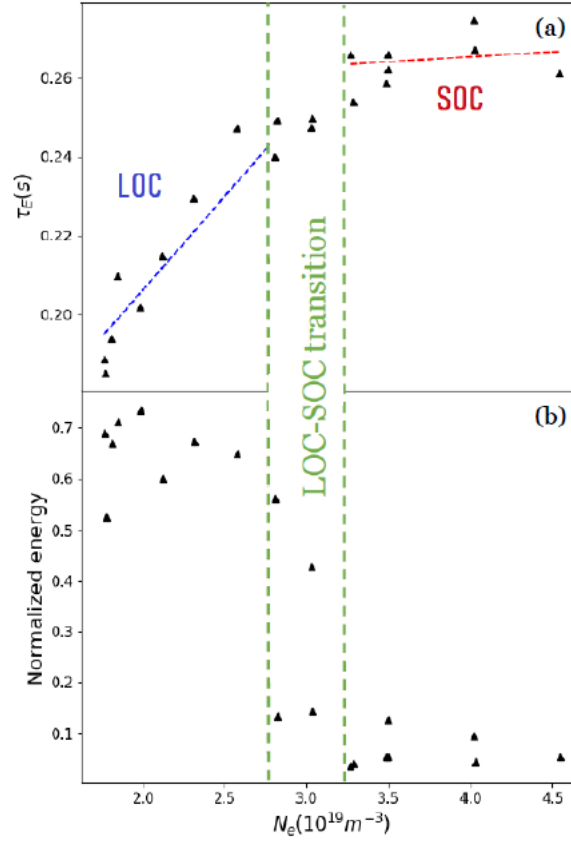


Fig. 5.9 Tore Supra confinement time versus density during the LOC–SOC transition at  $I_p = 1.2 \text{ MA}$  for  $r/a = 0.3 \pm 0.025$  and  $B = 3.8 \text{ T}$  from the (a) shot range of #41003 – #41013 and the (b) QC mode energy normalized by the BB energy as a function of the density.

### 5.2.2 Short Range Poloidal Correlation (SRPC)

As described in the 3<sup>rd</sup> chapter, antennas from correlation reflectometry (PCR) can be used to evaluate radial correlation lengths. In TEXTOR, SRPC lengths for turbulence have been measured using reflectometry and some spectral properties related to the QC modes have been revealed using Magnitude Squared Coherence (MSC) [130]. It was observed that the MSC allows the separation of spectral components and in particular shows a high correlation for the frequencies 50 to 150 kHz and -150 to -50 kHz corresponding to the QC modes. The MSC is defined as:

$$MSC(f) = \frac{|SD_{R_t G_t}(f)|^2}{SD_{R_t R_t}(f) \cdot G_{G_t G_t}(f)} \quad (5.23)$$

Where  $SD_{R_i G_i}(f)$  denotes cross power spectral density between the signals  $R_i$  and  $G_i$ , and  $SD_{R_i R_i}(f)$ ,  $SD_{G_i G_i}(f)$  for their spectral power density respectively.

Thanks to the specific SRPC properties of QC modes, a comparison can be made between the coherence from correlation reflectometry data at TEXTOR and the coherence using this algorithm, which allows the extraction of QC modes coming from the signal received by one of the correlation reflectometry antennas [see figure 3.9].

Figure 5.10 shows the initial (blue curve) and the extracted spectra (green curve) for both antennas. Due to the symmetry and the wave emission pattern, a mirror effect can be seen in the spectrum.

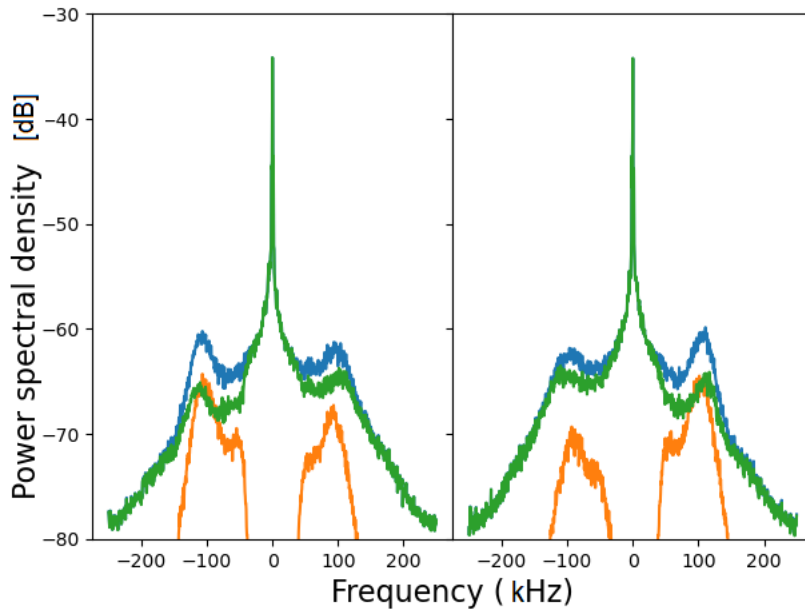


Fig. 5.10 Frequency spectrum of the initial signal from both antennas (blue curve), the QC modes (orange curve) and the signal after extraction of the QC modes (green curve).

After the QC mode extraction for both antenna signals have been processed separately using the first algorithm (see Appendix B), we performed MSC following the procedure described as follows. For the orange curve, the signals from the two reflectometry antennas (approx. 80 000 data points) are split into eight sets of 10 000 points, and then our method is applied to each of them. Thereafter, coherence is calculated pairwise between both antenna sets, and finally averaging of all coherence spectra is done. For the blue curve, equation 5.23 is performed between the whole signals of both antennas.

Furthermore, using the final QC mode extraction algorithm described in 5.1.3, a comparison can be made between the MSC of the two algorithms.

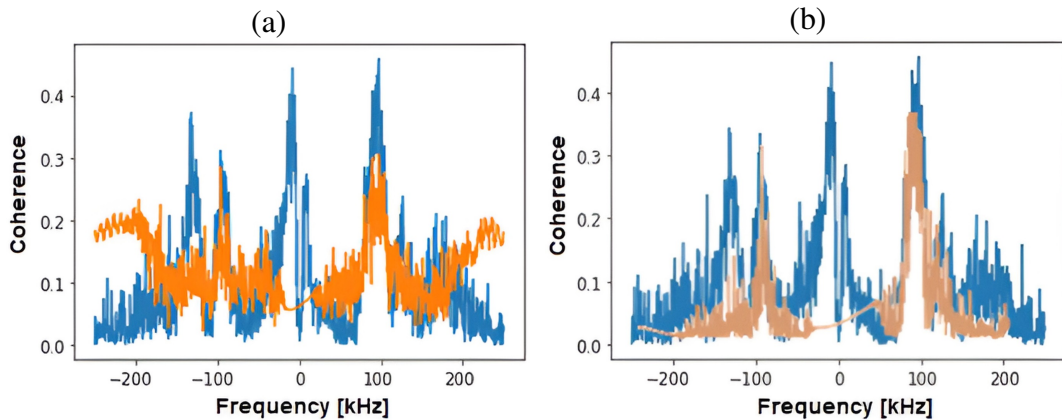


Fig. 5.11 (a) Coherence spectrum ( $MSC(f)$ ) of extracted QC modes (orange curve) and of signals from both antennas (blue curve) using the initial algorithm. (b) Coherence spectrum ( $MSC(f)$ ) of extracted QC modes (brown curve) and of signals from both antennas (blue curve) using the final algorithm.

As described earlier, the initial algorithm extracted not only the QC modes but also other residual spectral components that might be associated with them, this is illustrated in the figure 5.11(a) where the extracted coherence covers not only the QC modes interval frequency. However, using the final algorithm, only the QC modes coherence is highlighted [see figure 5.11(b)].

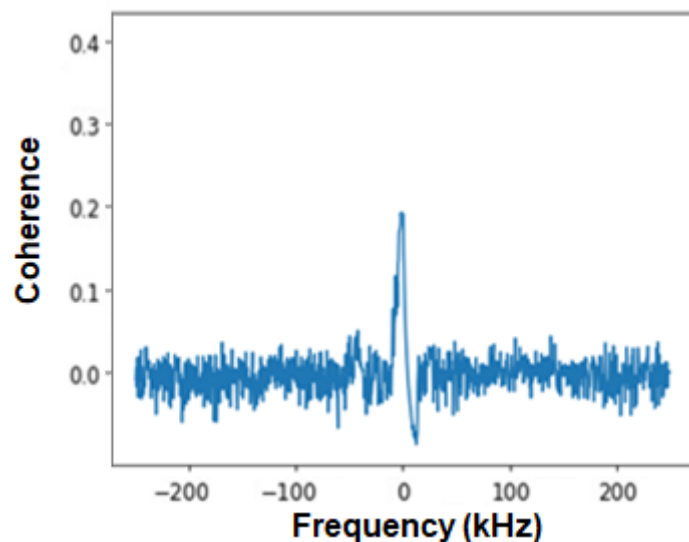


Fig. 5.12 Coherence spectrum of the extracted Broadband components using the final algorithm.

After extracting the QC modes from the signals, the component remaining in the same frequency interval as the QC modes is the BB component, which covers almost the entire

signal frequency interval. The figure 5.12 shows the MSC between the BB component of each signal, the coherence is approximately zero throughout the frequency interval even in the QC modes frequency interval, showing that the QC modes have been well extracted and separated from the BB component, therefore the poloidal coherence properties of the QC modes are no longer present in the QC modes frequency interval.

### 5.3 Towards multi-magnetic configuration study

The first version of the algorithm was specifically adapted to the Tore Supra database, which was then based on a single magnetic configuration.

The upgraded algorithm not only achieves a better extraction of the QC modes, but also facilitates the extraction of other spectral components.

Importantly, the upgraded algorithm version is versatile, making it suitable for other magnetic configurations. In addition to the raw signals discussed in the previous chapter, required inputs include plasma conditions ( $I_p, n_l, T, \rho, B, q_\psi, \beta, etc.$ ) and diagnostic conditions (plateau frequency, plateau duration, etc.). Prior to filtering out pathological signals during the data cleaning phase, a manual review is essential to ensure that the signals are consistent with the capabilities of the fusion device and the setup of the reflectometer.

It's well known that reflectometry signals come in different lengths. To deal with this, our algorithm uses parallel computation within the signals. For chunking purposes, a reference length of  $8192\mu s$  is used. As an example, a frequency sampling of  $1MHz$  will have 8192 time steps. Conversely, a frequency sample of  $5MHz$  will have  $8192 \times 5$  time steps.

Finally, the algorithm can be used to study the properties and dynamics of the QC modes and also the other spectral components in the different magnetic configurations that are the basis of this study: Limiter configuration (Tore Supra), Divertor configuration (WEST) and Island Divertor (W7X Stellarator).

# Chapter 6

## Dynamics & Properties of Quasi-Coherent Modes in different magnetic configurations

### Contents

---

<b>6.1</b>	<b>Systematic analysis of QC modes in ohmic plasmas . . . . .</b>	<b>104</b>
6.1.1	QC modes likelihood of occurrence . . . . .	104
6.1.2	Predominance of the QC modes in and outside $q = 1$ . . . . .	108
6.1.3	Energy content of QC modes on LFS and HFS . . . . .	110
<b>6.2</b>	<b>QC mode classes in connection with LF and BB components . . . . .</b>	<b>112</b>
6.2.1	Distinction between QC mode classes . . . . .	112
6.2.2	QC mode relationships with microturbulence at different $\rho$ and $q$ . . . . .	119
6.2.3	Energy content in the LF component at different $\rho$ and $q$ . . . . .	124
<b>6.3</b>	<b>Dynamics of QC modes and energy exchange with other components . . . . .</b>	<b>126</b>
6.3.1	Algorithm for the study of energy exchange . . . . .	126
6.3.2	Tracking of QC modes' intrinsic spectral bandwidth over time . . . . .	129
6.3.3	Evidence of energy exchange between components using causality . . . . .	130
6.3.4	QC modes in interaction with sawtooth . . . . .	130
6.3.5	Dynamics across different magnetic configurations . . . . .	131
<b>6.4</b>	<b>QC modes characteristics in ECRH plasmas . . . . .</b>	<b>135</b>
<b>6.5</b>	<b>Are QC modes properties and dynamics driven by universal mechanism? . . . . .</b>	<b>135</b>

---

As discussed in section 2.5.2, this research focuses on characterising the properties and dynamics of QC modes in the ohmic regime in different magnetic configurations.

An algorithm to extract each spectral component (low frequency component, QC modes, broadband component and noise) from the reflectometry frequency spectrum has been developed in the section 5.1. This approach ensures that both the statistical and physical properties of each component are preserved.

Having successfully extracted the QC modes, their properties and dynamics can be studied using the WEST and Tore Supra databases, the access to the W7X database is restricted: only a number of signals under specific conditions are available for evaluation.

## 6.1 Systematic analysis of QC modes in ohmic plasmas

The initial version of the QC mode extraction algorithm confirmed and extended previous results on the relationship between TEM and QC modes as shown in chapter 5 and in [131], the QC modes energy decreased over  $n_l$  (central line averaged density), but this preliminary study was carried out on the specific discharges of [131].

The algorithm was upgraded for a better extraction as described in the section 5.1.3 and then applied to other discharges to analyse the QC modes energy at  $I_p = \text{constant}$ . Indeed, QC modes of low amplitude and even some high amplitude QC modes were still observed in the SOC regime.

This leads us to examine how the QC modes are then distributed in  $n_l$  for each  $I_p$ .

### 6.1.1 QC modes likelihood of occurrence

Since QC modes are present in both the LOC and SOC sub-regimes, it is imperative to evaluate the likelihood of occurrence of QC modes in a  $I_p$  vs.  $n_l$  probability map and confirm whether these cases are frequent or rare, separately for the HFS ( $\rho < 0$ ) and the LFS ( $\rho > 0$ ). Indeed, if the QC modes are associated with the TEM, one would expect them to be stable or very low in the HFS. Only a few trapped electrons approach the HFS equatorial plane where the reflectometry measurements are performed. In addition, the drift wave turbulence is ballooned.

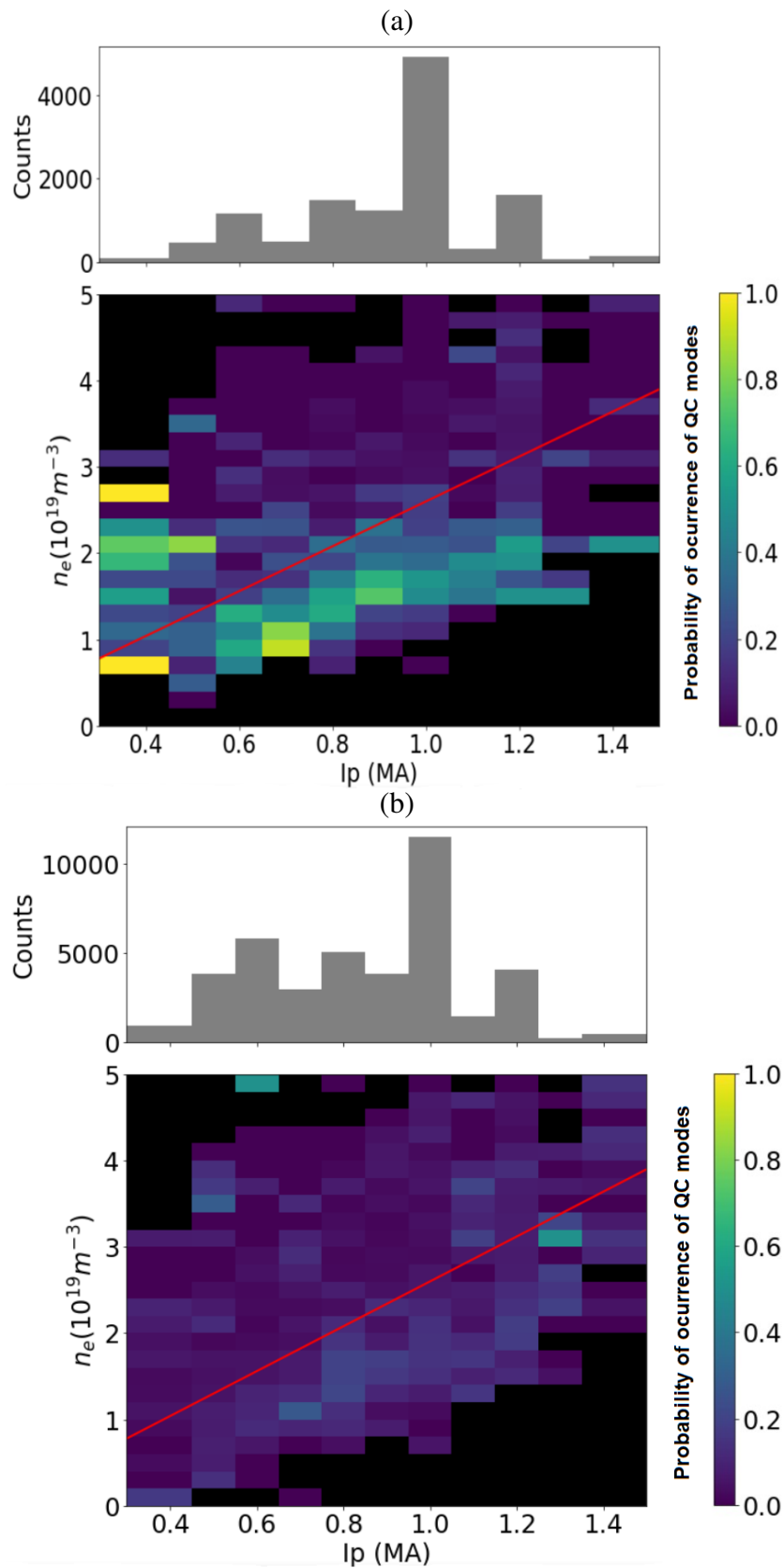


Fig. 6.1 Tore Supra, probability map of the occurrence of QC modes in the LFS(a) and HFS(b). The empirical scaling law to delineate the LOC and SOC sub-regimes is represented by the red line.

The empirical scaling used to differentiate between the LOC and SOC sub-regimes are  $n_{crit} = 2.6 \times I_p$  and  $n_{crit} = 5.3 \times I_p$  for Tore Supra and WEST respectively, as explained in 1.3.5 (red lines in figures 6.1 and 6.2).

For both Tore Supra and WEST, the highest probability of occurrence of QC modes is observed on the Low Field Side (LFS) mainly in the LOC sub-regime with an average probability of about 0.7 and 0.6 respectively and on the High Field Side (HFS) with about 0.4 and 0.3 respectively. As shown in the next subsection, this HFS occurrence is mainly due to the occurrence inside the  $q=1$  surface in Tore Supra (WEST access outside  $q=1$  on the HFS is very limited). This statistical study, carried out in different tokamak magnetic configurations, strengthens the link between the QC modes and the LOC sub-regime, hence the TEM instability.

However, apart from this 'class' of QC modes in the LOC sub-regime, 2 other classes were found in the SOC sub-regime, one at low current and another at high current. Both can be observed in Tore Supra, but in WEST only the first class can be seen, as the  $I_p$  range examined has lower  $I_p$  values.

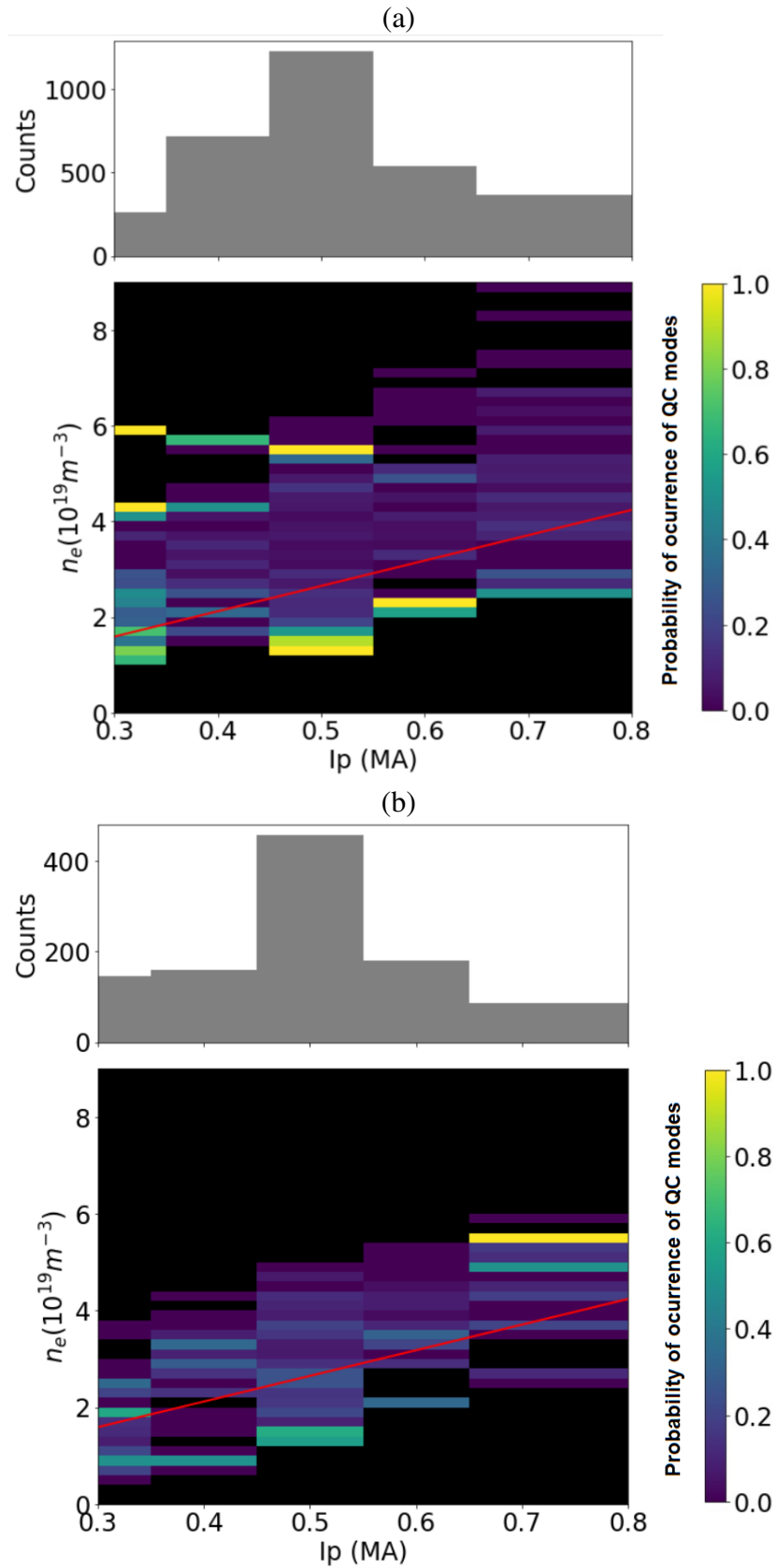


Fig. 6.2 WEST, probability map of the occurrence of QC modes in the LFS(a) and HFS(b). The empirical scaling law to delineate the LOC and SOC sub-regimes is represented by the red line.

### 6.1.2 Predominance of the QC modes in and outside $q = 1$

In order to study the occurrence of QC modes in more detail, an investigation is carried out using two main parameters as references: the safety factor, highlighted in the Neo-Alcator scaling [see section 1.3.5], which is intrinsically linked to  $I_p$  as described by the equation 1.7. The second parameter is the  $q = 1$  surface, which can be thought of as a transport barrier, as in the case of sawtooth oscillations damped by off-axis electron cyclotron resonance heating [132]. The  $q = 1$  surface can delineate different turbulent transport behaviours.

Consequently, partitions of  $q$  values were made so that intervals of  $q$  contained localised behaviour. Finally, three different safety factor ranges and three range positions with respect to the  $q = 1$  surface are resolved [see figure 6.3].

$$\begin{aligned} \text{Range 1 : } q_\psi &< 4.5 \\ \text{Range 2 : } q_\psi &\in [4.5, 6.1] \\ \text{Range 3 : } q_\psi &> 6.1 \end{aligned} \tag{6.1}$$

The partial probability of occurrence of QC modes is analysed, i.e. for each interval of  $n_e$  at different ranges [equation 6.1] and different positions relative to the  $q = 1$  surface, the number of occurrences of QC modes is divided by the number of signals in each interval.

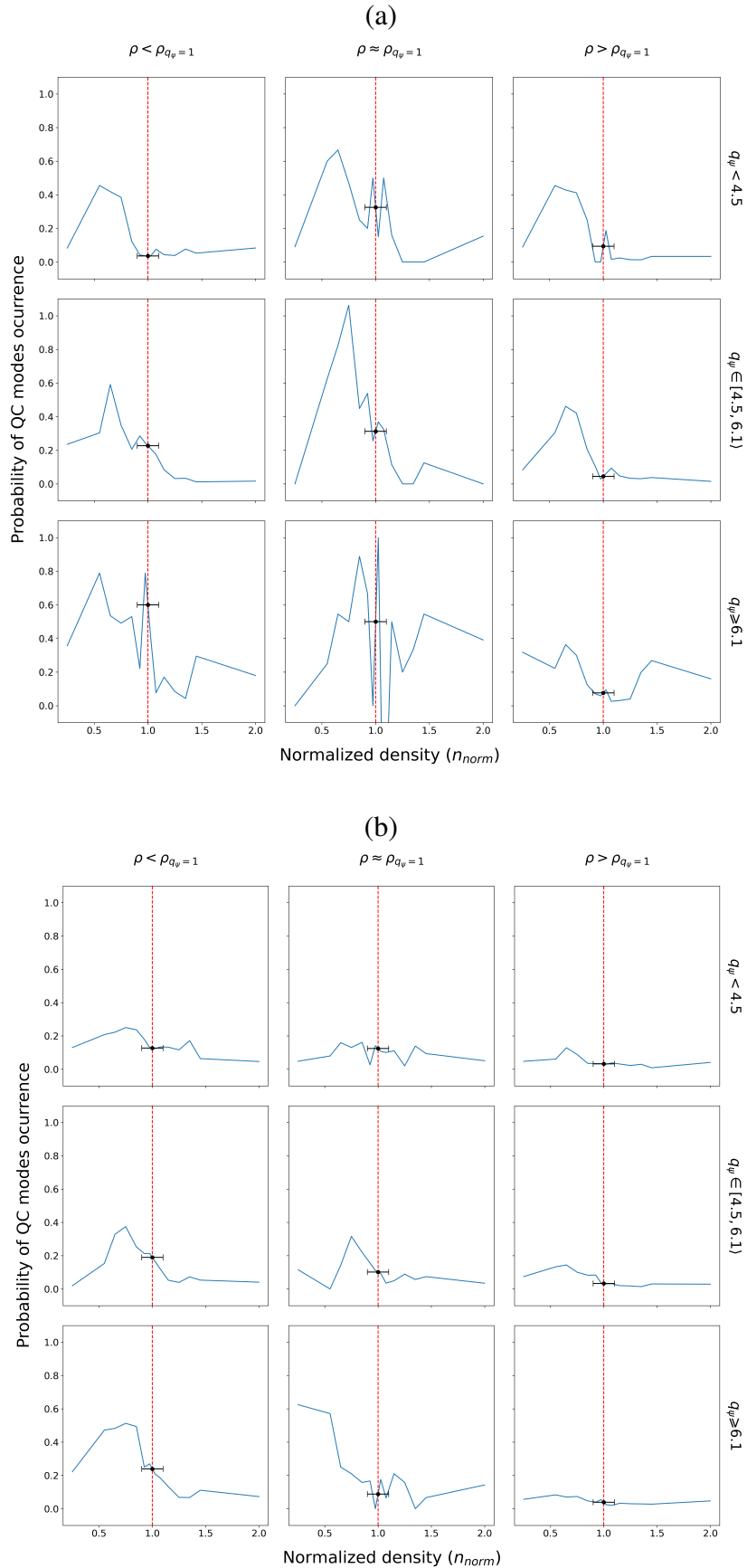


Fig. 6.3 Partial probability of occurrence of QC modes over the normalised electron density for different  $q$ , positioned inside, near and outside the  $q = 1$  surface for (a) the low field side and (b) the high field side of Tore Supra.

In the LFS of Tore Supra there is approximately the same probability of QC modes for  $\rho < \rho_{q=1}$  and  $\rho > \rho_{q=1}$ , with fluctuations in probability during the LOC-SOC transition. Around the  $q = 1$  surface ( $\rho \approx \rho_{q=1}$ ), the small number of events does not allow to obtain significant results. In the HFS, however, the QC modes are more likely to appear inside the  $q=1$  surface ( $\rho < \rho_{q=1}$ ) than outside ( $\rho > \rho_{q=1}$ ).

### 6.1.3 Energy content of QC modes on LFS and HFS

Regarding the amplitude of the QC modes, it has also been observed in previous studies [33] that they seem to increase to reach a maximum just before the LOC-SOC transition and then decrease again. The QC mode extraction algorithm makes it possible to quantify the energy of the QC modes and then to study this behaviour in more detail.

Let's define some parameters before this study, the spectral centroid of the QC modes,  $SC(\widehat{QC})$ , and the spectral bandwidth frequency of the QC modes,  $SB(\widehat{QC})$ , which is calculated as the average between the  $QCinterval$  in the negative frequencies and the positive frequencies. As defined in 4, both parameters can be expressed as follows.

$$\begin{aligned}
 SC(\widehat{QC}) &= \frac{\sum f \cdot Welch(QC(t))_f}{\sum Welch(QC(t))_f}, f \in QCinterval \\
 SB(\widehat{QC}) &= \sqrt{\frac{\sum (f - SC(\widehat{QC}))^2 \cdot Welch(QC(t))_f}{\sum Welch(QC(t))_f}}, f \in QCinterval
 \end{aligned} \tag{6.2}$$

The energy content in the QC modes and the energy content in the BB component over the QC interval are also defined as:

$$\begin{aligned}
 E_{QC} &= \sum_{f_1=f_{QCcentroid}-\Delta f}^{f_2=f_{QCcentroid}+\Delta f} Welch(QC(t))_f, f \in QCinterval \\
 E_{BB|QC} &= \sum_{f_1=SC(\widehat{QC})-\Delta f}^{f_2=SC(\widehat{QC})+\Delta f} Welch(BB)_f, f \in QCinterval
 \end{aligned} \tag{6.3}$$

As for the probability map of the occurrence of QC modes, the analysis of the energy content in the QC modes takes the HFS and LFS as a reference. It uses  $\frac{E_{QC}}{E_{BB|QC}}$  to study the evolution of the QC mode energy [see figure 6.4].

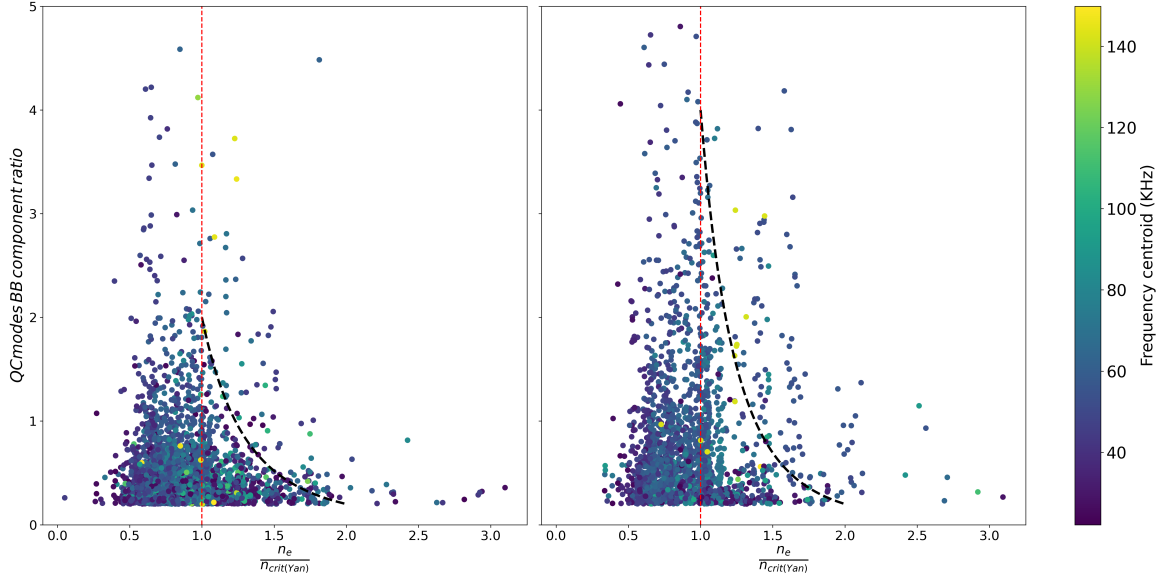


Fig. 6.4 QC mode energy versus BB component energy in the QC mode interval ( $\frac{E_{QC}}{E_{BB|QC}}$ ), as a function of  $n_e$  normalised using the empirical scaling of Yan Sun in HFS(a) and LFS(b). The frequency centroid corresponds to  $SC(\widehat{QC})$

The figure 6.4 illustrates this progression of the averaged energy ratio between the QC modes and the BB component across  $n_l$ . Initially, when the  $\frac{n_e}{n_{crit(Sun)}}$  value is approximately 0.5, the Broadband component predominantly emerges at the inception of the LOC regime. Subsequently, as the  $\frac{n_e}{n_{crit(Sun)}}$  value approaches 1, the Quasi-Coherent (QC) modes gain prominence, their influence increasing more in the Low Field Side (LFS) compared to the High Field Side (HFS).

Beyond this point, the dominance of the QC modes begins to diminish, revealing two divergent behaviours between the HFS and the LFS. In the HFS it follows  $\approx \frac{n_e}{n_{crit(Sun)}}^{-4.3}$ , while in the LFS it follows  $\approx \frac{n_e}{n_{crit(Sun)}}^{-3.3}$ . In addition, a set of QC modes with a relatively high energy ratio appears beyond  $n_e/n_{crit(Yan)} = 1$ . Even though the ratios ( $\frac{E_{QC}}{E_{BB|QC}}$ ) are more or less identical on the LFS and HFS sides, it is important to remember that the total energy in the BB component is much greater on the LFS side than on the HFS side [98].

This nuanced evolution of  $\frac{E_{QC}}{E_{BB}}$  could underline the interplay between the TEM and the microturbulence, highlighting some different intricate dynamics. Indeed, the transition is more abrupt in the LFS compared to the HFS.

The figure 6.4 then confirms that the amplitude of the QC modes, showing an increasing behaviour to reach a maximum just before the LOC-SOC transition and then decreasing again, is general to the whole database. In addition, the decay of the QC mode energy after the LOC-SOC transition has been quantified and outliers have been identified.

The analysis of the probability of occurrence of the QC modes, the QC mode dominance and the QC mode energy content strengthens the link between the QC mode and TEM instabilities in the ohmic regime.

## 6.2 QC mode classes in connection with LF and BB components

The different QC modes appearing around the  $I_p$  vs  $n_l$  map are regrouped and categorised as classes of QC modes. Besides the 'class' of QC modes corresponding to the QC modes associated with the TEM, there are 2 other classes localised in the SOC sub-regime: one at low current and another at high current [see figures 6.1 and 6.2].

As discussed previously, collisionality plays a role in TEM instability and could therefore influence the evolution of QC modes from the LOC to the SOC regime. In this context, QC modes in the SOC regime could represent a weakened version of those originating in the LOC regime, possibly transitioning to broadband turbulence. In addition, the low current class could correspond to a non-stationary phase during current build-up.

Overall, these different classes of QC modes could interact in different ways with the LF and BB components, and it is then necessary to find a way to distinguish them.

### 6.2.1 Distinction between QC mode classes

It is crucial to distinguish between these classes of QC modes. The spectral centroid of the QC modes over  $\frac{n_e}{n_{\text{crit}}}$  is examined for the Tore Supra and WEST tokamaks [see figure 6.5].

Two different branches in  $SC(\widehat{QC})$  are distinguished for Tore Supra (black circles), the first one remaining at low values from the LOC to the SOC sub-regimes and the second one showing a linear increase over  $n_l$ .

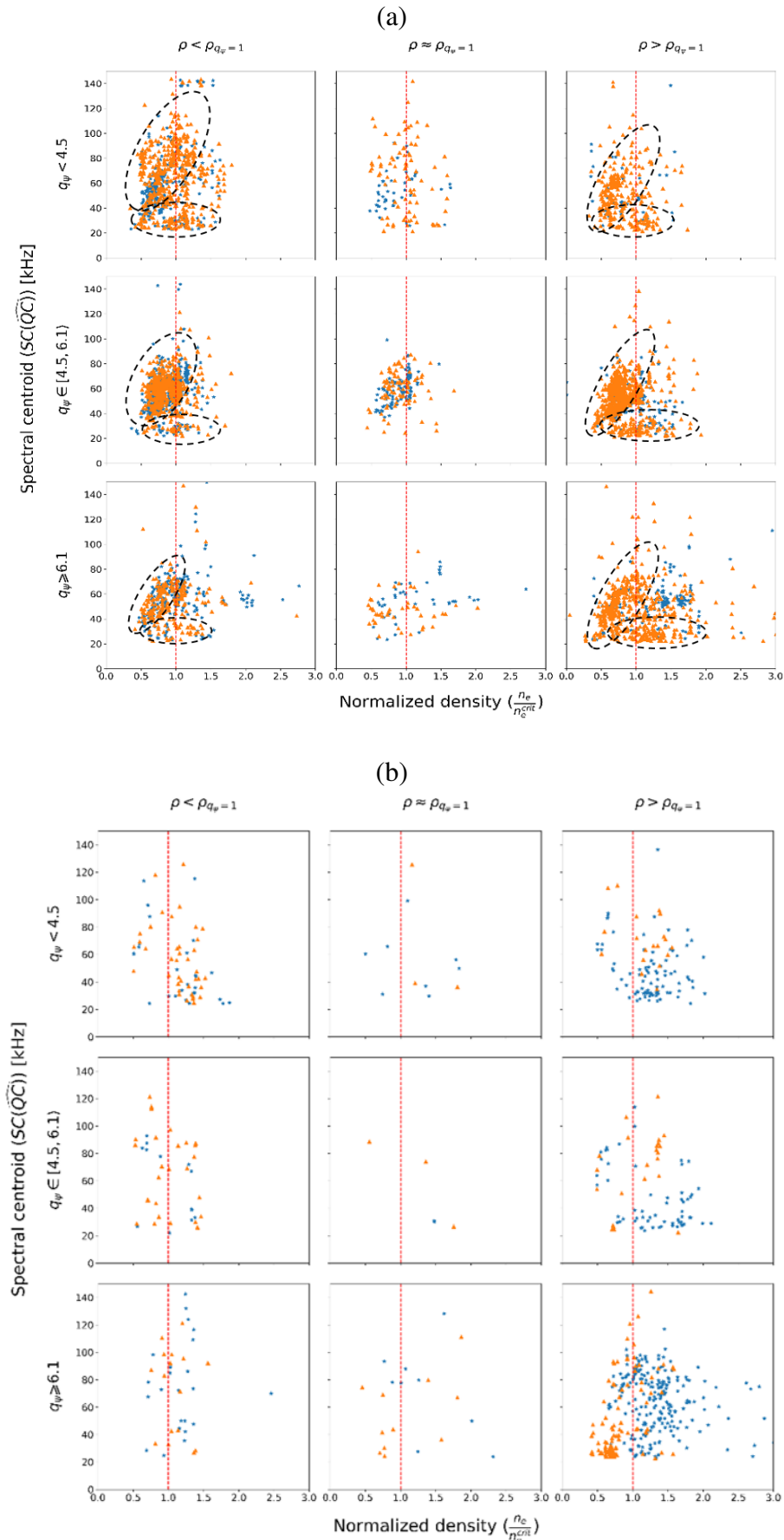


Fig. 6.5 Spectral centroid as a function of the electron density normalized Rice. Orange is for HFS and blue for LFS. (a)Tore Supra and (b)WEST tokamak.

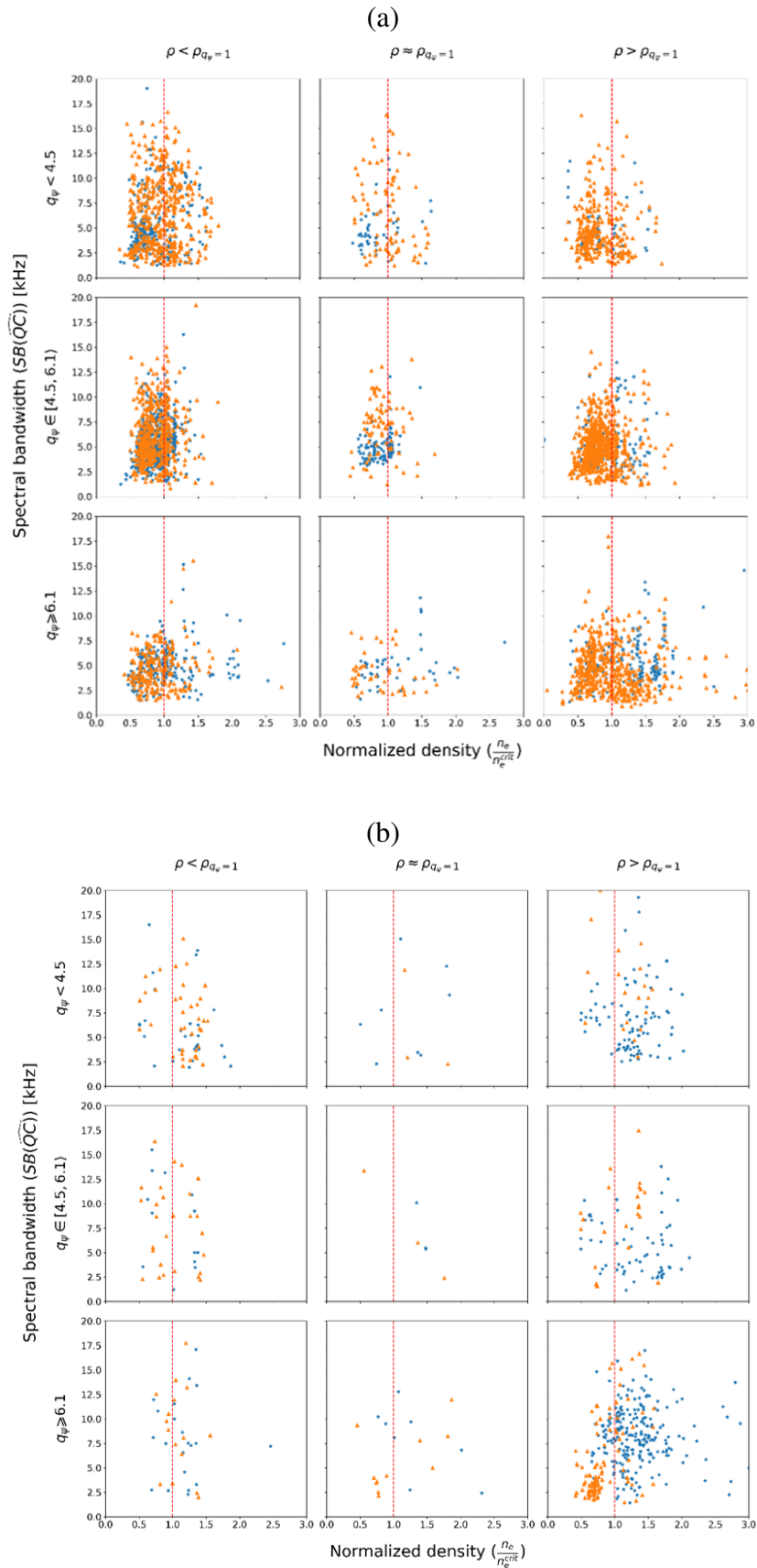


Fig. 6.6 Frequency bandwidth as a function of the electron density normalized Rice. Orange is for HFS and blue for LFS. (a)Tore Supra and (b)WEST tokamak.

The spectral bandwidth of the QC modes over  $\frac{n_e}{n_{crit}}$  for the Tore Supra and WEST tokamaks is also examined [Figure 6.6]. No distinguishing features are seen.

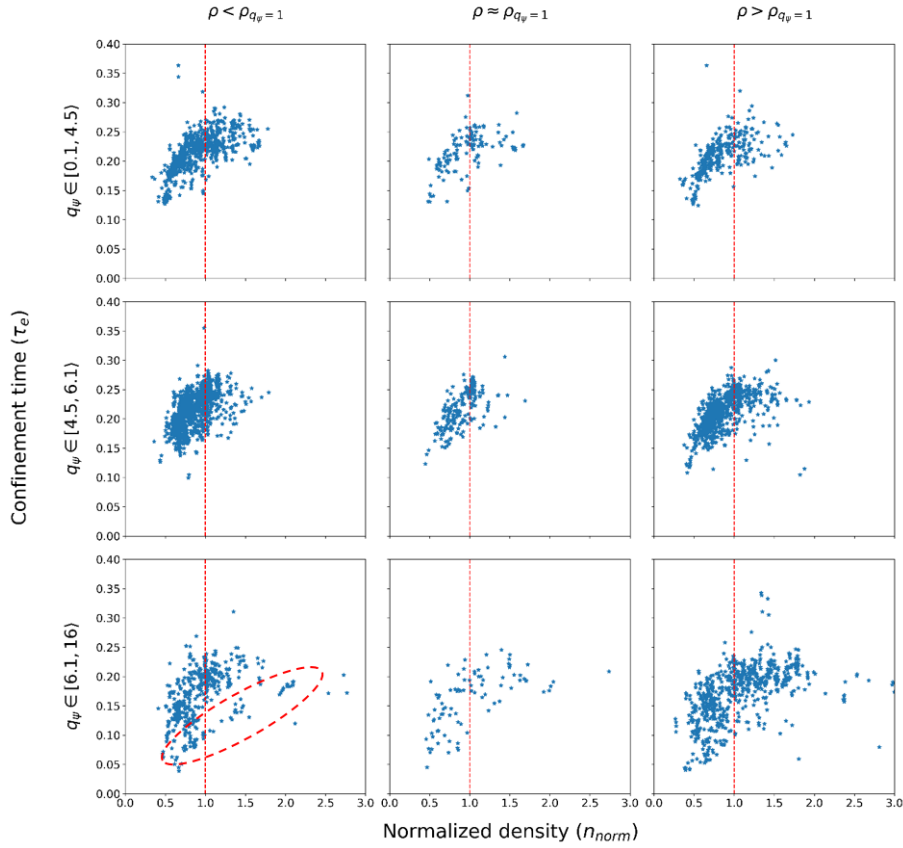


Fig. 6.7 Confinement time ( $\tau_s$ ) vs normalized density ( $n_{norm}$ ) at different  $\rho$  and  $q$ . Red line corresponds to  $n_{crit}$ .

In this configuration of ranges of  $q_\psi$  and relative position to the  $q = 1$  surface, the confinement time is also examined [figure 6.7]. Apart from the first branch of  $\tau_e$  at  $\rho < \rho_{q=1}$  and  $q_\psi \in [6.1, 16]$ , there is a second branch which also has a linear dependence on  $n_{norm}$ , but shifted from the first branch. It belongs to the class of low current QC modes. This sub-class of QC modes around the LOC-SOC transition is characterised by the appearance of LFQC and HFQC modes [see figure 6.8].

On the other side, the ratio  $\frac{SB(\widehat{QC})}{SC(\widehat{QC})}$  is also examined across  $\frac{n_l}{n_{crit}}$ , lowest values of this ratio indicates concentration of the energy near the spectral centroid of the QC modes. An increasing of this ratio is observed however its range is quite large.

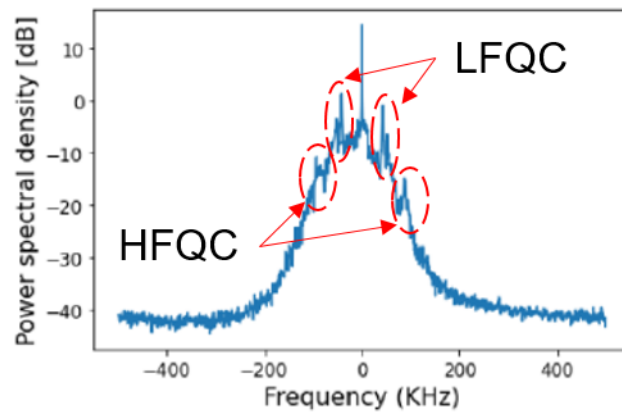


Fig. 6.8 Spectrum,  $I_p = 0.6MA$ ,  $n_e = 0.9 \times 10^{19}m^{-3}$  and  $\rho = -0.2$ , from the subclass of QC modes belonging to the  $\tau_e$  branch around the LOC-SOC transition. LFQC and HFQC are exhibited.

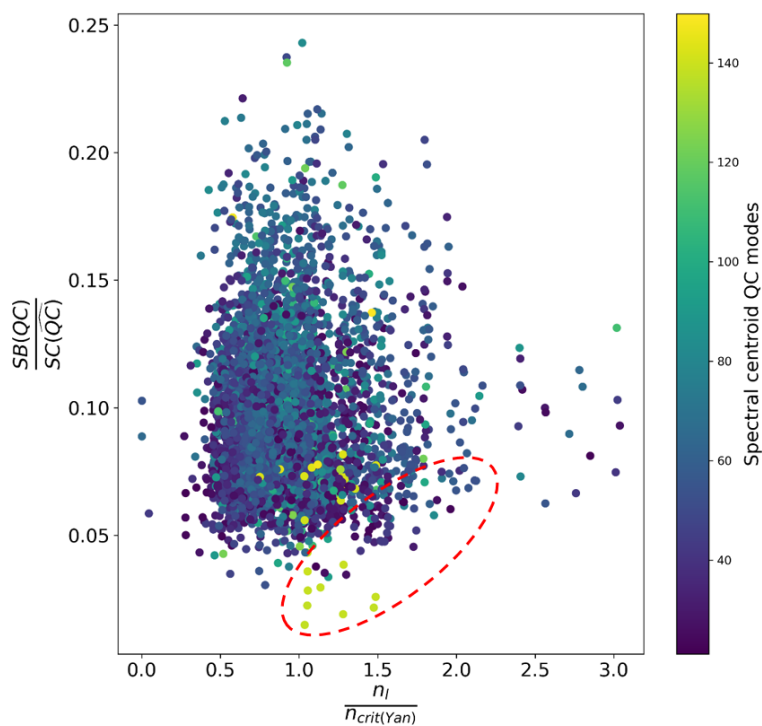


Fig. 6.9  $\frac{SB(\widehat{QC})}{SC(\widehat{QC})}$  over  $n_{norm}$ . The color bar represents the spectral centroid of the QC modes ( $SC(\widehat{QC})$ ).

A set of QC modes is highlighted within the red circle, representing the shot #46289. This sub-class of QC modes is associated with the class characterized by high  $I_p$  and high  $n_e$  (SOC regime). The figure 6.10, displays the Power Spectral Density of both the initial and final acquisitions of this shot. The QC modes are experiencing an increasing in their spectral centroid and spectral bandwidth.

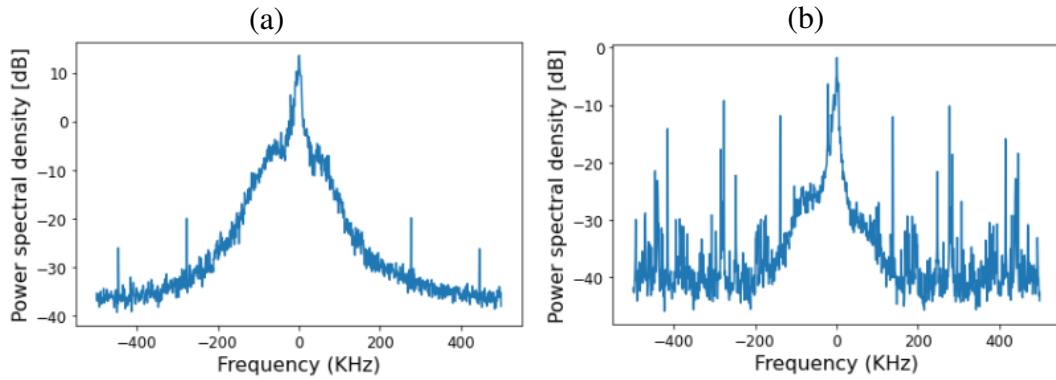


Fig. 6.10 Power spectral density of signals from shot #46289 at (a)  $t = 4.03s$  and (b)  $t = 4.08s$ ,  $I_p = 1.2MA$ ,  $n_l = 3.9 \times 10^{19}m^{-3}$ . The QC modes are experiencing an increasing in their spectral centroid and spectral bandwidth.

As described in the chapter 2, instabilities of different temporal and spatial scales may coexist, and a study of their scale invariance or power-law scaling may provide a way to distinguish between them. The characteristics of the multifractal spectrum, using wavelet leaders, of the initial signal ( $R(t)$ ) can be studied to identify potential scale invariance, intrinsic dynamics, between scales belonging to the QC modes and scales belonging to other spectral components [see Figure 6.11]. The power spectral density corresponding to class LOC (b) is symmetric and its multifractal spectrum is located at high values of  $h$  (Holder exponent), corresponding to the predominance of large scales, i.e. LF components. The power spectral density corresponding to the class LOC (c) is asymmetric and its multifractal spectrum is located at medium values of  $h$ , it includes more scales than (b). Finally, the power spectral density corresponding to class LOC (a) is also asymmetric and its multifractal spectrum is located at high values of  $h$  and also covers a wide range of  $h$  values, implying a more complex dynamic between the LF components and possibly the QC modes. The longer right tail of the multifractal spectrum in (b) and (c) corresponds to the greater dominance of specific modes compared to higher frequency modes.

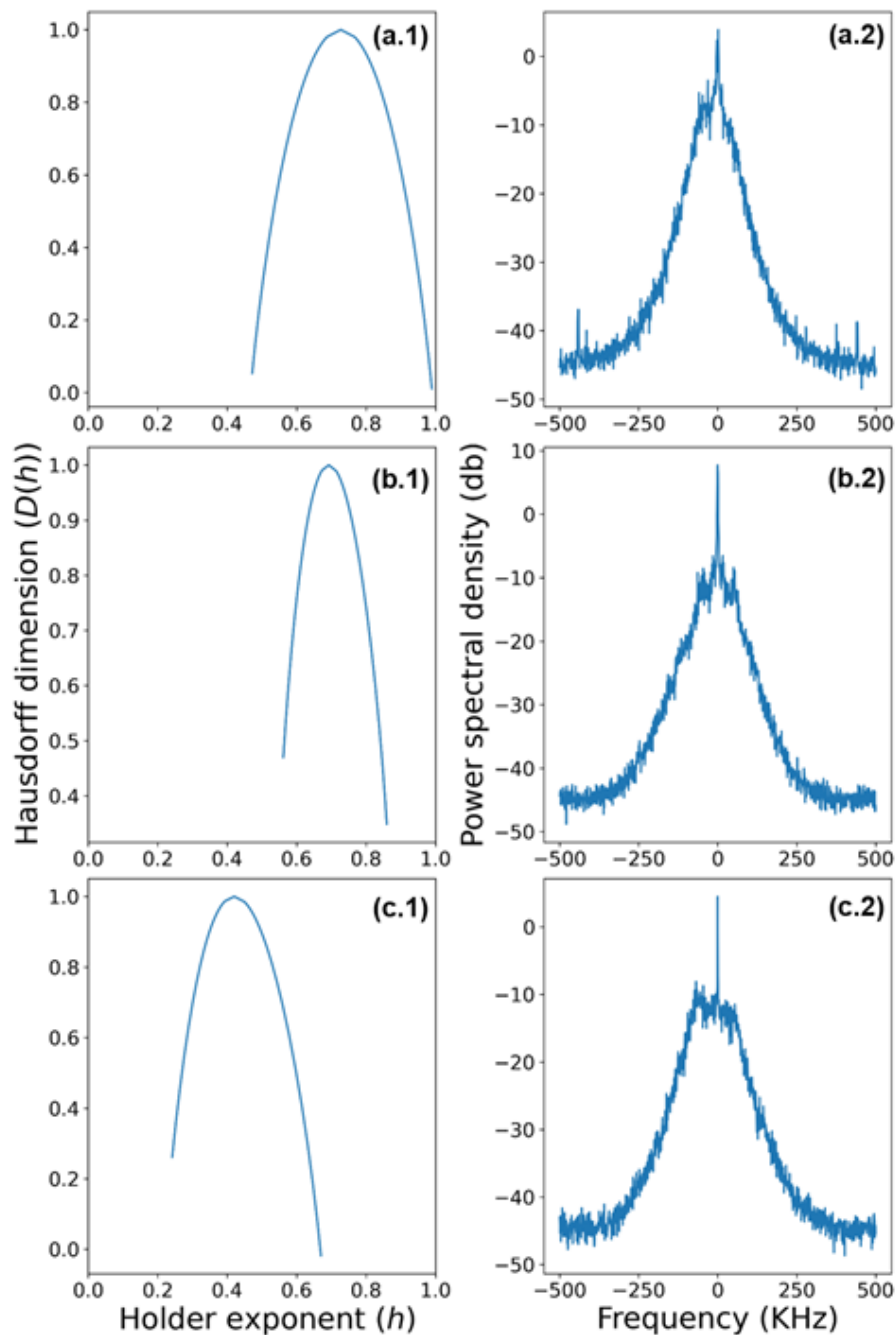


Fig. 6.11 Multifractal spectrum (a.1, b.1, c.1) and power spectral density (a.2, b.2, c.2) from the different classes of QC modes: (a) QC class low current,  $I_p = 0.4MA$ ,  $n_e = 3.03 \times 10^{19}m^{-3}$  and  $\rho = -0.72$ . (b) QC class LOC,  $I_p = 1MA$ ,  $n_e = 1.44 \times 10^{19}m^{-3}$  and  $\rho = -0.43$ . (c) QC class high current,  $I_p = 1.2MA$ ,  $n_e = 4.3 \times 10^{19}m^{-3}$  and  $\rho = 0.26$ .

After having seen some specific and statistical characteristics of the classes and sub-classes of QC modes, it is still complex to perform a discrimination of them, because different

scales are still mixed in:  $\tau$ ,  $I_p$ ,  $n_l$ ,  $\rho$ ,  $B_0$ , frequency centroid, frequency bandwidth, etc. It is then necessary to study other parameters such as the evolution of the energy content in the other spectral components.

### 6.2.2 QC mode relationships with microturbulence at different $\rho$ and $q$

The microturbulence is associated with the broadband (BB) component. From the equation 5.14,  $\beta$  and  $\mu$  characterise the spectral shape and the asymmetry or skewness of the BB component, respectively.

For Tore Supra at HFS and LFS there is a different behaviour between  $\rho < \rho_{q=1}$  and  $\rho > \rho_{q=1}$  [see figure 6.12]. From the LOC to the SOC sub-regimes, the spectral shape covers a wide range of values ( $1 < \beta < 4$ ) and then tends towards a Gaussian shape ( $\beta \approx 2$ ) in  $\rho < \rho_{q=1}$ . However, the averaged value of  $\beta$  remains flat across the LOC and SOC sub-regimes in  $\rho > \rho_{q=1}$  [see figure 6.12].

In the WEST tokamak the statistics are not sufficient, but a difference to the Tore Supra tokamak can still be seen in  $\rho > \rho_{q=1}$ . In the LOC sub-regime, low values of  $\beta$  are more prevalent, corresponding to Lorentzian-like shapes, then in the SOC sub-regime  $\beta$  covers a wide range of values [see figure 6.12].

As mentioned previously,  $\mu$  characterizes the asymmetry of the BB component. In Tore Supra, this asymmetry seems to diminish across the transition from LOC to SOC in  $\rho < \rho_{q=1}$ . However, in  $\rho > \rho_{q=1}$ ,  $\mu$  seems to remain in average at the same values across the transition [see figure 6.13].

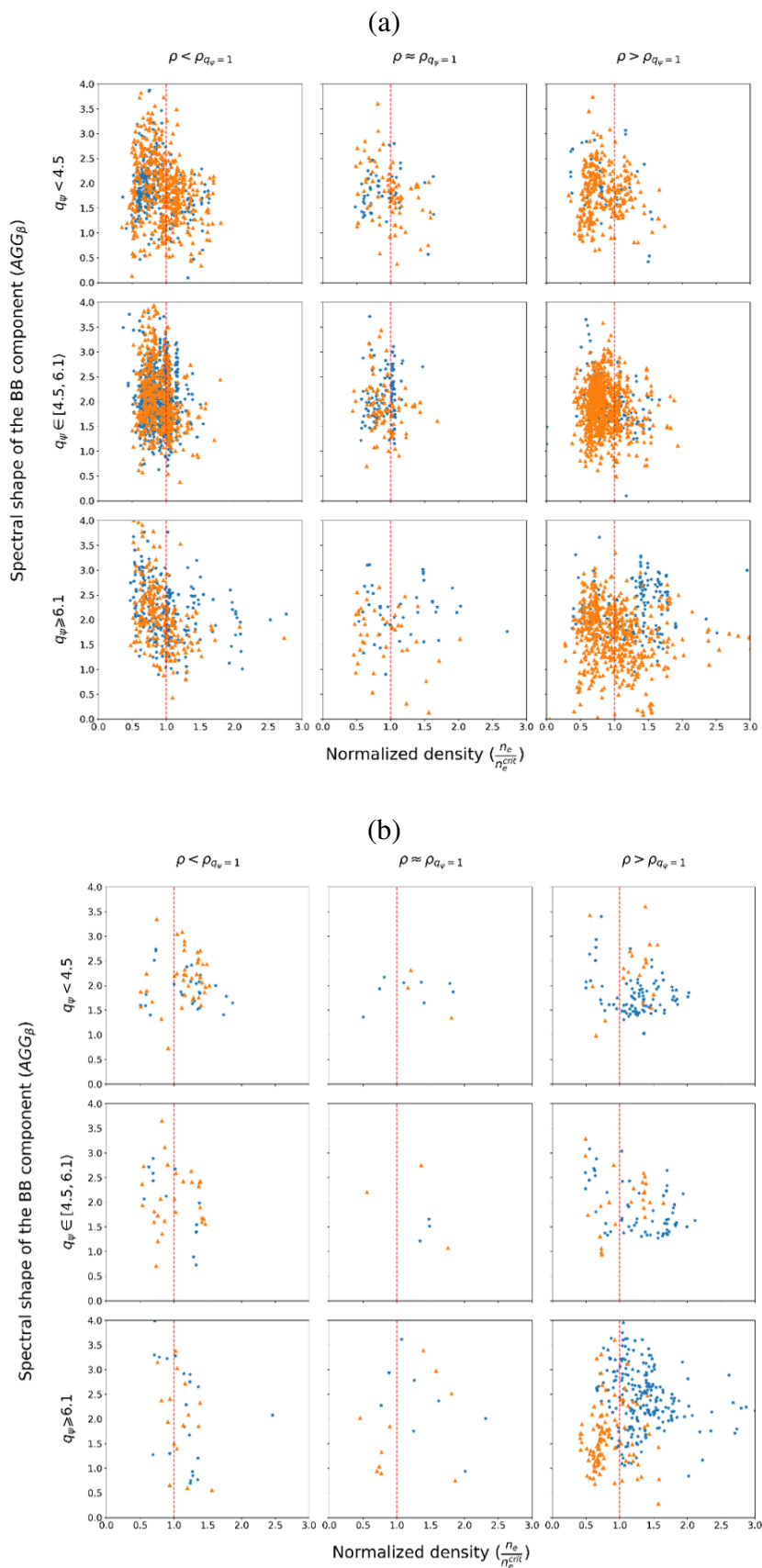


Fig. 6.12 Spectral shape ( $\beta$ ) of the BB component over the electron density. Orange for HFS and blue for LFS. (a) Tore Supra and (b) WEST Tokamak.

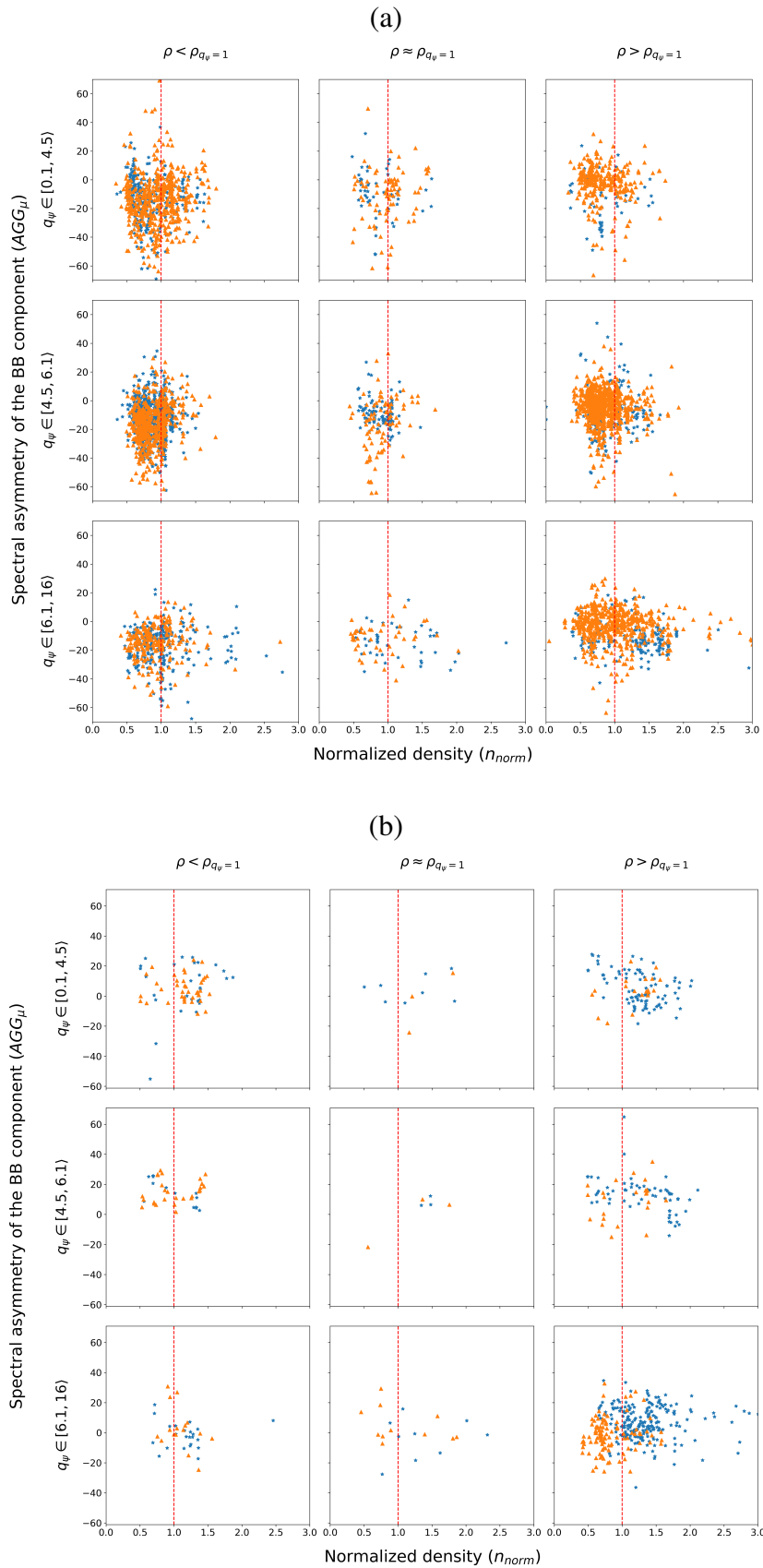


Fig. 6.13 Spectral asymmetry ( $\mu$ ) of the BB component over the electron density. Orange for HFS and blue for LFS. (a)Tore Supra and (b)WEST Tokamak.

Moreover, the energy content in the BB component ( $BB(t)$ ) is normalised to the energy of the initial signal ( $R(t)$ ) for comparison between different spectra.

$$\begin{aligned} E_{BB} &= \sum \text{Welch}(BB(t))_f, f \in \overline{BBinterval} \\ E_R &= \sum \text{Welch}(R(t))_f \end{aligned} \tag{6.4}$$

For WEST and Tore Supra, in  $\rho < \rho_{q=1}$ ,  $\frac{E_{BB}}{E_R}$  is quite low in the LOC sub-regime ( $\frac{E_{BB}}{E_R}$  values are lower in the HFS compared to the LFS), as  $\frac{E_{BB}}{E_R}$  moves to the SOC sub-regime, its values become higher. In  $\rho > \rho_{q=1}$ , for both HFS and LFS, the values of  $\frac{E_{BB}}{E_R}$  cover a wide range of values, for the LOC sub-regime, the values of  $\frac{E_{BB}}{E_R}$  are moderate and once it crosses the LOC-SOC transition, the  $\frac{E_{BB}}{E_R}$  is spread all around and tends to be high [see figure 6.14].

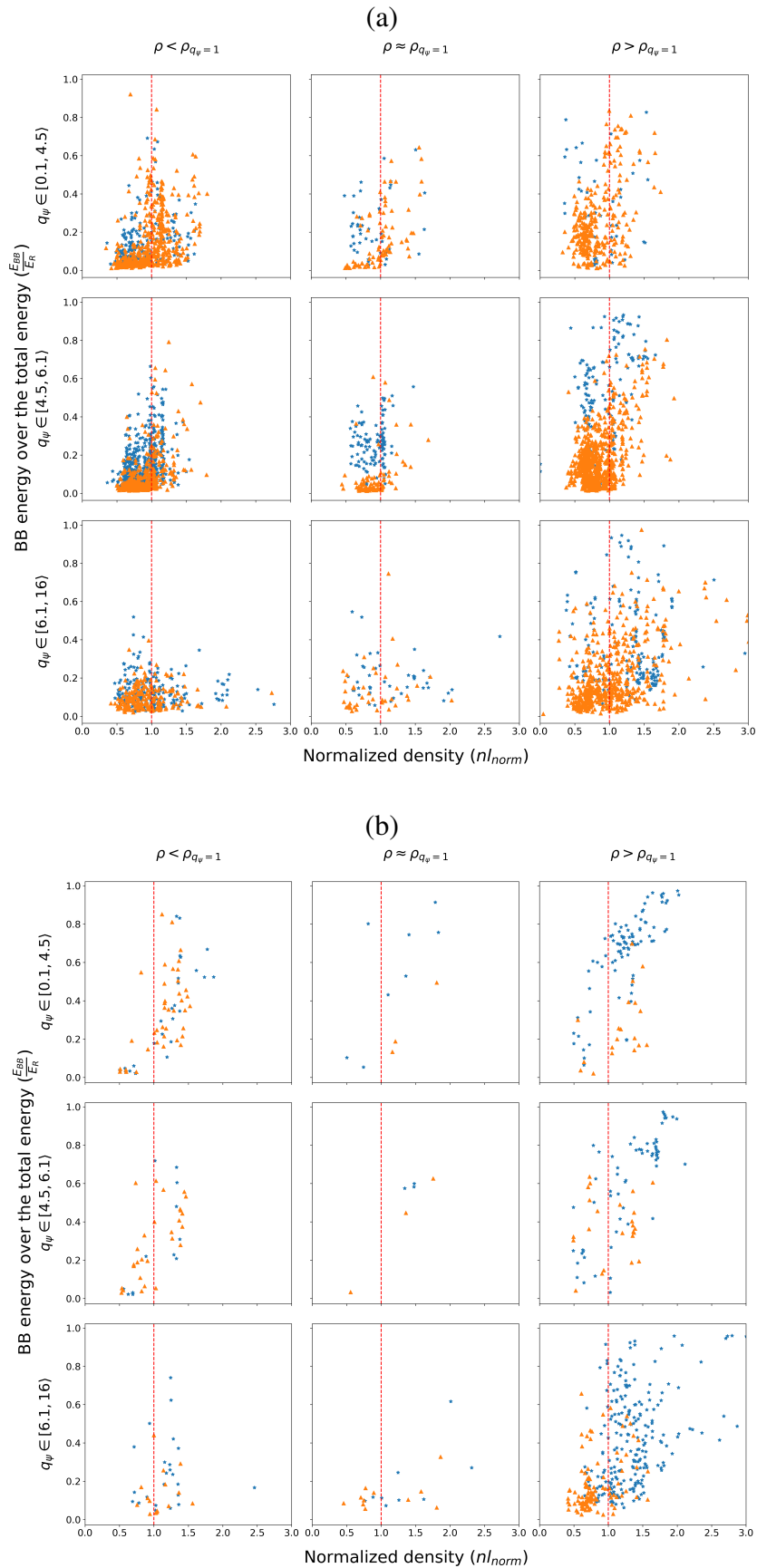


Fig. 6.14 BB component energy over the total energy of the signal ( $R(t)$ ) as a function of the density normalized. Orange is for HFS and blue for LFS. (a) Tore Supra and (b) WEST tokamak.

### 6.2.3 Energy content in the LF component at different $\rho$ and $q$

The energy content in the LF component is defined as  $E_{LF} = \sum Welch(LF(t))_f, f \in LFinterval$ .

The energy content in the LF component ( $LF(t)$ ) is normalised to the energy of the initial signal ( $R(t)$ ), as defined in the equation 6.4, for comparison between different spectra.

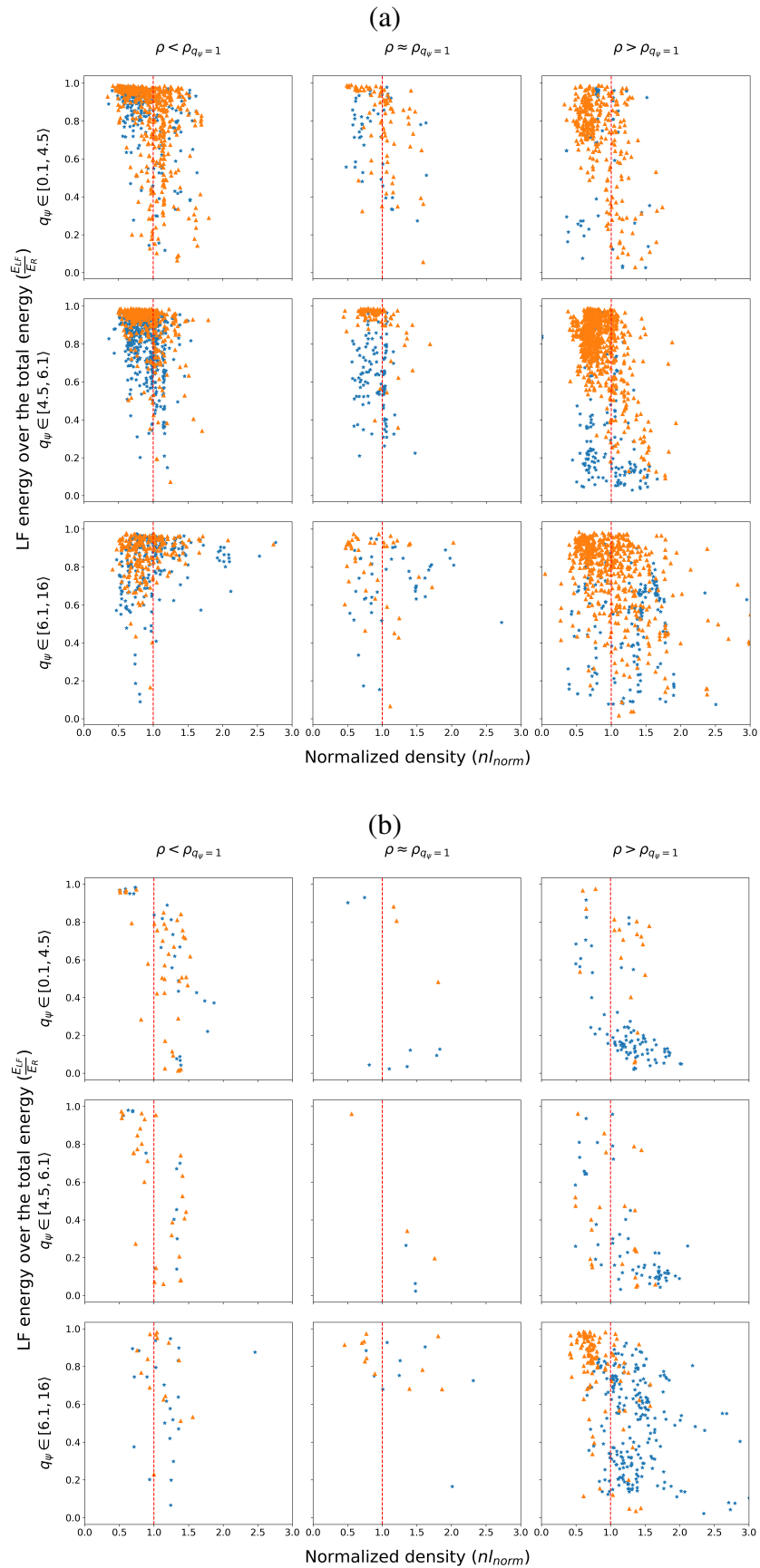


Fig. 6.15 LF component energy as a function of the electron density normalized Rice. Orange is for HFS and blue for LFS. (a)Tore Supra and (b)WEST tokamak.

$\frac{E_{LF}}{E_R}$  is widespread for Tore Supra and WEST, especially for  $\rho < \rho_{q=1}$  for both sub-regimes in the HFS and LFS. This behaviour becomes more widespread towards  $\rho > \rho_{q=1}$ . This raises the question whether the LF component could interact with the QC modes due to its high energy content.

In spite of the systematic study in which different trends have become apparent. It is relevant to look at the dynamics of the QC modes, in particular the energy exchange, as highlighted in the subsection 2.5.1.

## 6.3 Dynamics of QC modes and energy exchange with other components

The algorithm described in Chapter 5 allows the extraction of the different spectral components and then gives access to the temporal representation of each of them. In order to evaluate whether there is an interaction between the QC modes and the other spectral component, it is necessary to develop an algorithm based on the CWT, since it provides time and scale (frequency) information on the time evolution for all signal components. This algorithm would also allow the energy exchange to be investigated.

### 6.3.1 Algorithm for the study of energy exchange

The algorithm takes as input, on the one hand, the initial signal and its previously calculated spectral components ( $R(t)$ ,  $QC(t)$ ,  $BB(t)$ ,  $LF(t)$ ,  $Noise$ ) and, on the other hand, a range of scales in the CWT over which the energy exchange is studied. For the scale range, the minimum scale corresponds to the Nyquist frequency (maximum frequency and calculated based on frequency sampling) and the maximum scale (minimum frequency) is set as input. In the present work, the minimum frequency is set to  $1kHz$ .

Firstly, as the QC modes are the focus of the algorithm, the CWT scales associated with the QC modes are required. These scales are found by converting their QC mode frequency interval:  $scale_{QC} = \frac{6f_s}{2\pi frequency_{QC}}$ , where  $f_s$  is the frequency sampling. These scales contain the QC modes, but also part of the BB component and part of the noise.

The next step is to find a way to represent the dynamics of the QC modes, i.e. to separate the QC modes from the BB component and the noise, in other words to find a threshold that separates the CWT coefficients belonging to the QC modes from those belonging to the other components.

Thus, using the entire database, a subset of QC modes characterised by high amplitude ( $QC_{HA}$ ) is targeted to take advantage of their high energy density:

$$\frac{|CWT_{QC_{HA}}(s,t)|^2}{s^2} \quad (6.5)$$

Where,  $s$  corresponds to the CWT scales. These values are then projected into a one-dimensional vector in which the K-medians algorithm is then used to delineate the QC modes, the BB component and the noise.

$$\text{K-medians}\left(\frac{|CWT_{QC_{HA}}(s,t)|^2}{s^2}, 3\right) \quad (6.6)$$

In this clustering, the cluster associated with the QC modes is positioned at the highest values, followed by the cluster representing the BB component part and finally the cluster corresponding to the noise part. The limits QC modes - BB component and BB component - noise are then calculated. The threshold QC modes - BB component corresponding to the minimum normalised energy density (ED) of the QC modes derived from the previous clustering is:  $Threshold_{CWT_{QC(t)}} \approx Q_{0.8}(ED_{QC})$ , where  $Q_{0.8}(ED_{QC})$  corresponds to the 0.8 quantile of the energy density of the QC modes ( $ED_{QC} = \frac{|CWT_{QC}(s,t)|^2}{scale_{QC}^2}$ ). Note that this 0.8 quantile of the energy density represents the only dominant component capable of transferring energy to another mode in the associated scales.

The reason for using the energy density quantity is its ability to normalise information to the appropriate scale, thereby revealing the energy distribution within the time-frequency domain. The hypothesis is that once a sufficient energy level is reached in the CWT spectrum (i.e. the QC mode threshold), the energy density determined by the QC modes becomes a useful metric. This allows one to determine the CWT coefficients of the initial signal ( $CWT_{R(t)}$ ), which can potentially interact with the CWT coefficients of the QC modes  $CWT_{QC(t)}$ :

$$\frac{|CWT_{R(t)}(s,t)|^2}{s^2} \geq Threshold_{CWT_{QC(t)}} \quad (6.7)$$

Finally, the mode potentially interacting with the QC modes can be visualized as shown in the figure 6.16(a) for its negative frequencies.

Furthermore, to study the temporal evolution of the energy for the QC modes ( $E^{QC}$ ) and the mode in interaction ( $E^m$ ), the energy density ( $\frac{|CWT(s,t)|^2}{s^2}$ ) is integrated across scales for each  $t_0$  as follows:

$$E^{QC,m}(t_0) = \int_{s_1}^{s_2} \frac{|CWT_{R(t)}(s,t_0)|^2}{s^2} ds \quad (6.8)$$

Then, a normalization by its total energy ( $E_{tot}^{QC,m}$ ) is performed:

$$E_{norm}^{QC,m}(t_0) = \frac{E^{QC,m}(t_0)}{E_{tot}^{QC,m}} \quad (6.9)$$

Having  $E_{norm}^{QC,m}(t_0)$  and taking into account the intermittency over time, the next step is to estimate the energy evolution over time for the QC modes and the mode in interaction.

In addition, the normalised energy evolution of the BB component is also calculated as  $E_{norm}^{BB}(t_0) = \frac{|BB(t_0)|^2}{E_{tot}^{BB}}$ , where  $E_{tot}^{BB}$  is the total energy of the BB component.

The algorithm then allows access to the energy evolution of the QC modes, the mode in interaction (if it exists) and the BB component. A normalised energy evolution of all these components can then be plotted as shown in the figure 6.16.

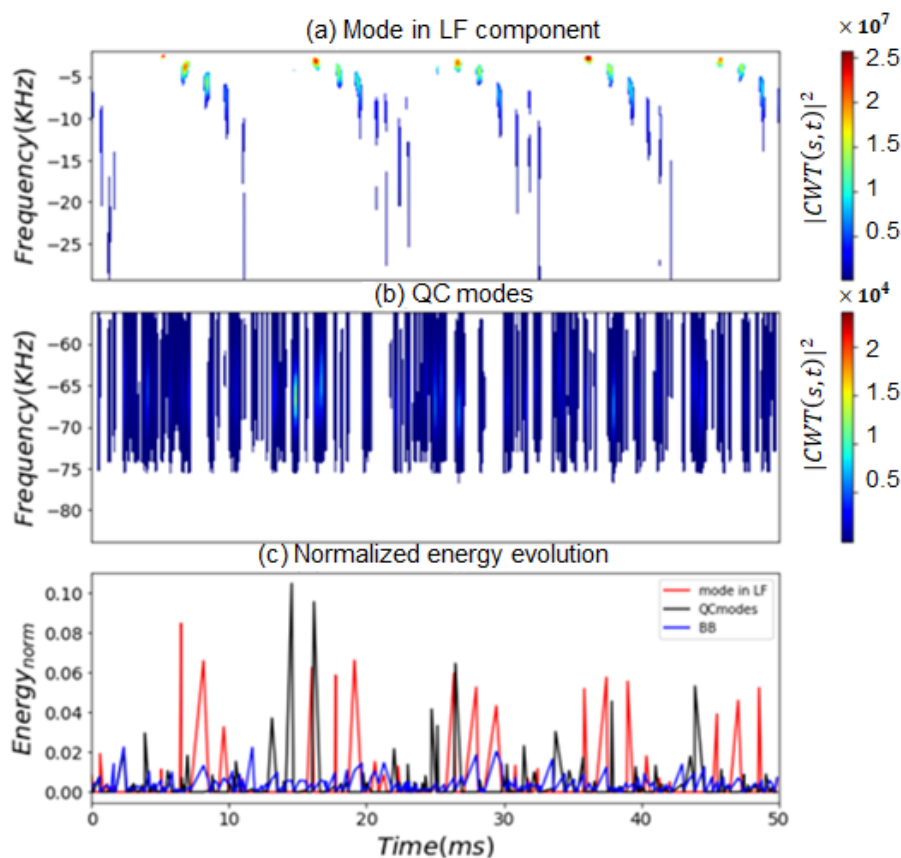


Fig. 6.16 The QC modes (b) and the LF component (a), potentially interacting, are represented by their energy ( $|CWT(s,t)|^2$ ). In (c) their normalised energy evolution for the LF, BB and QC modes. For a signal belonging to the discharge #38438 with  $I_p = 0.6MA$  and  $n_e = 2.2 \times 10^{19}m^{-3}$  and  $\rho = 0.02$ .

### 6.3.2 Tracking of QC modes' intrinsic spectral bandwidth over time

Having extracted the QC modes and the mode interacting with them ( $m$ ), the next step is to track their intrinsic spectral bandwidth (ISB) over time as follows:

$$ISB(t_0) = (\max freq^{QC,m}(t_0), \min freq^{QC,m}(t_0)) \quad (6.10)$$

This requires translating the information from the scale-time domain to the frequency-time domain according to the reallocation analysis described in 4.2.4.

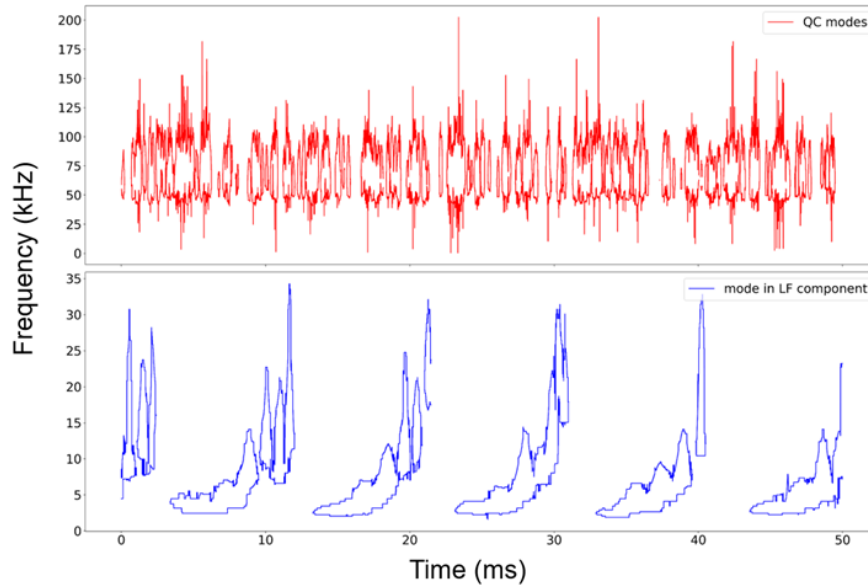


Fig. 6.17 Intrinsic spectral bandwidth ( $ISB$ ) across time for the QC modes and the mode in LF. For a signal belonging to the discharge #38438 with  $I_p = 0.6MA$  and  $n_e = 2.2 \times 10^{19}m^{-3}$  and  $\rho = 0.02$ .

Using the same signal as in figure 6.16, the ISB is calculated and shown in figure 6.17. The ISB of the LF component increases during the time intervals when there is a potential interaction between the QC modes and the mode in the LF component, after which the ISB narrows again. The ISB of the QC modes remains intermittent over time.

Given the range of QC mode classes, the identification of a common underlying physics requires a deeper exploration of the energy exchange. Indeed, the consideration of different interactions, based on the identification of a cause or source of energy exchange within the plasma core, is crucial for the control of a steady state.

### 6.3.3 Evidence of energy exchange between components using causality

For a deeper understanding of the dynamics of the QC modes, it is necessary to examine their causal relationship using the concept of transfer entropy as explained in the subsection 4.2.5. As seen earlier, modes in the LF component are seen to give energy to the QC modes.

The amplitudes,  $|QC_t|$  and  $|mt|$  (mode in interaction), are the relevant parameters for examining causality, since it is the effect of the LF mode on the QC modes that is being evaluated, not timing or synchronisation.

Since transfer entropy (TE) requires discretisation of the signal. Appropriate bins are determined to represent different signal levels according to their quantiles.

Once the signals are discretised, the entropy transfer from the signal  $|modeLF_t|$  to the signal  $|QC_t|$  is evaluated according to the equation 4.15. At each instant, local information is evaluated to follow the evolving uncertainties [see figure 6.18].

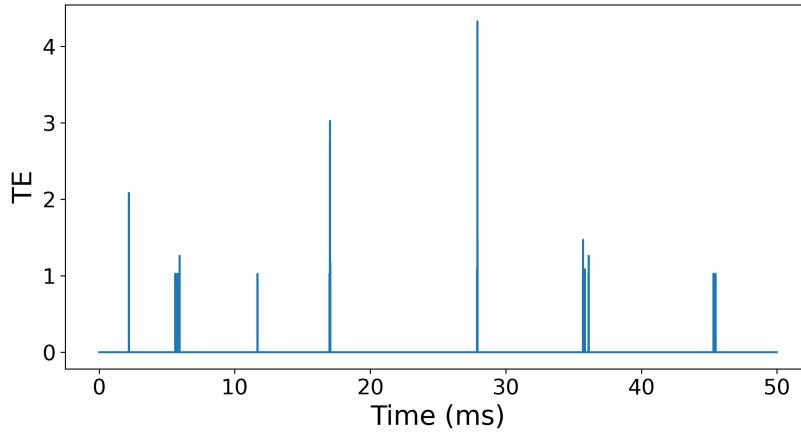


Fig. 6.18 Transfer Entropy across time between the QC modes and the mode in the LF component.  $I_p = 0.6MA$  and  $n_e = 2.2 \times 10^{19}m^{-3}$  and  $\rho = 0.02$

### 6.3.4 QC modes in interaction with sawtooth

As shown in the figure 6.16, most of the modes interacting with the QC modes are found in the LF component. In this case, the scenario of QC mode-sawtooth interaction is highlighted. As detailed in subsection 2, the sawtooth instability is a magnetohydrodynamic (MHD) type, potentially developing near the  $q=1$  surface. The parameters for the scanned position are  $\rho = 0.02$ ,  $I_p = 0.6MA$  and  $n_l = 2.2 \times 10^{19}m^{-3}$ . The frequency shift is particularly noticeable, shifting about 1kHz towards -25kHz with each sawtooth crash.

During the evolution of the energy, a decrease in the energy of the LF component of the mode is observed some time after the QC modes begin to grow up. A notable observation is the consistent increase in total energy in the BB with each appearance of QC modes.

This plasma scenario reveals a causality cascade: from the LF component to the QC modes and then from the QC modes to the BB component, providing a complex view of the interactions between the components and the energy dynamics within the plasma environment.

It provides a possible causal link between the MHD instabilities and the turbulence.

### **6.3.5 Dynamics across different magnetic configurations**

The previous energy exchange algorithm is used to study the dynamics of QC modes in different magnetic configurations (limiter, divertor and island divertor). As explained earlier, the importance of the energy exchange study lies in the fact that it could allow the identification of the mechanism behind the turbulent transport.

Thus, if a mechanism underlies a class of QC modes, the QC modes belonging to a class should have a similar energy exchange signature and also a consistent causal relationship with other spectral components. In other words, two relationships are considered: the QC modes that show a causal relationship from the LF component, since it was observed that a mode in the LF component could generate the QC modes, and secondly, the QC modes that show a causal relationship to the BB component, since it was highlighted in the previous signal that some QC modes can feed the microturbulence.

Signals from each database showing this causality cascade relationship will be retained for further analysis to determine whether similar dynamics are indeed at play and whether a congruent mechanism ultimately drives this plasma scenario.

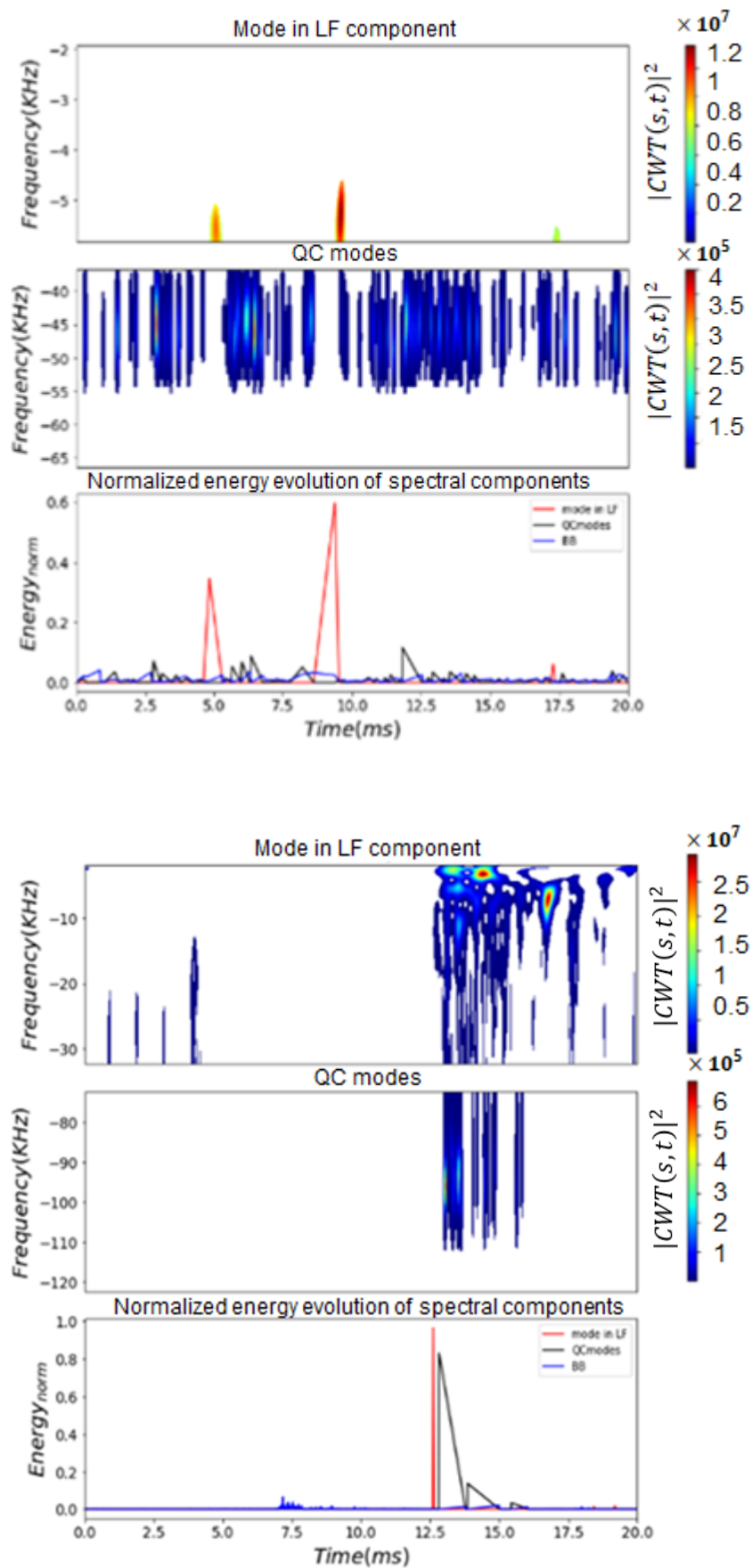


Fig. 6.19 Interaction of QC modes possessing causality cascade in Tore Supra,  $I_p = 0.7MA$ ,  $n_e = 1.17 \times 10^{19}m^{-3}$  and  $\rho = -0.22$ , and WEST tokamaks,  $I_p = 0.5MA$ ,  $n_e = 2.13 \times 10^{19}m^{-3}$  and  $\rho = -0.19$ .

The transfer entropy analysis for Tore Supra and WEST estimates the interval in which information is transferred from the LF component to the QC modes. For Tore Supra, this interval is narrower than for WEST, indicating less uncertainty. TE also shows the transferred information from the QC modes to the BB component.

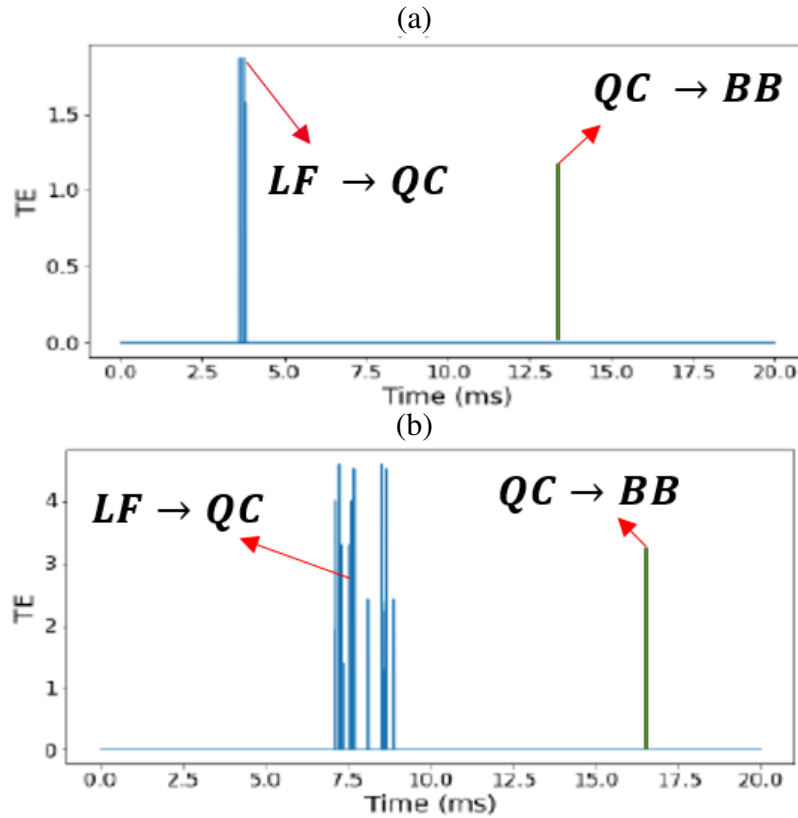


Fig. 6.20 Transfer entropy from the LF component to the QC modes (blue curve) and also from the QC modes to the BB component (green curve) for (a) Tore Supra,  $I_p = 0.7MA$ ,  $n_e = 1.17 \times 10^{19}m^{-3}$  and  $\rho = -0.22$ , and (b) WEST tokamaks,  $I_p = 0.5MA$ ,  $n_e = 2.13 \times 10^{19}m^{-3}$  and  $\rho = -0.19$ .

In Tore Supra, the LF component gives energy to the QC modes, then the QC modes grow progressively. Then the total energy of the broadband component increases. In WEST, the mode in the LF component seems to give energy to the QC modes through a cascade process, the QC modes quickly increase their energy and then it decreases progressively to finally excite the BB component [see figure 6.19].

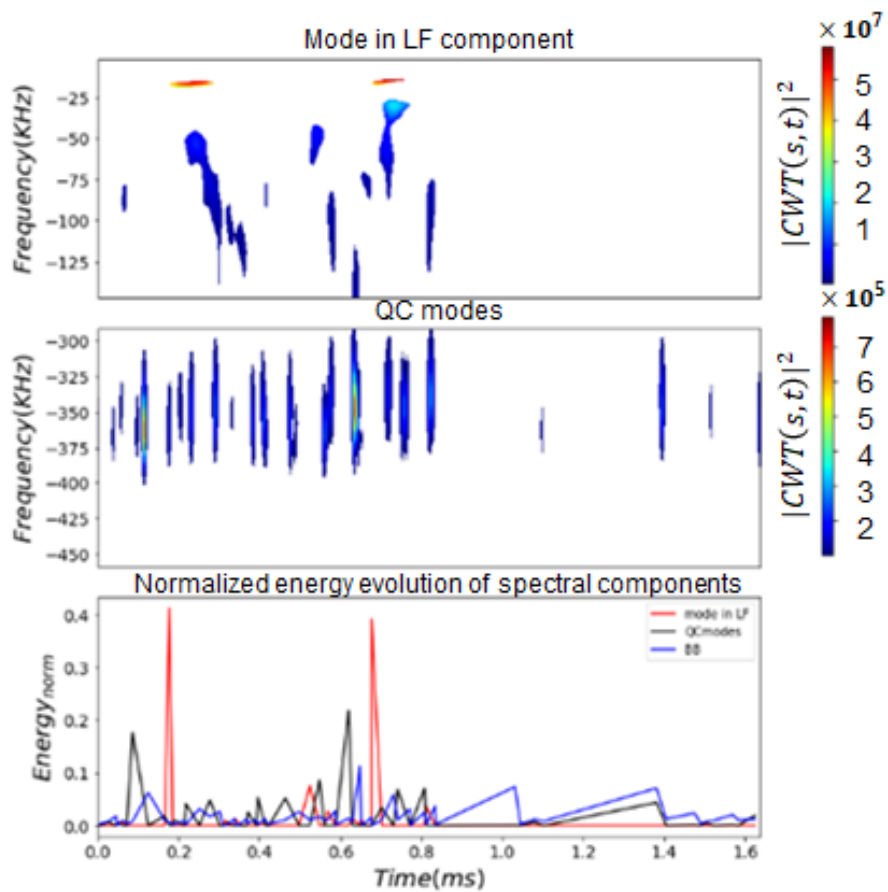


Fig. 6.21 QC modes dynamics in island divertor configuration for causality cascade relationship.  $P = 0.8MW$ ,  $n_e = 5 \times 10^{19}m^{-3}$  and standard configuration. Shot 230216020PCR (W7X).

In W7X, the LF component shifts up in frequency to give energy to the QC modes, and this latter excites the BB component [see figure 6.21].

The transfer entropy analysis in W7X shows the information going from the LF component to the QC modes at different times, this coincides with the transferred energy, which is highlighted in the figure 6.21.

However, a more detailed analysis is required to establish a correlation between this transfer energy (exchange energy algorithm), the transfer entropy and, most importantly, the time gradients, so that the link between the two can be established, as in the case of the QC mode sawtooth instability.

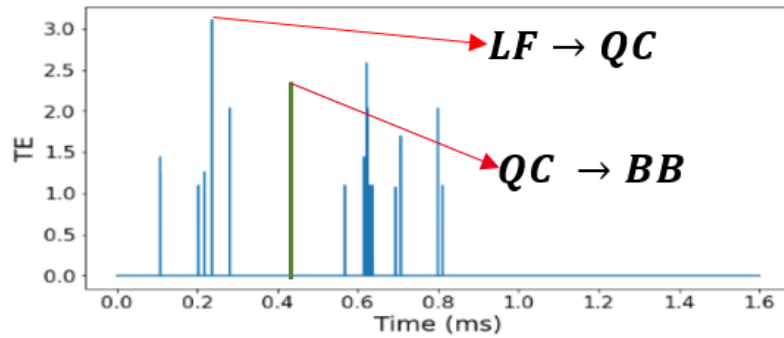


Fig. 6.22 Transfer entropy from the LF component to the QC modes (blue curve) and also from the QC modes to the BB component (green curve) for  $P = 0.8MW$ ,  $n_e = 5 \times 10^{19}m^{-3}$  and standard configuration. Shot 230216020PCR (W7X).

## 6.4 QC modes characteristics in ECRH plasmas

To further investigate the mechanism behind the QC mode classes, ECRH is analysed for different powers, in fact ECRH has been widely used to destabilise TEM in core tokamak plasmas [133]. The focus is on the study of the probability of occurrence of QC modes.

As shown in the figure 6.24, the QC modes can be excited by ECRH and then have a high amplitude, however, as shown in the figure 6.23, both Tore Supra and W7X show a decrease in the probability of occurrence of the QC modes as the heating power increases. This could be related to the detrapping particle rate.

This investigation could serve to elucidate the correlation between the trapped particle rate or the detrapping particle rate and the emergence of QC modes, focusing on the changes in their behaviour with power levels.

## 6.5 Are QC modes properties and dynamics driven by universal mechanism?

As mentioned earlier, there is a class of QC modes that have a higher probability of occurrence in the LOC regime and are susceptible to behaviour changes due to collisionality, potentially changing to BB-like behaviour. However, other classes of QC modes were also found, particularly in the SOC sub-regime, manifesting mainly in the LFS but also in the HFS with a lower probability value. In addition, other "sub-classes" of QC modes are observed, probably related to specific mechanisms, such as the one exhibiting LFQC and HFQC modes.

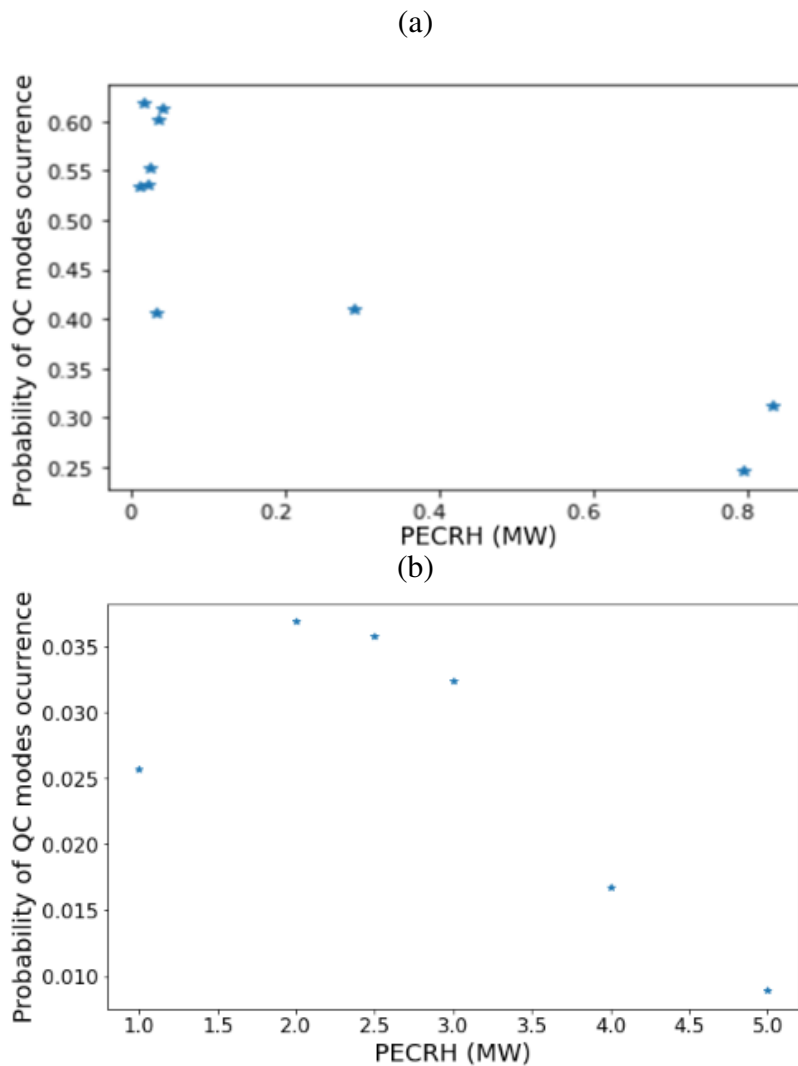


Fig. 6.23 Probability of occurrence of QC modes as a function of ECRH power (MW) for the Tore Supra tokamak(a) and the W7X stellarator, low-mirror configuration(b).

The predominance in the LFS compared to the HFS, may be due from the intrinsic problem of reflectometry itself, the non-local response to the spiral structures of fluctuations due to strong magnetic shear in the high-field side [134].

Other spectral components have also been studied, the main characteristics being the shape tending towards Gaussian and the high energy in the LF component. This led to the study of the dynamics, where frequency shifts and intermittency emerged as notable features during this investigation.

Experiments carried out in Tore Supra, WEST and W7-X showed similar patterns of behaviour based on the causality cascade concept. Correlations with ECRH may indicate a direct link with the detrapping particle rate, shedding light on a possible universal mechanism

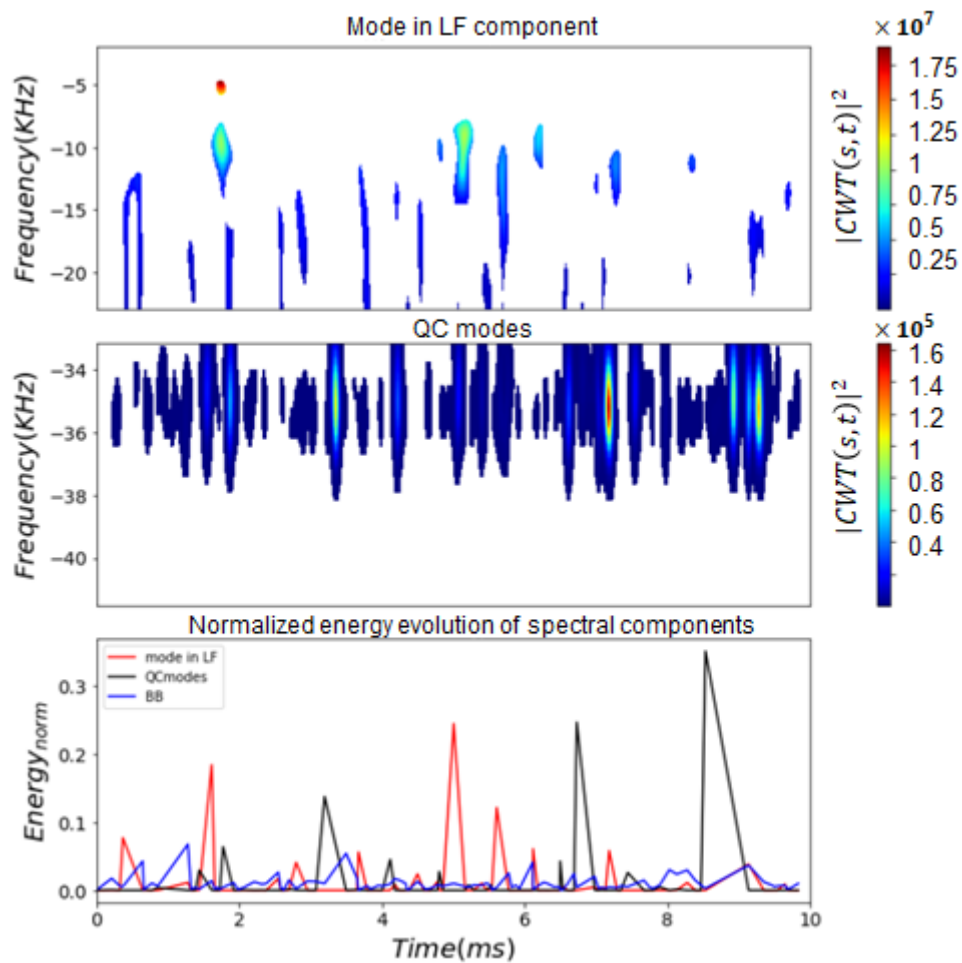


Fig. 6.24 Example of QC modes dynamics during ECRH phase.

of these modes. The discovery of consistent mechanisms across classes of QC modes would improve our understanding of turbulent transport. Indeed, the characterisation of the properties and dynamics of QC modes represents a first step towards the concept of a universal mechanism.



# Chapter 7

## Conclusion & Perspectives

### Contents

---

<b>7.1 Conclusion</b>	<b>139</b>
<b>7.2 Perspectives</b>	<b>141</b>
7.2.1 QC mode excitation and stabilisation	141
7.2.2 Classes of QC Modes and extension to MHD modes	142
7.2.3 Further developments to improve the energy exchange studies	143
7.2.4 Other applications of our algorithms	144

---

### 7.1 Conclusion

The aim of this thesis was to make a contribution to the understanding of the turbulent transport in the core of magnetically confined plasmas. Turbulent transport arises from electrostatic turbulence ( $\tilde{\phi}$ ), with two instabilities, the ion temperature gradient (ITG) and the trapped electron modes (TEM), dominant at low wave numbers  $k$ . Distinguishing them from experimental measurements of density fluctuations and identifying their interplay with other instabilities would allow a better understanding of turbulent transport.

Algorithms have been developed to extract the different spectral components (low frequency component, broadband component, QC modes and noise) from fixed frequency conventional reflectometry (CFR). These algorithms integrate signal processing and machine learning in an intelligent way (without ad hoc constraints), preserving the statistical and physical properties of each extracted component. It is important to note that this data processing

method is able to perform spectral decomposition of signals or time series from other sources such as electroencephalogram (EEG) and interferometry.

The ohmic confinement regimes have been studied because of the clear link between instability and confinement regime: in the Linear Ohmic Confinement (LOC) sub-regime, TEM seems to dominate, whereas in the Saturated Ohmic Confinement (SOC) sub-regime, ITG becomes dominant, inducing then distinct turbulent transport behaviours. Furthermore, Quasi-Coherent (QC) modes emerged as a potential signature of TEM in the reflectometry frequency spectrum: they are observed in LOC and disappear at the LOC-SOC transition.

It was first verified on TEXTOR and Tore Supra data that the extracted QC modes component retains its coherence and physical properties. The algorithm was then used to perform a statistical study of the QC modes in two magnetic configurations: Tore Supra (limiter) and WEST (divertor). A probability map of occurrence was constructed for both tokamaks, highlighting a 'class' of QC modes in the LOC sub-regime in the LFS with a probability of 0.7 and 0.6 respectively, and in the HFS with a probability of 0.4 and 0.3. In addition, a ratio of the energy content in the QC modes to the energy content in the broadband component showed a predominance of the QC modes as they approached the LOC-SOC transition, after which the energy of the QC modes started to decrease, showing a more abrupt behaviour in the LFS.

Looking deeper into the LOC-SOC transition, the probability of occurrence of the QC modes for both tokamaks in the LFS showed approximately the same probability of the QC modes for  $\rho < \rho_{q=1}$  and  $\rho > \rho_{q=1}$ , with many fluctuations of the probability during the LOC-SOC transition. Around the  $q=1$  surface ( $\rho \approx \rho_{q=1}$ ), the small number of events did not allow to obtain significant results. In the HFS, however, the QC modes were more likely to appear inside the  $q=1$  surface ( $\rho < \rho_{q=1}$ ) than outside ( $\rho > \rho_{q=1}$ ). These results strengthened the link between the QC mode and TEM instabilities in the ohmic regime: QC was overwhelmingly observed on the LFS below the LOC-SOC threshold, as expected for a mode similar to a ballooning instability excited by trapped electrons.

The remaining QC modes were found in the SOC sub-regime in 2 classes, one at low current and another at high current. The examined quantities: ratio (spectral band with above the spectral centroid) and multifractal spectrum showed differences with the class of QC modes in the LOC sub-regime, but the information content was too low to discriminate them.

The evolution of other spectral components was also systematically studied, such as the high energy content in the LF and the Gaussian tendency of the broadband component related to microturbulence. No discriminating information between classes was obtained from these analyses.

To go further in the analysis of these different QC mode classes and sub-classes, the time evolution of the energy exchange between time scales was introduced for the first time, i.e. the dynamics of the energy exchange between the LF component and the QC mode components. The dynamics between other components have also been carried out, in particular between QC mode components and the BB component.

Different signatures of QC mode dynamics were observed in different QC mode classes, especially between the LOC class and the SOC class.

Among these different QC mode dynamics, an interaction with the QC modes and the sawtooth instability belonging to the LF component was observed and analysed, possibly giving a link between the electrical turbulence ( $\tilde{\phi}$ ) and the MHD instabilities ( $\tilde{B}$ ), the nature of the link between the QC modes and the MHD activities is still open. Indeed, the analysis performed using the transfer entropy shows a possible causality from the sawtooth to the QC modes.

To further investigate the link between the QC modes and the LF component, the multi-magnetic configuration study was extended to another magnetic configuration, the W7X stellarator. It showed a similar signature of QC mode dynamics for QC modes being caused by the LF and provoking the BB component (bi-directional causality), all using the transfer entropy (TE) concept. This study may reveal a universal underlying mechanism. The poloidal velocity study by Kramer-Flecken [135] on Tore Supra and W7X goes in the same direction.

Bi-directional causality using TE allows a selection of signals from the whole database for deeper studies on universal mechanisms, possibly energy exchange between turbulence sources, etc.

## 7.2 Perspectives

### 7.2.1 QC mode excitation and stabilisation

Understanding the relationship between QC modes and TEM, and considering that TEMs are triggered by trapped electron modes, it follows that any detrapping mechanism, including collisions, turbulence-induced additional diffusion, changes in energy states caused by RF heating waves, and the like, could potentially lead to a reduction in TEM excitation and consequently a reduction in QC mode amplitude.

Furthermore, the evolution of global parameters such as temperature gradients during the sawtooth period can potentially influence the source of the TEM excitation, as shown in part. In the LOC sub-regime, the link between QC modes in the plasma core and TEM is clear. In other scenarios, however, questions arise about the mechanisms responsible for QC

mode generation. To answer these questions, it is essential to investigate factors such as the fraction of trapped particles and the detrapping rates. To investigate QC mode generation, studies can be carried out on variables such as the electron cyclotron heating power, changes in the magnetic configurations that affect the trapped particle fraction, and adjustments in the collision rates that affect the detrapping rates.

Turbulence simulations could also be performed to better understand the origin and disappearance of the QC mode. Gyrokinetic simulations of ohmic discharges at different densities could be performed to investigate the behaviour of the QC mode across the LOC-SOC transition. Coupled with a reflectometry synthetic diagnostic, the experimental data and the relative amplitude and bandwidth of the QC mode could be compared with the experimental data. Increasing the TEM driving term would also help to answer the question of what happens to the QC modes in a highly turbulent regime: do they disappear because of the increase in the BB level, or do they disappear because of the loss of coherence between the TEM micro-instabilities?

### 7.2.2 Classes of QC Modes and extension to MHD modes

In this thesis, three classes of QC modes were identified whose properties and dynamics revealed differences between them, but sub-classes were also found that limited the discrimination.

Gyrokinetic simulations (gyro-Bohm normalised weights from CGYRO [136]) have identified four main sub-dominant TEM 'classes'. In fact, there is likely to be a mixture of dominant and sub-dominant TEMs and ITG modes in both the LOC and SOC sub-regimes [22, 137, 138].

Further work would need to take into account the interplay between ITG and TEM in a multi-scale approach, while also considering sub-dominant modes.

Analysing the dynamics of the QC modes through the evolution of the intrinsic spectral bandwidth (ISB), as performed in the QC mode-sawtooth interaction, can provide a signature of this interplay. After obtaining characteristics of this ISB for each QC mode, such as statistical moments, a systematic analysis could be performed.

Moreover, as seen in this thesis, three thresholds (the averaged energy density, the symmetry and the spread) have been tuned using QC modes with high and low amplitude for their extraction. The algorithm could use the concept of threshold learning, from the output of discriminating classes of QC modes using ISB characteristics, the algorithm could learn each threshold QC mode class in a loop-like manner. The algorithm could also be extended to extract narrow-band components such as MHD modes. The development required to automatically extract each new component (averaged energy density, symmetry and spread)

could be accelerated by using an Extreme Learning Machine (ELM) neural network that can be rapidly trained on these different modes to classify them.

### 7.2.3 Further developments to improve the energy exchange studies

#### Governing equations

Since the signature of the QC modes is very diverse, it depends on the class to which they belong and on the plasma conditions. It would be helpful to discover the governing equations of these dynamics. In the course of this thesis, two previous different levels of discovering intrinsic relationships in signals have already been identified: learning statistical associations and deriving causal relationships from observations.

Once the different spectral components have been extracted, the next step would be to perform a dimensionality reduction in their temporal representation, using for example the concept of dictionary learning, where short-time signatures (wavelets, polynomial functions, etc.) are introduced into the 'dictionary' and the algorithm searches for the best sparse representation of the signal. The identification of nonlinear dynamics can then be performed using SINDy algorithms[139], in fact a recent study [140] combines Gaussian process regression, a non-parametric learning method, with SINDy (a parametric learning approach) to identify nonlinear dynamical systems from a Lotka-Volterra model.

#### Energy exchange in the micro-turbulence

The ultimate goal of this work was to unravel the intricate dynamics of the energy exchange within the different spectral components, with a particular focus on the BB component associated with micro-turbulence. The overall aim was to extract potential interactions between the identified turbulence sources, including ITG, TEM and ETG instabilities.

Remarkably, this investigation revealed connections between other spectral components, shedding more light on the dynamics of energy exchange. The method of mode decomposition played a key role, particularly in isolating the BB component, thereby constraining the possibilities of energy exchange within the microturbulence. Consequently, the study focused on unravelling the interplay between these instabilities and their intricate dynamics.

Indeed, the tools developed in the course of this thesis allow the automatic identification of signals with favourable characteristics, thus simplifying the process of selecting candidates for in-depth study. However, it's important to recognise that further analysis will be required to refine the criteria for identifying these 'good' signals.

The ultimate goal remains a comprehensive exploration of the intricate dynamics governing energy exchange within the BB component.

A key finding is that the dimensionality of signals such as the BB component signal can be artificially high, even when they appear to consist of thousands of features. In reality, these signals can often be expressed as functions of just a few underlying parameters. Therefore, the focus would be on finding a transformation of the signal that incorporates elements such as time and frequency information, and then highlighting these underlying parameters through an appropriate metric.

Once this metric is applied, manifold learning techniques come into play, attempting to uncover a low-dimensional manifold within the high-dimensional signal space. This approach aims to reduce complexity and establish links between the underlying parameters, as shown in Figure 7.1.

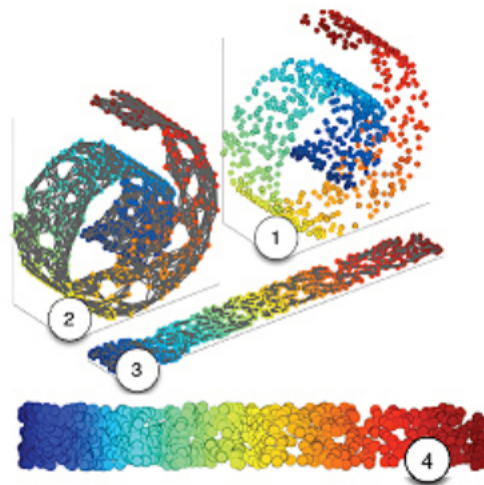


Fig. 7.1 Illustration of the manifold learning process from 1 to 4, where the different points are connected in a complex representation to finally show the intrinsic manifold.

#### 7.2.4 Other applications of our algorithms

The algorithms developed in this thesis can be applied to other turbulence measurements in plasmas (ECE, interferometry) and also to other fields such as brain activity analysis, heartbeat analysis, EEG, etc. Tests have already been carried out in the field of brain activity analysis, showing that it is fully feasible.

# References

- [1] M. Cooper, “Excessive speculation and oil price shock recessions: A case of wall street déjà vu all over again,” 2011.
- [2] L. Cozzi, T. Gould, S. Bouckart, D. Crow, T.-Y. Kim, C. McGlade, P. Olejarnik, B. Wanner, and D. Wetzel, “World energy outlook 2020,” *International Energy Agency: Paris, France*, pp. 1–461, 2020.
- [3] X. Garbet, “Introduction to turbulent transport in fusion plasmas,” *Comptes Rendus Physique*, vol. 7, no. 6, pp. 573–583, 2006.
- [4] S. Pfalzner, *An introduction to inertial confinement fusion*. CRC Press, 2006.
- [5] M. Edwards, P. Patel, J. Lindl, L. Atherton, S. Glenzer, S. Haan, J. Kilkenny, O. Landen, E. Moses, A. Nikroo, *et al.*, “Progress towards ignition on the national ignition facility,” *Physics of Plasmas*, vol. 20, no. 7, 2013.
- [6] N. Fleurot, C. Cavailler, and J. Bourgade, “The laser megajoule (lmj) project dedicated to inertial confinement fusion: Development and construction status,” *Fusion Engineering and design*, vol. 74, no. 1-4, pp. 147–154, 2005.
- [7] D. Escande, P. Martin, S. Ortolani, A. Buffa, P. Franz, L. Marrelli, E. Martines, G. Spizzo, S. Cappello, A. Murari, *et al.*, “Quasi-single-helicity reversed-field-pinch plasmas,” *Physical review letters*, vol. 85, no. 8, p. 1662, 2000.
- [8] C. Hidalgo, “Nuclear fusion as a solution to energy needsv.” <https://1dhx7rmv5f.execute-api.eu-west-1.amazonaws.com/generatepdf/generatepdf/?id=361838>.
- [9] A. Marinoni, O. Sauter, and S. Coda, “A brief history of negative triangularity tokamak plasmas,” *Reviews of Modern Plasma Physics*, vol. 5, no. 1, p. 6, 2021.
- [10] L. Spitzer Jr, “The stellarator concept,” *The Physics of Fluids*, vol. 1, no. 4, pp. 253–264, 1958.
- [11] C. Mercier, “Equilibrium and stability of a toroidal magnetohydrodynamic system in the neighbourhood of a magnetic axis,” *Nuclear Fusion*, vol. 4, no. 3, p. 213, 1964.
- [12] Y. Feng, M. Kobayashi, T. Lunt, and D. Reiter, “Comparison between stellarator and tokamak divertor transport,” *Plasma physics and controlled fusion*, vol. 53, no. 2, p. 024009, 2011.

- [13] T. S. Pedersen, R. König, M. Krychowiak, M. Jakubowski, J. Baldzuhn, S. Bozhenkov, G. Fuchert, A. Langenberg, H. Niemann, D. Zhang, *et al.*, “First results from divertor operation in wendelstein 7-x,” *Plasma Physics and Controlled Fusion*, vol. 61, no. 1, p. 014035, 2018.
- [14] Y. Xu, “A general comparison between tokamak and stellarator plasmas,” *Matter and Radiation at Extremes*, vol. 1, no. 4, pp. 192–200, 2016.
- [15] C. Nguyen, “Magneto-hydrodynamic activity and energetic particles-application to beta alfvén eigenmodes,” *arXiv preprint arXiv:0912.2613*, 2009.
- [16] J. Wesson and D. J. Campbell, *Tokamaks*, vol. 149. Oxford university press, 2011.
- [17] J. H. E. Proll, “Trapped-particle instabilities in quasi-isodynamic stellarators,” 2014.
- [18] F. F. Chen *et al.*, *Introduction to plasma physics and controlled fusion*, vol. 1. Springer, 1984.
- [19] E. Speth, “Neutral beam heating of fusion plasmas,” *Reports on Progress in Physics*, vol. 52, no. 1, p. 57, 1989.
- [20] J. Wilson, R. Parker, M. Bitter, P. Bonoli, C. Fiore, R. Harvey, K. Hill, A. Hubbard, J. Hughes, A. Ince-Cushman, *et al.*, “Lower hybrid heating and current drive on the alcator c-mod tokamak,” *Nuclear Fusion*, vol. 49, no. 11, p. 115015, 2009.
- [21] M. Gaudreau, A. Gondhalekar, M. Hughes, D. Overskei, D. t. Pappas, R. Parker, S. Wolfe, E. Apgar, H. Helava, I. Hutchinson, *et al.*, “High-density discharges in the alcator tokamak,” *Physical Review Letters*, vol. 39, no. 20, p. 1266, 1977.
- [22] J. Rice, J. Citrin, N. Cao, P. Diamond, M. Greenwald, and B. Grierson, “Understanding loc/soc phenomenology in tokamaks,” *Nuclear Fusion*, vol. 60, no. 10, p. 105001, 2020.
- [23] Y. Shimomura, N. Suzuki, M. Sugihara, T. Tsuda, K. Odajima, and T. Tsunematsu, “Empirical scaling of energy confinement time of l-mode and optimized mode and some consideration of reactor core plasma in tokamak,” tech. rep., Japan Atomic Energy Research Inst., 1987.
- [24] C. Angioni, A. Peeters, F. Ryter, F. Jenko, G. Conway, T. Dannert, H. Fahrbach, M. Reich, W. Suttrop, A. U. Team, *et al.*, “Relationship between density peaking, particle thermodiffusion, ohmic confinement, and microinstabilities in asdex upgrade l-mode plasmas,” *Physics of plasmas*, vol. 12, no. 4, 2005.
- [25] G. Conway, C. Angioni, R. Dux, F. Ryter, A. Peeters, J. Schirmer, C. Troester, A. U. Team, *et al.*, “Observations on core turbulence transitions in asdex upgrade using doppler reflectometry,” *Nuclear fusion*, vol. 46, no. 9, p. S799, 2006.
- [26] J. Rice, C. Gao, M. Reinke, P. Diamond, N. Howard, H. Sun, I. Cziegler, A. Hubbard, Y. Podpaly, W. Rowan, *et al.*, “Non-local heat transport, rotation reversals and up/down impurity density asymmetries in alcator c-mod ohmic l-mode plasmas,” *Nuclear Fusion*, vol. 53, no. 3, p. 033004, 2013.

- [27] I. Erofeev, E. Fable, C. Angioni, R. McDermott, A. U. Team, *et al.*, “Theory-based modeling of loc–soc transitions in asdex upgrade,” *Nuclear Fusion*, vol. 57, no. 12, p. 126067, 2017.
- [28] F. Romanelli, W. Tang, and R. White, “Anomalous thermal confinement in ohmically heated tokamaks,” *Nuclear fusion*, vol. 26, no. 11, p. 1515, 1986.
- [29] B. Grierson, C. Chrystal, S. Haskey, W. Wang, T. Rhodes, G. McKee, K. Barada, X. Yuan, M. Nave, A. Ashourvan, *et al.*, “Main-ion intrinsic toroidal rotation across the itg/tem boundary in diii-d discharges during ohmic and electron cyclotron heating,” *Physics of Plasmas*, vol. 26, no. 4, 2019.
- [30] P. Ennever, M. Porkolab, J. Candy, G. Staebler, M. Reinke, J. Rice, J. Rost, D. Ernst, C. Fiore, J. Hughes, *et al.*, “The effects of dilution on turbulence and transport in c-mod ohmic plasmas and comparisons with gyrokinetic simulations,” *Physics of Plasmas*, vol. 22, no. 7, 2015.
- [31] R. McDermott, C. Angioni, G. Conway, R. Dux, E. Fable, R. Fischer, T. Pütterich, F. Ryter, E. Viezzer, A. U. Team, *et al.*, “Core intrinsic rotation behaviour in asdex upgrade ohmic l-mode plasmas,” *Nuclear Fusion*, vol. 54, no. 4, p. 043009, 2014.
- [32] J. Rice, M. Greenwald, Y. Podpaly, M. Reinke, P. Diamond, J. Hughes, N. Howard, Y. Ma, I. Cziegler, B. Duval, *et al.*, “Ohmic energy confinement saturation and core toroidal rotation reversal in alcator c-mod plasmas,” *Physics of Plasmas*, vol. 19, no. 5, 2012.
- [33] H. Arnichand, R. Sabot, S. Hacquin, A. Krämer-Flecken, X. Garbet, J. Citrin, C. Bourdelle, G. Hornung, J. Bernardo, C. Bottereau, *et al.*, “Quasi-coherent modes and electron-driven turbulence,” *Nuclear Fusion*, vol. 54, no. 12, p. 123017, 2014.
- [34] L. Schmitz, L. Zeng, T. Rhodes, J. Hillesheim, E. Doyle, R. Groebner, W. Peebles, K. Burrell, and G. Wang, “Role of zonal flow predator-prey oscillations in triggering the transition to h-mode confinement,” *Physical review letters*, vol. 108, no. 15, p. 155002, 2012.
- [35] T. Tala, X. Garbet, *et al.*, “Physics of internal transport barriers,” *Comptes Rendus Physique*, vol. 7, no. 6, pp. 622–633, 2006.
- [36] L. Landau, “Theory of the superfluidity of helium ii,” *Physical Review*, vol. 60, no. 4, p. 356, 1941.
- [37] J. P. Freidberg, *Plasma physics and fusion energy*. Cambridge university press, 2008.
- [38] W. Horton, *Turbulent transport in magnetized plasmas*. World Scientific, 2012.
- [39] X. Garbet, P. Mantica, C. Angioni, E. Asp, Y. Baranov, C. Bourdelle, R. Budny, F. Crisanti, G. Cordey, L. Garzotti, *et al.*, “Physics of transport in tokamaks,” *Plasma Physics and Controlled Fusion*, vol. 46, no. 12B, p. B557, 2004.
- [40] C. Bourdelle, “Turbulent particle transport in magnetized fusion plasma,” *Plasma physics and controlled fusion*, vol. 47, no. 5A, p. A317, 2005.

- [41] X. Garbet, Y. Idomura, L. Villard, and T. Watanabe, “Gyrokinetic simulations of turbulent transport,” *Nuclear Fusion*, vol. 50, no. 4, p. 043002, 2010.
- [42] H. Mynick, “Transport optimization in stellarators,” *Physics of plasmas*, vol. 13, no. 5, 2006.
- [43] S. Moradi, J. Anderson, M. Romanelli, H.-T. Kim, X. Litaudon, S. Abduallev, M. Abhangi, P. Abreu, M. Afzal, K. Aggarwal, *et al.*, “Global scaling of the heat transport in fusion plasmas,” *Physical review research*, vol. 2, no. 1, p. 013027, 2020.
- [44] P. De Vries, K. M. Rantamäki, C. Giroud, E. Asp, G. Corrigan, A. Eriksson, M. De Greef, I. Jenkins, H. Knoop, P. Mantica, *et al.*, “Plasma rotation and momentum transport studies at jet,” *Plasma physics and controlled fusion*, vol. 48, no. 12, pp. 1693–1708, 2006.
- [45] G. Rewoldt, W. Tang, and R. Hastie, “Collisional effects on kinetic electromagnetic modes and associated quasilinear transport,” *The Physics of fluids*, vol. 30, no. 3, pp. 807–817, 1987.
- [46] F. Jenko, W. Dorland, M. Kotschenreuther, and B. Rogers, “Electron temperature gradient driven turbulence,” *Physics of plasmas*, vol. 7, no. 5, pp. 1904–1910, 2000.
- [47] W. Horton, J.-H. Kim, E. Asp, T. Hoang, T.-H. Watanabe, and H. Sugama, “Drift wave turbulence,” in *AIP Conference Proceedings*, vol. 1013, pp. 1–19, American Institute of Physics, 2008.
- [48] H. Chen and L. Chen, “How zonal flow affects trapped-electron-driven turbulence in tokamak plasmas,” *Physical Review Letters*, vol. 128, no. 2, p. 025003, 2022.
- [49] P. H. Diamond, S. Itoh, K. Itoh, and T. Hahm, “Zonal flows in plasma—a review,” *Plasma Physics and Controlled Fusion*, vol. 47, no. 5, p. R35, 2005.
- [50] K. Makwana, P. Terry, M. Pueschel, and D. Hatch, “Subdominant modes in zonal-flow-regulated turbulence,” *Physical Review Letters*, vol. 112, no. 9, p. 095002, 2014.
- [51] L. Chen, Z. Lin, and R. White, “Excitation of zonal flow by drift waves in toroidal plasmas,” *Physics of Plasmas*, vol. 7, no. 8, pp. 3129–3132, 2000.
- [52] J. Lang, Y. Chen, and S. E. Parker, “Gyrokinetic  $\delta f$  particle simulation of trapped electron mode driven turbulence,” *Physics of Plasmas*, vol. 14, no. 8, 2007.
- [53] E. Doyle, W. Houlberg, Y. Kamada, V. Mukhovatov, T. Osborne, A. Polevoi, G. Bateman, J. Connor, J. Cordey, T. Fujita, *et al.*, “Plasma confinement and transport,” *Nuclear Fusion*, vol. 47, no. 6, p. S18, 2007.
- [54] P. Guzdar, L. Chen, W. Tang, and P. Rutherford, “Ion-temperature-gradient instability in toroidal plasmas,” *The Physics of Fluids*, vol. 26, no. 3, pp. 673–677, 1983.
- [55] R. L. Dewar and A. Glasser, “Ballooning mode spectrum in general toroidal systems,” *The Physics of fluids*, vol. 26, no. 10, pp. 3038–3052, 1983.
- [56] B. Coppi and G. Rewoldt, “New trapped-electron instability,” *Physical Review Letters*, vol. 33, no. 22, p. 1329, 1974.

- [57] F. Merz and F. Jenko, “Nonlinear interplay of tem and itg turbulence and its effect on transport,” *Nuclear Fusion*, vol. 50, no. 5, p. 054005, 2010.
- [58] N. Bonanomi, P. Mantica, J. Citrin, T. Goerler, B. Teaca, and J. Contributors, “Impact of electron-scale turbulence and multi-scale interactions in the jet tokamak,” *Nuclear Fusion*, vol. 58, no. 12, p. 124003, 2018.
- [59] G. Hoang, C. Bourdelle, X. Garbet, G. Giruzzi, T. Aniel, M. Ottaviani, W. Horton, P. Zhu, and R. Budny, “Experimental determination of critical threshold in electron transport on tore supra,” *Physical review letters*, vol. 87, no. 12, p. 125001, 2001.
- [60] P. Hennequin, R. Sabot, C. Honoré, G. Hoang, X. Garbet, A. Truc, C. Fenzi, and A. Quéméneur, “Scaling laws of density fluctuations at high-k on tore supra,” *Plasma Physics and Controlled Fusion*, vol. 46, no. 12B, p. B121, 2004.
- [61] J. H. E. Proll, P. Helander, J. W. Connor, and G. Plunk, “Resilience of quasi-isodynamic stellarators against trapped-particle instabilities,” *Physical Review Letters*, vol. 108, no. 24, p. 245002, 2012.
- [62] R. Hastie, “Sawtooth instability in tokamak plasmas,” *Astrophysics and space science*, vol. 256, pp. 177–204, 1997.
- [63] J. P. Freidberg, “Ideal magnetohydrodynamics,” 1987.
- [64] S. Von Goeler, W. Stodiek, and N. Sauthoff, “Studies of internal disruptions and m=1 oscillations in tokamak discharges with soft—x-ray techniques,” *Physical Review Letters*, vol. 33, no. 20, p. 1201, 1974.
- [65] D. Campbell, R. Gill, C. Gowers, J. Wesson, D. Bartlett, C. Best, S. Coda, A. Costley, A. Edwards, S. Kissel, *et al.*, “Sawtooth activity in ohmically heated jet plasmas,” *Nuclear fusion*, vol. 26, no. 8, p. 1085, 1986.
- [66] Y. Nagayama, G. Taylor, M. Yamada, E. Fredrickson, A. Janos, and K. McGuire, “Ece image reconstruction of partial sawtooth crashes in ohmic plasmas,” *Nuclear fusion*, vol. 36, no. 4, p. 521, 1996.
- [67] H. Park, A. Donné, N. Luhmann Jr, I. Classen, C. Domier, E. Mazzucato, T. Munsat, M. Van De Pol, Z. Xia, T. team, *et al.*, “Comparison study of 2d images of temperature fluctuations during sawtooth oscillation with theoretical models,” *Physical review letters*, vol. 96, no. 19, p. 195004, 2006.
- [68] I. Chapman, “Controlling sawtooth oscillations in tokamak plasmas,” *Plasma Physics and Controlled Fusion*, vol. 53, no. 1, p. 013001, 2010.
- [69] J. Snipes, B. LaBombard, M. Greenwald, I. Hutchinson, J. Irby, Y. Lin, A. Mazurenko, and M. Porkolab, “The quasi-coherent signature of enhanced  $d\alpha$  h-mode in alcator c-mod,” *Plasma physics and controlled fusion*, vol. 43, no. 4, p. L23, 2001.
- [70] T. Dannert and F. Jenko, “Gyrokinetic simulation of collisionless trapped-electron mode turbulence,” *Physics of Plasmas*, vol. 12, no. 7, 2005.

- [71] F. Merz and F. Jenko, "Nonlinear saturation of trapped electron modes via perpendicular particle diffusion," *Physical review letters*, vol. 100, no. 3, p. 035005, 2008.
- [72] A. Melnikov, L. Eliseev, S. Lysenko, M. Ufimtsev, and V. Zenin, "Study of interactions between gamas and broadband turbulence in the t-10 tokamak," *Nuclear Fusion*, vol. 57, no. 11, p. 115001, 2017.
- [73] W. Zhong, Z. Shi, Z. Yang, G. Xiao, Z. Yang, B. Zhang, P. Shi, H. Du, X. Pan, R. Zhou, *et al.*, "Experimental observation of turbulence transition and a critical gradient threshold for trapped electron mode in tokamak plasmas," *Physics of Plasmas*, vol. 23, no. 6, 2016.
- [74] Y. Yang, M. Wan, W. H. Matthaeus, L. Sorriso-Valvo, T. N. Parashar, Q. Lu, Y. Shi, and S. Chen, "Scale dependence of energy transfer in turbulent plasma," *Monthly Notices of the Royal Astronomical Society*, vol. 482, no. 4, pp. 4933–4940, 2019.
- [75] J. Hirsch, B. Huberman, and D. Scalapino, "Theory of intermittency," *Physical Review A*, vol. 25, no. 1, p. 519, 1982.
- [76] V. Carbone, L. Sorriso-Valvo, E. Martines, V. Antoni, and P. Veltri, "Intermittency and turbulence in a magnetically confined fusion plasma," *Physical Review E*, vol. 62, no. 1, p. R49, 2000.
- [77] E. Mazzucato, "Microwave reflectometry for magnetically confined plasmas," *Review of Scientific Instruments*, vol. 69, no. 6, pp. 2201–2217, 1998.
- [78] F. Simonet, "Measurement of electron density profile by microwave reflectometry on tokamaks," *Review of scientific instruments*, vol. 56, no. 5, pp. 664–669, 1985.
- [79] P. Moreau, F. Clairet, J. Chareau, M. Paume, and C. Laviron, "Ultrafast frequency sweep heterodyne reflectometer on the tore supra tokamak," *Review of Scientific Instruments*, vol. 71, no. 1, pp. 74–81, 2000.
- [80] H. Bottollier-Curtet and G. Ichtchenko, "Microwave reflectometry with the extraordinary mode on tokamaks: Determination of the electron density profile of petula-b," *Review of scientific instruments*, vol. 58, no. 4, pp. 539–546, 1987.
- [81] F. Clairet, B. Ricaud, F. Briolle, S. Heuraux, and C. Bottereau, "New signal processing technique for density profile reconstruction using reflectometry," *Review of Scientific Instruments*, vol. 82, no. 8, 2011.
- [82] R. B. Morales, S. Heuraux, R. Sabot, S. Hacquin, F. Clairet, T. S. Team, *et al.*, "Reconstruction of hollow areas in density profiles from frequency swept reflectometry," *Plasma Science and Technology*, vol. 22, no. 6, p. 064005, 2020.
- [83] L. Vermare, F. Clairet, S. Heuraux, and G. Leclert, "Rational surface localization and mhd activity measurements using fast sweep reflectometry on tore supra," *Plasma physics and controlled fusion*, vol. 47, no. 11, p. 1895, 2005.
- [84] R. Sabot, F. Clairet, G. Conway, L. Cupido, X. Garbet, G. Falchetto, T. Gerbaud, S. Hacquin, P. Hennequin, S. Heuraux, *et al.*, "Recent results on turbulence and mhd activity achieved by reflectometry," *Plasma Physics and Controlled Fusion*, vol. 48, no. 12B, p. B421, 2006.

- [85] S. Sharapov, B. Alper, H. Berk, D. Borba, B. Breizman, C. Challis, A. Fasoli, N. Hawkes, T. Hender, J. Mailloux, *et al.*, “Alfvén wave cascades in a tokamak,” *Physics of Plasmas*, vol. 9, no. 5, pp. 2027–2036, 2002.
- [86] G. Hornung, *Study of plasma turbulence by ultrafast sweeping reflectometry on the Tore Supra tokamak*. PhD thesis, Aix-Marseille Université. École doctorale Physique et Sciences de la Matière, 2013.
- [87] C. Fanack, *Etude analytique et numérique de la réflectométrie dans un plasma fluctuant: modèles à une et deux dimensions*. PhD thesis, Nancy 1, 1997.
- [88] C. Fanack, I. Boucher, F. Clairet, S. Heuraux, G. Leclert, and X. Zou, “Ordinary-mode reflectometry: modification of the scattering and cut-off responses due to the shape of localized density fluctuations,” *Plasma physics and controlled fusion*, vol. 38, no. 11, p. 1915, 1996.
- [89] A. Krämer-Flecken, S. Soldatov, Y. Xu, and T. Zhang, “Correlation reflectometry in fusion plasmas—an application at textor,” *Plasma physics and controlled fusion*, vol. 53, no. 7, p. 074020, 2011.
- [90] J. Sanchez-Sanz and T. Estrada, “Diagnostic developments for the study of internal transport barriers,” *Plasma Physics and Controlled Fusion*, vol. 42, no. 12B, p. B341, 2000.
- [91] D. Prisiazhniuk, A. Krämer-Flecken, G. Conway, T. Happel, A. Lebschy, P. Manz, V. Nikolaeva, U. Stroth, A. U. Team, *et al.*, “Magnetic field pitch angle and perpendicular velocity measurements from multi-point time-delay estimation of poloidal correlation reflectometry,” *Plasma physics and controlled fusion*, vol. 59, no. 2, p. 025013, 2017.
- [92] C. Amador, R. Sabot, X. Garbet, Z. Guimarães-Filho, and J.-H. Ahn, “Determination of  $q$  during sawtooth from inverse evolution of baes in tore supra,” *Nuclear Fusion*, vol. 58, no. 1, p. 016010, 2017.
- [93] T. Windisch, A. Krämer-Flecken, J. Velasco, A. Könies, C. Nührenberg, O. Grulke, T. Klinger, *et al.*, “Poloidal correlation reflectometry at w7-x: radial electric field and coherent fluctuations,” *Plasma Physics and Controlled Fusion*, vol. 59, no. 10, p. 105002, 2017.
- [94] J. C. Hillesheim, *Studies of turbulence and flows in the DIII-D tokamak*. University of California, Los Angeles, 2012.
- [95] V. Vershkov, D. Shelukhin, S. Soldatov, A. Urazbaev, S. Grashin, L. Eliseev, A. Melnikov, *et al.*, “Summary of experimental core turbulence characteristics in ohmic and electron cyclotron resonance heated discharges in t-10 tokamak plasmas,” *Nuclear fusion*, vol. 45, no. 10, p. S203, 2005.
- [96] V. Vershkov, V. Andreev, A. Borshegovskiy, V. Chistyakov, M. Dremin, L. Eliseev, E. Gorbunov, S. Grashin, A. Khmara, A. Y. Kislov, *et al.*, “Recent results of the t-10 tokamak,” *Nuclear Fusion*, vol. 51, no. 9, p. 094019, 2011.

- [97] Y. Sun, R. Sabot, G. Hornung, S. Heuraux, S. Hacquin, and G. Verdoolaege, “Parametrization of reflectometry fluctuation frequency spectra for systematic study of fusion plasma turbulence,” *Review of Scientific Instruments*, vol. 89, no. 7, p. 073504, 2018.
- [98] Y. Sun, R. Sabot, S. Heuraux, X. Garbet, S. Hacquin, G. Hornung, and G. Verdoolaege, “Experimental trends of reflectometry frequency spectra emerging from a systematic analysis of the tore supra database,” *Physics of Plasmas*, vol. 26, no. 3, p. 032307, 2019.
- [99] M. Chowdhury and A. W. Sadek, “Advantages and limitations of artificial intelligence,” *Artificial intelligence applications to critical transportation issues*, vol. 6, no. 3, pp. 360–375, 2012.
- [100] R. Anirudh, R. Archibald, M. S. Asif, M. M. Becker, S. Benkadda, P.-T. Bremer, R. H. Budé, C.-S. Chang, L. Chen, R. Churchill, *et al.*, “2022 review of data-driven plasma science,” *arXiv preprint arXiv:2205.15832*, 2022.
- [101] A. Pavone, J. Svensson, A. Langenberg, U. Höfel, S. Kwak, N. Pablant, R. Wolf, *et al.*, “Neural network approximation of bayesian models for the inference of ion and electron temperature profiles at w7-x,” *Plasma Physics and Controlled Fusion*, vol. 61, no. 7, p. 075012, 2019.
- [102] A. Jalalvand, A. A. Kaptanoglu, A. V. Garcia, A. O. Nelson, J. Abbate, M. E. Austin, G. Verdoolaege, S. L. Brunton, W. W. Heidbrink, and E. Kolemen, “Alfvén eigenmode classification based on ece diagnostics at diii-d using deep recurrent neural networks,” *Nuclear Fusion*, vol. 62, no. 2, p. 026007, 2021.
- [103] R. Churchill, B. Tobias, Y. Zhu, D.-D. team, *et al.*, “Deep convolutional neural networks for multi-scale time-series classification and application to tokamak disruption prediction using raw, high temporal resolution diagnostic data,” *Physics of Plasmas*, vol. 27, no. 6, 2020.
- [104] R. Churchill, C. Chang, J. Choi, R. Wang, S. Klasky, R. Kube, H. Park, M. Choi, J. Park, M. Wolf, *et al.*, “A framework for international collaboration on iter using large-scale data transfer to enable near-real-time analysis,” *Fusion Science and Technology*, vol. 77, no. 2, pp. 98–108, 2021.
- [105] A. Pavone, J. Svensson, S. Kwak, M. Brix, R. Wolf, and J. Contributors, “Neural network approximated bayesian inference of edge electron density profiles at jet,” *Plasma Physics and Controlled Fusion*, vol. 62, no. 4, p. 045019, 2020.
- [106] C. Furia and R. Churchill, “Normalizing flows for likelihood-free inference with fusion simulations,” *Plasma Physics and Controlled Fusion*, vol. 64, no. 10, p. 104003, 2022.
- [107] J. Degraeve, F. Felici, J. Buchli, and Neunert, “Magnetic control of tokamak plasmas through deep reinforcement learning,” *Nature*, vol. 602, no. 7897, pp. 414–419, 2022.
- [108] S. Mallat, *A wavelet tour of signal processing*. Elsevier, 1999.

- [109] G. Kaiser, “Continuous wavelet transforms,” in *A Friendly Guide to Wavelets*, pp. 60–77, Springer, 2011.
- [110] I. Daubechies, “The wavelet transform, time-frequency localization and signal analysis,” *IEEE transactions on information theory*, vol. 36, no. 5, pp. 961–1005, 1990.
- [111] M. Farge, “Wavelet transforms and their applications to turbulence,” *Annual review of fluid mechanics*, vol. 24, no. 1, pp. 395–458, 1992.
- [112] C. Torrence and G. P. Compo, “A practical guide to wavelet analysis,” *Bulletin of the American Meteorological society*, vol. 79, no. 1, pp. 61–78, 1998.
- [113] K. Dragomiretskiy and D. Zosso, “Variational mode decomposition,” *IEEE transactions on signal processing*, vol. 62, no. 3, pp. 531–544, 2013.
- [114] N. E. Huang, Z. Shen, S. R. Long, M. C. Wu, H. H. Shih, Q. Zheng, N.-C. Yen, C. C. Tung, and H. H. Liu, “The empirical mode decomposition and the hilbert spectrum for nonlinear and non-stationary time series analysis,” *Proceedings of the Royal Society of London. Series A: mathematical, physical and engineering sciences*, vol. 454, no. 1971, pp. 903–995, 1998.
- [115] M. Van Steen, “Graph theory and complex networks,” *An introduction*, vol. 144, pp. 1–287, 2010.
- [116] B. Carreras, R. Balbin, B. Van Milligen, M. Pedrosa, I. Garcia-Cortes, E. Sanchez, C. Hidalgo, J. Bleuel, M. Ender, H. Thomsen, *et al.*, “Characterization of the frequency ranges of the plasma edge fluctuation spectra,” *Physics of Plasmas*, vol. 6, no. 12, pp. 4615–4621, 1999.
- [117] J. Zajac, E. Dufkova, V. Weinzettl, V. Budaev, and S. Nanobashvili, “Multifractal analysis of plasma turbulence in biasing experiments on castor tokamak,” *Czechoslovak Journal of Physics*, vol. 55, pp. 1615–1621, 2005.
- [118] F. Auger and P. Flandrin, “Improving the readability of time-frequency and time-scale representations by the reassignment method,” *IEEE Transactions on signal processing*, vol. 43, no. 5, pp. 1068–1089, 1995.
- [119] W. S. Noble, “What is a support vector machine?,” *Nature biotechnology*, vol. 24, no. 12, pp. 1565–1567, 2006.
- [120] S. Ding, X. Xu, and R. Nie, “Extreme learning machine and its applications,” *Neural Computing and Applications*, vol. 25, pp. 549–556, 2014.
- [121] M. Müller, “Dynamic time warping,” *Information retrieval for music and motion*, pp. 69–84, 2007.
- [122] L. Kaufman and P. J. Rousseeuw, *Finding groups in data: an introduction to cluster analysis*. John Wiley & Sons, 2009.
- [123] E. Schubert, J. Sander, M. Ester, H. P. Kriegel, and X. Xu, “DbSCAN revisited, revisited: why and how you should (still) use dbSCAN,” *ACM Transactions on Database Systems (TODS)*, vol. 42, no. 3, pp. 1–21, 2017.

- [124] A. Kaiser and T. Schreiber, “Information transfer in continuous processes,” *Physica D: Nonlinear Phenomena*, vol. 166, no. 1-2, pp. 43–62, 2002.
- [125] G. Dif-Pradalier, P. Ghendrih, Y. Sarazin, E. Caschera, F. Clairet, Y. Camenen, P. Donnel, X. Garbet, V. Grandgirard, Y. Munschy, *et al.*, “Transport barrier onset and edge turbulence shortfall in fusion plasmas,” *Communications Physics*, vol. 5, no. 1, p. 229, 2022.
- [126] B. P. Van Milligen, U. Hoefel, J. Nicolau, M. Hirsch, L. García, B. Carreras, C. Hidalgo, *et al.*, “Study of radial heat transport in w7-x using the transfer entropy,” *Nuclear Fusion*, vol. 58, no. 7, p. 076002, 2018.
- [127] X. Zhu and Z. Ghahramani, “Learning from labeled and unlabeled data with label propagation,” *ProQuest Number: INFORMATION TO ALL USERS*, 2002.
- [128] M. Morikawa and A. Nakamichi, “A simple model for pink noise from amplitude modulations,” *arXiv preprint arXiv:2301.11176*, 2023.
- [129] A. Krämer-Flecken, S. Soldatov, Y. Xu, H. Arnichand, S. Hacquin, R. Sabot, T. team, *et al.*, “Long-range correlation properties of quasi-coherent modes at textor,” *New journal of physics*, vol. 17, no. 7, p. 073007, 2015.
- [130] A. Krämer-Flecken, V. Dreval, S. Soldatov, A. Rogister, V. Vershkov, *et al.*, “Turbulence studies with means of reflectometry at textor,” *Nuclear fusion*, vol. 44, no. 11, p. 1143, 2004.
- [131] L. Salazar, S. Heurax, R. Sabot, A. Krämer-Flecken, T. S. Team, T. Team, *et al.*, “Extraction of quasi-coherent modes based on reflectometry data,” *Plasma physics and controlled fusion*, vol. 64, no. 10, p. 104007, 2022.
- [132] S. Neudatchin, D. Shelukhin, and N. Mustafin, “Peculiar properties of internal transport barrier formation near the  $q=1$  and  $q=2$  surfaces in tokamaks,” in *Journal of Physics: Conference Series*, vol. 907, p. 012015, IOP Publishing, 2017.
- [133] Y. Shi, W. Ko, J. Kwon, P. Diamond, S. Lee, S. Ko, L. Wang, S. Yi, K. Ida, L. Terzolo, *et al.*, “Ech effects on toroidal rotation: Kstar experiments, intrinsic torque modelling and gyrokinetic stability analyses,” *Nuclear Fusion*, vol. 53, no. 11, p. 113031, 2013.
- [134] V. Vershkov, D. Sarychev, G. Notkin, D. Shelukhin, M. Buldakov, Y. N. Dnestrovskij, S. Grashin, N. Kirneva, V. Krupin, L. Klyuchnikov, *et al.*, “Review of recent experiments on the t-10 tokamak with all metal wall,” *Nuclear Fusion*, vol. 57, no. 10, p. 102017, 2017.
- [135] A. Kramer-Flecken, “Observation of quasi coherent modes in w7-x and relation to tokamaks.” 2023.
- [136] J. Candy, E. A. Belli, and R. Bravenec, “A high-accuracy eulerian gyrokinetic solver for collisional plasmas,” *Journal of Computational Physics*, vol. 324, pp. 73–93, 2016.
- [137] N. Cao, J. Rice, P. Diamond, A. White, S. Baek, M. Chilenski, J. Hughes, J. Irby, M. Reinke, P. Rodriguez-Fernandez, *et al.*, “Hysteresis as a probe of turbulent bifurcation in intrinsic rotation reversals on alcator c-mod,” *Nuclear Fusion*, vol. 59, no. 10, p. 104001, 2019.

- 
- [138] N. Cao, J. Rice, P. Diamond, A. White, M. Chilenski, P. Ennever, J. Hughes, J. Irby, M. Reinke, P. Rodriguez-Fernandez, *et al.*, “Evidence and modeling of turbulence bifurcation in l-mode confinement transitions on alcator c-mod,” *Physics of Plasmas*, vol. 27, no. 5, 2020.
- [139] K. Kaheman, J. N. Kutz, and S. L. Brunton, “Sindy-pi: a robust algorithm for parallel implicit sparse identification of nonlinear dynamics,” *Proceedings of the Royal Society A*, vol. 476, no. 2242, p. 20200279, 2020.
- [140] J. Hsin, S. Agarwal, A. Thorpe, and D. Fridovich-Keil, “Gpsindy: Data-driven discovery of equations of motion,” *arXiv preprint arXiv:2309.11076*, 2023.
- [141] V. V. Vasiliev and L. V. Fedorov, “To the schwarzschild solution in general relativity,” *Journal of Modern Physics*, vol. 9, no. 14, pp. 2482–2494, 2018.
- [142] D. Gabor, “Theory of communication. part 1: The analysis of information,” *Journal of the Institution of Electrical Engineers-part III: radio and communication engineering*, vol. 93, no. 26, pp. 429–441, 1946.
- [143] Y. Li and H. Wu, “A clustering method based on k-means algorithm,” *Physics Procedia*, vol. 25, pp. 1104–1109, 2012.
- [144] D. Sculley, “Web-scale k-means clustering,” in *Proceedings of the 19th international conference on World wide web*, pp. 1177–1178, 2010.
- [145] D. Arthur and S. Vassilvitskii, “K-means++ the advantages of careful seeding,” in *Proceedings of the eighteenth annual ACM-SIAM symposium on Discrete algorithms*, pp. 1027–1035, 2007.

## Abstract

One way to achieve fusion on Earth is through toroidal magnetic confinement, in which the main devices are tokamaks and stellarators. One of the main limiting phenomena is turbulence. This is the result of a mixture of instabilities on different temporal and spatial scales. The aim of this thesis was to contribute to the understanding of turbulent transport, which is the interaction of this turbulence with the plasma properties, in magnetically confined plasmas, focusing on the characterisation of density fluctuations and their dynamics using reflectometry.

From the signal spectrum provided by reflectometry, each spectral component was extracted using an algorithm developed in this thesis. It performs this spectral decomposition (Low frequency component, Broadband component, QC modes and noise) in an intelligent way (without ad hoc constraints), preserving its statistical and physical information. Particular attention has been paid to a specific spectral component, the so-called QC modes because of its link with TEM, an instability acting in turbulent transport.

Thanks to the algorithm, the properties and dynamics of the QC modes have been studied, allowing a statistical study and a detailed analysis of the interaction with other spectral components in different magnetic configurations: ToreSupra (limiter), WEST (divertor) and W7X (island divertor). This work is qualified as exploratory because there were no methods to access these QC mode properties and dynamics.

The statistical studies carried out with the ToreSupra and WEST database provided a probability map of the occurrence of the QC modes in the ohmic confinement regime, confirming their link with the TEM, but also 2 more classes, one at low current and another at high current were found.

The broadband component was also analysed as it is thought to be related to the microturbulence. Since the spectral amplitude of the BB component is computed with the Asymmetric Generalised Gaussian (AGG), mainly  $\mu$  and  $\beta$ , which correspond to the asymmetry and shape of the spectrum, show a variation during the transition.

On the other hand, the analysis of the dynamics of the QC modes by means of an algorithm developed in this thesis showed a recurrent interaction between the QC modes and the modes in the LF component. Finally, in order to better discriminate the QC modes, the concept of transfer entropy is used to analyse the causality in this interaction. Some cases show the interaction between the LF component corresponding to the sawtooth instability and the QC modes. All this analysis of dynamics and also causality is then applied to ToreSupra, WEST and W7X, where there is a similar dynamic for signals with bi-directional causality, i.e. not only from the LF component to the QC modes, but also from the QC modes to the BB component. In addition, the ECRH is also examined for the TS database, which shows a decrease in the probability of QC modes as the ECRH power increases. Since these QC modes appear in different magnetic configurations, the ultimate objective is to discover if all these QC modes are produced by the same mechanism, since it is believed that there must be a universal mechanism underlying the physics in fusion plasmas, this is still under investigation.

## Résumé

L'un des moyens de parvenir à la fusion sur Terre est le confinement magnétique toroïdal, dont les principaux dispositifs sont les tokamaks et les stellarators. L'un des principaux

paramètres limitants est la turbulence, qui résulte d'un mélange d'instabilités à différentes échelles temporelles et spatiales. L'objectif de cette thèse est de contribuer à la compréhension du transport turbulent, qui est l'interaction de cette turbulence avec les propriétés du plasma, dans les plasmas magnétiquement confinés, en se concentrant sur la caractérisation des fluctuations de densité et de leur dynamique à l'aide de la réflectométrie.

A partir du spectre du signal fourni par la réflectométrie, chaque composante spectrale a été extraite à l'aide d'un algorithme développé dans cette thèse. Il effectue cette décomposition spectrale (composante LF, composante BB, modes QC et bruit) de manière intelligente (sans contraintes ad hoc), en préservant ses informations statistiques et physiques. Une attention particulière a été accordée à une composante spectrale, les modes QC, en raison de son lien avec TEM, une instabilité agissant dans le transport turbulent.

Grâce à l'algorithme, les propriétés et la dynamique des modes QC ont été étudiées, permettant une étude statistique et une analyse détaillée de l'interaction avec d'autres composantes spectrales dans différentes configurations magnétiques : ToreSupra (limiteur), WEST (divertor) et W7X (island divertor). Ce travail est qualifié d'exploratoire car il n'existait pas de méthodes permettant d'accéder aux propriétés et à la dynamique de ces modes QC.

Les études statistiques réalisées avec les bases de données ToreSupra et WEST ont fourni une carte de probabilité de l'occurrence des modes QC dans le régime de confinement ohmique, confirmant leur lien avec le TEM, mais aussi 2 classes supplémentaires, l'une à faible courant et l'autre à fort courant, ont été trouvées.

La composante BB a également été analysée, car elle est liée à la microturbulence. Puisque l'amplitude spectrale de la composante BB est trouvée avec l'AGG, principalement  $\mu$  et  $\beta$ , qui correspondent à l'assymétrie et à la forme du spectre, montrent une variation au cours de la transition.

D'autre part, l'analyse de la dynamique des modes QC au moyen d'un algorithme développé dans cette thèse a montré une interaction récurrente entre les modes QC et les modes de la composante BF. Enfin, afin de mieux discriminer les modes QC, le concept d'entropie de transfert est utilisé pour analyser la causalité dans cette interaction. Certains cas montrent l'interaction entre la composante LF correspondant à l'instabilité sawtooth et les modes QC. Cette analyse de la dynamique et de la causalité est ensuite appliquée à ToreSupra, WEST et W7X, où l'on observe une dynamique similaire pour les signaux à causalité bidirectionnelle, c'est-à-dire non seulement de la composante LF vers les modes QC, mais aussi des modes QC vers la composante BB. En outre, l'ECRH est également examiné pour la base de données TS, qui montre une diminution de la probabilité des modes QC à mesure que le PECRH augmente. Comme ces modes QC apparaissent dans différentes configurations magnétiques, l'objectif ultime est de découvrir si tous ces modes QC sont produits par le même mécanisme, car on pense qu'il doit y avoir un mécanisme universel sous-jacent à la physique dans les plasmas de fusion, sujet qui est encore à l'étude.



# Appendix A

## Exploratory phase for spectral components discrimination

Once the pathological signals have been removed, the search for discrimination of the spectral components can begin. As mentioned in Chapter 2, turbulence is the result of different instabilities with possible energy exchange between their different components, so distinguishing them is complex. However, several approaches can be tried from the general roadmap described in Chapter 4.

### A.1 First attempt: direct classification

First, a direct classification of the different instability components was attempted on the raw signals. This method used the DBSCAN, a clustering technique described in the previous chapter, and the metric concept, which aimed to find a vector space in which the different components could be separated.

The metric concept of general relativity was explored, characterised by a variable tensor field over elements [141]. The central idea was to find invariant values by optimising the  $\alpha$  and  $\beta$  coefficients [see equation A.1]. After this process, DBSCAN was used to search for density clusters over the metric representation:

$$\text{Signal} : R(t) = A_{(t)} \cdot e^{\phi(t)}, dM^2 = \alpha_{(\phi)} \cdot dA^2 + \beta_{(t)} \cdot dt^2 \quad (\text{A.1})$$

These different clusters would give an idea of the energy transfer rate. Although some structures emerged [see figure A.1], it was difficult to identify the components, the main problem being the computing time and the huge amount of data. This route was not taken in this first step.

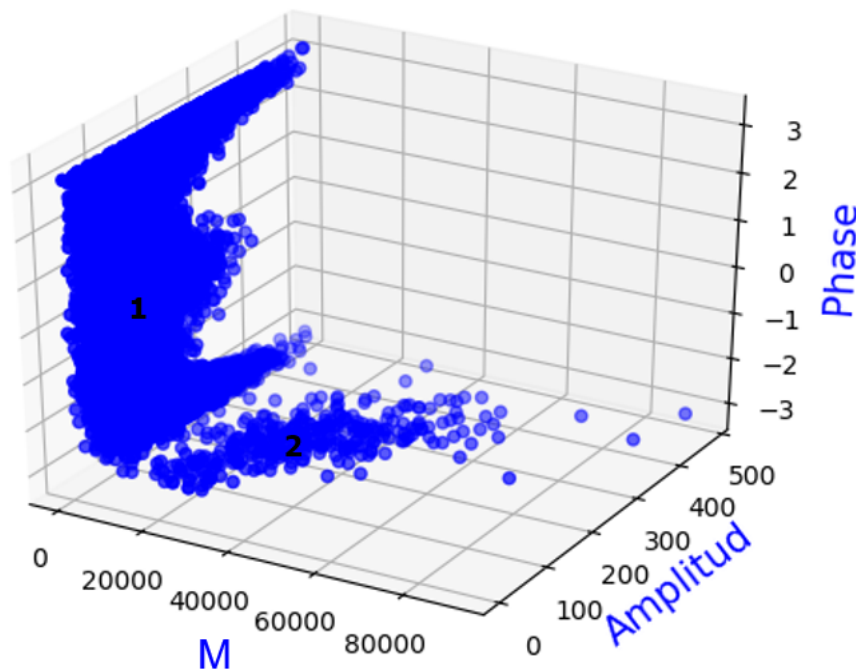


Fig. A.1 Emerging structures (1 and 2) found with M (metric vector) and DBSCAN algorithm from a signal belonging to the shot TS #48002.

It is clear from this analysis that direct application of clustering to the raw reflectometry signal for classification is not appropriate. This is due to the lack of a priori knowledge of potential emerging clusters and the mixing of different time scales. As a result, a preliminary data transformation prior to the classification process is essential to cope with the complexity of the signals.

## A.2 Second attempt: data cleaning

The idea here was to perform data cleaning in either the time domain or the frequency domain to reduce the uncertainty from the spectral components.

In the time domain, "classical methods" were tried on the signal amplitude ( $|R(t)|$ ), such as the convolution of the signal with a specific kernel to find patterns along the signal, and locally weighted scatter-plot smoothing (LOESS) to achieve smoothing as described in section 4.2 [see figure A.2], but the uncertainty was too high due to the lack of information on the temporal shape of the different spectral components. And when constructing the power spectral density (PSD) of the smoothed signal, the spectral components couldn't be properly identified because of the lack of information on their spectral shape and because the noise in each frequency bin couldn't be estimated.

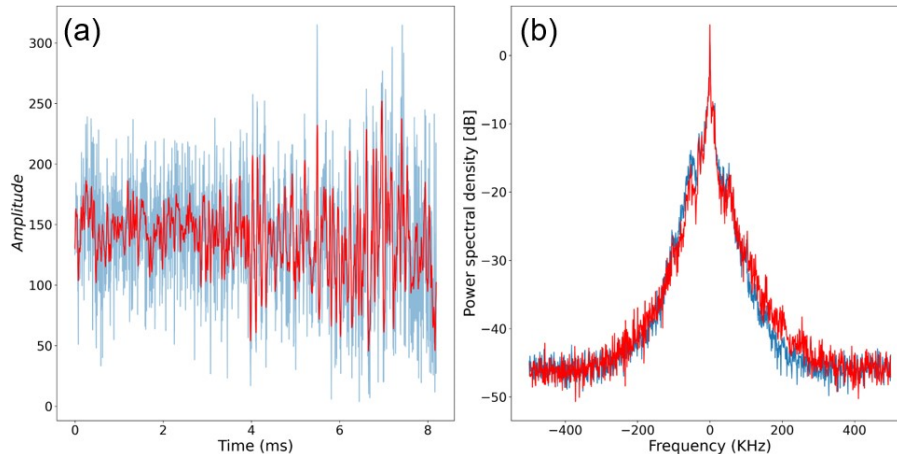


Fig. A.2 (a) Original amplitude signal (blue) and the smoothed amplitude signal (red). (b) PSD of the original signal (blue) and the smoothed signal (red).  $I_p = 1MA$ ,  $n_e = 2.6 \times 10^{19}m^{-3}$  and  $\rho = 0.15$ . ToreSupra discharge #31104.

Analysis of reflectometry signals in either the time or frequency domain is limited. In the time domain, different scales can be mixed at different times. Frequency domain analysis, as described in the previous study [see section 3.7], implies stationarity: invariance of the turbulence properties over time. To get rid of this stationarity, it's necessary in this study to take into account both the time and the frequency domain to finally get access to the dynamics of the spectral components.

### A.3 Third attempt: data transformation

Finally, a transformation that takes into account the time and frequency of the signal was sought to highlight its characteristics.

As proposed by Gabor in his theory of communication [142], "time-frequency atoms" are required, which have a minimal spread in a time-frequency plane: the idea is to decompose the signal over a dictionary of elementary waves.

In this approach, the short-time Fourier transform was used as a first attempt to access their dynamics. However, the Heisenberg box (TF tiling) associated with this transform is constant along the frequency and time axes [see figure 4.2], resulting in a mixture of time and frequency scales due to the convolution between the time-window Fourier transform and the observed frequencies, leading to a blurred time-frequency representation.

On the other hand, the wavelet transform provides a variable Heisenberg box in the TFR [see figure 4.2]. Within the wavelet transform, the Discrete Wavelet Transform (DWT), the Undecimated Wavelet Transform (UWT) and the Stationary Wavelet Transform (SWT),

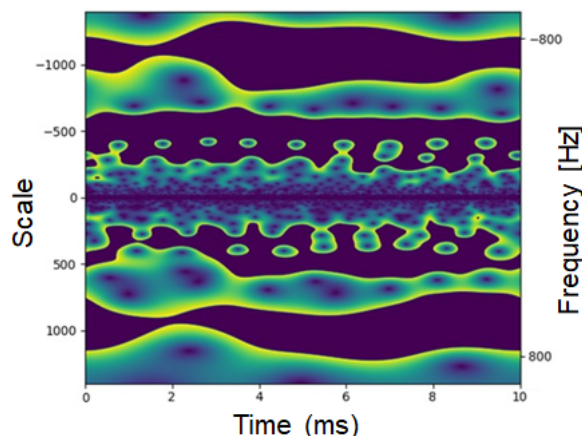


Fig. A.3 Patterns identified by the Autoencoder neural network corresponding to large scales (small frequencies)

which are orthogonal projections of the signal, have been used to remove noise and to try to access different modes. However, a non-orthogonal projection proved to be necessary to deal with fluctuations. This can be done using the Continuous Wavelet Transform.

In the context of reflectometry signals (complex-valued signals), a complex wavelet must be used to deal with angle (position) and modulus (energy). The complex Morlet wavelet [see equation A.2] is the one chosen, and also because it is useful in detecting fluctuations, our main objective.

$$\psi_{Morlet}(t) = |s|^{-0.5} \cdot \pi^{-0.25} \cdot e^{6(\frac{t-f_s}{s})j} \cdot e^{-0.5(\frac{t-f_s}{s})^2}$$

$s$  : scale (A.2)

$f_s$  : frequency sampling

A convolutional autoencoder neural network was attempted to highlight patterns across scales and time [see figure A.3]. The key idea in this approach was to divide the CWT spectrum into several time windows, then take each of them as input to try to build the latent space [see section 4.2]; this approach assumed the same distribution of latent parameters all along the signal duration. This architecture would look for intrinsic features in the CWT spectrum.

The main limitations were computation time and learning. The CWT approach was found to be suitable for highlighting patterns, but additional algorithms were needed to deal with the characteristics of the different spectral components in order to extract them.

Given the presence of different spectral components, it's necessary to reduce the complexity within the reflectometry signal spectrum by extracting these different spectral components.

From this, the QC modes are chosen to be extracted first, due to their properties as pointed out in the 2.5.2 section.



# Appendix B

## Extraction of the QC modes: Initial algorithm

A description of this first extraction algorithm is given in the figure B.1. The main steps in this algorithm are the screening technique and a clustering technique. The first technique is designed to exploit the cross-correlation and density energy properties of the QC modes and the second technique involves a vector space projection and a clustering algorithm to pick up the part of the signal corresponding to the QC modes. However, this approach could lead to the inclusion of elements irrelevant to QC mode characterisation.

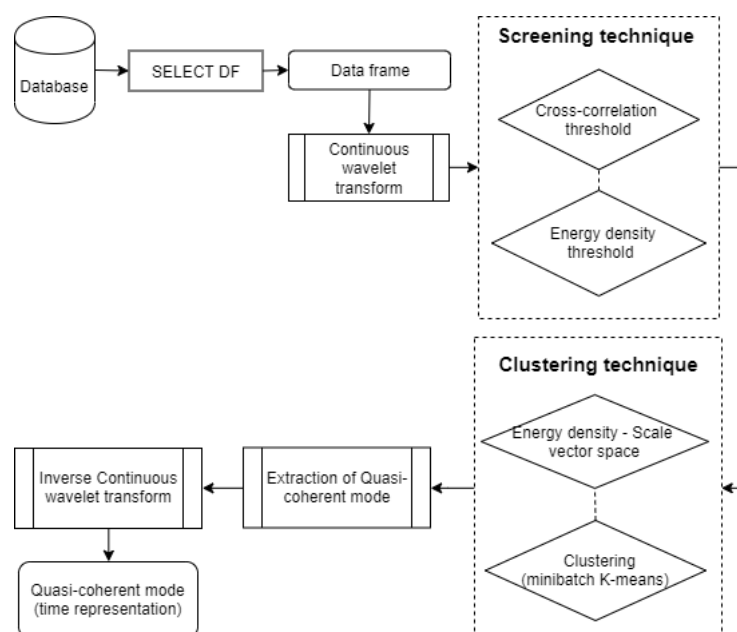


Fig. B.1 Data-flow diagram: rounded rectangle for data, rectangle double line for process and rhombus for proposed techniques.

To describe this first extraction algorithm, the complex-valued reflectometry signal from the Tore Supra database, shot #32093,  $t = [11.1151; 11.1397\text{s}]$  and  $F = 118.8\text{ GHz}$ , which exhibits strong QC modes, is used as an illustrative example.

## B.1 Screening technique

The CWT is obtained from the reflectometry signal ( $R_t$ ) [Figure B.2 (a)] and a minimum frequency is manually set prior to screening to exclude the frequencies associated with the LF component. The reference scale in the CWT is a scale where the averaged energy density (ED) represents a local maximum over time, this is called the high-ED scale  $s_{hed}$  and is located in the frequency range associated with the QC mode. There is a separate reference scale for negative ( $s_{hed}^-$ ) and positive ( $s_{hed}^+$ ) scales [see figure B.2 (b)].

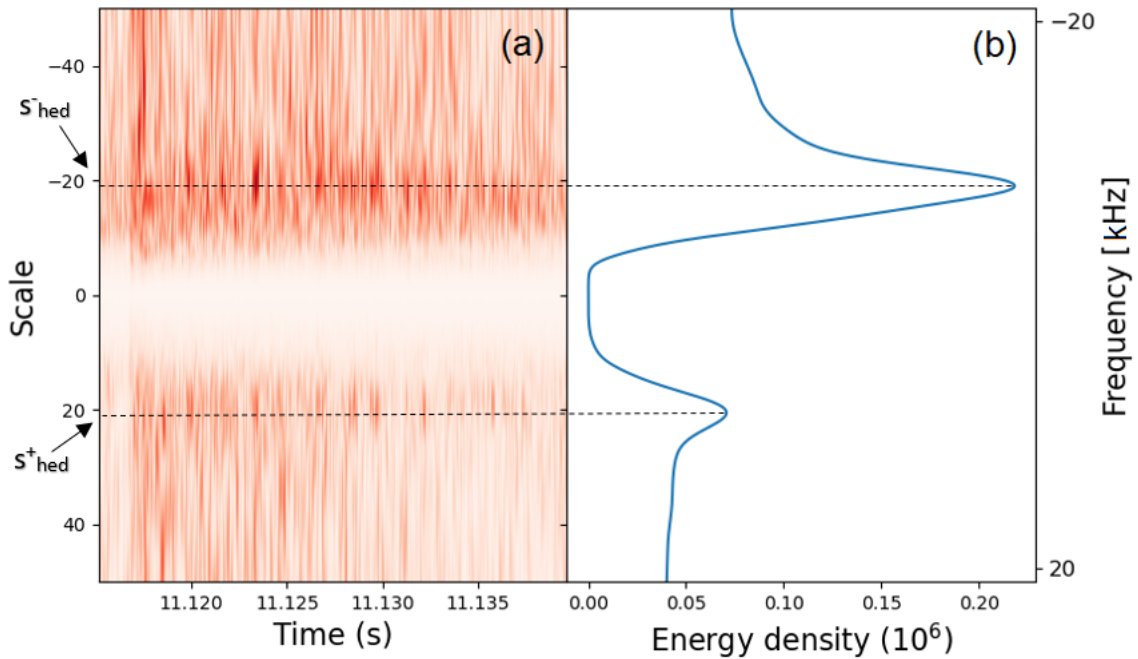


Fig. B.2 CWT modulus of (a)  $f(t)$  and (b) the averaged ED as a function of scales.

Hard thresholding techniques are used for this screening. The cross-correlation (CC) threshold, which is used for all signals from each discharge (in this case from the Tore Supra database), is estimated from reflectometry measurements with strong QC amplitude ( $G_t$ ), because the QC modes are more likely to be distinguished from other spectral components. These latter  $G_t$  signals belong to the Tore Supra shot range of #32263 – #32265, i.e. 3

discharges and 20 signals. The energy density (ED) threshold is calculated separately for each signal.

- CC threshold: This threshold, based on the minimum CC for existence of QC modes, is used as a threshold to enhance the SNR, and the latter can be deduced from B.1:

$$SNR = \frac{\mu(|CWT_{G_t}(s,t)|)}{\sigma(|CWT_{G_t}(s,t)|)} \quad (\text{B.1})$$

where  $CWT_{G_t}(s,t)$  is the CWT of the chosen signal  $G(t)$ .  $\mu$  and  $\sigma$  correspond to the mean and standard deviation, respectively. The threshold is then estimated:

$$Threshold_{CC} \approx \frac{\sum_{n=1}^{N=20} SNR_n}{20} \quad (\text{B.2})$$

Then, for each signal  $R_t$ , a CC operation is performed between shed and other scales  $s$  (either positive or negative scales) and then normalised by their standard deviation,  $\sigma_{shed}$  and  $\sigma_s$  respectively, as shown in the following equation:

$$CC_{normalized}(R,s) = \frac{|s_{shed}(t)|^2 \otimes |s(t)|^2}{\sigma_{shed} \cdot \sigma_s} \quad (\text{B.3})$$

Finally, hard thresholding ( $T_{h1}$ ) is applied (figure B.3):

$$T_{h1} = \begin{cases} CWT_{R_t}(s,t), & |CC_{normalized}| \geq Threshold_{CC} \\ 0, & |CC_{normalized}| < Threshold_{CC} \end{cases} \quad (\text{B.4})$$

- ED threshold: This threshold is based on the minimum ED for existence of QC modes. In that regard, for a signal  $R_t$ , every  $|CWT_{R_t}(s,t)|^2$  from all  $s$  and  $t$  is taken, and projected into a one dimensional vector. In the beginning, a tentative of the estimation was done on its probability density function by doing convolutions with predefined kernels, such as Gaussian and cosine kernels. Nevertheless, it was not efficient because of the low precision in distinguishing components. This led us to a parametric approach, in which we could predefine the number of components or clusters.

Since the LF component is not considered, the remaining components are: the BB component, the noise and the QC modes as a third component. Three clusters are then selected as input to apply the K-means algorithm [143] [see section 4.2.5], an unsupervised machine learning algorithm that minimises the intra-cluster variances. The K-means algorithm allows a separation of these 3 clusters within the one dimensional

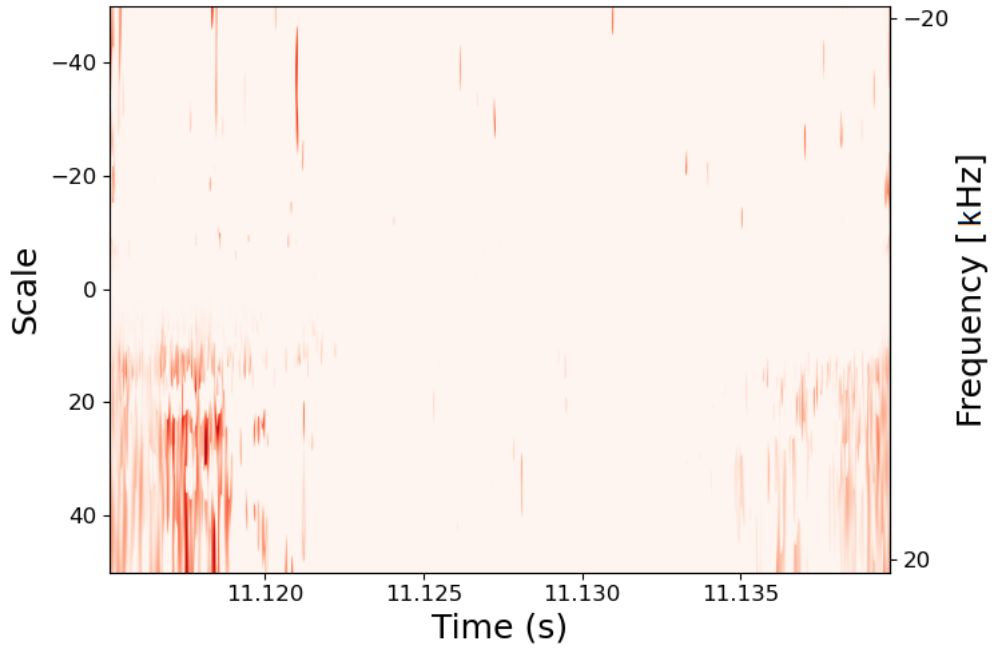


Fig. B.3  $|CWT_{R_t}(s, t)|$  after CC threshold for signal from Tore Supra shot #32093,  $t = [11.1151; 11.1397\text{s}]$  and  $F = 118.8\text{ GHz}$ .

vector formed by the  $|CWT_{R_t}(s, t)|^2$  values and gives then the boundaries among them ( $max1$  and  $max2$ ):

$$\begin{aligned}
 ED_{(cluster1)} &\in [min1, max1]; \\
 ED_{(cluster2)} &\in [max1, max2]; \\
 ED_{(cluster3)} &\in [max2, max3]
 \end{aligned}
 \tag{B.5}$$

as the noise must be represented by the cluster having the lowest  $|CWT_{R_t}(s, t)|^2$  values (cluster1) and the QC modes can be located either at cluster2 or cluster2, the noise superior limit ( $max1$ ) is taken as the reference for the existence of QC modes taking into account its ED properties:

$$Threshold_{ED} \approx max1
 \tag{B.6}$$

Finally, hard thresholding ( $T_{h2}$ ) is applied (Fig B.4):

$$T_{h2} = \begin{cases} CWT_{R_i}(s,t), & |CWT_{R_i}(s,t)|^2 \geq Threshold_{ED} \\ 0, & |CWT_{R_i}(s,t)|^2 < Threshold_{ED} \end{cases} \quad (B.7)$$

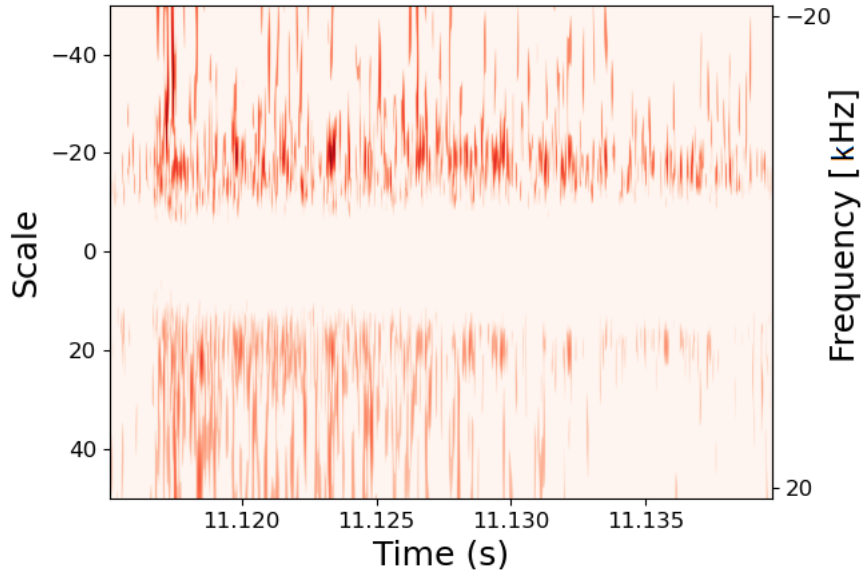


Fig. B.4  $|CWT_{R_i}(s,t)|$  after ED threshold for signal from Tore Supra shot #32093,  $t = [11.1151; 11.1397s]$  and  $F = 118.8$  GHz.

The objective is to carry out a mesh that is able to capture at least the QC modes and thus to eliminate the majority of the noise. To achieve this goal, the ED and CC "patterns" resulting from the hard thresholding are subjected to a union operation to combine the properties of the ED and CC thresholds:

$$CWT_{R_i}(s,t)_{screened} = T_{h1} \cup T_{h2} \quad (B.8)$$

## B.2 Clustering technique

Once the screening technique has been performed separately for negative and positive scales, a second process is required to extract the QC modes from the screened CWT representation.

- ED vector space: The choice of this vector space relies on combining the properties of the ED and CWT scales (named  $s$ ) identified by the screening technique. This vector

space follows the characteristics of a Euclidean space ( $\mathbb{R}^2$ ). First, all  $|CWT_{R_t}(s,t)|^2$  and  $s$  belonging to  $CWT_{R_t}(s,t)_{screened}$  are normalized as the following:

$$s_{normalized} = \frac{s}{s_{max}}$$

$$|CWT_{R_t}(s,t)|_{normalized}^2 = \frac{|CWT_{R_t}(s,t)|^2}{|CWT_{R_t}(s,t)|_{max}^2} \quad (\text{B.9})$$

Then, the vector space is set as following:

$$\mathbf{V} = (s_{normalized}, |CWT_{R_t}(s,t)|_{normalized}^2) \quad (\text{B.10})$$

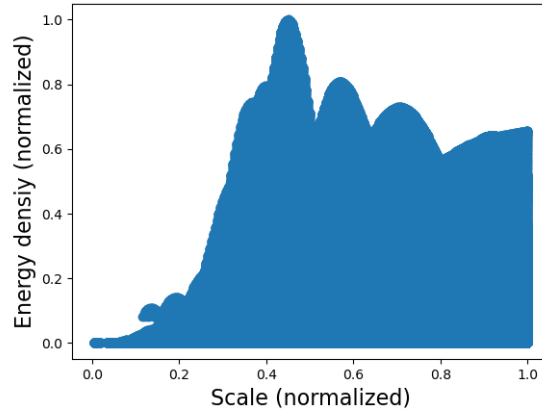


Fig. B.5 Projection of  $CWT_{R_t}(s,t)_{screened}$  into ED-scale vector space.

- Clustering

This part seeks to identify the QC mode cluster in the vector space  $\mathbf{V}$  [see figure B.6]. It is based on the mini-batch K-means; compared to the K-means algorithm, the main idea is to use small random batches of examples of a fixed size, so that they can be stored in memory. In each iteration, a new random sample from the data set is obtained and used to update the clusters, and this is repeated until convergence [144].

As discussed previously, the number of components or clusters existing is equal to 3. Some other parameters have to be set also for the mini-batch K-means algorithm: k-means++ method [145] for initialization of cluster centers, batch size equal to 1024 and the random state for random number generator equal to 0 [see section 4.2.5]. This algorithm is thus applied into the ED-scale vector space  $\mathbf{V}$ .

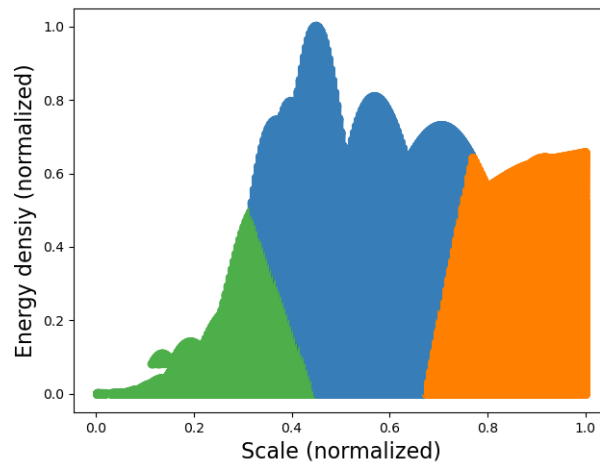


Fig. B.6 Clustering technique on  $\mathbf{V}$  by mini-batch K-means, noise cluster (green), QC cluster (blue) and BB cluster (orange).

The QC mode cluster is identified thanks to the  $s_{hed}$  previously selected. This scale must be present in the QC cluster. As mentioned before, this procedure is performed separately for negative and positive scales. Once the QC mode clusters are identified for both, they are projected back into the CWT space for reconstruction and the Inverse Continuous Wavelet Transform (ICWT) is applied to obtain the QC mode cluster in time representation [see figure B.7].

Thus, we can obtain the frequency spectrum of the initial signal, the QC modes and the initial signal without QC modes [see figure B.8].

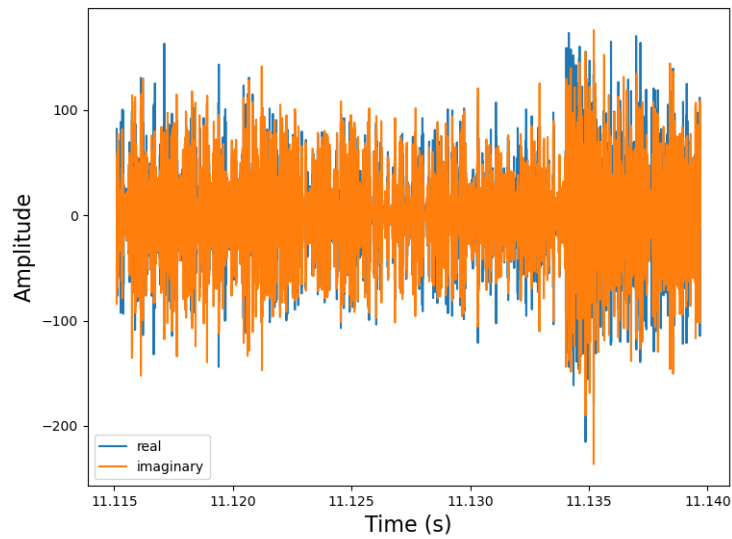


Fig. B.7 Time plot of the QC modes. Blue and orange curves represent the real and imaginary parts, respectively.

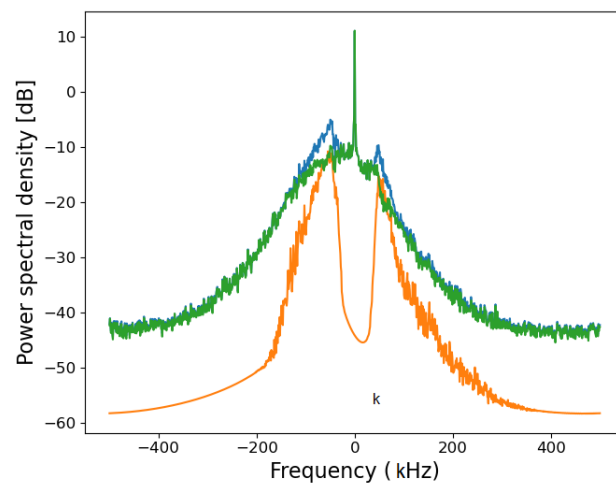


Fig. B.8 Frequency spectrum of initial signal (blue curve), QC modes (orange curve) and signal after extraction of QC modes (green curve).

## **Appendix C**

# **Spectral decomposition of the LF component**

The MCVMD, as described in section 4.2, is used to decompose the LF component into the central peak corresponding to the direct reflection, two co-lateral spectral components (one for negative frequencies and the other for positive frequencies) and the noise.

